A HIGH RESOLUTION STUDY OF PROTON RESONANCES IN ^{57}Co

by

William Alter Watson III

Department of Physics
Duke University

A dissertation submitted in partial fulfillment of the requirements for the degree of Doctor of Philosophy in the Department of Physics in the Graduate School of Arts and Sciences of Duke University

1980

ABSTRACT

(Physics)

A HIGH RESOLUTION STUDY OF PROTON RESONANCES IN ^{57}Co

by

William Alter Watson III

Department of Physics
Duke University

An abstract of a dissertation submitted in partial fulfillment of the requirements for the degree of Doctor of Philosophy in the Department of Physics in the Graduate School of Arts and Sciences of Duke University

1980

A HIGH RESOLUTION STUDY OF PROTON RESONANCES IN ^{57}Co

by

William Alter Watson III

Excitation functions for the reactions $^{56}Fe(p,p)$ and $^{56}Fe(p,p')$ were measured from E_p = 3.1 to 4.0 MeV at laboratory angles of 89°, 106°, 124°, 149°, and 160°. These experiments were performed using the high resolution system of the TUNL FN tandem accelerator; the overall energy resolution varied between 420 and 500 eV. The excitation functions were analyzed with a multi-level, multi-channel R-matrix formalism. Over 340 resonances were observed, about half of which were d-wave resonances. Angular distributions of de-excitation γ-rays were measured for those ℓ=2 resonances with appreciable inelastic cross sections, as well as for selected ℓ=1 resonances (a total of about 140 resonances). The γ-ray data was of particular value in determining the j-value for certain resonances.

Isobaric analogues of the following states in ^{57}Fe were observed: the $5/2^-$ state at 2.207 MeV, the $9/2^+$ state at 2.445 MeV, the $5/2^+$ state at 2.506 MeV, the $3/2^-$ state at 2.565 MeV, and the $1/2^-$ state at 2.697 MeV. Each of these analogue states had observable fine structure. The distributions were fit to a theoretical curve to obtain

values for the analogue state energies, reduced widths, spreading widths, and asymmetry parameters. Spectroscopic factors were calculated and compared with the parent state spectroscopic factors obtained in (d,p) studies.

The statistical properties of the observed levels were investigated in terms of the random matrix theory. Reduced width distributions were calculated and show good agreement with the Porter-Thomas distribution. The comparison also provides an estimate of the number of weak levels unobserved. Nearest neighbor spacing distributions were calculated for the $1/2^+$, $1/2^-$, $3/2^-$, $3/2^+$, and $5/2^+$ sequences and compared with the Wigner distribution. These spacing distributions are also compared with a more exact distribution derived from the orthogonal ensemble in which higher order spacing distributions are included to compensate for missing levels. In this latter comparison, the agreement is quite good and is limited only by the smallness of the sample sets.

The $1/2^+$ level sequence is found to be quite pure--having no or few missing or spurious levels. This set of 56 s-wave resonances is probably the best set of proton resonances (for statistical studies) observed to date, and is comparable in quality to the neutron data sets which form the bulk of the experimental evidence for the random matrix theory. The results of statistical tests of the quality of the data set (the Dyson F-statistic and the Dyson-Mehta Δ_3 statistic) are consistent with no (or few) missing levels.

In addition, good agreement is found between the experimental and theoretical values of the adjacent spacing correlation coefficient and the widths of the k-th order spacing distributions for k=0 to 10.

Strength functions were calculated for each of the sequences for which sufficient levels were observed ($1/2^+$, $1/2^-$, $3/2^-$, $3/2^+$, and $5/2^+$). The effects of missing levels were included in the calculation. General agreement with previous work is found.

The spin dependence of the level density is calculated, again including the correction for missing levels. Good agreement is found with Gilbert and Cameron's (1965) prediction for the spin cutoff parameter.

ACKNOWLEDGEMENTS

I would like to offer a sincere thanks to my advisor, Dr. E. G. Bilpuch, for his support and encouragement during my graduate studies. His understanding during the last six months is especially appreciated. I am greatly indebted to Dr. G. E. Mitchell for many interesting and helpful discussions, as well as for help in the preparation of this dissertation.

A special thanks goes to C. R. Westerfeldt for many patient hours spent repairing equipment, and for his help in running the experiments. Additional thanks go to Dr. K. B. Sales, K. M. Whatley, and Dr. B. H. Chou for their assistance in taking portions of the data. I would also like to thank Dr. W. K. Wells for some interesting discussions and for help in the early stages of these experiments.

The cheerful and willing help of Mr. S. E. Edwards in the maintainance of the electronics is gratefully acknowledged. Special thanks are due Mrs. Joseph Bailey for the careful preparation of the figures for this dissertation, and to Mr. R. Rummel and Mr. A. Lovette for their help in maintaining the accelerator systems. Thanks also go to many others at the laboratory for their help or suggestions.

I owe a special thanks to my family for their support throughout my life. I would also like to thank C. T. for

her patience during the course of this work. I am eternally grateful to J. and J. for their loving support over the last few months.

This work was supported in part by the United States Department of Energy. Some of the data analysis was performed at the Triangle Universities Computation Center, which is supported in part by the National Science Foundation.

TABLE OF CONTENTS

LIST OF FIGURES

LIST OF TABLES

Great are the works of the Lord;

They are studied by all who delight in them.

Psalm 111:2 (NASV)

A HIGH RESOLUTION STUDY OF PROTON RESONANCES IN ^{57}Co

Chapter 1

INTRODUCTION

For more than ten years, high resolution proton scattering experiments have proven valuable in the study of many statistical and non-statistical nuclear phenomena. The analysis of the excitation functions in terms of R-matrix cross sections has provided a wealth of spectroscopic information on isobaric analogue states, level densities and strength functions, as well as statistical information on the distribution of reduced widths and level spacings. The investigation of the fine structure patterns of analogue states is one area in which a high resolution beam is particularly useful, especially when the background level density is high. For statistical phenomena, the excellent energy resolution provides a greater sensitivity to very narrow resonances, and therefore enables one to obtain a more complete set of resonances with which to test theoretical predictions.

The present work is part of a continuing program of proton elastic and inelastic scattering experiments performed at the Triangle Universities Nuclear Laboratory. In the majority of these experiments, protons with energies

from 1 to 3 MeV have been scattered from thin solid targets of even-even nuclei with masses from A = 24 to 66. Some gas targets have been used, and recently a study of selected odd mass nuclei has begun. This previous work used an analyzer-homogenizer to provide excellent energy resolution. With this system, the energy of a secondary (molecular hydrogen) beam is measured in an electrostatic analyzer, and a voltage is applied to the target to offset the observed fluctuations. Some early success in extending this method to higher energies (and higher masses) was achieved with the TUNL tandem Van de Graaff accelerator with a neutral beam as the secondary beam. This method was experimentally difficult, and was replaced four years ago with a technique using an improved terminal control system. With this system, the energy of the primary beam is analyzed by a pair of 90^{o} magnets, and a correction voltage is applied via an optical feedback path to the terminal itself. This system in described in chapter 3, which contains a discussion of the experimental equipment and procedures.

The purpose of this dissertation is to present the results of recent $^{56}Fe(p,p)$ and $^{56}Fe(p,p')$ scattering experiments. These reactions were previously studied with high resolution by Lindstrom for the energy range 2.0 to 3.3 MeV. The present work overlaps and extends the region, covering the interval from 3.1 to 4.0 MeV. The purpose of these experiments was to extend the study to higher energies where higher orbital angular momenta could be observed (due

to more favorable penetrabilities) and where the inelastic channels would be stronger (for the same reason). The compound nucleus ^{57}Co was chosen for study because from the earlier work it was known to have an acceptable level density. Furthermore, the energy of the first excited state in ^{56}Fe (847 keV) made de-excitation γ-ray studies feasible, and placed the inelastically scattered proton group in an acceptable region of the proton spectrum. Under such favorable circumstances, these experiments were expected to provide additional useful information for the study of analogue states and statistical phenomena.

Since the R-matrix theory provides a framework for all the later analysis, the following chapter contains a discussion of that theory, with particular attention to the details relevant to the present problem. The data and R-matrix fits are presented in chapter 4, and tables of the resonance parameters are included in an appendix.

The final results are divided into two chapters, one for the non-statistical phenomena and a second for the statistical phenomena. Chapter 5 begins with a review of the theory of analogue states and fine structure, and concludes with a discussion of the five observed fragmented analogues. The random matrix model is summarized in the first four sections of chapter 6, including a discussion of statistical tests of data and theory. Experimental results are given in the last half of the chapter, concluding with an analysis of the statistical properties of the observed $1/2^+$ resonances.

Chapter 2

THEORETICAL BACKGROUND:
R-MATRIX THEORY

2.1 Introduction

Reactions in nuclear physics are often classified into one of two general, limiting categories: 'direct' reactions and 'compound nuclear' reactions. The distinguishing feature between these two processes is the interaction time during which the target and projectile are in close proximity. In direct reactions, this is approximately the time it takes for the projectile to 'cross' the target, about 10^{-21} seconds. The existence of a process other than direct reactions became apparent in the early 1930's when rapid fluctuations were observed in neutron capture cross sections. These γ-ray transitions have widths of about one electron volt, corresponding to lifetimes of 10^{-15} seconds. On a time scale characteristic of direct reactions, these transitions are slow and hence unlikely. To explain the observed strength of the resonances, Bohr stated in 1936 that "it is therefore clear that the duration of the

encounter must be extremely long compared with the time interval, circa 10^{-21} sec., which the neutron would use in simply passing through a space region of nuclear dimensions."

Bohr went on to explain the mechanism for forming what is now referred to as the compound nucleus: upon reaching the target, the projectile interacts strongly and shares its energy with one or more nucleons. Each energetic particle then interacts again with more nucleons, and those with still others, until the initial energy is distributed throughout the whole system--this is the compound nuclear state. So thorough is this mixing that the nucleus can no longer 'remember' how it was formed, and it can not readily decay because no one nucleon has enough energy to escape the attraction of the others. This gives rise to the very long lifetimes observed for the compound nucleus, lifetimes many orders of magnitude longer than for direct reactions. Eventually, of course, a single particle (or group of particles) collects enough of the original energy, and the system again fragments into parts.

Rigorous mathematical treatments of this mechanism were slowly worked out, starting with Kapur and Peierls in 1938 and culminating in a review article by Lane and Thomas in 1958. Wigner and Eisenbud were the authors of the most useful of these formalisms, known as the 'R-Matrix Theory'. Throughout the following review of this theory, the notation of Lane and Thomas will be followed as much as possible.

Like most of the successful treatments of scattering via a compound nucleus, the R-matrix theory divides space into two regions: for separations greater than some distance a_c, it is assumed that the potential is well known and that the Schroedinger equation can be solved exactly. For distances less than a_c, no form need be given for the potential V(r), except that it be Hermitian (for reasons obvious later). Instead, the existence of a complete set of solutions to the Schroedinger equation in the internal region is assumed, and the scattering amplitudes are expressed in terms of properties of these formal states, such as their eigenenergies. The difficulty with the theory lies in relating these 'internal quantities' to the measurable external quantities, the differential cross sections. This connection, while mathematically complex, is equivalent to equating the logarithmic derivatives of the internal and external solutions at the boundary $r_c = a_c$ (the standard continuity condition). For simple processes and a central potential (elastic scattering, for example) the equivalence is exact.

R-matrix theory only treats processes in which the initial and final states are two-body states. Three-body break-up (which is energetically forbidden at low and moderate energies) can only be handled as a succession of two-body decays. Capture processes are not easily dealt with because of the need to quantize the electromagnetic fields. Fortunately, these processes can be ignored for the present analysis.

If each possible initial and final mass subdivision of the system is labeled with all relevant quantum numbers (total J, m_1, m_2, internal spins I_1 and I_2 of the fragments, etc.), and these quantities are collectively referred to as a 'channel', then the process can be described as follows: the system 'enters' the compound nucleus via an 'entrance channel' and decays through an 'exit channel'. Channels which are not allowed by some conservation law are called 'closed'; allowed channels are 'open'. The interface between the compound nucleus and the channel is called the channel 'surface' S_c. In fact, the whole process has been likened to a microwave cavity (compound state) coupled to many waveguides (channels) (Blatt and Weisskopf, 1952).

2.2 R-Matrix Theory

When the colliding particles are sufficiently far apart, the Hamiltonian H in the equation $H\psi = E\psi$ can be separated into four parts:

$$H = H_{cm} + H_{rel} + H_{\alpha_1} + H_{\alpha_2} \qquad (2.1)$$

where H_{cm} describes the center of mass motion, H_{rel} describes the relative motion of the two particles, and H_{α_1} and H_{α_2} describe the internal states of the two fragments. ψ then becomes a product of wavefunctions of the form

$$\psi = \Phi_{cm}\, \chi_{rel}\, \psi_{\alpha_1}\, \psi_{\alpha_2} \qquad (2.2)$$

and the Schroedinger equation separates into four equations. Ψ_{cm} is a plane wave describing the center of mass motion and will be ignored hereafter. The two internal wavefunctions ψ_{α_1} and ψ_{α_2} with spins I_1 and I_2 will be coupled together to form states of a particular 'channel spin', $s = I_1 + I_2$, and projection $\nu = i_1 + i_2$:

$$\psi_{\alpha s \nu} = \sum (I_1 I_2 i_1 i_2 | s \nu) \psi_{I_1 i_1} \psi_{I_2 i_2} \qquad (2.3)$$

The boundary between the internal region and the external region occurs at the 'channel radius', a_c, which in the present analysis is taken to be the sum of the radii of the two particles:

$$a_c = r_o (A_1^{1/3} + A_2^{1/3}) \qquad (2.4)$$

where A_1 and A_2 are the mass numbers of the two fragments and r_o is a radius independent of A (taken to be 1.17 fm in this analysis, as discussed in section 6.7). To solve the relative motion equation the following quantities are introduced:

M_c = the reduced mass = $m_1 m_2/(m_1+m_2)$

E_c = the energy of relative motion

r_c = the relative separation

k_c = the relative wavenumber = $\frac{(2M_c E_c)^{1/2}}{\hbar}$

v_c = the relative velocity = $\hbar k_c / M_c$

$\rho_c = k_c r_c$

hence,

$$(-\frac{\hbar^2}{2M_c}\nabla_{r_c}^2 + V(r_c) - E_c)\chi = 0 \qquad (2.5)$$

For the external region, $V(r) = Z_1 Z_2 e^2/r$ and the equation again separates:

$$\chi_c = [u(r)/r] i^l Y_l^m(\theta,\phi) \qquad (2.6)$$

where the Y_ℓ^m are the usual spherical harmonics and u(r) satisfies the equation

$$u'' - [\ell(\ell+1)/\rho^2 + 2\eta/\rho \mp 1]u = 0 \qquad (2.7)$$

The prime denotes $d/d\rho$, $\eta = Z_1 Z_2 e^2/\hbar v$, and the minus (plus) sign corresponds to positive (negative) energies. For $E > 0$, equation (2.7) has two solutions, F_ℓ and G_ℓ, which are regular and irregular, respectively, at the origin. These functions, commonly called Coulomb functions, have as asymptotic forms

$$\begin{aligned} F_\ell &\propto \sin(\rho - \eta \ln(2\rho) - \ell\pi/2 + \sigma_{\alpha\ell}) \\ G_\ell &\propto \cos(\rho - \eta \ln(2\rho) - \ell\pi/2 + \sigma_{\alpha\ell}) \end{aligned} \qquad (2.8)$$

For convenience in scattering processes the following combinations (whose asymptotic forms are spherical waves) are defined:

$$\begin{aligned} I_{c+} &= (G_\ell - iF_\ell)\exp(i\omega_c) \propto \exp[-i(\rho - \eta \ln\rho - \ell\pi/2 + \sigma_{\alpha 0})] \\ O_{c+} &= (G_\ell + iF_\ell)\exp(-i\omega_c) \propto \exp[i(\rho - \eta \ln\rho - \ell\pi/2 + \sigma_{\alpha 0})] \end{aligned} \qquad (2.9)$$

where $\omega_c = \omega_{\alpha\ell} = \sigma_{\alpha\ell} - \sigma_{\alpha 0} = \sum_{\ell'=1}^{\ell} \tan^{-1}(\eta/\ell')$. For negative energies, only the solution which vanishes at infinity is allowed:

$$O_{c-} = W(-\eta, \ell+1/2; 2\rho) \propto \exp[-\rho - \eta \ln(2\rho)] \qquad (2.10)$$

where W is the Whittaker function. In the absence of a Coulomb field ($\eta=0$), F_ℓ and G_ℓ are simply related to the spherical Bessel functions and I_{c+} and O_{c+} are similarly related to the Hankel functions.

At this point it is convenient to introduce the set of functions $\{\varphi\}$, called the 'surface functions', which are defined as

$$\varphi_{\alpha s \ell v m} = \frac{1}{r_c}\, i^\ell Y_\ell^m \psi_{\alpha s v} \qquad (2.11)$$

and where the normalization of the φ's is chosen such that

$$\int_S \varphi^*_{\alpha s \ell v m} \varphi_{\alpha' s' \ell' v' m'} = \delta_{\alpha s \ell v m, \alpha' s' \ell' v' m'}$$

Linear combinations of these functions may be defined to have good total angular momentum J and projection M:

$$\varphi_{\alpha s \ell I M} = \sum_{v+m=M} (s l v m | J M)\, \varphi_{\alpha s \ell v m} \qquad (2.12)$$

The complete wavefunctions now take the form

$$\begin{aligned} \mathcal{Q}_{c+} &= I_{a+}\, \varphi_c / v^{1/2} \\ \mathcal{O}_{c+} &= O_{c+}\, \varphi_c / v^{1/2} \end{aligned} \qquad (2.13)$$

where $\mathcal{Q}$ and $\mathcal{O}$ are normalized to unit flux. A general solution can thus be written in the form

$$\Psi = \sum x_c \mathcal{O}_c + y_c \mathcal{Q}_c \qquad (2.14)$$

where $\sum |x_c|^2 = \sum |y_c|^2 = 1$ (unit flux in and out). For a given set of incoming waves (specific values of y_c) a complete knowledge of the scattering system would make possible the determination of x_c. In matrix notation,

$$x_c = - \sum_{c'} U_{cc'}\, y_{c'} \qquad (2.15)$$

where U is the collision matrix for the system. The linear relation between x_c and y_c implied by equation (2.15) is a consequence of the linear form of the Schroedinger equation: wavefunctions add linearly.

To understand the relation between the collision matrix U and the cross section σ, defined as

$$\sigma_c = \frac{\text{outgoing flux in channel c}}{\text{incoming flux}}$$

consider the simple case of very low energy neutron scattering (i.e., ℓ=0 only). Ignoring spin, the solutions

are of the form

$$\mathcal{I}_c = \left(\frac{1}{r_c}\right) \exp(-ik_c r_c) \left(\frac{1}{4\pi V_c}\right)^{1/2}$$
$$\mathcal{O}_c = \left(\frac{1}{r_c}\right) \exp(+ik_c r_c) \left(\frac{1}{4\pi V_c}\right)^{1/2} \qquad (2.16)$$

where, as before, $\mathcal{I}_c$ and $\mathcal{O}_c$ are normalized to unit flux. Assuming mono-energetic neutrons ($k=k_\alpha$), $y_c = \delta_{\alpha c}$. Hence

$$\Psi_\alpha = \mathcal{I}_\alpha - \sum_{c'} U_{\alpha c'} \mathcal{O}_{c'} \qquad (2.17)$$

The flux scattered into a channel $\beta \neq \alpha$ is given by

$$\lim_{r_\beta \to \infty} \frac{\hbar}{2iM_\beta} \int_{S_\beta} (\Psi_\beta^* \nabla \Psi_\beta - i\Psi_\beta \nabla \Psi_\beta^*) \cdot dS_\beta$$

(where $\Psi_\beta = -U_{\alpha\beta}\mathcal{O}_\beta$)

$$= \frac{\hbar k_\beta}{M_\beta} |U_{\alpha\beta}|^2 \frac{1}{4\pi V_\beta} 4\pi$$
$$= |U_{\alpha\beta}|^2 \qquad (2.18)$$

In this case $\mathcal{I}$ is the $\ell=0$ component of an incident plane wave with momentum k_α and incident flux = k_α^2/π. This may be obtained from an expansion of exp(ikz) in terms of spherical waves:

$$e^{ikz} = \frac{\pi^{1/2}}{kr} \sum_\ell (2\ell+1)\, i^\ell (e^{ikr} - e^{-ikr}) Y_\ell^0 \qquad (2.19)$$

The reaction cross section for cold neutrons is therefore

$$\sigma_{\alpha\beta} = \frac{|U_{\alpha\beta}|^2}{k_\alpha^2/\pi} = \pi \lambda^2 |U_{\alpha\beta}|^2 \qquad (2.20)$$

A more general derivation which allows for elastic scattering, $\ell \neq 0$, and charged particles, yields the expression (see Lane and Thomas, 1958, pp. 291-292)

$$d\sigma_{\alpha s v, \alpha' s' v'} / d\Omega_{\alpha'} = |A_{\alpha s v, \alpha' s' v'}(\Omega_{\alpha'})|^2 \qquad (2.21)$$

where the amplitude of the outgoing wave, $A_{\alpha s v, \alpha' s' v'}$, is given

by $$A_{\alpha s\nu,\alpha' s'\nu'} = \frac{\pi^{1/2}}{K_\alpha}\{-C_{\alpha'}(\theta_{\alpha'})\delta_{\alpha\alpha'} + i\sum_{\ell'm'\ell}(2\ell+1)^{1/2} \cdot [e^{2i\omega_{\alpha'\ell'}}\delta_{\alpha'\ell's'\nu'm';\alpha\ell s\nu 0} - U_{\alpha's'\ell'\nu'm';\alpha s\ell\nu 0}] \cdot Y_\ell^m(\Omega_{\alpha'})\} \quad (2.22)$$

with

$$C_\alpha(\theta_\alpha) = \frac{1}{(4\pi)^{1/2}}\eta_\alpha \csc^2(\theta_\alpha/2)\exp[-2i\eta_\alpha \ln\sin(\theta_\alpha/2)]$$

Lane and Thomas next sum over ν' and average over ν, finally arriving at their equation (2.6) which is the expression used to fit the data in this experiment.

In summary, the cross section can be expressed in terms of the collision matrix U, the elements of which are coefficients in the total wavefunction expansion. What is still lacking is the relation between the scattering matrix and the quantities describing the internal region.

At this point one could assume a particular form for the potential V(r) in the internal region, solve for the general solutions as before, and equate the logarithmic derivatives across the boundary to obtain the solution in all of configuration space. But then the validity of the results would depend on how well V(r) was chosen. In R-matrix theory one instead treats the problem in a more formal manner.

Assume a complete set of wavefunctions $\{\chi_{\lambda IM}\}$ in the internal region such that

$$H\chi_\lambda = E_\lambda \chi_\lambda \quad (2.23)$$

(The existence of such a set depends on the hermeticity of H). By putting simple boundary conditions on χ_λ it is possible to demonstrate orthogonality as well as derive an equation which will be useful later.

First consider two solutions χ_1 and χ_2 such that

$$H\chi_1 = E_1\chi_1 \qquad H\chi_2 = E_2\chi_2 \tag{2.24}$$

Multiplying the first equation by χ_2^*, multiplying the complex conjugate of the second equation by χ_1, subtracting the first from the second, and integrating over the entire internal region gives

$$\int_\tau (\chi_1 E \chi_2^* - \chi_2^* E \chi_1)\, d\tau = \int_\tau [\chi_1 (H\chi_2)^* - \chi_2^* (H\chi_1)]\, d\tau \tag{2.25}$$

where, as before, $H = -\frac{\hbar^2}{2M}\nabla_r^2 + V(r)$. Assuming $V(r)$ is Hermitian,

$$\int \chi_2^* (V\chi_1)\, d\tau = \int (V\chi_2)^* \chi_1\, d\tau \tag{2.26}$$

Therefore

$$(E_2 - E_1)\int \chi_2^* \chi_1\, d\tau = \int [\chi_1 (-\tfrac{\hbar^2}{2M}\nabla^2\chi_2^*) - \chi_2^* (-\tfrac{\hbar^2}{2M}\nabla^2\chi_1)]\, d\tau \tag{2.27}$$

From Green's theorem,

$$\int_\tau \chi_2^* \nabla^2 \chi_1\, d\tau = \int_S \chi_2^* \nabla\chi_1 \cdot dS - \int_\tau \nabla\chi_2^* \cdot \nabla\chi_1\, d\tau \tag{2.28}$$

therefore,

$$(E_2 - E_1)\int \chi_2^* \chi_1\, d\tau = \int_S \frac{\hbar^2}{2} [\chi_2^* (\tfrac{1}{M}\nabla\chi_1) - \chi_1 (\tfrac{1}{M}\nabla\chi_2^*)] \cdot dS \tag{2.29}$$

where S is the surface bounding the volume τ. Remembering that the set $\{\varphi\}$ (equation (2.11)) is complete on the surface S, it is possible to expand χ and grad(χ) on the surface:

$$\begin{aligned} \chi|_S &= \sum v_c \varphi_c & v_c &= \int \varphi_c^* \chi\, dS \\ \nabla\chi|_S &= \sum d_c \varphi_c & d_c &= \int \varphi_c^* \nabla\chi \cdot dS \end{aligned} \tag{2.30}$$

where v_c and d_c are the coefficients of the expansion of the value of χ and the derivative of χ on the surface S_c, $\sum_c S_c = S$. Substituting back into equation (2.29) gives

$$(E_2 - E_1)\int \chi_2^* \chi_1\, d\tau \tag{2.31}$$

$$= \frac{\hbar^2}{2}\left[\left(\sum_c v^*_{2c}\,\varphi_c^*\right)\left(\sum_{c'} d_{1c'}\frac{1}{M_{c'}}\varphi_{c'}\right) - \left(\sum_c v_{1c}\,\varphi_c\right)\left(\sum_{c'} d^*_{2c'}\frac{1}{M_{c'}}\varphi^*_{c'}\right)\right] dS$$

Using the orthonormality property of the $\{\varphi_c\}$ yields

$$(E_2 - E_1)\int \chi_2^*\chi_1\, d\tau = \sum \frac{\hbar^2}{2M_c}\left(v^*_{2c}\,d_{1c} - v_{1c}\,d^*_{2c}\right) \qquad (2.32)$$

Assuming that χ_1 and χ_2 behave the same under time reversal, it is possible to show that v_c and d_d are real (see Lane and Thomas). Thus:

$$(E_2 - E_1)\int \chi_2^*\chi_1\, d\tau = \sum \frac{\hbar^2}{2M_c}\left(v_{2c}\,d_{1c} - v_{1c}\,d_{2c}\right) \qquad (2.33)$$

Introducing the boundary condition

$$B_c = \frac{d_c}{v_c} \qquad (2.34)$$

where B_c is independent of λ, gives the desired result:

$$(E_2 - E_1)\int \chi_2^*\chi_1\, d\tau = \sum \frac{\hbar^2}{2M_c}\left(v_{2c}B_c v_{1c} - v_{1c}B_c v_{2c}\right)$$
$$= 0 \qquad (2.35)$$

So if $E_2 \neq E_1$, χ_2 and χ_1 are orthogonal. Notice that the boundary condition used here is the analogue of the logarithmic derivative evaluated at the surface S_c. To see this, assume the wavefunction in the internal region could be written as follows (not generally true):

$$\chi = \sum_c u_c\,\varphi_c$$

then

$$v_c = u_c(a_c), \qquad d_c = \left.\frac{du_c}{dr}\right|_{r=a_c}$$

thus

$$B = \left.\frac{du/dr}{u}\right|_{r=a_c}$$

In general the total wavefunction in the interior region can be expanded in terms of the $\{\chi_\lambda\}$:

$$\Psi(E) = \sum_\lambda A_\lambda\,\chi_\lambda \qquad (2.36)$$

where

$$A_\lambda = \int \chi_\lambda^* \Psi \, d\tau$$

Applying equation (2.35) to Ψ and χ_λ,

$$(E_\lambda - E)\int \chi_\lambda^* \Psi \, d\tau = \sum_c \frac{\hbar^2}{2M_c}(v_{\lambda c}\, d_{\psi c} - v_{\psi c}\, d_{\lambda c}) \tag{2.37}$$

therefore

$$A_\lambda = \frac{1}{E_\lambda - E} \sum_c \frac{\hbar^2}{2M_c} v_{\lambda c}(d_{\psi c} - v_{\psi c} B_c) \tag{2.38}$$

$$\Psi(E) = \sum_\lambda \frac{1}{E_\lambda - E} \sum_c \frac{\hbar^2}{2M_c} v_{\lambda c}(d_{\psi c} - v_{\psi c} B_c) \tag{2.39}$$

From equation (2.30),

$$v_{\psi c'} = \int \varphi_{c'}^* \Psi \, d\tau = \sum_{\lambda c} \frac{1}{E_\lambda - E} \frac{\hbar^2}{2M_c} v_{\lambda c}(d_{\psi c} - v_{\psi c} B_c) \tag{2.40}$$

$$= \sum_c \sum_\lambda \frac{\hbar^2}{2M_c} \frac{v_{\lambda c} \cdot v_{\lambda c}}{E_\lambda - E} (d_{\psi c} - v_{\psi c} B_c)$$

Defining the new quantities

$$\begin{aligned} V_c &= (\hbar^2/2M_c a_c)^{1/2} v_{\psi c} \\ D_c &= (\hbar^2 a_c/2M_c)^{1/2} d_{\psi c} \\ \gamma_{\lambda c} &= (\hbar^2/2M_c a_c)^{1/2} v_{\lambda c} \end{aligned} \tag{2.41}$$

gives the R-matrix relation

$$V_{c'} = \sum R_{c'c}(D_c - B_c V_c) \tag{2.42}$$

where

$$R_{c'c} = \sum \frac{\gamma_{\lambda c'} \gamma_{\lambda c}}{E_\lambda - E} \tag{2.43}$$

The R-matrix thus relates the value of the total wavefunction on the surface (V_c) to its derivative on the surface (D_c). The next step is to require that this same relationship hold true when the external solution Ψ_{ext} is evaluated on the same surfaces in the same way:

$$\Psi_{ext}(E) = \sum_c (x_c Q_c + y_c Q_c) \tag{2.44}$$

$$\begin{aligned} V_c &= (\hbar^2/2M_c a_c)^{1/2} \int \varphi_c^* \Psi_{ext} dS \\ &= (\hbar^2/2M_c a_c)^{1/2} (x_c Q_c + y_a I_c)/v^{1/2} \end{aligned} \tag{2.45}$$

$$D_c = (\hbar^2 a_c/2M_c)^{1/2} (x_c Q_c' + y_c I_c')/v^{1/2} \tag{2.46}$$

where the prime denotes d/dr . Re-writing:

$$V_c = (\hbar^2/2)^{1/2}[\rho_c^{-1/2} O_c x_c + \rho_c^{-1/2} I_c y_c]$$
$$D_c = (\hbar^2/2)^{1/2}[\rho^{1/2} O_c' x_c + \rho^{1/2} I_c' y_c] \qquad (2.47)$$

Substituting these expressions into the R-matrix relation, equation (2.42), gives

$$\rho_c^{-1/2} O_c x_c + \rho_c^{-1/2} I_c y_c$$
$$= \sum_{c'} R_{cc'}[(\rho_{c'}^{1/2} O_{c'}' x_{c'} + \rho_{c'}^{1/2} I_{c'}' y_{c'}) - B_{c'}(\rho_{c'}^{-1/2} O_{c'} x_{c'} + \rho_{c'}^{-1/2} I_{c'} y_{c'})] \qquad (2.48)$$

Because the following algebra is easier in matrix notation, all of the above quantities will be redefined to be square matrices. (With the exception of the R-matrix, all are diagonal.) Then equation (2.48) can be written

$$\rho^{-1/2} O\, x + \rho^{-1/2} I\, y \qquad (2.49)$$
$$= R\,[(\rho^{1/2} O' x + \rho^{1/2} I' y) - B(\rho^{-1/2} O\, x + \rho^{-1/2} I\, y)]$$

Collecting terms in x and y:

$$(\rho^{-1/2} O - R\rho^{1/2} O' + RB\rho^{-1/2} O)\, x$$
$$= (-\rho^{-1/2} I + R\rho^{1/2} I' - RB\rho^{-1/2} I)\, y \qquad (2.50)$$

This equation has the form $x = -Uy$ where

$$U = [\rho^{-1/2} O - R(\rho^{1/2} O' - B\rho^{-1/2} O)]^{-1}[\rho^{-1/2} I - R(\rho^{1/2} I' - B\rho^{-1/2} I)] \qquad (2.51)$$

Thus the U matrix is expressed in terms of known functions and their derivatives evaluated at a particular radial distance $r_c = a_c$, and in terms of the quantities of the internal region, the E_λ and $\gamma_{\lambda c}$. Unfortunately, U also seems to depend on the somewhat arbitrary boundary conditions B_c and upon the channel radii a_c. In fact, it can be shown that U is independent of these boundary conditions as long as reasonable choices are made, but the proof is non-trivial (see Lane and Thomas).

To simplify the above equation, the following quantities are introduced:

$$L_c = \rho_c O_c'/O_c = S_c + iP_c \qquad \mathcal{L}_c = \rho_c I_c'/I_c = L_c^* \tag{2.52}$$

L_c ($\mathcal{L}_c$) is the logarithmic derivative of the outgoing (incoming) wave in channel c evaluated at the channel surface. S_c and P_c are the real and imaginary parts of L_c, and for positive energy channels are evaluated as follows:

$$\begin{aligned} L_c &= \frac{\rho_c (G_c' + iF_c')}{G_c + iF_c} \\ S_{c+} &= \frac{\rho_c (F_c F_c' + G_c G_c')}{F_c + G_c} \\ P_{c+} &= \frac{\rho_c (F_c' G_c - G_c' F_c)}{F_c + G_c} = \frac{\rho_c}{F_c^2 + G_c^2} \end{aligned} \tag{2.53}$$

where use has been made of the Wronskian relation, F'G-G'F=1 (independent of r). Other useful quantities are

$$\begin{aligned} \Omega_{c+} &= (I_c/O_c)^{1/2}\big|_{r=a_c} = \exp[i(\omega_c - \phi_c)] \\ \mathcal{B}_c &= \rho_c/(I_c O_c) \end{aligned} \tag{2.54}$$

where $\phi_c = \tan^{-1}(F_c/G_c)$ = the hard sphere phase shift (so called because it is the phase shift obtained when scattering from an infinitely repulsive sphere). Substituting these quantities back into the expression for the collision matrix gives

$$\begin{aligned} U &= \rho^{1/2} O^{-1} [1 - R(L-B)]^{-1} [1 - R(L^*-B)] \rho^{-1/2} I \\ &= \Omega \mathcal{B}^{1/2} [1 + \frac{1}{1 - R(L-B)} R(2iP)] \mathcal{B}^{-1/2} \Omega \end{aligned} \tag{2.55}$$

To see how such an expression is used, consider the case of neutron scattering (ℓ=0). The reaction cross-section from equation (2.20) was

$$\sigma_{\alpha\beta} = \pi \lambda^2 |U_{\alpha\beta}|^2$$

where now $U_{\alpha\beta} = \Omega_\alpha \mathcal{B}_\alpha^{1/2} [1 - R(L-B)]^{-1}_{\alpha\delta} R_{\delta\beta}(2iP_\beta) \mathcal{B}_\beta^{-1/2} \Omega_\beta$

For positive energies,

$$\mathcal{B}_\alpha = \rho_\alpha / (I_\alpha Q_\alpha) = \rho / (F^2 + G^2) = P_\alpha \tag{2.56}$$

$$|U_{\alpha\beta}| = \left| \left[\frac{1}{1 - R(L-B)} R \right]_{\alpha\beta} \right| 2P_\alpha^{1/2} P_\beta^{1/2} \tag{2.57}$$

If E is very near one energy (E_λ) and very far from all others (single level approximation),

$$R_{cc'} \cong \frac{\gamma_{\lambda c} \gamma_{\lambda c'}}{E_\lambda - E} \tag{2.58}$$

If only two channels are open,

$$R = \frac{1}{E_\lambda - E} \begin{bmatrix} \gamma_\alpha^2 & \gamma_\alpha \gamma_\beta \\ \gamma_\alpha \gamma_\beta & \gamma_\beta^2 \end{bmatrix} \tag{2.59}$$

Define $L^o = L - B$. Then

$$1 - RL^o = \begin{bmatrix} 1 - \frac{\gamma_\alpha^2 L_\alpha^o}{E_\lambda - E} & - \frac{\gamma_\alpha \gamma_\beta L_\beta^o}{E_\lambda - E} \\ - \frac{\gamma_\alpha \gamma_\beta L_\alpha^o}{E_\lambda - E} & 1 - \frac{\gamma_\beta^2 L_\beta^o}{E_\lambda - E} \end{bmatrix} \tag{2.60}$$

$$(1-RL^o)^{-1} = \begin{bmatrix} 1 - \frac{\gamma_\alpha^2 L_\beta^o}{E_\lambda - E} & \frac{\gamma_\alpha \gamma_\beta L_\beta^o}{E_\lambda - E} \\ \frac{\gamma_\alpha \gamma_\beta L_\alpha^o}{E_\lambda - E} & 1 - \frac{\gamma_\alpha^2 L_\alpha^o}{E_\lambda - E} \end{bmatrix} \frac{1}{1 - \frac{(\gamma_\alpha^2 L_\alpha^o + \gamma_\beta^2 L_\beta^o)}{E_\lambda - E}} \tag{2.61}$$

$$[(1-RL^o)^{-1} R] = \gamma_\alpha \gamma_\beta \frac{1}{E_\lambda - E - \gamma_\alpha^2 L_\alpha^o - \gamma_\beta^2 L_\beta^o} \tag{2.62}$$

$$U = \frac{2P_\alpha^{1/2} \gamma_\alpha P_\beta^{1/2} \gamma_\beta}{E_\lambda - E - \gamma_\alpha^2 (S_\alpha - B_\alpha) - \gamma_\beta^2 (S_\beta - B_\beta) - i(\gamma_\alpha^2 P_\alpha + \gamma_\beta^2 P_\beta)} \tag{2.63}$$

Define $\Gamma_c = 2P_c \gamma_c^2$; $\Delta_c = \gamma_c^2 (S_c - B_c)$. Then

$$U_{\alpha\beta} = \frac{\Gamma_\alpha^{1/2} \Gamma_\beta^{1/2}}{(E_\lambda - \Delta_\alpha - \Delta_\beta) - E - i(\Gamma_\alpha + \Gamma_\beta)/2} \tag{2.64}$$

$$= \pi \lambda^2 \frac{\Gamma_\alpha^{1/2} \Gamma_\beta^{1/2}}{(E' - E)^2 + \Gamma^2/4} \tag{2.65}$$

where $E'_\lambda = E_\lambda - \Delta_\lambda$, $\Delta_\lambda = \Delta_\alpha + \Delta_\beta$, and $\Gamma = \Gamma_\alpha + \Gamma_\beta$. This is the well known Breit-Wigner form for the reaction cross-section. At this point it is possible to assign a physical significance to each of the various parameters used in the derivation. Obviously, Γ is the width of the resonance and Γ_α and Γ_β are the partial widths in channel α and β. From the definition

$$\Gamma_c = 2 P_c \gamma_c^2$$

comes the identification of γ^2 as the 'reduced width amplitude' and P_c as the 'penetration factor' or 'penetrability'. From the definition

$$\gamma_{\lambda c} = (\hbar^2/2M_c a_c)^{1/2} \int \varphi_c^* \chi_\lambda dS$$

$\gamma_{\lambda c}$ is essentially the amplitude of the eigenstate χ_λ at the surface S_c (where S_c is defined by $\varphi_c \neq 0$). Equating P_c with the probability of penetrating the barrier at $r_c = a_c$, Γ_c becomes a product of the probability of being at the channel surface (γ_c^2) times the probability of going through the barrier (P_c). Or in other words, Γ_c is a measure of the leakage of the wavefunction through the surface into channel c.

The peak in this reaction cross section occurs at E'_λ which is shifted in energy from the eigenenergy by an amount Δ_λ where, again,

$$\Delta_{\lambda c} = \gamma_{\lambda c}^2 (S_c - B_c)$$

Hence S_c is aptly labeled the shift function. In practice, B_c is set equal to S_c and the resonance energies extracted from the cross sections are equal to E_λ (i.e., $\Delta_\lambda = 0$).

This is not strictly correct since B_c was assumed independent of λ, and hence independent of energy, while S_c is a slowly varying function of energy. Relaxing the energy independence of the boundary conditions destroys the orthogonality of the basis states (equation (2.35)), and through this non-orthogonality affects the definition of the reduced width amplitude. The final result (not intuitively obvious) is a slight error in extracting the widths for the levels. If the resonances are well separated and few channels are open, the error is negligible. For high level density (overlapping resonances) the effect may not be small, but has nevertheless been ignored for the purposes of this analysis. Lynn (1968) discusses some of these problems in greater detail in the context of neutron resonance reactions.

Besides providing a way to extract resonance parameters from the data, the R-matrix formalism will be used in chapter 5 in a discussion of analogue states, and in chapter 6 in a discussion of the statistical properties of eigenvalues and widths. In both of these later sections, attention will be restricted to a single value of the total spin, J. This is physically reasonable because J is a conserved quantity--J and H commute. This approach also follows naturally from the R-matrix formalism: the channels were defined to have definite values of J, which leads to an

R-matrix which is diagonal in J:

$$R = \begin{bmatrix} R_{J_1} & 0 & \cdots \\ 0 & R_{J_2} & \cdots \\ \vdots & \vdots & \vdots \end{bmatrix} \tag{2.66}$$

Likewise, U is diagonal in J:

$$U = \begin{bmatrix} U_{J_1} & 0 & \cdots \\ 0 & U_{J_2} & \cdots \\ \vdots & \vdots & \vdots \end{bmatrix} \tag{2.67}$$

where U_{J_1} is only a function of R_{J_1}. In other words, the eigenvalue and reduced width amplitudes for one value of J are completely independent of those corresponding to other values of J. (Of course the cross section, which is defined for a reaction and not a fixed value of J, does contain terms which are not diagonal in J). In later discussions, attention will be restricted to a single submatrix R_{J_1} and a single submatrix U_{J_1}.

Chapter 3

EXPERIMENTAL EQUIPMENT AND PROCEDURE

3.1 The High Resolution System

3.1.1 Accelerator Control

The experiments described in this dissertation were performed using the TUNL FN tandem Van de Graaff accelerator. The accelerator is equipped with a special feedback system with which it is possible to achieve excellent beam energy stability. This high resolution system (see figure 3.1 for a schematic layout of the laboratory and the feedback control) is essentially a Gere type control system with an additional higher frequency correction applied to the stripper canal by a high voltage amplifier located in the terminal. The following discussion describes the system and its operation in general terms. A more complete treatment of the feedback equations has been given by Bleck (1978).

The accelerated beam is analyzed by two 90° bending magnets, and an error signal is obtained by two slits placed downstream from the magnets. The intercepted currents are amplified by matched three stage pre-amplifiers: 1) current

Figure 3.1 A Schematic Diagram of the Three Loop Control System.

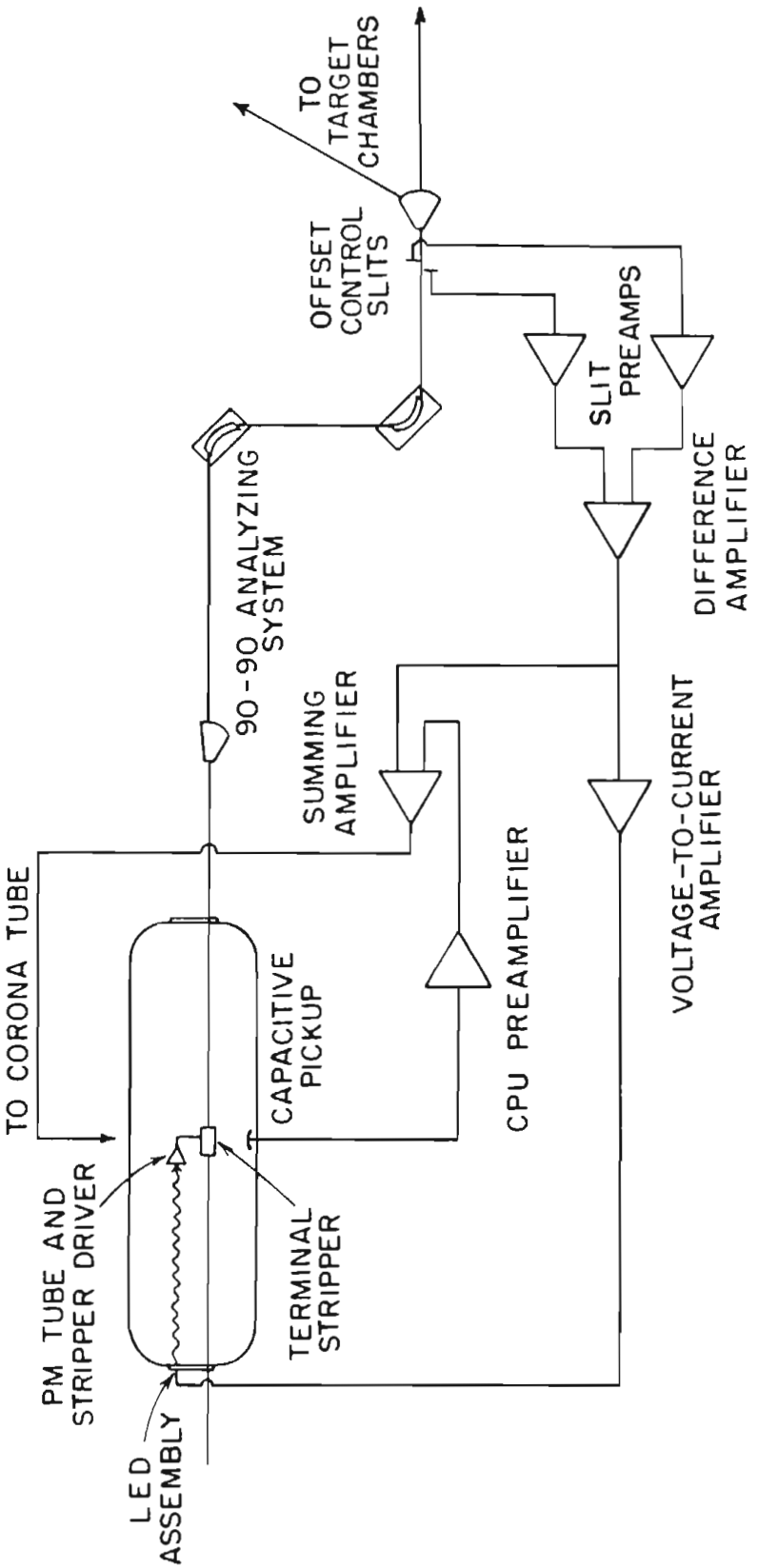

TRIPLE LOOP CONTROL SYSTEM

to voltage, 2) logarithmic gain (to minimize spurious signals due to intensity fluctuations), and 3) a line driver. These signals are sent to a difference amplifier, the output of which is added to the signal from a capacitive pick-up (CPU), and the sum of these two drives a standard corona control circuit. Thus far the system performs like a Gere control system. As in other systems, the slit difference signal may be replaced (in the absence of the beam, for example) by a signal from a generating voltmeter (GVM). At TUNL this switching may be done automatically by circuitry which detects the no-beam condition to change from SLIT control to GVM control.

This two loop system was improved with the addition of a higher frequency feedback loop: in addition to its use in the corona system, the slit difference signal drives a light emitting diode (LED) mounted on a window at the low energy end of the tandem accelerator. The light signal is carried to the terminal by a lucite light-pipe and is detected by a photo-multiplier. The signal drives a high voltage amplifier, the output of which modulates the charge exchange or stripper canal. This closes the third feedback loop and removes those components of the beam energy fluctuations which are of too high a frequency to be handled by the corona system, which is limited by finite ion transit times.

It is possible in principle to remove almost all fluctuations from the beam in this fashion, leaving only the incoherent spread in energy from the source, plus the spread

due to straggling in the charge exchange canal and in the target. In practice other limitations arise. One limitation is the magnitude of the correction signal that can be applied to the stripper. To improve this a newer terminal amplifier was installed with a 12 kV supply (a 50% improvement over the old). Also, various changes have been made in the current pre-amplifiers to reduce the noise originating there. Efforts are now under way to minimize fluctuations in the high voltage supplies of the terminal amplifier. These fluctuations (800 Hz, approximately 80 V) can actually be seen in the slit difference signal when the system is in operation. Another problem is oscillations in the feedback loop which limit the useful gain of the system (and hence the corrections to the beam). Despite these limitations, the system routinely gives 450 eV resolution, FWHM. The best resolution achieved thus far was an overall energy resolution of 375 eV for a narrow resonance in $^{54}Fe(p,p)$.

3.1.2 Magnet Control

For the high resolution system to work, it is important that the 90^{o}-90^{o} analyzing magnets be very stable. The magnets are voltage programmable and are field-locked with standard NMR (Nuclear Magnetic Resonance) techniques. A schematic of the power supply and the associated field control devices is shown in figure 3.2. For the sake of

Figure 3.2 The Analyzing Magnet Control System.

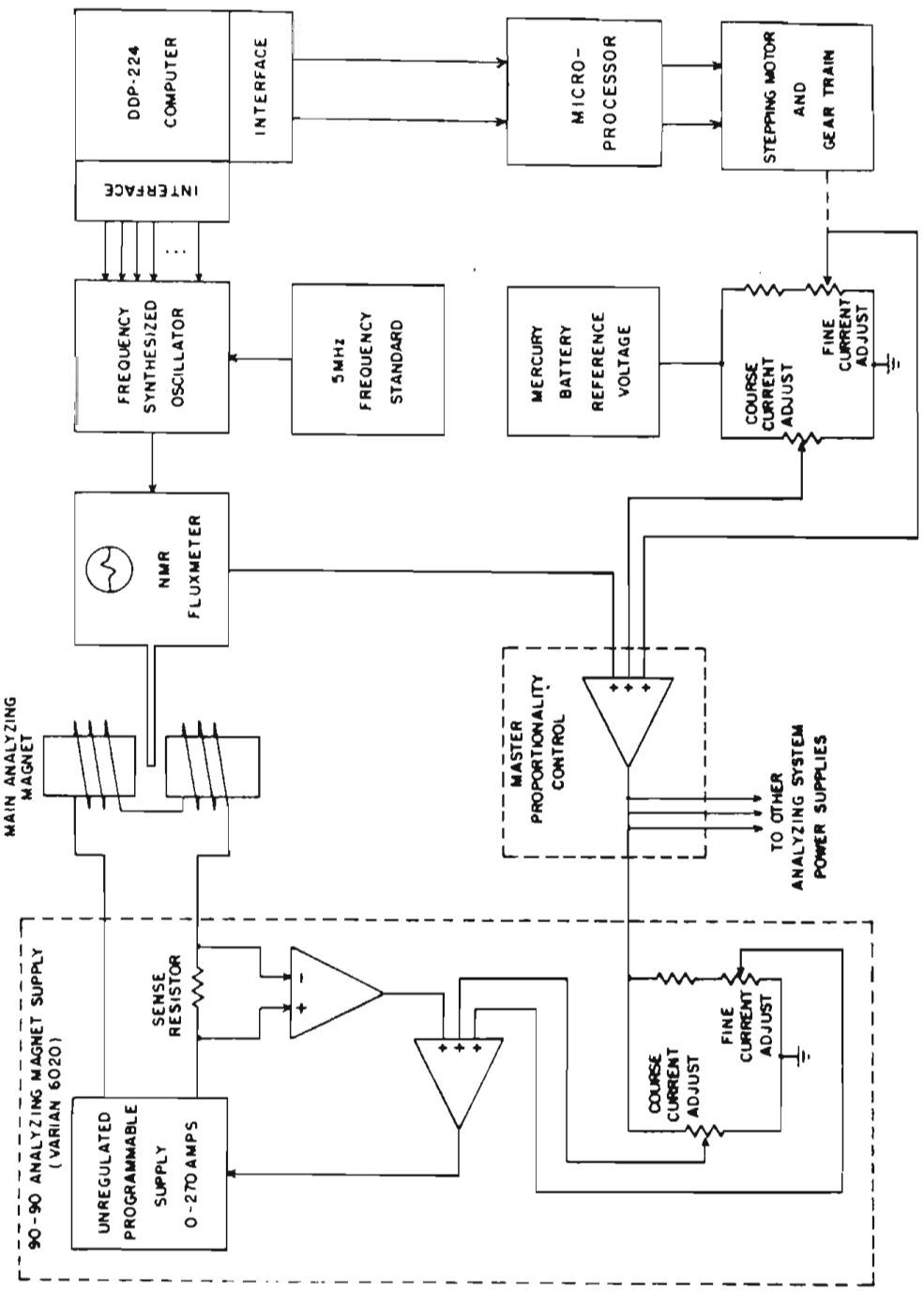

ANALYZING MAGNET POWER SUPPLY

stability, the voltage source for high resolution work is a pair of mercury batteries and two voltage dividing resistor pots, coarse and fine. The fine pot is turned, through a 400:1 gear reduction, by a Slo-Syn synchronous stepping motor. The stepping motor can be made to turn either manually or on command from the data taking computer through a microprocessor. In this way very small energy increments (less than 100 eV out of several MeV) can be made quickly, repetitively, and reliably.

The field locking of the magnets is achieved by sending an RF signal to an NMR probe in the magnet. The field near the probe is modulated at 50 Hz by a small electro-magnet. As the local field is varied (assuming the RF frequency is correct) a resonance is observed in the RF power absorbed by the probe. The position of this resonance relative to the center of the 50 Hz modulation is used to derive a correction signal which is summed with the voltage from the fine and coarse pots and applied to the magnets. Thus, as the magnets start to drift, the resonance is shifted away from the center of the modulation, and a correction signal is generated to drive the resonance back toward center.

To maintain this type of field stabilization as the energy is increased it is necessary to change the frequency for each energy step. This is accomplished by a digitally programmed frequency synthesizer (Fluke model 6039A), using a 5 MHz frequency standard. Thus it is possible to simultaneously increment both the magnet programming voltage

and the NMR frequency entirely under computer control. In practice, this means that excitation functions of over 500 points (100 eV steps) can be taken in 10 hours or less. At that point it becomes necessary to re-adjust those magnets which are not voltage programmed.

3.2 Targets

The targets for these experiments consisted of a thin layer (approximately 2 μgm/cm^2) of isotopically enriched (99.9%) ^{56}Fe evaporated onto thin carbon backings. Self supporting carbon foils (Arizona Carbon Foil Co.) of 5 μgm/cm^2 thickness were used for the lower energy excitation curves and most of the γ-ray angular distributions. At higher energies, however, the inelastic peak in the spectrum was partially overlapped by the elastic carbon peak, first at 160° and later at 150°. To extend the energy range in which the inelastic peak could be analyzed, efforts were made to use thinner self supporting foils. It was found that foils of less than two μgm/cm^2 would not survive in the beam for more than a few hours. Considerably better results were obtained when these thin foils were supported on a smooth layer of formvar (polyvinyl formal resin, Shawinigan Resins Corp.).

To produce these targets a film of formvar is made by dropping a small amount of the liquid into a pan of water. The film formed in this way is then lifted onto a target ring and allowed to dry. Later, carbon foils of thickness down to 0.7 μgm/cm^2 are floated on water and lifted onto the formvar covered rings. The prepared rings (either the 5 μgm/cm^2 self supporting foils or the 1-2 μgm/cm^2 formvar backed foils) are placed in the evaporator approximately ten inches from the heater assembly (separated from it by a shutter). The isotope to be evaporated is placed in a carbon crucible which sits in the high current heater. The current is slowly increased until the isotope is completely reduced, a process taking several 15 minute periods over many hours. After the reduction is complete, as evidenced by a steady vacuum for currents above those required for reduction, the temperature of the crucible is raised above the melting temperature of iron, the shutter is opened, and a layer of isotope is deposited onto the foils. Finally the targets are moved to the target chamber or placed in storage under vacuum to minimize deterioration by oxidation.

A typical spectrum for a target with a thin carbon backing is shown in figure 3.3a. This particular spectrum was taken at 3.63 MeV at $\theta_{LAB} = 149.4^{o}$. The inelastic peak can be seen just to the left of the ^{12}C peak. Contaminants include ^{13}C, ^{14}N, ^{16}O, and ^{28}Si.

Figure 3.3 (a) Charged particle spectrum taken at 3.63 MeV at $\theta_{LAB} = 149.4^{o}$. The carbon peak is shown one-eighth scale.

(b) Charged particle spectrum taken at 3.63 MeV at $\theta_{LAB} = 124.4^{o}$. The carbon peak has been gated out.

(c) γ-ray spectrum taken at 3.317 MeV at $\theta = 157^{o}$.

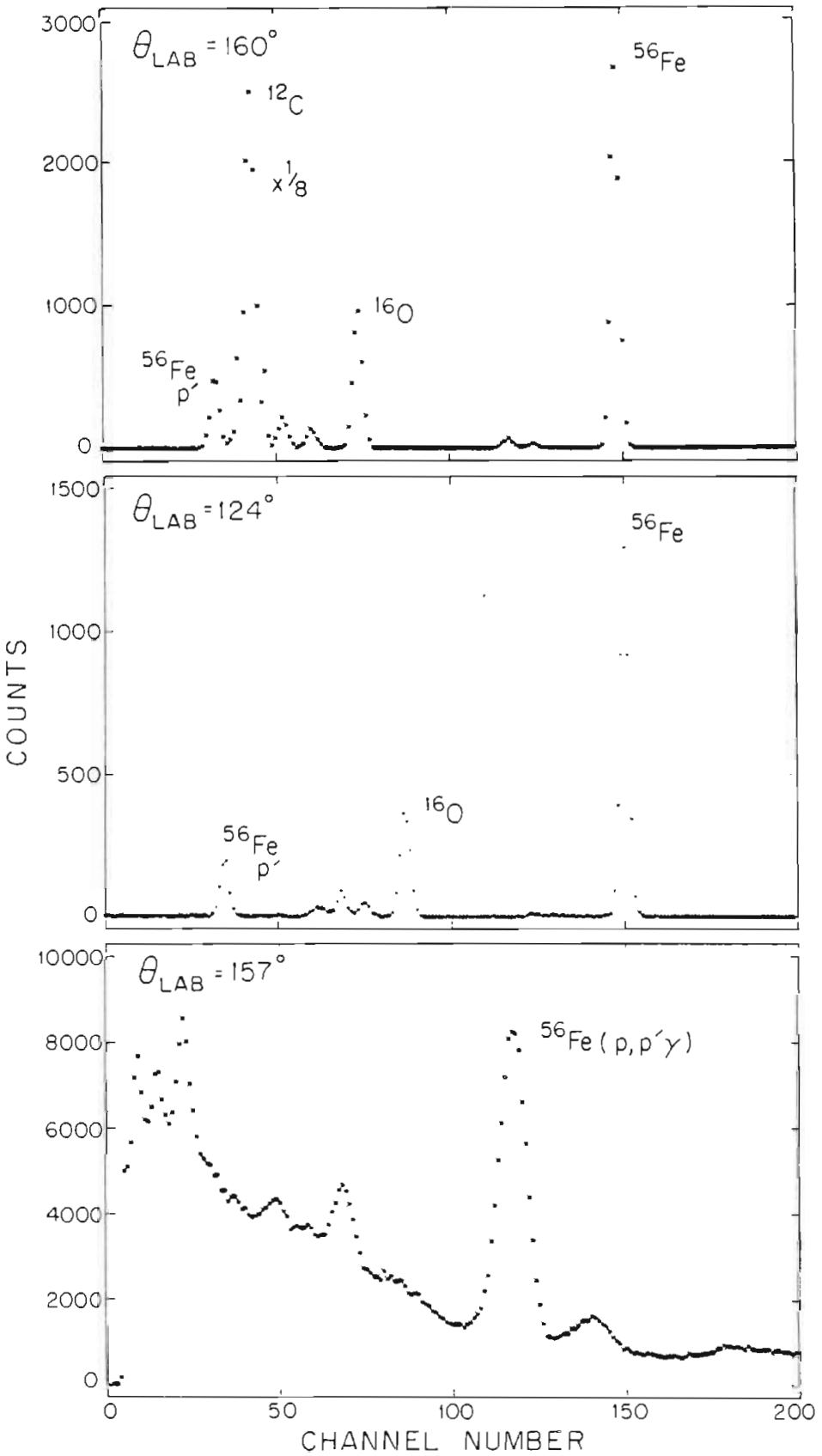
θLAB = 160°
12C
x 1/8
56Fe
16O
56Fe p´
θLAB = 124°
56Fe
16O
56Fe p´
θLAB = 157°
56Fe (p, p´γ)
COUNTS
CHANNEL NUMBER
3000
2000
1000
0
1500
1000
500
0
10000
8000
6000
4000
2000
0
0
50
100
150
200

3.3 Scattering Chambers and Counting Electronics

Two scattering chambers were used in these experiments: one for the proton excitation functions, and a second for the γ-ray angular distributions. The proton experiments were performed with the 60 cm diameter chamber on the 60^{o} left port of the 70^{o}-70^{o} switching magnet. A top view of this chamber showing the placement of the beam collimators and charged particle detectors appears in figure 3.4. The beam was defined by a 2.5 mm aperture located 40 cm from the target, and by a pair of crossed 2 mm slits 10 cm from the target, giving rise to a 2 mm square beam spot on the target. A turbo-mechanical pump maintained a vacuum of $2x10^{-6}$ torr within the chamber.

A split faraday cup (four quadrants) was used to collect the beam current and aid in keeping the beam centered on the target. Signals from each quadrant went to a feedback pre-amplifier which provided control signals for the beam line steerers plus a summed current output to the beam current integrator.

Silicon surface barrier detectors were mounted on moveable tracks at laboratory angles of 89^{o}, 106^{o}, 124^{o}, 149^{o}, and 160^{o}. Detector properties are summarized in table 3.1. The scattered protons were collimated for each detector by a pair of tantalum collimators held by an aluminum snout. The solid angles, chosen to yield approximately equal counting rates in each detector, were

Figure 3.4 Top view of charged particle chamber showing the placement of the beam collimators and detectors.

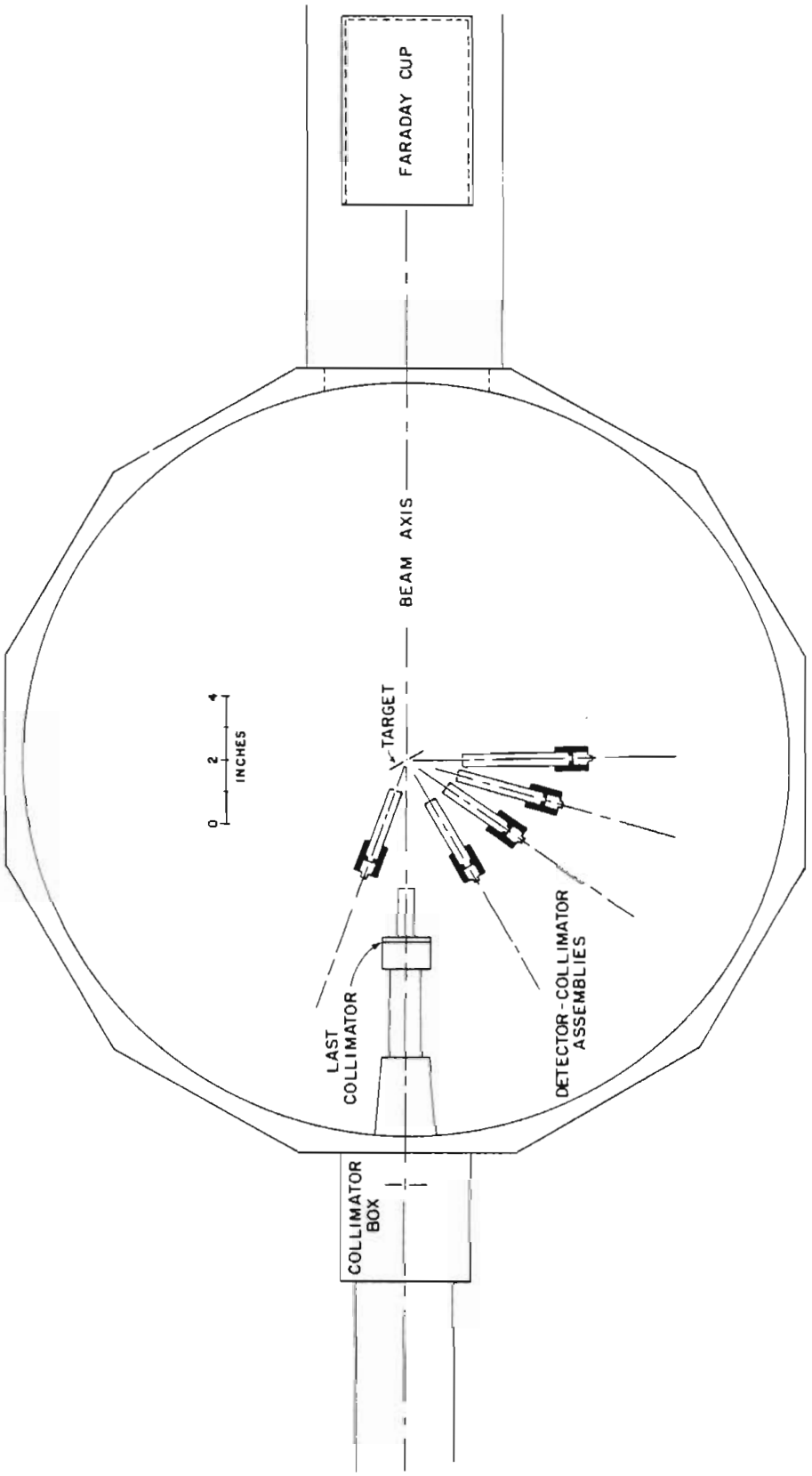
FARADAY CUP
BEAM AXIS
TARGET
0
2
4
INCHES
LAST
COLLIMATOR
DETECTOR-COLLIMATOR
ASSEMBLIES
COLLIMATOR
BOX

Table 3.1 Charged Particle Detector Properties

θ_{LAB}	89°	106°	124°	149°	160°
Ortec Serial Number	17-565E	13-455E	13-455C	16-867D	16-868C
Nominal Detector Resolution (keV)	17.	13.	13.	16.	16.
Bias Voltage (volts)	200.	135.	135.	250.	250.
Active Area (mm^2)	50.	50.	50.	50.	50.
Solid Angle (msr)	1.9	2.4	3.1	4.5	5.8
Distance to Target (cm)	13.0	11.1	9.5	9.5	8.3

defined by the collimator closest to the detector. The second collimator limited the area of the target (and chamber) visible to the detector, thereby reducing the low energy background in the spectrum.

A schematic diagram of the counting electronics is shown in figure 3.5. The preamplifiers (Ortec 109A's, located at the target chamber) drive Ortec 452 spectroscopy amplifiers via cables linking the target and control rooms. The bipolar outputs of each amplifier are fed to two timing single channel analyzers (TSCA), one serving as an upper and lower discriminator, the second as a window to reject the carbon peak. The unipolar output of the amplifier goes to a linear gate stretcher which is gated by the TSCA's through the coincidence module. Thus, the carbon peaks and signals too large or small are not sent to the Analogue to Digital Converter (ADC), and the dead time in the ADC is therefore minimized. All of the linear signals are summed and sent to the ADC, while the outputs of the coincidence modules are fed to a router, enabling the computer to re-sort the events to the proper spectrum. Figure 3.3.b shows a spectrum (taken at θ_{LAB}= 149.4° at 3.63 MeV) with the ^{12}C peak gated out.

The γ-ray angular distributions were taken using a thin walled scattering chamber located on the 0° port of the switching magnet. Five 7.6x7.6 cm NaI(Tl) crystals were arranged outside the 20 cm diameter chamber, 18 cm from the target, and a single silicon surface barrier detector was

Figure 3.5 Schematic Diagram of the Counting Electronics

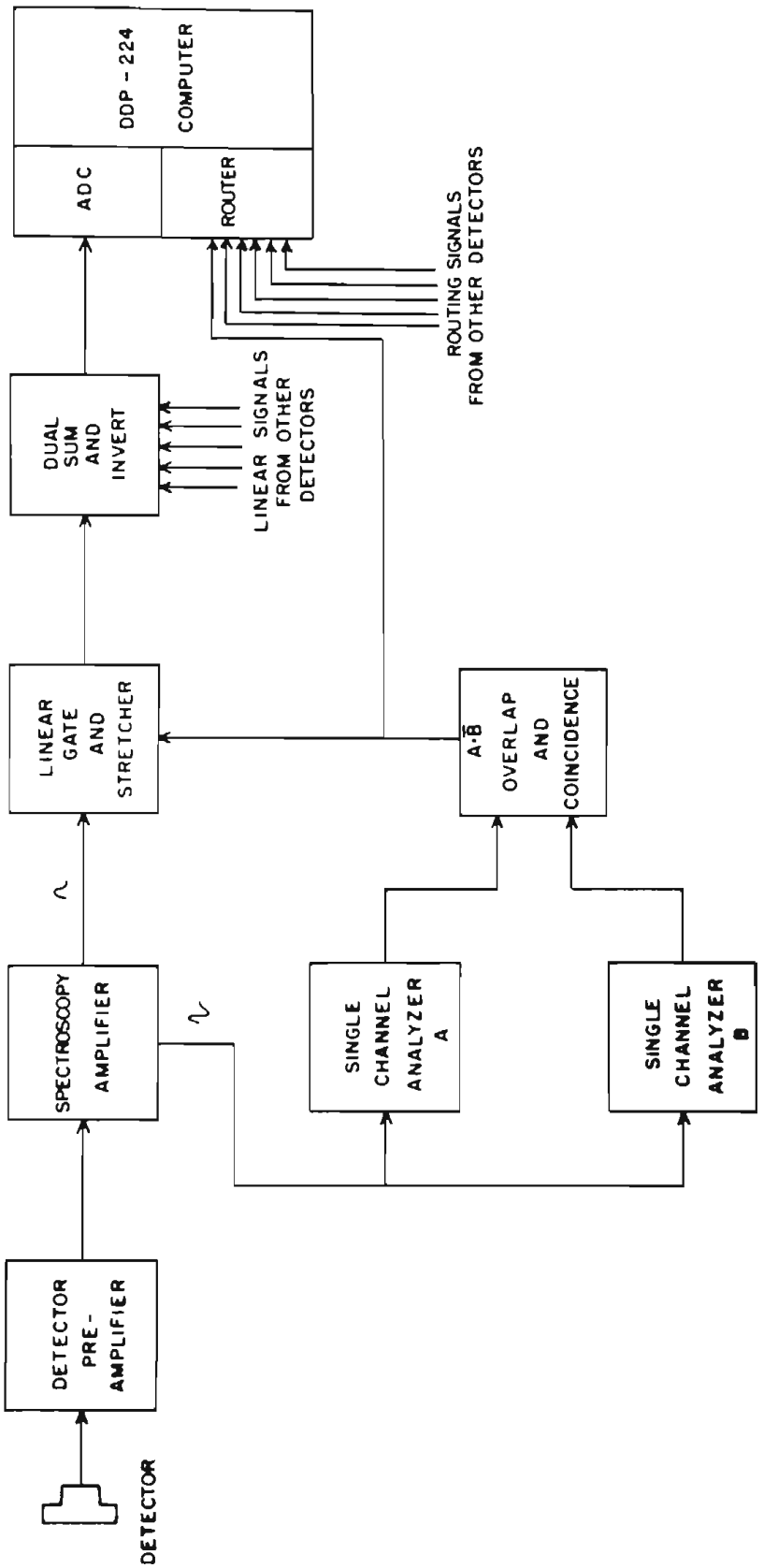
DETECTOR
DETECTOR PRE-AMPLIFIER
SPECTROSCOPY AMPLIFIER
SINGLE CHANNEL ANALYZER A
SINGLE CHANNEL ANALYZER B
A·B̄ OVERLAP AND COINCIDENCE
LINEAR GATE AND STRETCHER
DUAL SUM AND INVERT
LINEAR SIGNALS FROM OTHER DETECTORS
ROUTING SIGNALS FROM OTHER DETECTORS
ADC
ROUTER
DDP - 224 COMPUTER

mounted at θ_{LAB} = 160° inside the chamber. The charged particle detector helped to identify each resonance to be studied.

The beam was collimated by two aperatures, 4.4 mm and 2.8 mm, approximately 60 cm from the target. The beam current was collected in a faraday cup 3 m from the chamber. The pre-amplifiers for the five Harshaw dual inline crystals were mounted at the base of each photo-multiplier.

The counting electronics for this part of the experiment were essentially the same as previously described. The second TSCA was not needed for the γ-ray spectra, and the lower level discriminators were raised to gate out the 511 keV gamma peak in order to reduce the dead time in the ADC. A typical spectrum is shown in figure 3.3.c.

3.4 Experimental Procedure

The excitation functions were measured in steps of 90-200 eV, corresponding to frequency steps of 150-300 Hz for the synthesizer. Spectra were accumulated for an integrated beam current of 90-180 μC, depending on target thickness. These parameters gave 5000-8000 counts in the elastic peak for each angle. Each set of spectra was then written onto tape while the magnets were stepped to the next energy and the NMR frequency was incremented. On-line

analysis was performed at each step, summing the peaks of interest and storing the sums in a yield curve. The yield curves and spectra were available to the operator for monitoring the progress of the experiment. Before each long yield curve was taken, the analyzing magnets were cycled over their full range twice. When this procedure was not used, energy shifts of several keV were observed for resonances from one month to the next. With this procedure, energy measurements were repeatable to within one keV.

This same procedure was used to find each resonance studied in the γ-ray experiment. A short yield curve was taken from approximately 2 keV below the resonance to a kilovolt above the resonance. This yield curve was later used to estimate the off-resonance background to be subtracted from the angular distributions. After taking the yield curve, the energy was returned to the resonance energy and spectra were accumulated for at least 2400 μC.

Relative efficiencies for the NaI(Tl) crystals were obtained using two methods: 1) γ-ray sources placed in the target position, and 2) angular distributions of resonances of known spin. The second method was preferred, as it was subject to the same systematic errors as the angular distributions being studied.

Chapter 4

DATA AND PRELIMINARY ANALYSIS

4.1 Preparation of Yield Curves

Off-line analysis of the excitation curves proceeded in a manner similar to that previously described for on-line analysis. Each set of spectra was read from tape, and the peaks of interest were summed and stored in a yield curve. For this analysis, more care was taken to fit the background than was done on-line.

For the elastic peaks, a linear background was assumed, and several channels to the left and right of the peak were sampled to generate the background (which was typically less than 1% of the peak). The inelastic peaks posed a more difficult problem in that the background was frequently larger than the peak to be summed. For peaks well separated from the elastic carbon peak, i.e., a dozen channels or more, a least-squares fit to a third-order polynomial was performed. The fit spanned fifty channels or more, excluding the region containing the peak and including (possibly unequal) regions on both sides of the peak. For

peaks not as well separated from the carbon peak other functional forms were used for the background, including inverse polynomials and exponentials of polynomials. The last form was used, for example, to fit a Gaussian lineshape to the entire carbon peak.

It must be pointed out that each peak was not fit individually by the experimenter. A program was written that could perform these analyses automatically. The operator read in one set of spectra, fit each peak, and then allowed the computer to continue reading and fitting each peak with the same type background and fitting region the operator originally used. It was also necessary to shift these regions up in channel number as the energy of the peak moved upward. A relativistic kinematics routine performed this function automatically whenever necessary.

In most cases where the peaks overlapped, systematic errors in the background determination were made, either subtracting too much (giving negative yields off resonance) or too little (giving positive yields off resonance). These errors were slowly varying in energy, so it was possible to remove them in a later step. A preliminary R-matrix fit to the data was performed (in a manner described in the next section) to locate all resonances and estimate their widths. Next the inelastic yield curves were fit to a polynomial, excluding regions in which the resonance yield could be expected to be positive, and including regions sufficiently far away from resonances so that the resonance yield would

be zero. An assumption implicit in this procedure is that there are no direct or non-resonance processes which would give a non-zero yield off resonance. However, prior to this correction, no significant off resonance yield was observed at $\theta_{LAB} = 124.4^{o}$, an angle at which there was always a good separation between the inelastic peak and the carbon peak. This observation and the fact that penetrabilities in this mass and energy region considerably suppress the direct processes justify the use of this method.

Up to this point, each yield curve was treated as a separate entity, with no effort made to connect them together. A continuous excitation function was created by choosing a set of resonances whose energies were fairly well established (by repetition), and shifting each yield curve until the energies of the reference levels were internally consistent. Occasionally, when two reference points were contained in one yield curve, this resulted in a conflict. It became apparent that slow drifts in the energy of the machine (on the order of 100 eV/hour) caused some yield curves to be slightly compressed or expanded in energy. It was decided that the simplest and most reasonable way to correct for this problem was to perform a linear transformation of the yield curve energies of the form

$$E' = E + \Delta E + \Delta S(E-E_o)$$

where ΔE is the shift in energy at $E=E_o$ and ΔS is a change in energy scale, usually zero and never more than 4%.

One additional operation performed on the yield curves was to convolute each with a Gaussian function of width 100 eV. This had no observable effect on the elastic data--it is equivalent to changing the resolution from 425 eV to 437 eV, an insignificant change. On the other hand, this manipulation improved considerably the appearance of the inelastic yield curves. The point scatter in the (p,p') curves is caused in large part by the statistical uncertainty in the background subtraction. Averaging this over several points improves the statistics and reduces the point scatter.

4.2 Angular Distributions

4.2.1 De-excitation Gamma-rays

The short γ-ray yield curves were processed in a manner similar to that described above. A simple exponential background was fit to a region including several channels to the left of the peak and 20-30 channels to the right. The spectra taken on resonance were analyzed in a manner identical to that for the yield curves. There was usually a positive yield off-resonance, indicating a contaminant γ-ray very close in energy to the 847 keV de-excitation γ-ray. To correct for this problem, the yield off-resonance for 120 μC was multiplied by the ratio of integration currents (μC on resonance / 120 μC) and subtracted from the resonance yield. Because of the large backgrounds in this part of the

experiment, this was not an insignificant correction, and the resulting yields were not considered reliable to better than 10%.

The angular distributions were used as a aid in making spin assignments, primarily to distinguish $d_{5/2}$ resonances from $d_{3/2}$ resonances. Expressions for these distributions as functions of the allowed decay amplitudes are:

$$W_{3/2^+}(\theta_\gamma) \propto 1 + \frac{1}{\sum_{l's'} |\langle l',s'\rangle|^2} \{ \frac{1}{2} |\langle 0,3/2\rangle|^2 - \frac{3}{10} |\langle 2,3/2\rangle|^2 - \frac{2}{35} |\langle 2,5/2\rangle|^2 - \frac{2}{5}\sqrt{\frac{3}{7}}\,\mathrm{Re}(\langle 2,3/2\rangle\langle 2,5/2\rangle^*)\} Q_2 P_2(\cos\theta_\gamma) \tag{4.1}$$

$$W_{5/2^+}(\theta_\gamma) \propto 1 + \frac{1}{\sum_{l's'} |\langle l',s'\rangle|^2} \{ \frac{4}{7} |\langle 0,5/2\rangle|^2 - \frac{2}{35} |\langle 2,3/2\rangle|^2 + \frac{2}{35} |\langle 2,5/2\rangle|^2 - \frac{96}{245}\mathrm{Re}(\langle 2,3/2\rangle\langle 2,5/2\rangle^*)\} Q_2 P_2(\cos(\theta_\gamma) \tag{4.2}$$

$$+ \frac{1}{\sum_{l's'} |\langle l',s'\rangle|^2} \{-\frac{4}{7} |\langle 0,5/2\rangle|^2 + \frac{2}{7} |\langle 2,5/2\rangle|^2 - (48/49)\mathrm{Re}(\langle 2,3/2\rangle\langle 2,5/2\rangle^*)\} Q_4 P_4(\cos\theta_\gamma) \tag{4.3}$$

where $Q_K = J_K(kr)/J_o(kr)$ and J_K is the cylindrical Bessel function. For the experimental arrangement used, $Q_2 = 0.96$ and $Q_4 = 0.81$. For $d_{5/2}$ resonances there is a high probability that a_4 will be appreciable (greater than 0.2 in magnitude), while for $d_{3/2}$ resonances a_4 is zero. Therefore, the observation of a large a_4 for a d-wave resonance gives a spin assignment of $d_{5/2}$.

All d-wave resonances from E_p = 3.1 - 4.0 MeV satisfying the relation

$$\frac{(2J+1)\,\Gamma_p\,\Gamma_{p'}}{\Gamma_p + \Gamma_{p'}} > 10 \text{ eV}$$

were observed in the (p,p'γ) reaction, 110 d-wave resonances in all. Half of these were assigned spins of 5/2 on the basis of their γ-ray angular distributions. Only 20 were assigned spins of 3/2 in this manner. The remaining distributions were of too poor a quality to provide spin assignments. Figures 4.1c and 4.1d show fits to two resonances, a $d_{5/2}$ resonance at E_p = 3.7126 and a $d_{3/2}$ resonance at 3.6295.

4.2.2 (p,p') Distributions

In some cases, the angular distributions of the inelastically scattered protons were sufficient to make spin assignments. For example, if a p-wave resonance had an anisotropic p' distribution, it was assigned a spin of 3/2. Only a few d-wave resonances had distributions which were not linear in $\cos^2\theta$ within experimental errors. These few were assigned spins of 5/2. Unfortunately, the most probable p' distributions for $d_{5/2}$ resonances do not distinguish them from $d_{3/2}$ resonances. Sample distributions and fits of (p,p') angular distributions are shown in figures 4.1a and 4.1b.

From the preceeding comments it is obvious that an experimental bias exists towards assigning a spin of 5/2 to d-wave resonances. If either distribution is clearly non-linear, an assignment can be confidently made. Only if the data is very good and the distributions linear can a choice of 3/2 be made. This bias is one possible contribution to the observed anomaly in the d-wave level densities.

Figure 4.1 (a) Angular distribution of inelastically scattered protons for a $3/2^+$ resonance at E_p = 3.7126 MeV.

(b) Angular distribution of inelastically scattered protons for a $5/2^+$ resonance at E_p = 3.6295 MeV.

(c) Gamma-ray angular distribution for a $3/2^+$ resonance at E_p = 3.7126 MeV.

(d) Gamma-ray angular distribution for a $5/2^+$ resonance at E_p = 3.6295 MeV.

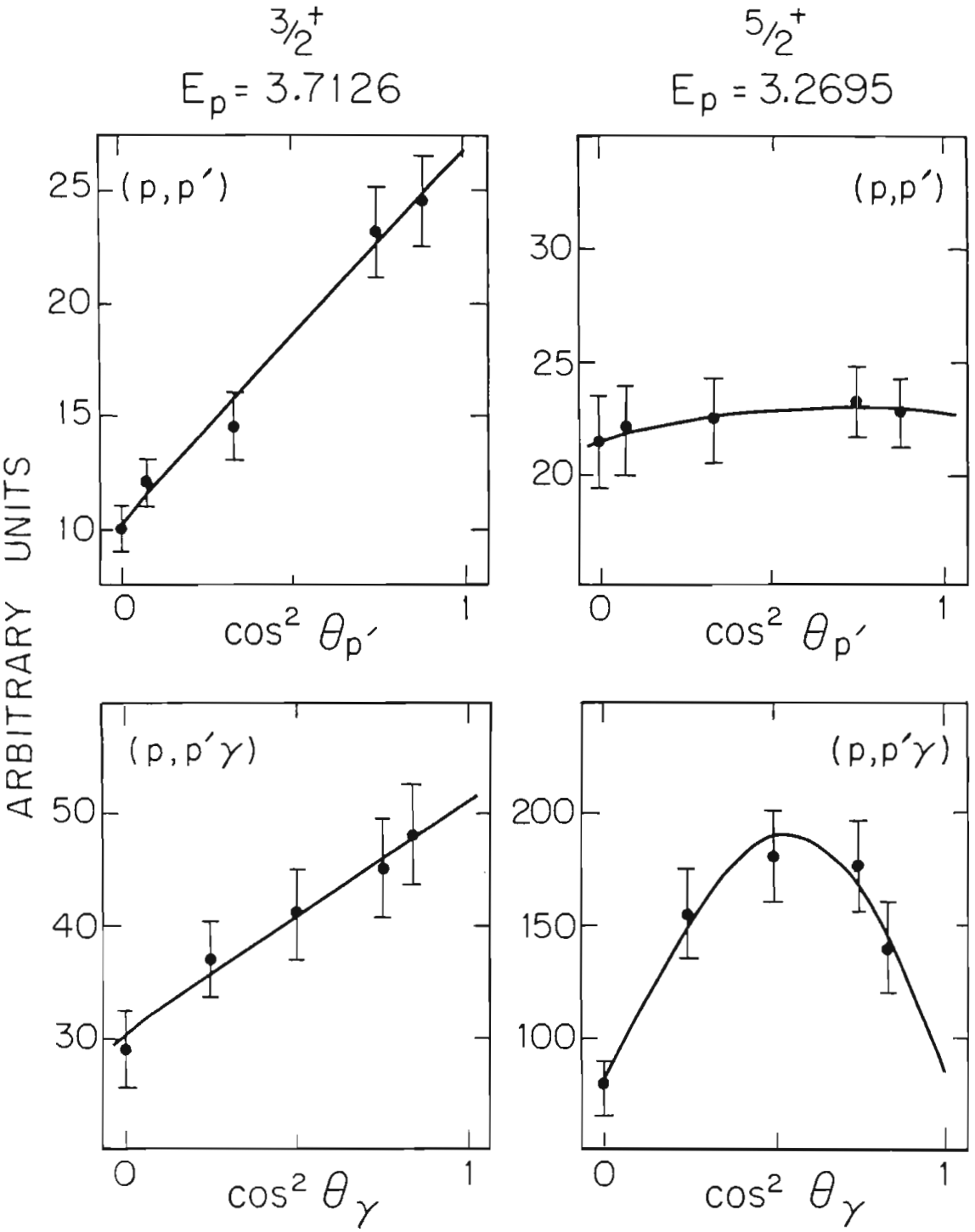
3/2+
Ep = 3.7126
5/2+
Ep = 3.2695
ARBITRARY UNITS
(p,p′)
(p,p′γ)
cos² θp′
cos² θγ
25
20
15
10
30
40
50
100
150
200
0
1

4.3 R-Matrix Fitting Procedure

4.3.1 MULTI

The program MULTI used to perform the R-matrix analysis evolved over the years from one written in 1969 by Sellin. The equations in this code for calculating the cross-section were taken from Lane and Thomas (1958). The current version of the program can calculate total and differential cross sections for up to 35 competing channels, including the effects of up to 300 resonances with as many as 9 different J^{π} values. The cross sections can be simultaneously generated for six angles and 1000 energies and compared with 1000 data points. Any of these constraints can easily be lifted if necessary.

The program takes as input various parameters describing the open channels (masses, Q-values, channel radii, etc.) plus parameters describing the resonances (spin, parity, energy, widths in each channel, etc.). Cross sections are then calculated, including Coulomb, resonance, and hard sphere scattering. In the present work, elastic scattering and inelastic scattering to the first excited state in ^{56}Fe are assumed to be the only open channels. The (p,n) channel is closed, and other inelastic channels were unobserved (and are expected to be insignificant from penetrability considerations). The capture channel, not treated in R-matrix theory, was also ignored, since gamma-ray widths are almost always negligible when particle channels are open.

In order to compare the cross sections with the data, MULTI convolutes the theoretical curves with a resolution function corresponding to the effects of the spread in incident beam energy and energy loss in the target. The function chosen for this smearing was half Gaussian (leading edge) and half Lorentzian. This shape was used to approximate the asymmetric energy distribution in the beam (due to straggling in the gas stripper) as well as the effects of a finite target. Parameters for the resolution function were obtained by fitting narrow resonances with appreciable inelastic yields, because for these resonances the line shape observed in the (p,p') cross section is just the smear function itself (convolution of the smear function with a very narrow spike). Best fits were obtained with a total width (FWHM) varying between 420 and 500 eV for different sections of data. The ratio of half widths used, W_L/W_G, was 1.2. Five percent changes in either of these parameters had no noticeable effect.

The data is normalized to the cross section and the two are plotted together for visual comparison. The fitting procedure then consists of varying all the resonance parameters until a good fit is obtained. Continuous sections of data were fit as a whole wherever possible. In many cases, changes of yield occured in the data which necessitated normalizing different sections of a yield curve independently. Two causes of this problem were 1) motion of the beam on the target, which might not be of uniform

thickness, and 2) large changes in the beam intensity. The latter caused changes in the dead-time in the ADC which were not completely corrected for in the beam current integration electronics.

4.3.2 Spin Assignments

For most resonances, the excitation curves are sufficient to distinguish the ℓ values of each resonance, because each ℓ has a characteristic shape (see figure 4.2 for examples). But for very weak resonances, or for resonances observed primarily in the inelastic channel, shape discrimination may be ambiguous. There is also some difficulty when neighboring levels are unresolved. Small s- and p-waves are only visible at back angles where their shapes are very similar. Fortunately, most of the s-waves were large enough to show a dip at 90^{o}, allowing a definite spin assignment to be made. It is therefore unlikely that there are spurious levels in the observed s-wave sequence.

For the p-wave resonances, shape analysis was sufficient to distinguish spins for widths where $(2J+1)\Gamma_p >$ 120 eV, about half of the p-waves observed. For many p-waves, the p' distributions gave a spin assignment. Small p-waves in the neighborhood of the $3/2^-$ analogue state at 3.89 MeV were assigned spins of $3/2^-$, although these assignments are uncertain.

The shapes of the d-wave resonances are almost identical at all angles studied, with the greatest difference between $5/2^+$ and $3/2^+$ occuring at 124.4^{o}. At

Figure 4.2 Resonance shapes for

(1) a 20 eV $1/2^+$ resonance,

(2) a 20 eV $1/2^-$ resonance,

(3) a 15 eV $3/2^-$ resonance,

(4) a 15 eV $3/2^+$ resonance,

(5) a 10 eV $5/2^+$ resonance,

(6) a 10 eV $5/2^-$ resonance,

(7) a 9 eV $9/2^+$ resonance.

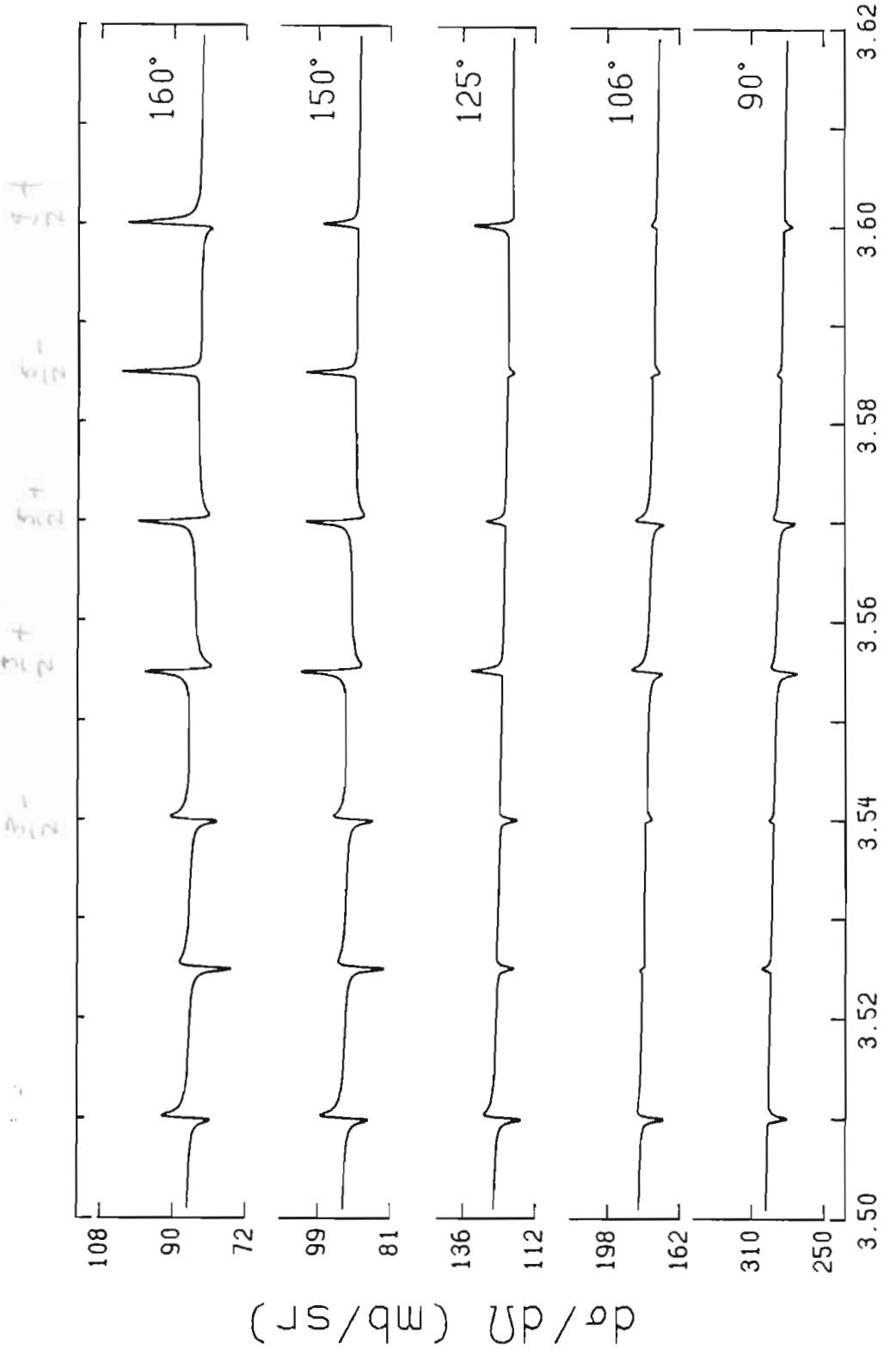
160°
150°
125°
106°
90°
108
90
72
99
81
136
112
198
162
310
250
3.50
3.52
3.54
3.56
3.58
3.60
3.62
dσ/dΩ (mb/sr)
Ep (MeV)

this angle a d-wave is seen as a peak in the cross section--125° is a zero of $P_2(\theta)$, so there is no interference between Rutherford scattering and the $\ell=2$ resonance at this angle. For small levels with appreciable inelastic widths ($\Gamma_{p'} > \Gamma_p$), the size of this peak is not much greater than statistical errors, and the spins cannot be distinquished. But for those levels with little or no inelastic width the peak for a $d_{3/2}$ level is about 50% larger than the peak for a comparable $d_{5/2}$ level. This is shown in figure 4.2 where the widths have been adjusted to give equal modulations of the cross section at 160°. Vertical scales were chosen so that a 10% change in cross section is of comparable size for each angle.

The only resonances with $\ell>2$ occurred in the neighborhood of isobaric analogue states: an f-wave analogue state at E_p = 3.43 MeV and a g-wave analogue state at E_p = 3.71 MeV. For these levels the spin assignments were taken from the parent state in ^{57}Fe -- $5/2^-$ for the f-wave resonances, $9/2^+$ for the g-wave resonances.

4.4 Differential Cross Sections and Reduced Widths

Differential cross sections for the reactions ^{56}Fe(p,p) and ^{56}Fe(p,p') were measured from E_p = 3.1 to 4.0 MeV, for laboratory angles ranging from 89° to 160°. Figure 4.3 shows the elastic cross section measurements for three of

Figure 4.3 Differential cross sections from E_p = 3.1 to 4.0 MeV. The solid line is a fit to the data.

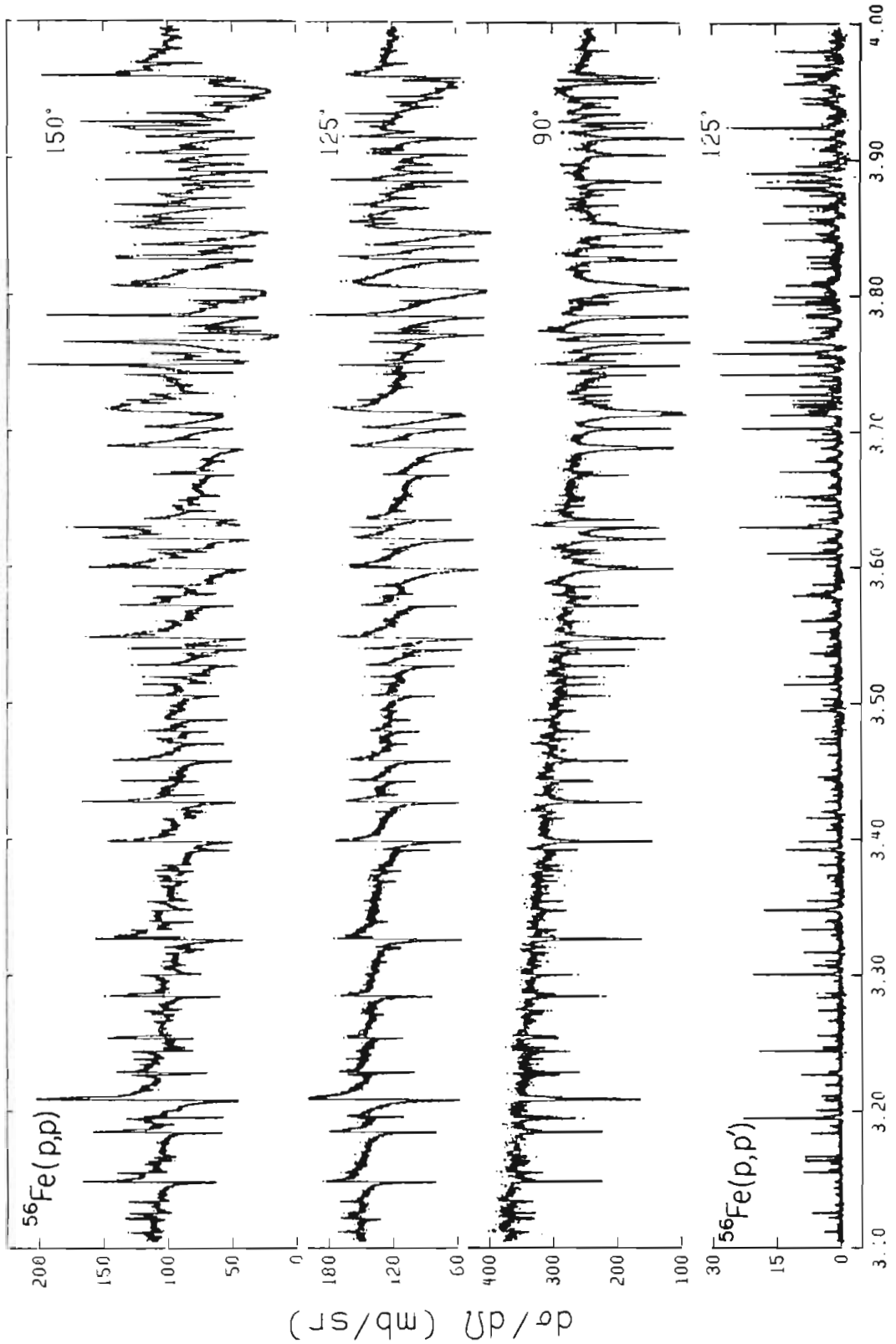
150°
125°
90°
125°
^{56}Fe(p,p)
^{56}Fe(p,p')
dσ/dΩ (mb/sr)
E_P (MeV)

those angles (θ_{cm} = 90°, 125°, and 150°), and the inelastic cross section for one angle, 125°. The solid line through the points is the fit generated by a multi-level, multi-channel R-matrix code, as described previously. The next six figures each contain 150 keV of data, and present all angles in each reaction for which data was taken in that interval. Scales were chosen so that a 10% change in cross section gave the same vertical displacement for each angle.

346 resonances were used to fit the data, consisting of 56 s-wave resonances, 100 p-waves, 180 d-waves, and a few f- and g-waves. A large percentage of these resonances had measureable widths for at least one inelastic channel. Analyses of the properties of these level sequences are given in later sections.

Isobaric analogues of the 14th and 17th through 20th excited states of ^{57}Fe were identified in this data. Three of these account for the most prominent features in the data. The cluster of strong inelastic resonances near E_p = 3.75 MeV (figure 4.3) is due primarily to a $5/2^+$ analogue state. The d-wave shape is also recognizable in the elastic cross section at 150°. The somewhat weaker group of inelastic resonances near 3.89 MeV is part of a $3/2^-$ analogue state. The largest feature in the elastic cross section, at 3.95 MeV, is a strong $1/2^-$ analogue state. This resonance is easily recognized at all three angles shown: a rise at 90°, a dip at 125°, and a dip followed by a rise at 150°.

Figure 4.4 Differential cross sections from E_p = 3.10 to 3.25 MeV. The solid line is a fit to the data.

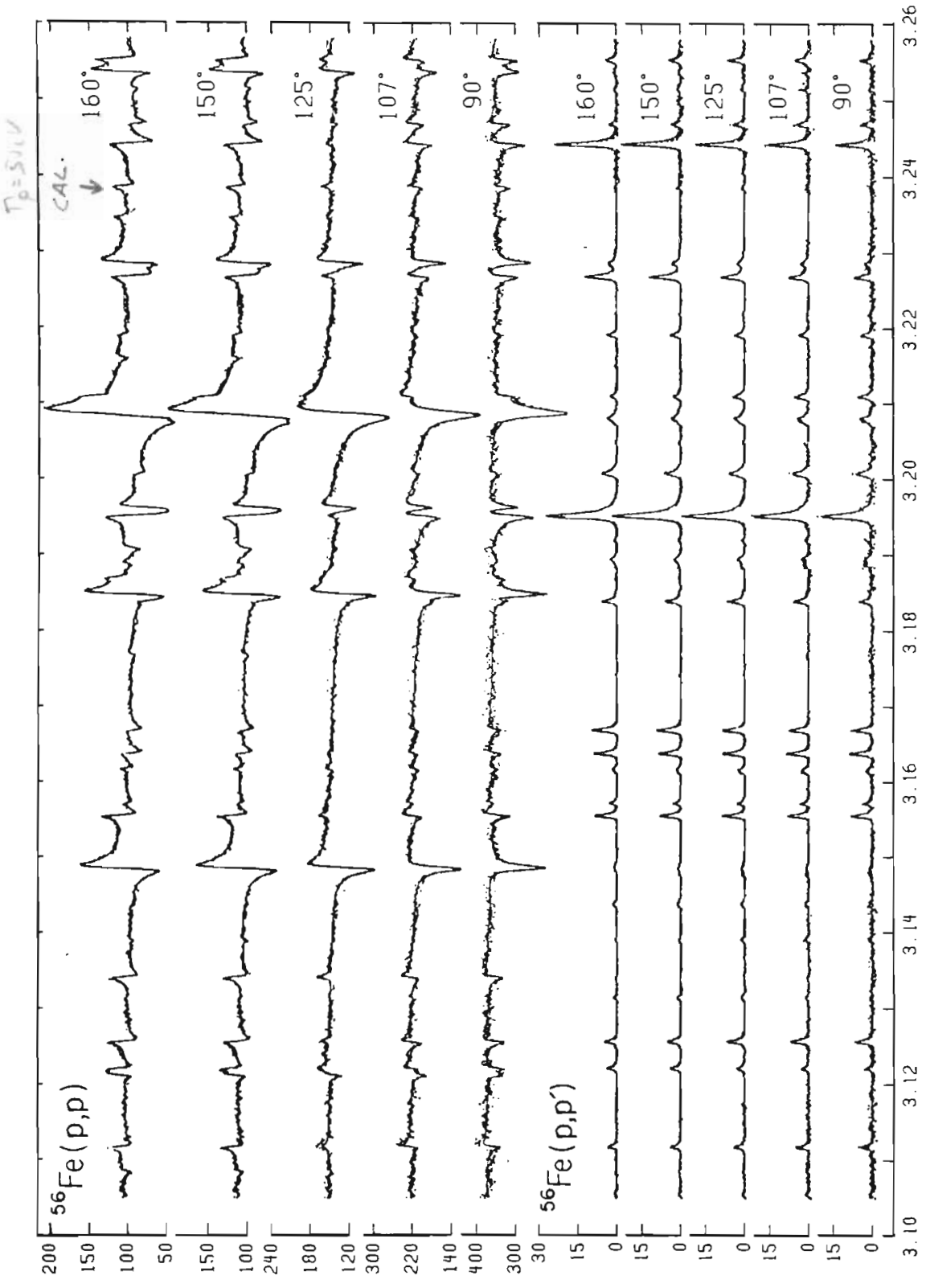
^{56}Fe(p,p)
^{56}Fe(p,p')
160°
150°
125°
107°
90°
CAL.
T_p=5MeV
dσ/dΩ (mb/sr)
E_p (MeV)
3.10
3.12
3.14
3.16
3.18
3.20
3.22
3.24
3.26

Figure 4.5 Differential cross sections from E_p = 3.25 to 3.40 MeV. The solid line is a fit to the data.

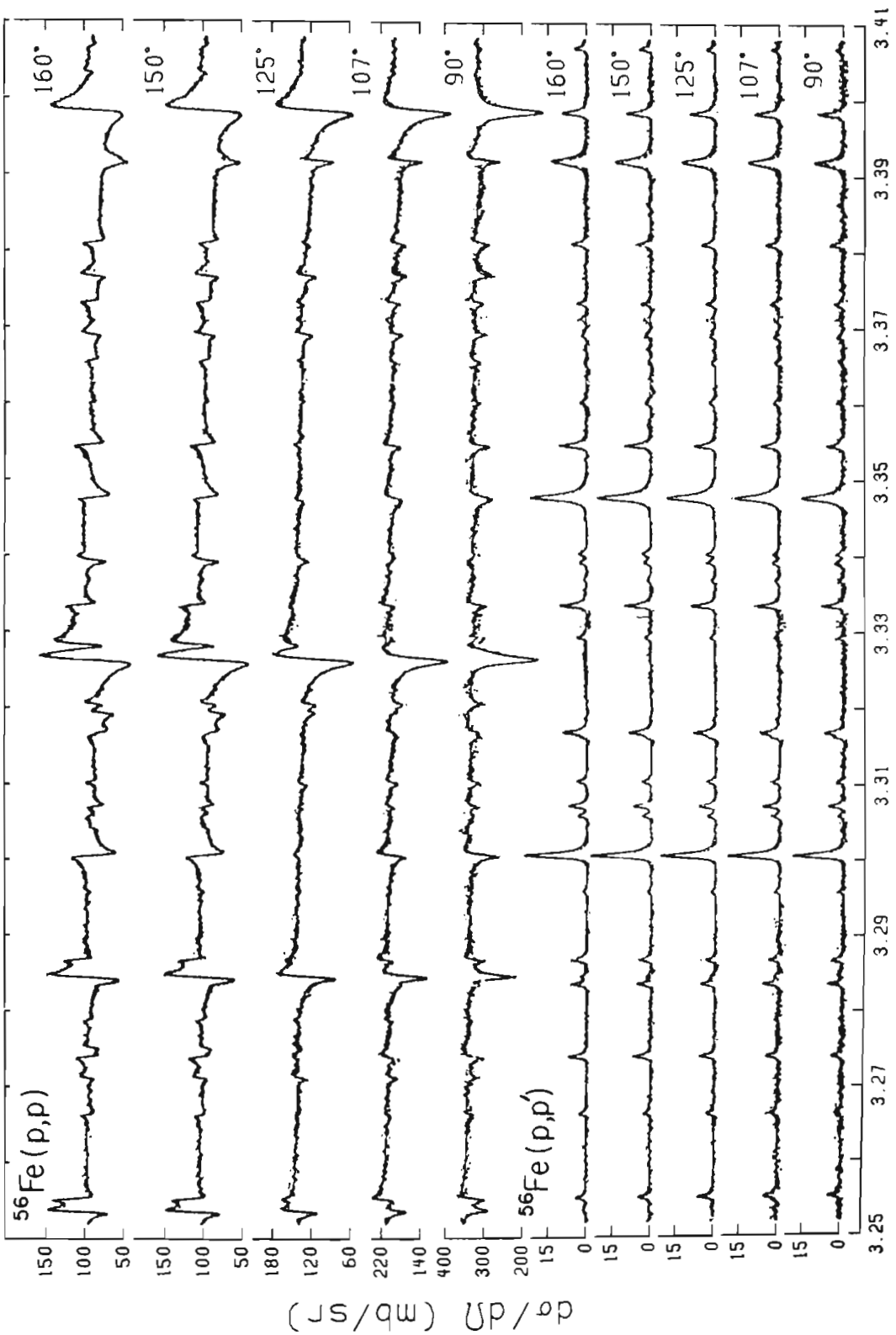
^{56}Fe(p,p)
^{56}Fe(p,p')
160°
150°
125°
107°
90°
dσ/dΩ (mb/sr)
E_p (MeV)
3.25
3.27
3.29
3.31
3.33
3.35
3.37
3.39
3.41

Figure 4.6 Differential cross sections from E_p = 3.40 to 3.55 MeV. The solid line is a fit to the data.

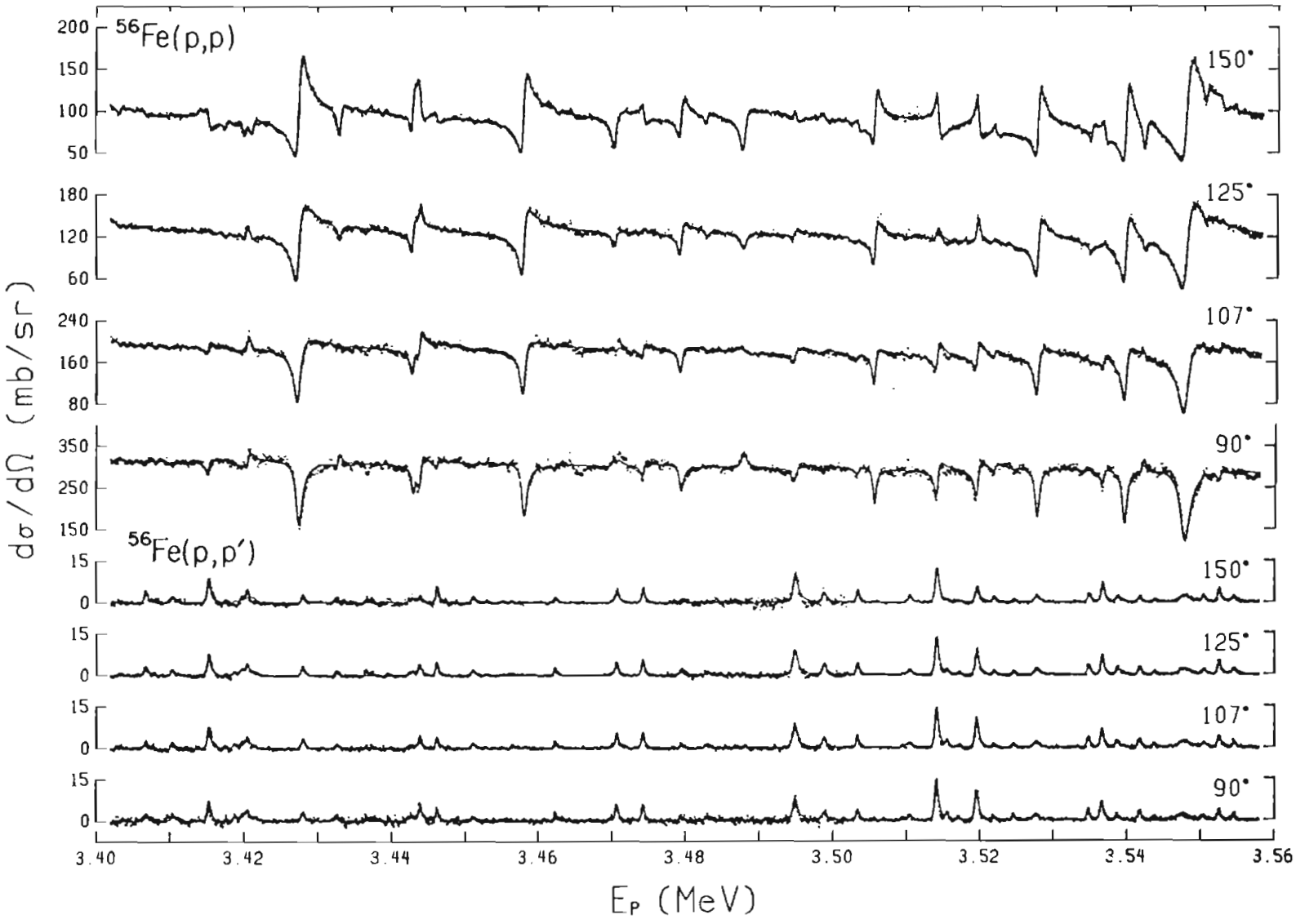
^{56}Fe(p,p)
150°
125°
107°
90°
^{56}Fe(p,p′)
150°
125°
107°
90°
dσ/dΩ (mb/sr)
E_P (MeV)
3.40
3.42
3.44
3.46
3.48
3.50
3.52
3.54
3.56

Figure 4.7 Differential cross sections from E_p = 3.55 to 3.70 MeV. The solid line is a fit to the data.

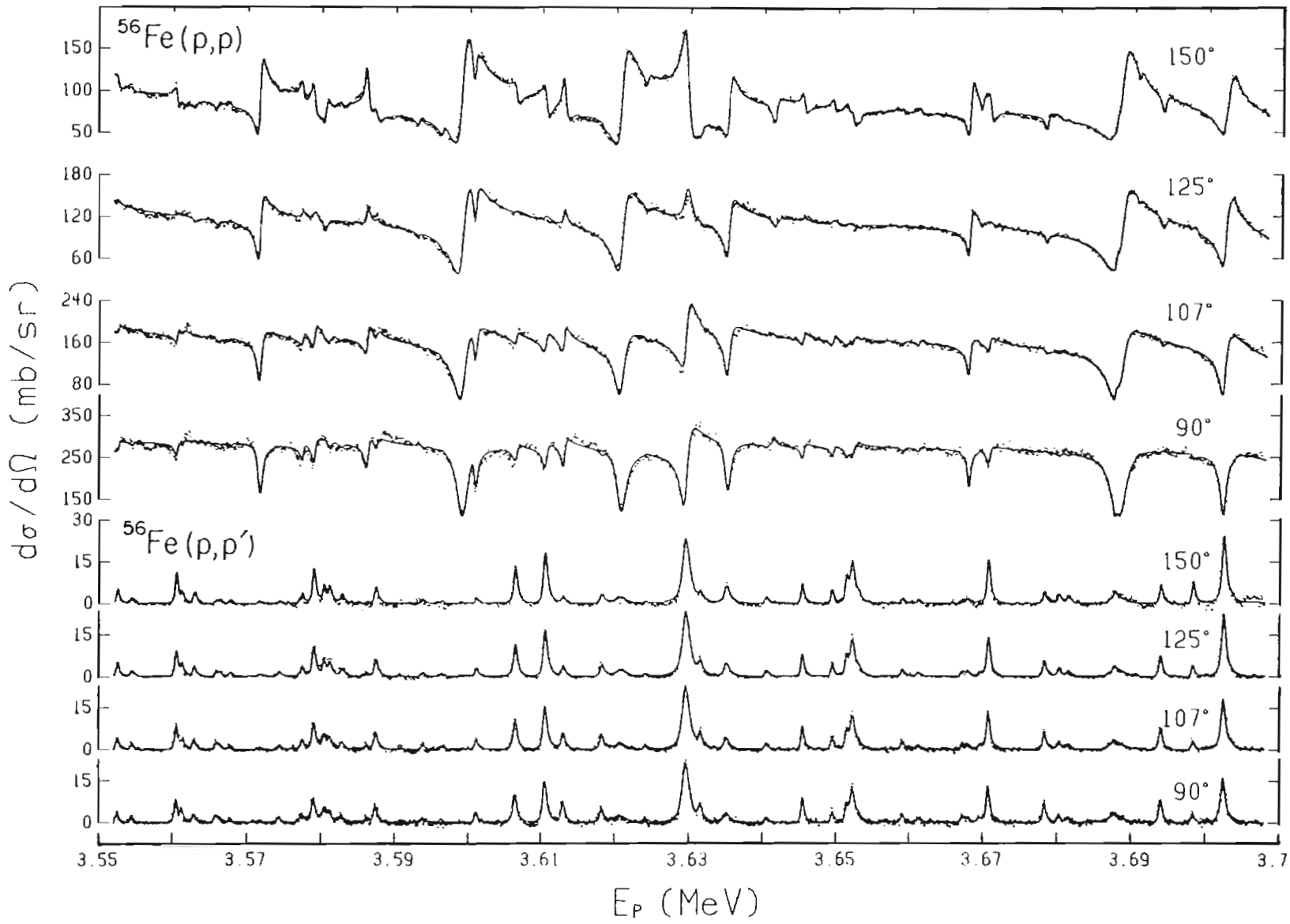
56Fe(p,p)
150°
125°
107°
90°
56Fe(p,p′)
150°
125°
107°
90°
dσ/dΩ (mb/sr)
150
100
50
180
120
60
240
160
80
350
250
150
30
15
0
3.55
3.57
3.59
3.61
3.63
3.65
3.67
3.69
3.71
Ep (MeV)

Figure 4.8 Differential cross sections from E_p = 3.70 to 3.85 MeV. The solid line is a fit to the data.

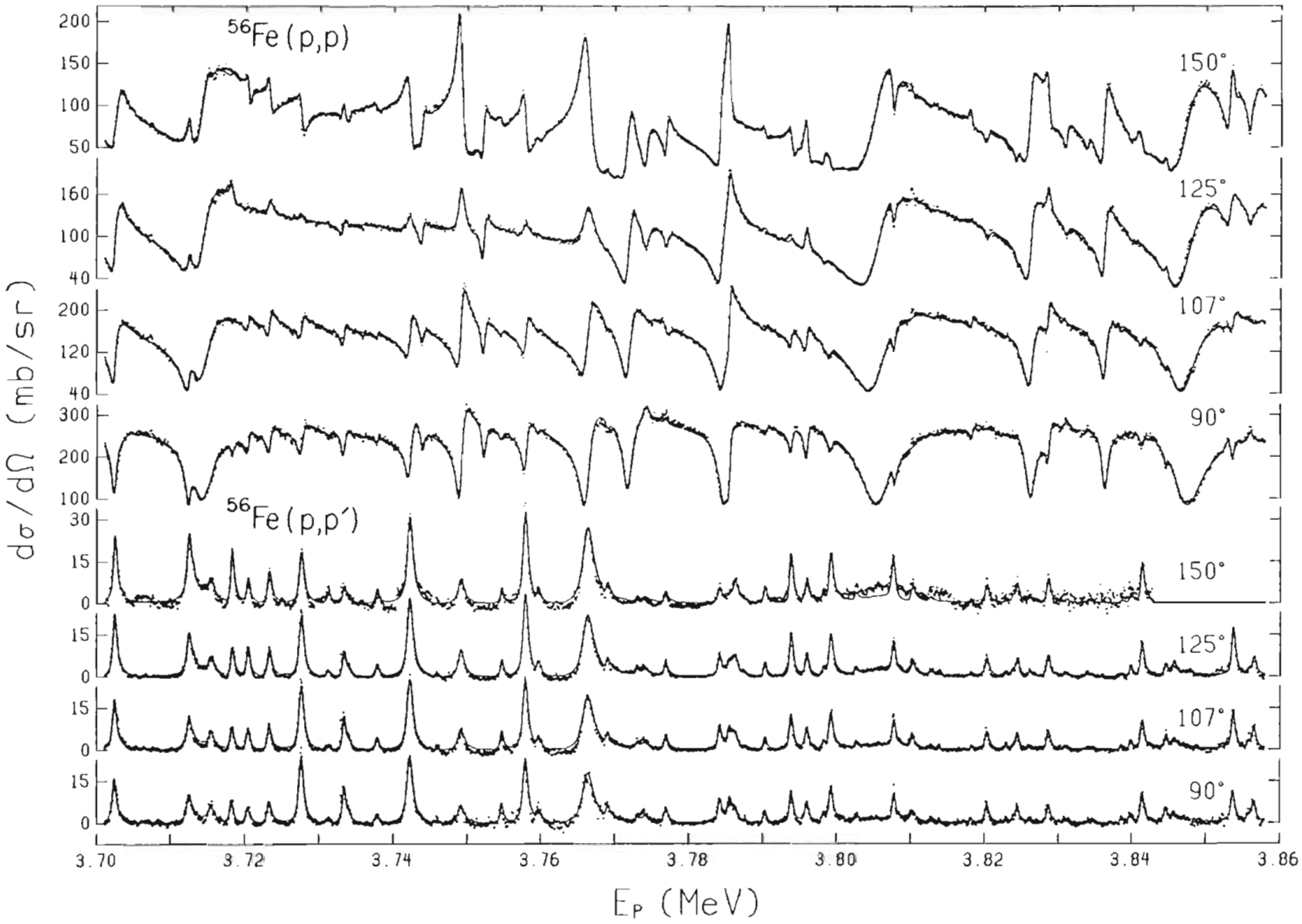
^{56}Fe (p,p)
150°
125°
107°
90°
^{56}Fe (p,p′)
150°
125°
107°
90°
dσ/dΩ (mb/sr)
E_P (MeV)
3.70
3.72
3.74
3.76
3.78
3.80
3.82
3.84
3.86

Figure 4.9 Differential cross sections from E_p = 3.85 to 4.00 MeV. The solid line is a fit to the data.

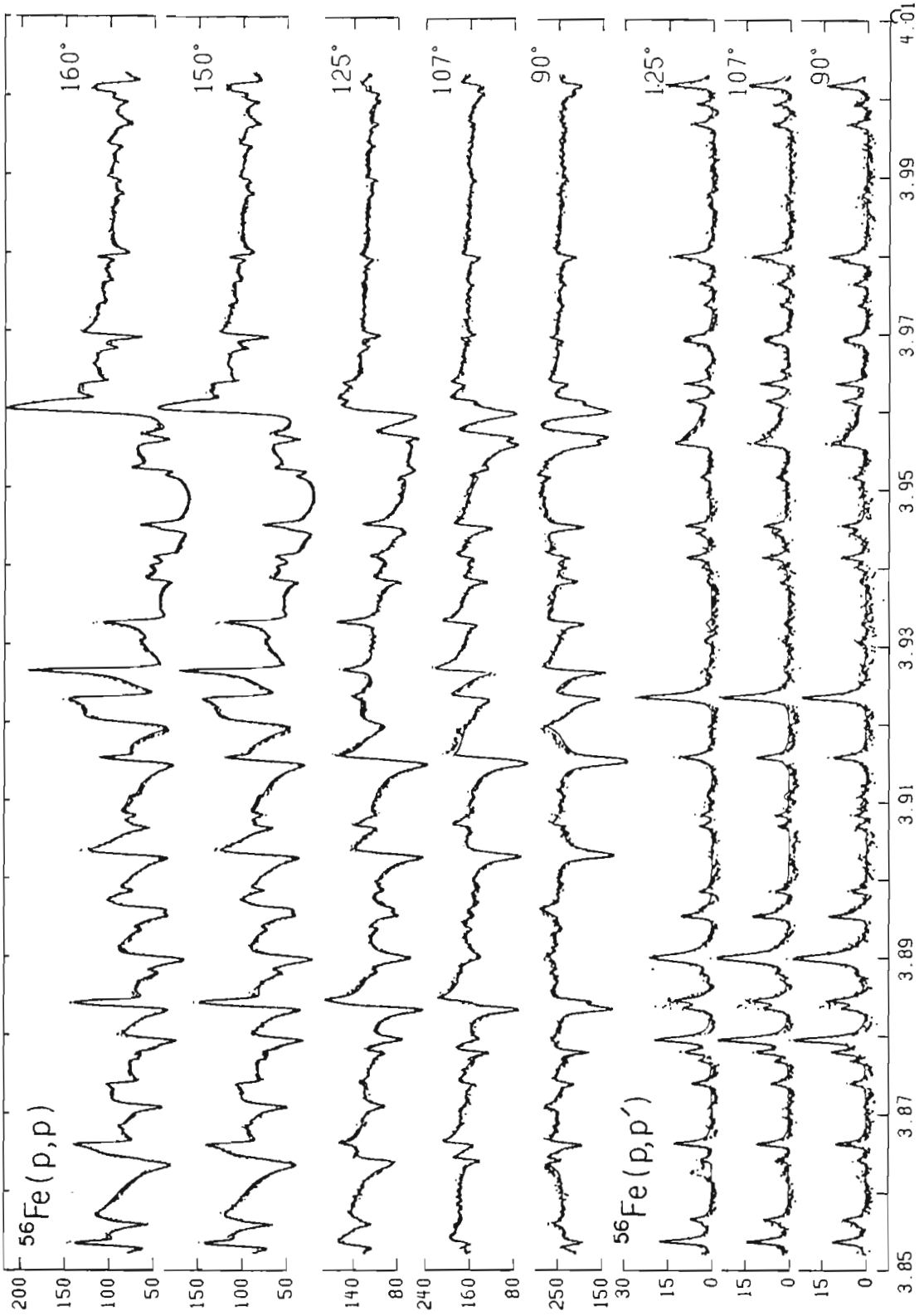
^{56}Fe(p,p)
^{56}Fe(p,p′)
160°
150°
125°
107°
90°
dσ/dΩ (mb/sr)
E_p (MeV)
3.85
3.87
3.89
3.91
3.93
3.95
3.97
3.99
4.01

In addition to presenting the cross sections and R-matrix fits, it is also useful to plot the observed strength in each channel as a function of energy. This is done in figures 4.10 to 4.15, where the running sum of reduced widths is plotted vs. energy. Analogue states stand out as rapid increases in the accumulated strength over a narrow energy interval. Each of the above mentioned analogue states are easily recognized in these plots. Further analysis of the analogue states is given in the next chapter.

Figure 4.10(a) Sum of elastic reduced widths vs. energy for the $1/2^+$ levels.

(b) Sum of inelastic reduced widths vs. energy for the $1/2^+$ levels.

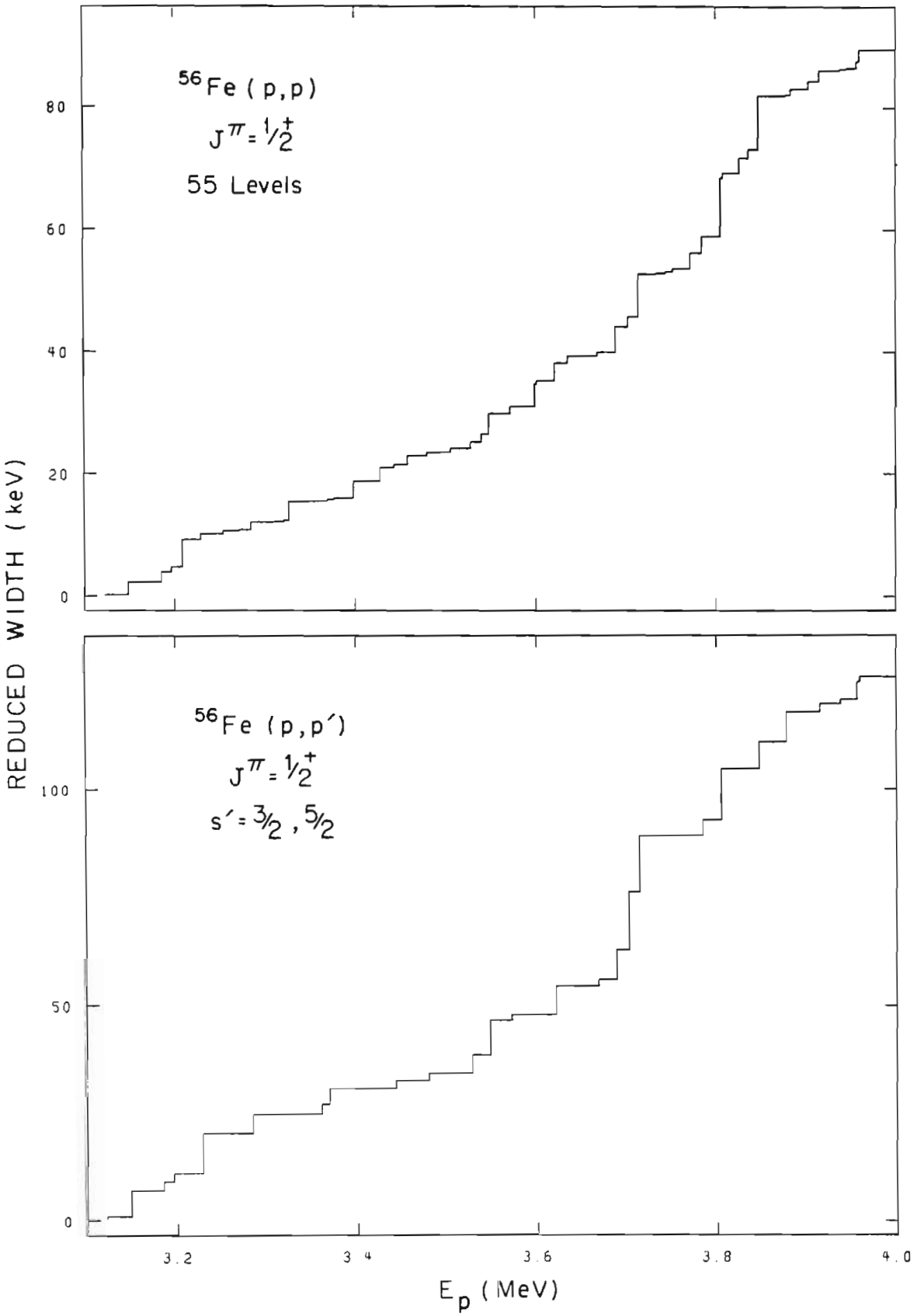
^{56}Fe (p,p)
$J^{\pi} = 1/2^{+}$
55 Levels
^{56}Fe (p,p′)
$J^{\pi} = 1/2^{+}$
$s' = 3/2 , 5/2$
REDUCED WIDTH (keV)
0
20
40
60
80
0
50
100
3.2
3.4
3.6
3.8
4.0
E_p (MeV)

Figure 4.11(a) Sum of elastic reduced widths vs. energy for the $1/2^-$ levels.

(b) Sum of inelastic reduced widths vs. energy for the $1/2^-$ levels.

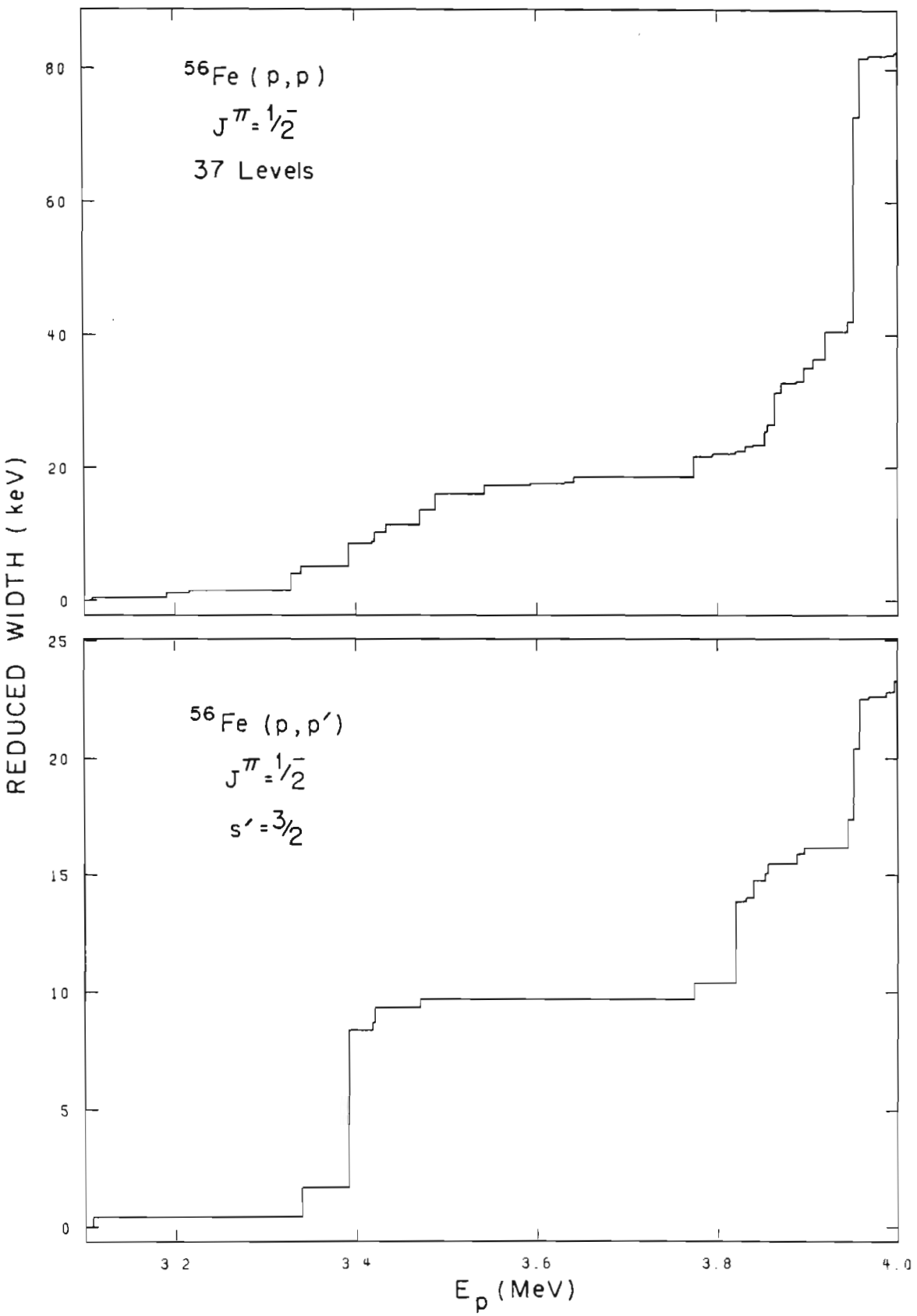
^{56}Fe (p, p)
$J^{\pi} = 1/2^-$
37 Levels
^{56}Fe (p, p′)
$J^{\pi} = 1/2^-$
$s' = 3/2$
REDUCED WIDTH (keV)
E_p (MeV)
0
20
40
60
80
0
5
10
15
20
25
3.2
3.4
3.6
3.8
4.0

Figure 4.12(a) Sum of elastic reduced widths vs. energy for the $3/2^-$ levels.

(b) Sum of inelastic reduced widths for channel spin s'=3/2 vs. energy for the $3/2^-$ levels.

(c) Sum of inelastic reduced widths for channel spin s'=5/2 vs. energy for the $3/2^-$ levels.

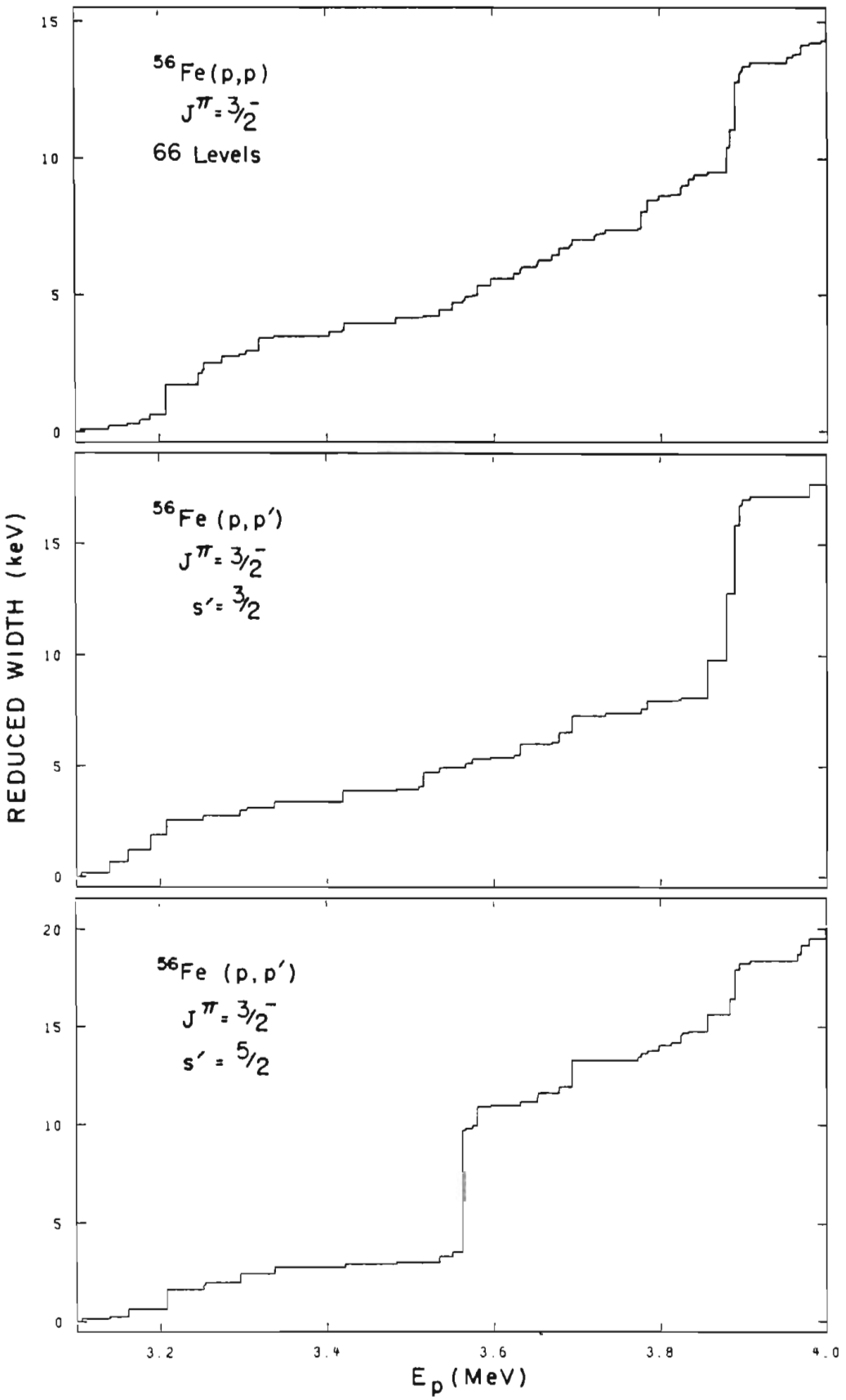
^{56}Fe(p,p)
$J^{\pi} = 3/2^-$
66 Levels
^{56}Fe (p,p')
$J^{\pi} = 3/2^-$
$s' = 3/2$
^{56}Fe (p,p')
$J^{\pi} = 3/2^-$
$s' = 5/2$
REDUCED WIDTH (keV)
E_p (MeV)
0
5
10
15
20
3.2
3.4
3.6
3.8
4.0

Figure 4.13(a) Sum of elastic reduced widths vs. energy for the $3/2^+$ levels.

(b) Sum of inelastic reduced widths for the channel $\ell'=0$ vs. energy for the $3/2^+$ levels.

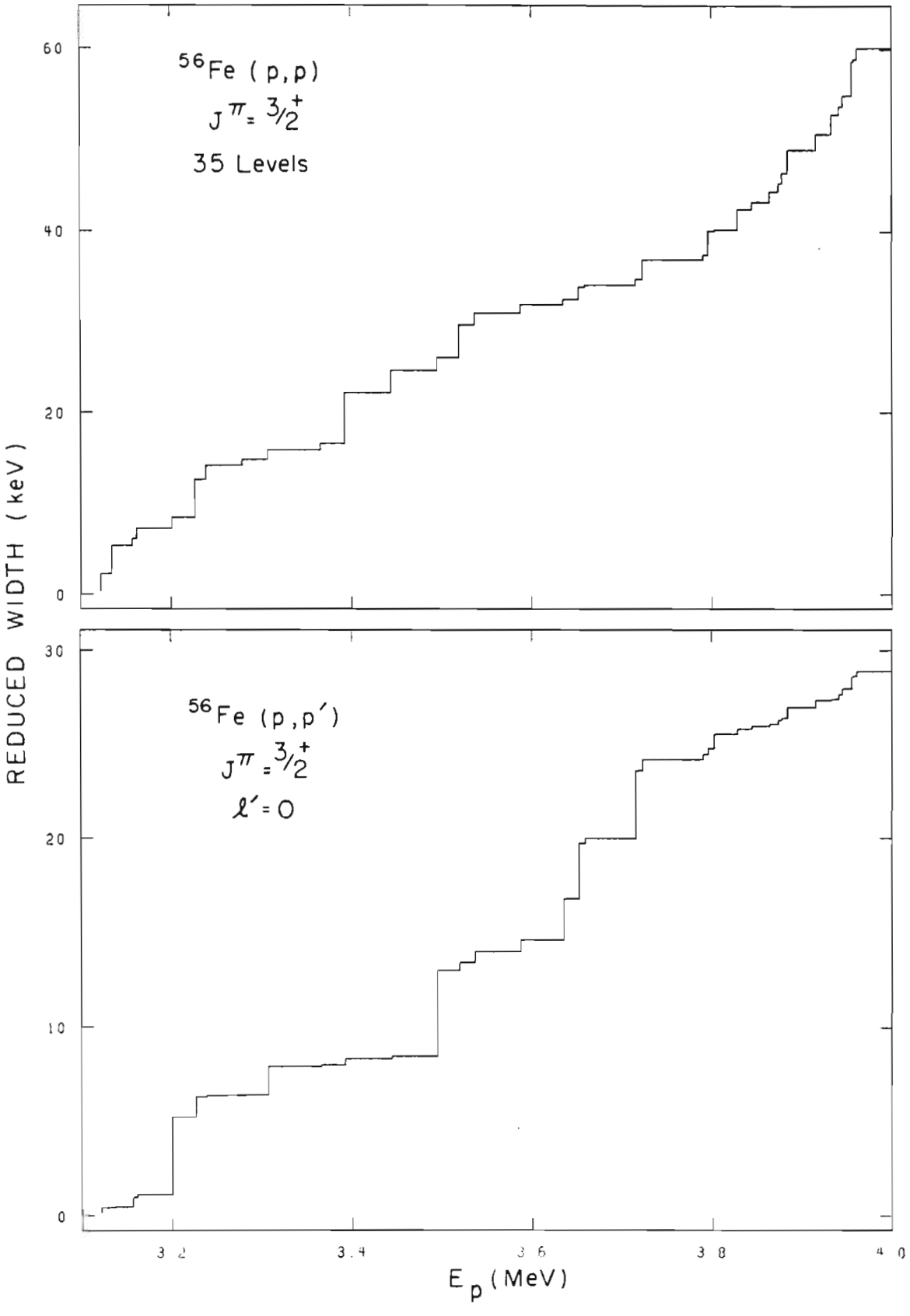
^{56}Fe (p,p)
$J^{\pi} = 3/2^{+}$
35 Levels
^{56}Fe (p,p′)
$J^{\pi} = 3/2^{+}$
$\ell' = 0$
REDUCED WIDTH (keV)
E_p (MeV)
0
20
40
60
10
30
3.2
3.4
3.6
3.8
4.0

Figure 4.14(a) Sum of elastic reduced widths vs. energy for the $5/2^+$ levels.

(b) Sum of inelastic reduced widths for the channel $\ell'=0$ vs. energy for the $5/2^+$ levels.

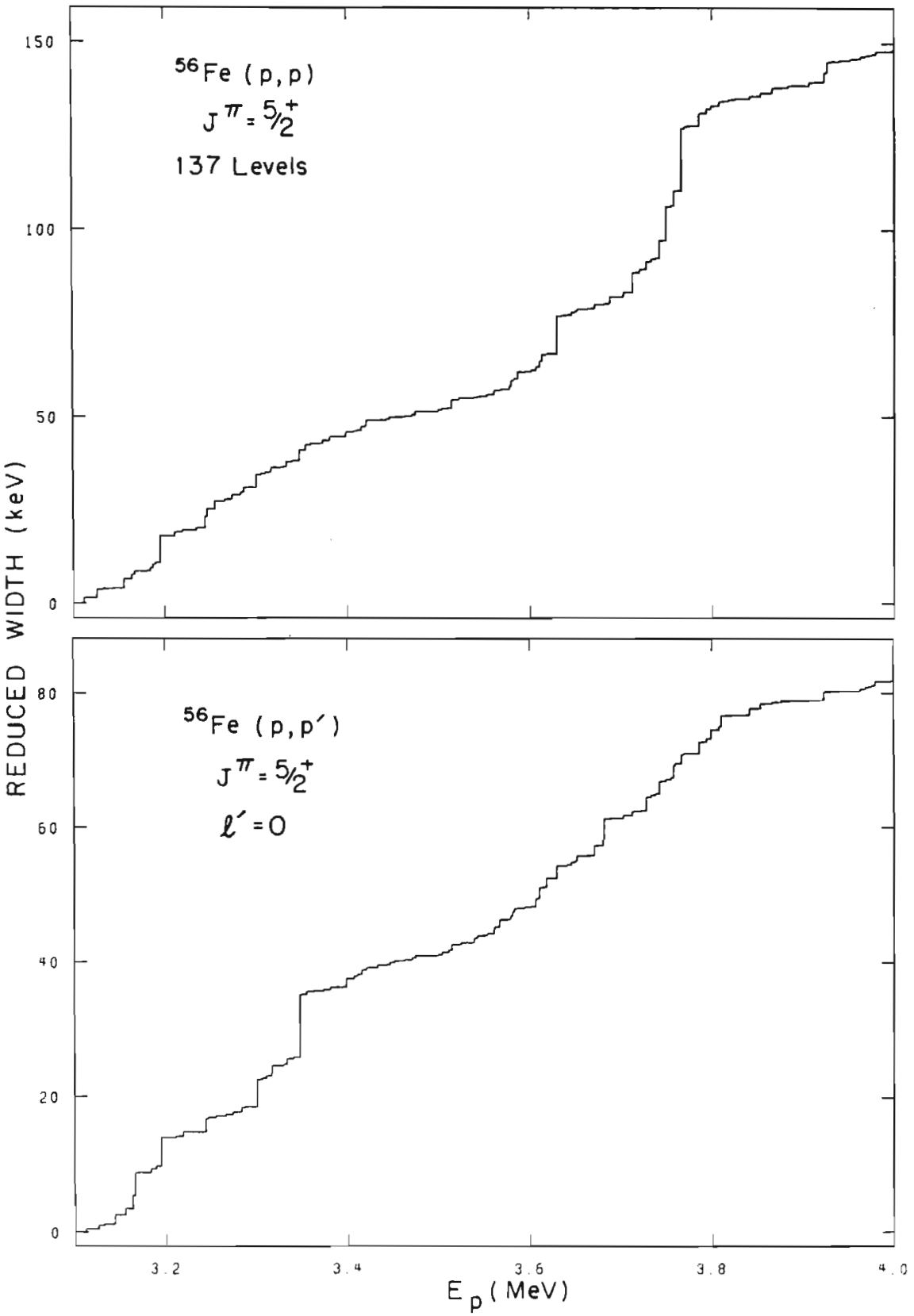
^{56}Fe (p, p)
$J^{\pi} = 5/2^{+}$
137 Levels
^{56}Fe (p, p′)
$J^{\pi} = 5/2^{+}$
$\ell' = 0$
REDUCED WIDTH (keV)
E_p (MeV)
0
50
100
150
20
40
60
80
3.2
3.4
3.6
3.8
4.0

Figure 4.15(a) Sum of elastic reduced widths vs. energy for the $5/2^-$ levels.

(b) Sum of elastic reduced widths vs. energy for the $9/2^+$ levels.

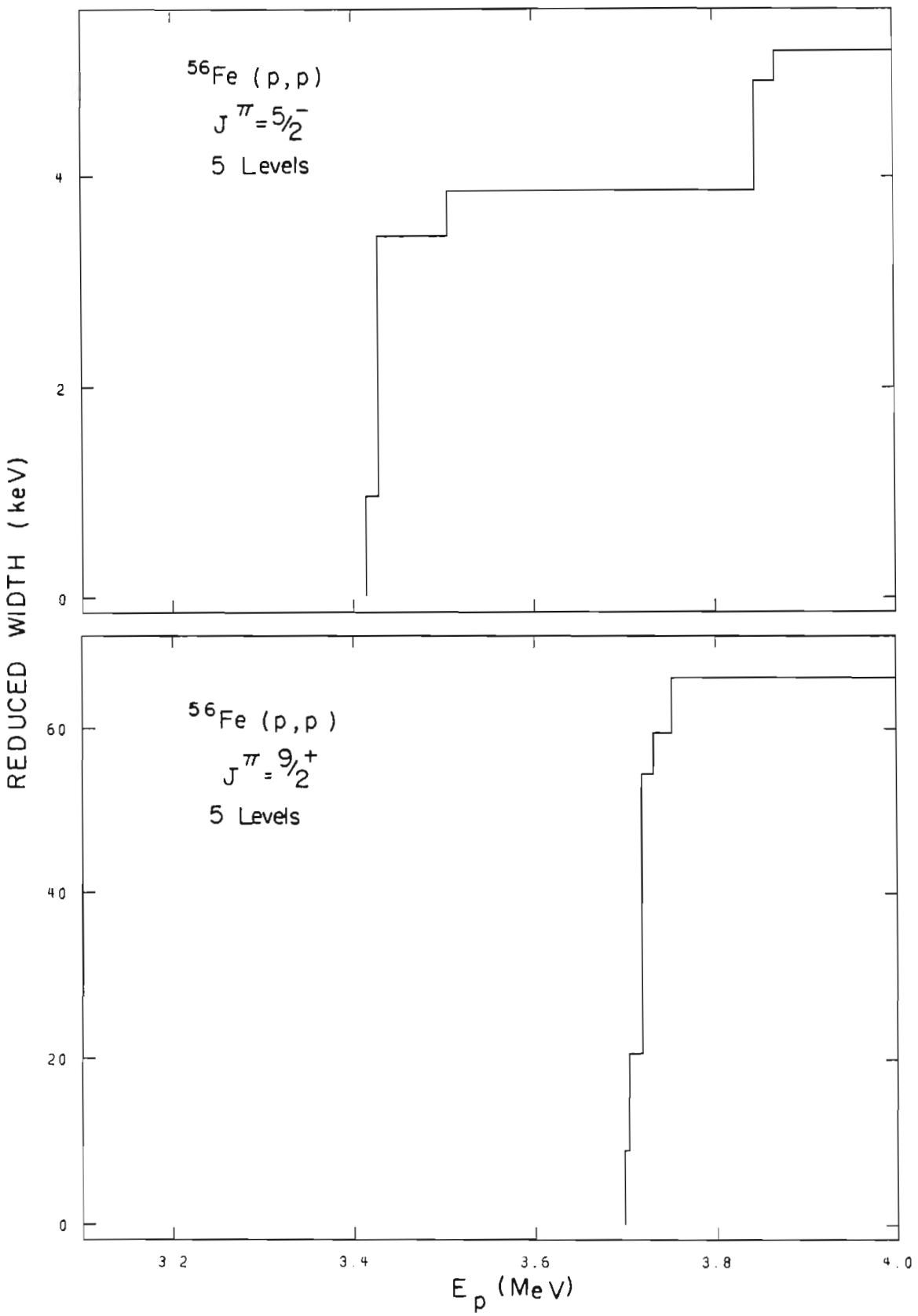
^{56}Fe (p,p)
$J^{\pi} = 5/2^-$
5 Levels
^{56}Fe (p,p)
$J^{\pi} = 9/2^+$
5 Levels
REDUCED WIDTH (keV)
0
2
4
0
20
40
60
3.2
3.4
3.6
3.8
4.0
E_p (MeV)

Chapter 5

ISOBARIC ANALOGUE RESONANCES

5.1 Introduction

Symmetries (and approximate symmetries) have long been used as a basis for understanding the complex systems encountered in the study of atomic nuclei. The classification of nuclear states by quantum numbers corresponding to such conserved quantities as energy, total angular momentum, and parity is a natural consequence of symmetries involving rotations and reflections in space-time. The symmetry of the nuclear force under the interchange of neutrons and protons leads to another quantum number, the isobaric spin (isospin).

The isospin formalism was introduced in analogy to particle spin by Heisenberg (1932) not long after the discovery of the neutron. In this framework, neutrons and protons are treated as two states of the same particle (the nucleon) differing only in the third component of the isospin vector (t_z=+1/2 for neutrons, -1/2 for protons). As pointed out by Wigner (1937) the total isospin of a nucleus

($\underset{\sim}{T} = \sum_i \underset{\sim}{t}_i$) is a good quantum number only to the extent that the Coulomb interactions (which obviously distinguish neutrons and protons) can be neglected in comparison with the nuclear interactions.

For many years it was believed that the Z^2 dependence of the Coulomb force would make isospin useless for heavier nuclei, and so most of the early applications of isospin were restricted to light nuclei. This early work established the existence of isobaric analogue states (IAR)--states that differed only in the exchange of a neutron for a proton. Evidence for IAR in heavier nuclei was provided by Anderson and Wong (1962). They measured strong neutron groups in (p,n) reactions leading to excited states of the residual nucleus which differed in energy from the target by the Coulomb energy of the extra proton. Lane (1962) interpreted these results in terms of "quasi-elastic scattering" (charge exchange) using an isospin dependent optical model Hamiltonian. Two years later Fox, Moore, and Robson (1964) observed IAR in the compound nucleus in $^{88}Sr(p,n)$ and $^{89}Y(p,n)$ excitation functions.

The first evidence for fine structure in analogue states (the result of mixing between the IAR and the background states of higher level density) was provided by Richard et al. (1964) in the reaction $^{92}Mo(p,p)$. Although the fine structure was not completely resolved, a definite dip in the magnitude of the fluctuations on the high energy side of the analogue was seen. This asymmetry was explained

by Robson (1965) in terms of mixing of the analogue and background states in the external region (outside the nuclear surface). A large number of well-resolved fine structure patterns have since been observed, and an excellent summary is given by Bilpuch et al. (1976)

Many different theoretical approaches have been used successfully to treat the fine structure problem, including various shell model approaches (e.g., Fallieros, 1966, Mahaux and Weidenmüller, 1967, MacDonald and Mekjian, 1968) and treatments based on Feshbach's projection operator formalism (1958,1962) (e.g., Kerman and De Toledo Piza, 1968). Lane and Robson (1967) and Lane (1969) have treated the problem as a line-broadening phenomenon using the Kapur and Peierls (1938) R-matrix theory. While each method has its own advantages and disadvantages, an R-matrix approach will be followed in this work. For simplicity, the Wigner-Eisenbud form of the R-matrix will be used so that certain results from chapter 2 may be applied directly.

In summarizing the theory of analogue states, there are three important points to be brought out: 1) the difference in energy between the parent state (neutron + core or target) and the analogue state (proton + core or target); 2) the relation between the reduced widths of the parent and analogue states; and 3) the fine structure pattern caused by the mixing of the analogue state with the background states of the proton + target system. The first topic is the most straightforward, and in simple terms the energies of the

states differ by the Coulomb energy of the extra proton. Theoretical predictions of the Coulomb energy difference and comparisons with experiment are given in the last section of this chapter (5.4). The next section (5.2) contains a brief discussion of analogue states using the coupled channels approach of Lane (1962) and following the treatment of Robson (1965). This derivation only considers two channels (neutron and proton) and has the advantage of simply displaying the relationship of parent and analogue using an isospin dependent shell model potential. In section 3, R-matrix techniques will be applied to the more general fine structure problem, including multiple channel effects. The object will be to derive an expression describing the distribution of fine structure widths near an analogue resonance. This treatment follows Lane (1969), but uses the Wigner-Eisenbud boundary conditions (instead of those of Kapur and Peierls) and uses the Lorentz weighted strength function of MacDonald and Mekjian (1967) and Kerman and De Toledo Piza (1968). Section 4 gives a comparison with the present data.

5.2 Coupled Isospin Channels

Just as the neutron and proton are members of an isospin doublet ($T = 1/2$, $T_z = \pm 1/2$), there exist states in nuclei which are members of isospin multiplets. All members

of a multiplet have identical wavefunctions (ideally) with the exception of that part which specifies the charge of the state ($T_z=(N-Z)/2$). Each state can be generated from the others by successive applications of the charge-changing operators $T^{\pm}$ (the isospin raising and lowering operators). Because changing a neutron into a proton increases the Coulomb energy of a state (and hence its excitation energy) normally only the two most neutron rich members of a multiplet can be found experimentally: the $T_z=T$ and $T_z=T-1$ members. The former state is referred to as a 'parent' state and is typically a state of low excitation energy. The latter state is the isobaric analogue state. The following discussion examines the relationship of these two states using an isospin dependent optical model Hamiltonian.

Consider the particle + core system described by the Hamiltonian

$$H = T_R + V_C(1/2 - t_z) + U_0 + U_1 \underset{\sim}{t}\cdot\underset{\sim}{T} \qquad (5.1)$$

where T_R = the kinetic energy, $-(\hbar^2/2M)\nabla^2$

V_C = the Coulomb potential energy

U_0, U_1 = the isospin independent and dependent potentials, respectively

$\underset{\sim}{t}$ = the isospin of the particle

$\underset{\sim}{T}$ = the isospin of the core

Wavefunctions will be written as products of a radial function, a channel function (containing spin and angle functions), and an isospin function:

$$|\Psi\rangle = |\chi\rangle\,|\varphi\rangle\,|t,t_z\rangle \qquad (5.2)$$

For the proton + core system (|pC>) the isospin wavefunction is

$$|pC\rangle = |p\rangle\,|C\rangle = |1/2,-1/2\rangle\,|T_o,T_o\rangle \tag{5.3}$$

where $T_o=(N-Z)/2$ is the isospin of the core. Using standard angular momentum coupling algebra, |pC> can be expressed in terms of states $|t_1\ t_2\ T,T_z\rangle$ of good total isospin $\underset{\sim}{T}=\underset{\sim}{t}_1+\underset{\sim}{t}_2$:

$$\begin{aligned}|pC\rangle = (2T_o+1)^{-1/2}(&|T_o\ 1/2\ T_o+1/2,T_o-1/2\rangle \\ &+ (2T_o)^{1/2}|T_o\ 1/2\ T_o-1/2,T_o-1/2\rangle)\end{aligned} \tag{5.4}$$

Similarly,

$$|nC\rangle = |T_o\ 1/2\ T_o+1/2,T_o+1/2\rangle \tag{5.5}$$

These isospin coupled states can likewise be expanded in terms of the physical, uncoupled states:

$$\begin{aligned}|T_>\rangle &= |T_o\ 1/2\ T_o+1/2,T_o-1/2\rangle \\ &= (2T_o+1)^{-1/2}(|1/2,-1/2\rangle|T_o,T_o\rangle \\ &\qquad + (2T_o)^{1/2}|1/2,1/2\rangle|T_o,T_o-1\rangle) \\ &= (2T_o+1)^{-1/2}(|pC\rangle + (2T_o)^{1/2}|nA\rangle)\end{aligned} \tag{5.6}$$

$$\begin{aligned}|T_<\rangle &= |T_o\ 1/2\ T_o-1/2,T_o-1/2\rangle \\ &= (2T_o+1)^{-1/2}((2T_o)^{1/2}|pC\rangle - |nA\rangle)\end{aligned}$$

where |A> is the analogue of the target state:

$$|A\rangle = \hat{T}^-|C\rangle = \hat{T}^-|T_o,T_o\rangle = |T_o,T_o-1\rangle \tag{5.7}$$

$\hat{T}^-$ is the normalized isospin lowering operator which changes a neutron into a proton. After some simple algebra one can show

$$\begin{aligned}(\underset{\sim}{t}\cdot\underset{\sim}{T})|pC\rangle &= (T_o/2)^{1/2}|nA\rangle - (T_o/2)|pC\rangle \\ (\underset{\sim}{t}\cdot\underset{\sim}{T})|nA\rangle &= (T_o/2)^{1/2}|pC\rangle + (T_o/2)|nA\rangle\end{aligned} \tag{5.8}$$

Therefore the Hamiltonian H leads to the coupled equations

$$\begin{aligned}(T_\kappa - E_p + V_c + U_o - U_1\,T_o/2)\chi_{pC} &= -(T_o/2)^{1/2}U_1\chi_{nA} \\ (T_\kappa - E_n + U_o + U_1\,(T_o-1)/2)\chi_{nA} &= -(T_o/2)^{1/2}U_1\chi_{pC}\end{aligned} \tag{5.9}$$

where E_n is simply related to E_p by the Coulomb energy difference

$$E_n = E_p - \Delta_c \tag{5.10}$$

These equations can be approximately uncoupled by transforming to basis vectors of good isospin:

$$\begin{aligned}(T_K - E_p + \Delta_c + U_o + U_1 T_o/2)\chi_> &= (\Delta_c - V_c)/(2T_o+1)\ (\chi_> + (2T_o)^{1/2}\chi_<) \\ (T_K - E_p + V_c + U_o - U_1(T_o+1)/2)\chi_< &= (\Delta_c - V_c)/(2T_o+1)\ ((2T_o)^{1/2}\chi_> - \chi_<)\end{aligned} \tag{5.11}$$

In the internal region, $V_c \approx \Delta_c$ and the isospin states are approximately eigenstates of the Hamiltonian H. In the external region, however, χ_{nA} and χ_{pC} are strongly coupled.

For the n + C system, equation (5.1) gives

$$(T_K - E_n + U_o + U_1 T_o/2)\chi_{nC} = 0 \tag{5.12}$$

which, by comparison with equation (5.11) shows

$$\chi_>(E_p - \Delta_c) \approx \chi_{nC}(E_n) \tag{5.13}$$

In other words, one part of the p + C wavefunction has the same spatial dependence as the n + C system.

While we are ultimately interested in the multi-channel situation, it is helpful to consider the simpler case of elastic scattering. Using Robson's notation, the R-matrix is calculated using the isospin eigenstates:

$$R_I = \begin{bmatrix} R_{>>} & 0 \\ 0 & R_{<<} \end{bmatrix} \tag{5.14}$$

where $R_{>>} = \sum_\lambda \frac{\gamma_{\lambda n}^2}{E_\lambda^n - E} = \frac{\gamma_{\lambda n}^2}{E_\lambda^n - E}$

$$R_{<<} = \sum_\mu \frac{\gamma_\mu^2}{E_\mu - E}$$

and $\chi_> = \chi_{nA}$ has been used to calculate $R_{>>}$, with a single level approximation for the $T_>$ states. The latter assumption is justified due to the low density of the low-lying states of the n + C system. The off-diagonal terms of R are zero under the assumption of no internal mixing. To calculate the R-matrix for the physical channels, define

$$\underset{\sim}{\chi} = \begin{pmatrix} \chi_{pc} \\ \chi_{nA} \end{pmatrix} \qquad \underset{\sim}{\chi}_I = \begin{pmatrix} \chi_> \\ \chi_< \end{pmatrix} \tag{5.15}$$

then $\underset{\sim}{\chi}_I = O\underset{\sim}{\chi}$, where $O = \frac{1}{(2T_o+1)^{1/2}} \begin{bmatrix} 1 & (2T_o)^{1/2} \\ (2T_o)^{1/2} & -1 \end{bmatrix}$

From the R-matrix relations

$$\chi = R\,(a_c \tfrac{d}{dr_c} - B_<)\chi \qquad \chi_I = R_I(a_c \tfrac{d}{dr_c} - B_<)\chi_I \tag{5.16}$$

one can show

$$R = O^{-1}\, R_I O = \begin{bmatrix} R_{pp} & R_{pn} \\ R_{np} & R_{nn} \end{bmatrix} \tag{5.17}$$

thus

$$\begin{aligned} R_{pp} &= \tfrac{1}{2T_o+1}\,(R_{>>} + 2T_o R_{<<}) \\ R_{np} &= \tfrac{1}{2T_o+1}\,(2T_o)^{1/2}(R_{>>} - R_{<<}) = R_{pn} \\ R_{nn} &= \tfrac{1}{2T_o+1}\,(2T_o R_{>>} + R_{<<}) \end{aligned} \tag{5.18}$$

From equation (2.54) the collision matrix is

$$U_{pp} = e^{2i(\omega_c - \phi_c)}\,(1 + (1 - RL^o)^{-1} R(2iP))_{pp} \tag{5.19}$$

For energies below the neutron threshold,

$$\begin{aligned} L^o = L - B &= \begin{bmatrix} L_p - B_c & 0 \\ 0 & S_n^- - B_c \end{bmatrix} = \begin{bmatrix} L_p^o & 0 \\ 0 & 0 \end{bmatrix} \\ L_p^o &= (S_p^+ - S_n^-) + iP_p \end{aligned} \tag{5.20}$$

where the boundary conditions were chosen to match those of

the bound neutron. A little algebra leads to Robson's equation (2.27):

$$U_{pp} = e^{2i(\omega_c - \phi_c)} \left(1 + 2iP_p (1 - R_{pp}L_p^o)^{-1} R_{pp}\right)$$

$$= e^{2i(\omega_c - \phi_c)} \left(1 + \frac{i\Gamma_A}{E_A - E_p - i\Gamma_A/2} + \right. \qquad (5.21)$$

$$\left. 2iP_p f_p^2 \left(1 - \frac{2T_o}{2T_o+1} R_{<<} L_p^o f_p\right)^{-1} \left(\frac{2T_o}{2T_o+1}\right) R_{<<} \right)$$

where $\Gamma_A = 2P_p \gamma_{n\lambda}^2 / (2T_o+1)$

$$E_A = (E_\lambda^{(p)} + \Delta_c) - (S_p^+ - S_n^-)\gamma_{n\lambda}^2/(2T_o+1) = E_> + \Delta_{TE}$$

$$f_p = (E_> - E_p) / (E_A - E_p - i\Gamma_A/2)$$

Thus the scattering matrix consists of three terms corresponding to Rutherford scattering, scattering through the analogue state, and scattering through the background states contained in $R_{<<}$. The analogue energy is shifted from the neutron bound state energy by two terms: 1) the Coulomb energy difference, and 2) the level shift due to a change in boundary conditions between the neutron and the proton channels (the Thomas-Ehrman shift, 1951).

The reduced width of the analogue state,

$$\gamma_A^2 = \gamma_{n\lambda}^2 / (2T_o+1) \qquad (5.22)$$

is reduced by the factor $(2T_o+1)^{-1}$ which arises from the isospin coupling algebra. Thus in comparing analogue spectroscopic factors ($\Gamma_A/\Gamma_{s.p.}$, where $\Gamma_{s.p.}$ = the single particle width) obtained in proton scattering with those obtained in (d,p) reactions leading to the parent state, this factor must be taken into account. This is usually done by dividing $\Gamma_{s.p.}$ by $(2T_o+1)$.

The last term in U_{pp} contains the effects of the background states (in $R_{<<}$) modulated by the factor of f_p.

I.e., those background states with $E_{p\mu} \approx E_A$ are enhanced. If $\Delta_A \neq 0$, this enhancement is asymmetric, and has a minimum at $E_p = E_> = E_A - \Delta_{TE}$. The asymmetry is caused by the difference in boundary conditions, which in turn reflects differences in the wavefunctions in the external region. For this reason, boundary mismatch is referred to as "external mixing". Internal mixing (through the term $V_c - \Delta_c$) has been neglected in this treatment.

5.3 Fine Structure of Analogue States

In equation (5.21) of the previous section, the widths of the background states are shown to be modified by the presence of the analogue state. This result can be obtained in a more general fashion without resorting to the specific assumptions used in that derivation. Consider a special state $|\lambda>$ and a set of states $|\mu>$ which are eigenstates of an approximate Hamiltonian H^0. The boundary conditions will be expressed through the use of the Bloch operator (1957), given by

$$L = \sum_c |c\rangle (\hbar^2/2M_c) \frac{\delta(r_c - a_c)}{r_c} \left(\frac{d}{dr_c} r_c - b_c \right) \langle c| \qquad (5.23)$$

where the boundary condition in channel c is b_c. Thus,

$$L^0|\lambda> = L^0|\mu> = 0 \qquad (5.24)$$

where L^0 specifies the boundary conditions of the unmixed states. Let the states $|\nu>$ be eigenstates of the full Hamiltonian H with boundary conditions given by L. From equation (2.42)

$$R_{cc'} = \sum \frac{\gamma_{\nu c}\gamma_{\nu c'}}{E_\nu - E} \tag{5.25}$$

For convenience the definition of γ may be written as

$$\gamma_{\nu c} = \left(\frac{\hbar^2}{2M_c}\right)^{1/2} \langle c \left|\frac{\delta(r_c - a_c)}{r_c}\right| \nu \rangle \tag{5.26}$$

where the delta function selects out the channel surface $r_c = a_c$. Thus,

$$\begin{aligned} R_{cc'} &= \sum \frac{\langle c \left|\frac{\delta(r_c - a_c)}{r_c}\right| \nu\rangle\langle\nu\left|c'\right.\rangle \left|\frac{\delta(r_{c'} - a_{c'})}{r_{c'}}\right.}{} \left(\frac{\hbar^2}{2M_c}\right)^{1/2}\left(\frac{\hbar^2}{2M_{c'}}\right)^{1/2} \\ &= \left(\frac{\hbar^2}{2M_c^{1/2}M_{c'}^{1/2}}\right) \langle c \left|\frac{\delta(r_c - a_c)}{r_c}\right| \frac{1}{H + L - E} \left|\frac{\delta(r_{c'} - a_{c'})}{r_{c'}}\right. c'\rangle \\ &= \left(\frac{\hbar^2}{2M_c^{1/2}M_{c'}^{1/2}}\right) \langle c \left|\frac{\delta(r_c - a_c)}{r_c}\right| G \left|\frac{\delta(r_{c'} - a_{c'})}{r_{c'}}\right. c'\rangle \end{aligned} \tag{5.27}$$

where we have used $\sum_\nu |\nu\rangle\langle\nu| = 1$. The inclusion of L, as discussed by Lane (1969) and Bloch (1957), makes (H+L) Hermitian and thus able to commute with infinite sums. Following Lane, define

$$\begin{aligned} \Delta H &= H - H^o \\ \Delta L &= L - L^o \\ h &= \Delta H + \Delta L \end{aligned} \tag{5.28}$$

Then

$$\begin{aligned} G &= (H + L - E)^{-1} \\ G^o &= (H^o + L^o - E)^{-1} \end{aligned}$$

Straightforward algebra gives

$$G = G^o(1 - hG) \tag{5.29}$$

$$= (1 + G^o h)^{-1} G^o \tag{5.30}$$

This may also be re-written as

$$G = (1 - Gh)G^o = G^o(1 + hG^o)^{-1} \tag{5.31}$$

G^o is a sum of two terms, the first of which contains the state $|\lambda\rangle$ and the second of which has no reference to $|\lambda\rangle$:

$$\begin{aligned} G^o &= \sum_\lambda \frac{|\lambda\rangle\langle\lambda|}{E_\lambda - E} + \sum_\mu \frac{|\mu\rangle\langle\mu|}{E_\mu - E} \\ &= G^o_\lambda + G^o_\infty \end{aligned} \tag{5.32}$$

G may be similarly resolved into G_λ and G_∞, where G_∞ is defined in analogy to equation (5.32):

$$G_\infty = G^o_\infty (1 + hG^o_\infty)^{-1} \tag{5.33}$$

Therefore

$$G^o_\infty = (1 - G_\infty h)^{-1} G_\infty \tag{5.34}$$

Substituting (5.32) and (5.34) into (5.30):

$$G = (1-G_\infty h)^{-1} G_\infty (1-hG) + G^o_\lambda (1-hG) \tag{5.35}$$

$$G = G_\infty + (1-G_\infty h) G^o_\lambda (1-hG_\infty - hG_\lambda) \tag{5.36}$$

Using the definition of G^o_λ,

$$G = (1-G_\infty h)|\lambda\rangle \frac{1}{E_\lambda - E} \langle\lambda|(1-hG_\infty - hG_\lambda) \tag{5.37}$$

Define

$$|g_\lambda\rangle = (1 - G_\infty h)|\lambda\rangle \tag{5.38}$$

$$\langle\tilde{g}_\lambda| = \langle\lambda|(1 - hG_\infty)$$

Then

$$(E_\lambda - E + |g_\lambda\rangle\langle\lambda| h) G_\lambda = |g_\lambda\rangle\langle\tilde{g}_\lambda|$$

$$G_\lambda = \frac{|g_\lambda\rangle\langle\tilde{g}_\lambda|}{E_\lambda - E + \phi_\lambda} \tag{5.39}$$

where

$$\phi_\lambda = \langle\lambda|h|g_\lambda\rangle = \langle\lambda|h - hG_\infty h|\lambda\rangle \tag{5.40}$$

Finally,

$$G = G_\infty + \frac{|g_\lambda\rangle\langle\tilde{g}_\lambda|}{E_\lambda - E + \phi_\lambda} \tag{5.41}$$

which yields

$$R_{cc'} = R^{(pot)}_{cc'} + \frac{\alpha_{\lambda c}\alpha_{\lambda c'}}{E_\lambda - E + \phi_\lambda} \tag{5.42}$$

where

$$\alpha_{\lambda c} = \left(\frac{\hbar^2}{2M_c}\right)^{1/2} \langle c \frac{\delta(r_c - a_c)}{r_c}|g_\lambda\rangle \tag{5.43}$$

$R_{cc'}$ has now been formally separated into the two desired pieces. Following Lane, we simplify G_∞:

$$G_\infty = G^o_\infty (1 + hG^o_\infty)^{-1}$$

$$= Q_\lambda G^o Q_\lambda (1 + hQ_\lambda G^o Q_\lambda)^{-1}$$

$$= Q_\lambda (Q_\lambda (H+L) Q_\lambda - E)^{-1} Q_\lambda$$

where $Q_\lambda = 1 - |\lambda><\lambda|$.

It is convenient to expand G_∞ in terms of states $|\eta>$ which are eigenstates of $Q_\lambda(H+L)Q_\lambda$, where

$$Q_\lambda H Q_\lambda |\eta> = E_\eta |\eta>$$
$$L|\eta> = 0 \qquad (5.44)$$

Thus,

$$G_\infty = \sum_\eta |\eta><\eta| / E_\eta - E \qquad (5.45)$$

and from equations (5.40) - (5.43)

$$R_{cc'} = \sum_\eta \frac{\gamma_{\eta c}\gamma_{\eta c'}}{E_\eta - E} + \frac{\alpha_{\lambda c}\alpha_{\lambda c'}}{E_\lambda - E - \phi_\lambda} \qquad (5.46)$$

$$\alpha_{\lambda c} = \gamma_{\lambda c} - \sum_\eta \gamma_{\eta c} <\eta|h|\lambda> / (E_\eta - E) \qquad (5.47)$$

$$\phi_\lambda = <\lambda|h|\lambda> - \sum_\eta \frac{|<\eta/h/\lambda>|^2}{E_\eta - E} \qquad (5.48)$$

Following the development of the previous section it would now be possible to calculate the cross section from this R-matrix and compare that with experiment. Instead, consider the distribution of widths in the neighborhood of the analogue state. Because the quantities $\alpha_{\lambda c}$ and ϕ_λ are rapidly varying functions of energy, it is desirable to average them over an interval greater than the average level spacing (so that an average over many levels is obtained) but preferably smaller than the width of the analogue state. To accomplish this it is most convenient to use a Lorentz-weighted average of level dependent quantities f_ν:

$$<f_\nu \rho_\nu> = \frac{I}{\pi} \int \frac{f_\nu \rho_\nu(E')dE'}{(E'-E)^2 + I^2} \qquad (5.49)$$

where the level density is $\rho_\nu = \sum_\nu \delta(E - E_\nu)$. Therefore

$$<f_\nu \rho_\nu> = \frac{I}{\pi} \sum_\nu f_\nu / ((E_\nu - E)^2 + I^2) \qquad (5.50)$$

This follows MacDonald (1980), where I equals the half width of the Lorentzian averaging interval. Equation (5.50) gives the average per unit energy of the quantity f_ν. Thus the strength function, defined as the average reduced width per unit interval, is

$$S_{cc'}(E,I) = \langle \gamma_{\nu c}\gamma_{\nu c'}/\rho_\nu \rangle \tag{5.51}$$

$$= \frac{I}{\pi} \sum \frac{\gamma_{\nu c}\,\gamma_{\nu c'}}{(E_\nu - E)^2 + I^2} \tag{5.52}$$

$$= \frac{1}{\pi}\,\mathrm{Im}\,(R_{cc'}(E+iI)) \tag{5.53}$$

Equation (5.53) follows from (5.52) and the definition of the R-matrix, plus the analyticity of R. Equation (5.52) can be evaluated directly from experimentally determined quantities. What remains, then, is to evaluate (5.53) using (5.46):

$$S_{cc'}(E,I) = \frac{1}{\pi}\mathrm{Im}\left(R^{pot}_{cc'}(E+iI) + \frac{\alpha_{\lambda c}(E+iI)\,\alpha_{\lambda c'}(E+iI)}{E_\lambda - E + \phi_\lambda(E+iI) - iI}\right) \tag{5.54}$$

To simplify this define

$$S_B = \frac{1}{\pi}\,\mathrm{Im}(R^{pot}_{cc'}(E+iI)) \tag{5.55}$$

$$= \frac{I}{\pi}\sum \frac{\gamma_{\lambda c}\,\gamma_{\lambda c'}}{(E_\lambda - E)^2 + I^2}$$

$$\gamma_{\lambda c}\, e^{i\phi_c} = \alpha_{\lambda c}(E+iI) \tag{5.56}$$

$$E_A = E_\lambda + \mathrm{Re}(\phi_\lambda(E+iI)) \tag{5.57}$$

$$\Gamma_s = -2\,\mathrm{Im}(\phi_\lambda(E+iI)) + 2I \tag{5.58}$$

S_B is therefore the "background" strength function.

$$S_{cc}(E,I) = S_B + \frac{\gamma_A^2}{\pi}\,\frac{(\Gamma_s/2)\cos 2\phi_c + (E_A - E)\sin 2\phi_c}{(E_A - E)^2 + (\Gamma_s/2)^2} \tag{5.59}$$

Assuming that I is large enough to remove the fluctuations in γ_A^2, E_A, and Γ_s, equation (5.59) shows that the widths are distributed as an asymmetric Lorentzian. The width of the distribution, Γ_s, is

$$\Gamma_s = -2\langle \lambda | \Delta L | \lambda \rangle + 2I \sum_\eta \frac{|\langle \eta | h | \lambda \rangle|^2}{(E_\eta - E)^2 + I^2} + 2I \tag{5.60}$$

$$= -2(-i\sum_c \gamma_{\lambda c}^2 P_c) + 2 < |\langle \nu|h|\lambda\rangle|^2> + 2I \qquad (5.61)$$

$$= \Gamma_\lambda + \Gamma^\downarrow + 2I \qquad (5.62)$$

where the spreading width, $\Gamma^\downarrow$, is a measure of the mixing of the analogue and background states through the interaction h. Assuming only external mixing, $\Gamma^\downarrow$ can be approximated as

$$\Gamma^\downarrow = 2I \sum_{\nu c} \gamma_{\nu c}^2 |\Delta L_c|^2 \gamma_{\lambda c}^2 / [(E_\nu - E)^2 + I^2]$$

$$= \sum_c 2\pi S_{\nu c} \gamma_{\lambda c}^2 |\Delta L_c|^2 \qquad (5.63)$$

which is the estimate given by Robson (1965). The analogue energy is given by

$$E_A = E_\lambda + \mathrm{Re}(\phi_\lambda(E+iI))$$

$$= E_\lambda + \mathrm{Re}(\langle\lambda|h|\lambda\rangle) - \mathrm{Re}\left(\sum_\nu \frac{|\langle\nu|h|\lambda\rangle|^2 (E_\nu - E)}{(E_\nu - E)^2 + I^2}\right) \qquad (5.64)$$

The last term is in general small due to the cancelation of terms above and below the analogue. Thus

$$E_A = E_\lambda + \mathrm{Re}(\langle\lambda|\,\Delta H|\lambda\rangle) + \mathrm{Re}(\langle\lambda|\,\Delta L|\lambda\rangle) \qquad (5.65)$$

Since $|\lambda>$ is the analogue state before the extra Coulomb interaction is turned on,

$$\langle\lambda|\,\Delta H|\lambda\rangle = \langle\lambda|V_c|\lambda\rangle = \Delta_c \qquad (5.66)$$

$$\langle\lambda|\,\Delta L|\lambda\rangle = \sum_c \gamma_{\lambda c}^2 (S_n^-(E_n) - S_p^+(E_p) - iP_p^+) \qquad (5.67)$$

where S_p^+, S_n^- are the proton and neutron shift functions and P_p^+ is the proton penetrability. Thus

$$E_A = E_\lambda + \Delta_c - \sum_c \gamma_{\lambda c}^2 (S_p^+(E_p) - S_n^-(E_n)) \qquad (5.68)$$

Again, the first term is the Coulomb energy shift and the second is the Thomas-Ehrman shift.

From equation (5.48),

$$\gamma_{Ac} e^{i\phi_c} = \gamma_{\lambda c} - \sum_\nu \frac{\gamma_{\nu c}\langle\nu|h|\lambda\rangle}{(E_\nu - E)^2 + I^2} \{(E_\nu - E) + iI\} \qquad (5.69)$$

Neglecting the terms $(E_\nu - E)$ as before gives

$$\gamma_{Ac} e^{i\phi_c} = \gamma_{\lambda c} - i\pi \langle \gamma_{\nu c} \langle \nu|h|\lambda\rangle \rho_\nu \rangle \qquad (5.70)$$

Taking the real parts of both sides gives

$$\gamma_{Ac}\cos\phi_c = \gamma_{\lambda c} + \pi\ \mathrm{Im}\{\langle\gamma_{nc}\langle n|h|\lambda\rangle\rho_n\rangle\} \tag{5.71}$$

The second term can be overestimated by assuming that the reduced width amplitude γ_{nc} and the matrix element are completely correlated, thus in analogy with equation (5.67),

$$\gamma_{Ac}\cos\phi_c = \gamma_{\lambda c} + \pi\langle\gamma_{nc}(\gamma_{nc}\gamma_{\lambda c}\Delta P_c)\rho_n\rangle \tag{5.72}$$

$$= \gamma_{\lambda c}\sec\phi_c\,(1 + \pi S_B P_\rho)$$

where $S_B = \langle\gamma_n^2\rho_n\rangle$ is the background strength function. For proton scattering below the Coulomb barrier, $S_B P_\rho \ll 1$, thus

$$\gamma_{Ac} = \gamma_{\lambda c}\sec\phi_c \tag{5.73}$$

If the reduced width amplitude and the matrix element are uncorrelated in sign (random phase approximation), $\phi_c = 0$, and $\gamma_{Ac} = \gamma_{\lambda c}$.

One criterion by which to judge whether the mixing is weak or strong is the difference in eigenenergies between the unperturbed states $|n\rangle$ and the observed states $|\nu\rangle$. From equation (5.46) and (5.25), the eigenenergies E_ν are given by

$$E_\lambda - E + \phi_\lambda(E) = 0 \qquad \text{at } E = E_\nu \tag{5.74}$$

$$E_\lambda - i\Gamma_\lambda/2 - E - \sum_n \frac{\langle n|h|\lambda\rangle^2}{E_n - E} = 0 \tag{5.75}$$

Weak mixing is defined by $|E_n - E_\nu| \ll D$, thus

$$\sum \frac{\langle n|h|\lambda\rangle^2}{E_n - E_\nu} \approx \frac{\langle n|h|\lambda\rangle^2}{E_n - E_\nu} \tag{5.76}$$

where only the term with $|E_n - E_\nu| \ll D$ has been kept. Finally,

$$E_n - E_\nu = \frac{\langle n|h|\lambda\rangle^2}{E_\lambda - E_\nu - i\Gamma_\lambda/2} \tag{5.77}$$

$$\frac{|\langle n|h|\lambda\rangle|^2}{[(E_A - E_\nu)^2 + \Gamma_\lambda^2/4]} \ll D \tag{5.78}$$

If the matrix element is replaced by its average value, and E_ν is chosen to be near E_A,

$$D\Gamma^{\downarrow}/2\pi \ll D[(E_A - E_\nu)^2 + (\Gamma_\lambda/2)^2]^{1/2} < D(D^2 + \Gamma_\lambda^2/4)^{1/2} \quad (5.79)$$

or

$$\frac{\Gamma^{\downarrow}/2}{(D^2+\Gamma_\lambda^2/4)} \ll 1 \quad (5.80)$$

Lane defines the mixing parameter as

$$\lambda = \frac{\Gamma^{\downarrow}/}{(D^2+\Gamma_\lambda^2/4)} \quad (5.81)$$

For most experimental cases, λ is between 1% and 30%, indicating weak to intermediate mixing.

Equation (5.59) may be re-written (Lane, 1969) as

$$S(E,I) = S_B \frac{(E_A-\Delta_A-E)^2 + \omega^2/4}{(E_A-E)^2 + (\Gamma_s/2)^2} \quad (5.82)$$

where

$$\Delta_A = -[\gamma_A^2/(2\pi S_B)]\sin 2\phi_c \quad (5.83)$$

$$\omega^2 = \gamma_A^2 \cos 2\phi \left(\frac{2\Gamma_s}{\pi S_B}\right) - 4\Delta_A^2 \quad (5.84)$$

From this form it is apparent that the strength function has a minimum at $E = E_A - \Delta_A$. Experimentally this minimum (if observed) occurs above the analogue state so that $\Delta_A < 0$. Thus, from equation (5.83), $\phi_c > 0$.

Another function useful in fitting experimental data is the integral of (5.59) from some arbitrary lower limit to the energy E, which is to be compared with the sum of reduced widths up to the same energy. For this analysis, the summed strength function is defined as

$$SS(E,I) = \int_{-\infty}^{E} \langle \gamma^2 \rho \rangle dE' \quad (5.85)$$

$$= \frac{I}{\pi}\int_{-\infty}^{\infty} \gamma^2 \rho \left\{\frac{1}{I}\tan^{-1}\left(\frac{E-E''}{I}\right) + \frac{\pi}{2I}\right\} dE''$$

$$= \sum_n \gamma_n^2 \left(\frac{1}{\pi}\tan^{-1}\left(\frac{E-E_n}{I}\right) + 1/2\right)$$

The last expression is a "smoothed" step function, therefore SS(E,I) can be written

$$SS(E,I) = \sum_{E_n<E} \gamma_n^2 + \varepsilon(E) \qquad (5.86)$$

where $\varepsilon(E)$ is the error in approximating SS(E) by the sum up to E of the reduced widths, and takes on positive and negative values with equal probability. From equation (5.59),

$$\begin{aligned} SS(E,I) &= \int_{-\infty}^{E} S(E',I)dE' = \int_{-\infty}^{E_A} S\, dE' + \int_{E_A}^{E} S\, dE' \qquad (5.87) \\ &= \text{const.} + S_B(E-E_A) + \frac{\gamma_A^2}{\pi}\cos 2\phi_c \tan^{-1}\left(\frac{E-E_A}{\Gamma_s/2}\right) \\ &\quad - \frac{\gamma_A^2}{2\pi}\sin 2\phi_c \ln\left[\left(\frac{E-E_A}{\Gamma_s/2}\right)^2+1\right] \end{aligned}$$

where all energy independent terms have been absorbed into the integration constant.

5.4 Experimental Results

5.4.1 Identification of IAR

Isobaric analogue states are identified in the spectrum of a nucleus as an anomalous peak in the strength function occurring at an energy which differs by approximately the Coulomb energy difference from a state of the same J^π in the parent nucleus:

$$E_P = E_n + \Delta_c = B_n + \Delta_c + E_X \qquad (5.88)$$

where B_n is the binding energy of the last neutron in the parent nucleus and E_X is the excitation energy of the parent state. The equation is approximate in that the Thomas-Ehrman shift and higher order terms have been dropped. The

Coulomb energy E_c may be estimated as the potential energy of a uniformly charged sphere of radius $r_o A^{1/3}$:

$$E_c = 3/5\ e^2/r_o\ Z^2/A^{1/3} \qquad (5.89)$$

which gives

$$\Delta E_c(T-1,T) = 6/5\ e^2/r_o\ (A/2-T+1/2)/A^{1/3}$$

where $T = T_> = T_o + 1/2$. For $^{56}Fe(p,p)$ this works out to be about 10 MeV. A more accurate semi-empirical form given by Jänecke (1969) is

$$\Delta E_c = \{1389\ Z_< - 2041\}/A^{1/3}\ \text{keV} \qquad (5.90)$$

This expression gives a value of 8.85 MeV for the system studied.

With this number as a guide, five analogue states were positively identified: a $5/2^-$ state with a parent state excitation energy of E_x = 2.207 MeV, a $9/2^+$ state with E_x = 2.445 MeV, a $5/2^+$ state with E_x = 2.506 MeV, a $3/2^-$ state with E_x = 2.565 MeV, and a $1/2^-$ state with E_x = 2.697 MeV. Each of these states had observable fine structure and is discussed separately below. Two $3/2^-$ levels observed near E_p = 3.21 MeV are possible fragments corresponding to an ℓ=1 state of uncertain spin for which E_x = 1.975 MeV. However, they are within 1 keV of a 1/2+ resonance having a width of 1 keV, so that detailed analysis was impossible. The $5/2^-$ state at E_x = 2.117 was not seen in this experiment--it is half as strong (from (d,p) measurements) as the $5/2^-$ level at E_x = 2.207, the analogue of which was at the limits of observability for this experiment. No analogue assignment could be made for the 1/2+ state at E_x = 2.454; the expected

proton width (1.3 keV) was too small to distinguish the analogue state from an abundance of strong 1/2+ levels. The ℓ=1 state at E_x = 2.335 was likewise indistinguishable from the background.

5.4.2 Coulomb Energies

The Coulomb energy differences for the six observed analogue states are summarized in table 5.1. The experimental values, given by equation 5.1 with B_n = -7.646 MeV, range from 8.803 MeV to 8.903 MeV, with uncertainties of 5 keV. The agreement with Jänecke's estimate (8.85 MeV) is thus quite good: the average of the five numbers is 8.845 MeV. The 100 keV spread in these measurements can be attributed to differences from one analogue to the next in the Thomas-Ehrman shift. Unfortunately, this shift cannot be calculated with any confidence (unless the state in question is very nearly a single particle state), because all reduced widths (even for closed channels) contribute to this term (see equation (5.68)). As will be seen in the next section, each of the five analogues, except the $1/2^-$ analogue, has a small proton spectroscopic factor. Thus, it is not possible to calculate quantitatively the Thomas-Ehrman shift.

5.4.3 Fine Structure

The fine structure parameters were determined by fitting the strength function given by equation (5.59) to the experimental strength function given by equation (5.52),

Table 5.1 Coulomb Energy Differences

J^{π}	E_p (MeV)	E_x (MeV)	ΔE_c (MeV)
$5/2^-$	3.422	2.207	8.803
$9/2^+$	3.713	2.454	8.840
$5/2^+$	3.763	2.506	8.833
$3/2^-$	3.890	2.565	8.903
$1/2^-$	3.958	2.687	8.848

and by fitting the integrated strength function (equation (5.87)) to the observed integrated strength (equation (5.85)). The two methods generally gave consistent results for the analogue energy, the analogue reduced width, and the spreading width ($\pm$5 keV). The asymmetry angles agreed to within 5^{o}, which is about the magnitude of the error for either method. There was mild disagreement for the strength function in some cases, and this will be discussed separately below for each analogue state.

The biggest problem in this analysis involved choosing a value for the smearing width, I. This width must be large enough to average over many levels, but not so large as to destroy any useful information. In general, a lower limit of 2I = 5D (were D = the average spacing) was chosen; i.e., the width of the Lorentzian function was at least five times the average spacing. Fits were obtained both for this minimum value for I, and for a second value twice as large as the first. In this way some estimate of the dependence of the solutions on I could be made.

The first two analogue states ($5/2^{-}$ and $9/2^{+}$) are similar in several respects. Both had very small background strength functions, so that the only resonances observed belonged to the analogue states. An upper limit for the background strength function can be obtained by assuming that the weakest analogue fragment observed was larger than the strongest background width. One background level out of 40 will have a width greater than five times the average

width. These two or three levels (for the present level density) would contain 1/6 of the total strength. Thus the background strength must be less than 12-18 times the width of the weakest level observed, and the strength function is this number divided by the 900 keV interval of observation. This puts an upper limit of 0.005 on the $5/2^-$ strength function, and a limit of 0.05 on the $9/2^+$ strength function. The best fit value for the $5/2^-$ state was 0.0 ± 0.001, and for the $9/2^+$ state it was 0.001 ± 0.005.

The fine structure fits for the $5/2^-$ state are shown in figure 5.1 for I=20 keV. One weak level was observed rather far to the right of the center of the analogue, yielding a negative mixing angle (or positive asymmetry). This is not significant, however, because the uncertainty in this parameter is larger than its magnitude. The spreading width (7 keV) is approximately equal to the average spacing, and thus the mixing can be classified as intermediate ($\lambda = 0.3$). The analogue state fine structure parameters are summarized in table 5.2.

The $9/2^+$ analogue state (figure 5.2) contains four rather symmetrically placed levels, again consistent with no asymmetry. The spreading width for this distribution is approximately 5 keV, so that the $9/2^+$ state may be classified as an example of weak mixing ($\lambda = 0.15$). The figure was prepared for I = 25 keV, but no significant differences in the parameters were observed for I = 50 keV.

Figure 5.1 (a) Lorentz-weighted strength function for the $5/2^-$ analogue state at E_p = 3.422 MeV. The data is shown as a dashed curve, and the fit is shown as a solid curve. The half-width of the averaging interval is I=20 keV.

(b) Integrated strength function for the $5/2^-$ analogue state. The solid line is a least squares fit to the data.

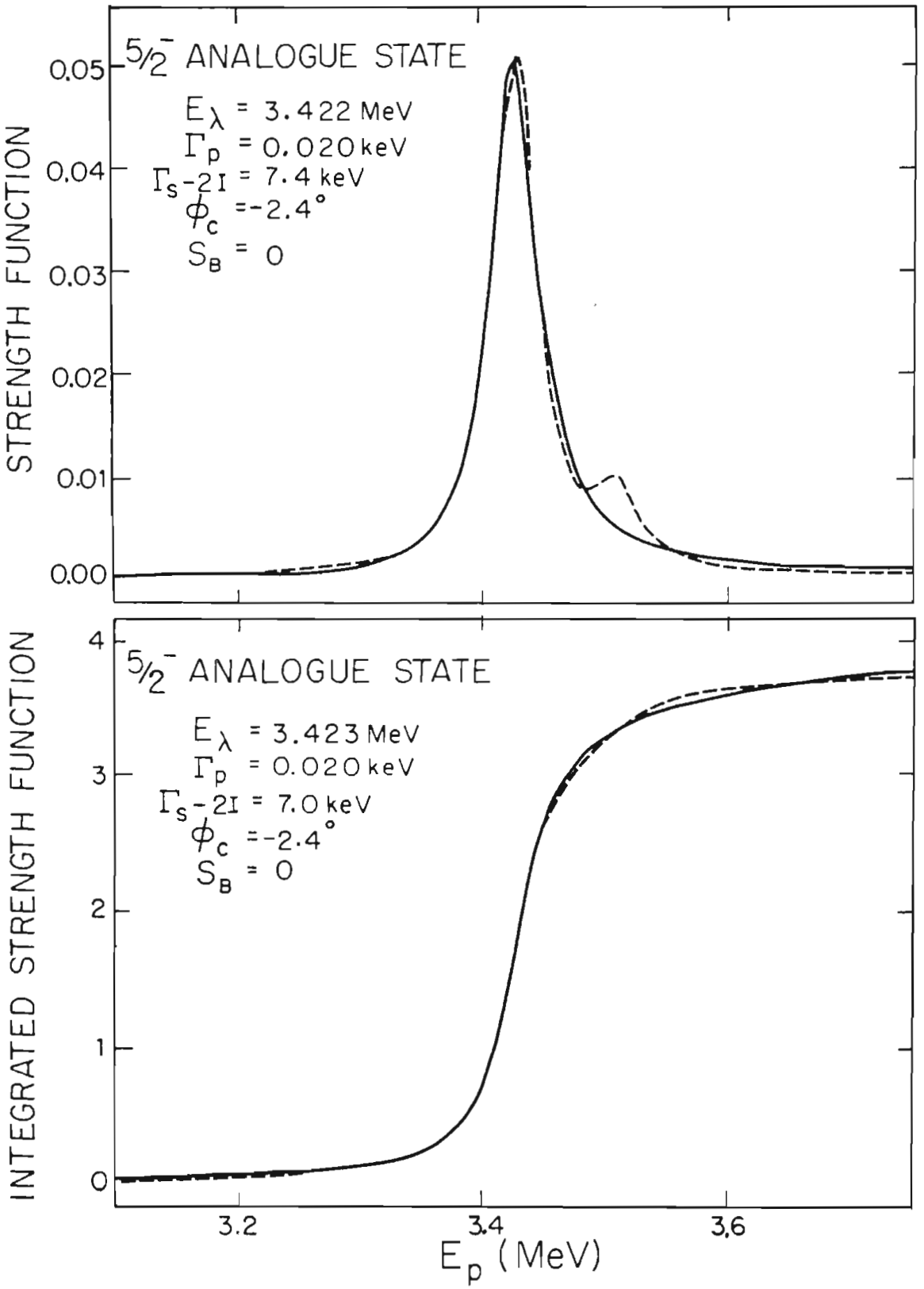
5/2⁻ ANALOGUE STATE
E_λ = 3.422 MeV
Γ_p = 0.020 keV
Γ_s-2I = 7.4 keV
ϕ_c = -2.4°
S_B = 0
STRENGTH FUNCTION
0.05
0.04
0.03
0.02
0.01
0.00
5/2⁻ ANALOGUE STATE
E_λ = 3.423 MeV
Γ_p = 0.020 keV
Γ_s-2I = 7.0 keV
ϕ_c = -2.4°
S_B = 0
INTEGRATED STRENGTH FUNCTION
4
3
2
1
0
3.2
3.4
3.6
E_p (MeV)

Table 5.2 Fine Structure Parameters

J^{π}	E_p (MeV)	γ_λ^2 (keV)	Γ_λ (keV)	$\Gamma^{\downarrow}$ (keV)	ϕ_c (deg)	Δ_λ (keV)	S_B
5/2-	2.422 ±0.005	3.4 ±0.4	0.020 ±0.002	7.2 ±4.0	-2.4 ±3.5	....	<0.001
9/2+	3.713 ±0.002	60. ± 2.	0.057 ±0.002	5.6 ±4.0	0. ±2.	....	<0.002
5/2+	3.763 ±0.015	50. ±15.	3.6 ±1.5	24. ±12.	8. ±8.	-30. ±30.	0.075
3/2-	3.890 ±0.002	3.0 ±0.2	0.94 ±0.07	2.0 ±5.0	7. ±5.	-10. ±20.	0.013 ±0.002
1/2-	3.958 ±0.010	46. ±18.	15.5 ± 4.0	6.5 ±5.0	12. ±9.	-80. ±40.	0.04 ±0.04

Figure 5.2 (a) Lorentz-weighted strength function for the $9/2^+$ analogue state at E_p = 3.713 MeV. The solid curve is a least squares fit to the fine structure distribution.

(b) Integrated strength function for the $9/2^+$ analogue state. The width of the Lorentzian is 25 keV.

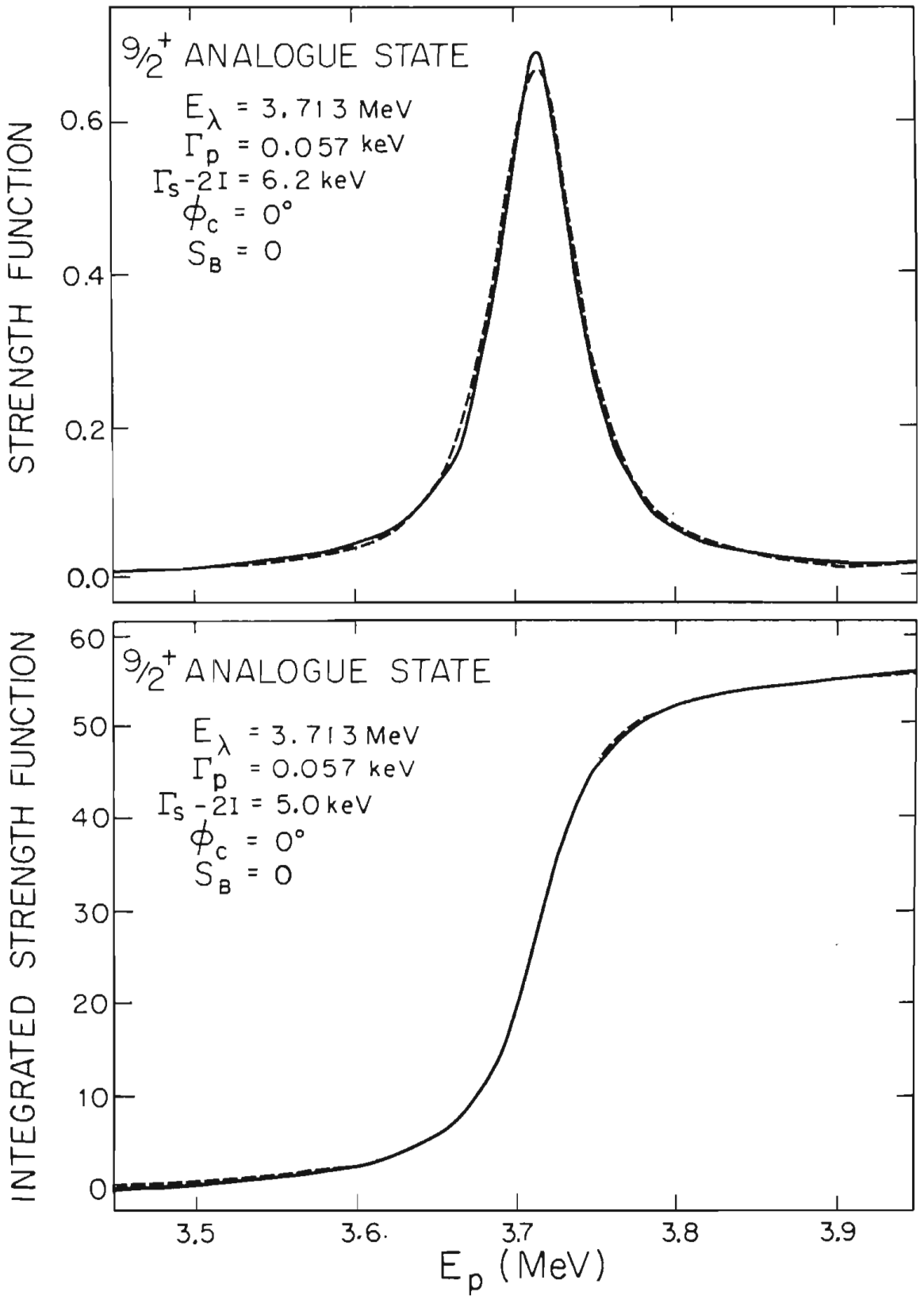
9/2+ ANALOGUE STATE
E_λ = 3.713 MeV
Γ_p = 0.057 keV
Γ_s - 2I = 6.2 keV
ϕ_c = 0°
S_B = 0
STRENGTH FUNCTION
0.0
0.2
0.4
0.6
9/2+ ANALOGUE STATE
E_λ = 3.713 MeV
Γ_p = 0.057 keV
Γ_s - 2I = 5.0 keV
ϕ_c = 0°
S_B = 0
INTEGRATED STRENGTH FUNCTION
0
10
20
30
40
50
60
3.5
3.6
3.7
3.8
3.9
E_p (MeV)

Figure 5.3 (a) Lorentz-weighted strength function for the $5/2^+$ analogue state at E_p = 3.763 MeV. The width of the Lorentzian is 50 keV (see text for discussion).

(b) Integrated strength function for the $5/2^+$ analogue state. The solid curves are least squares fits to the data (dashed curves).

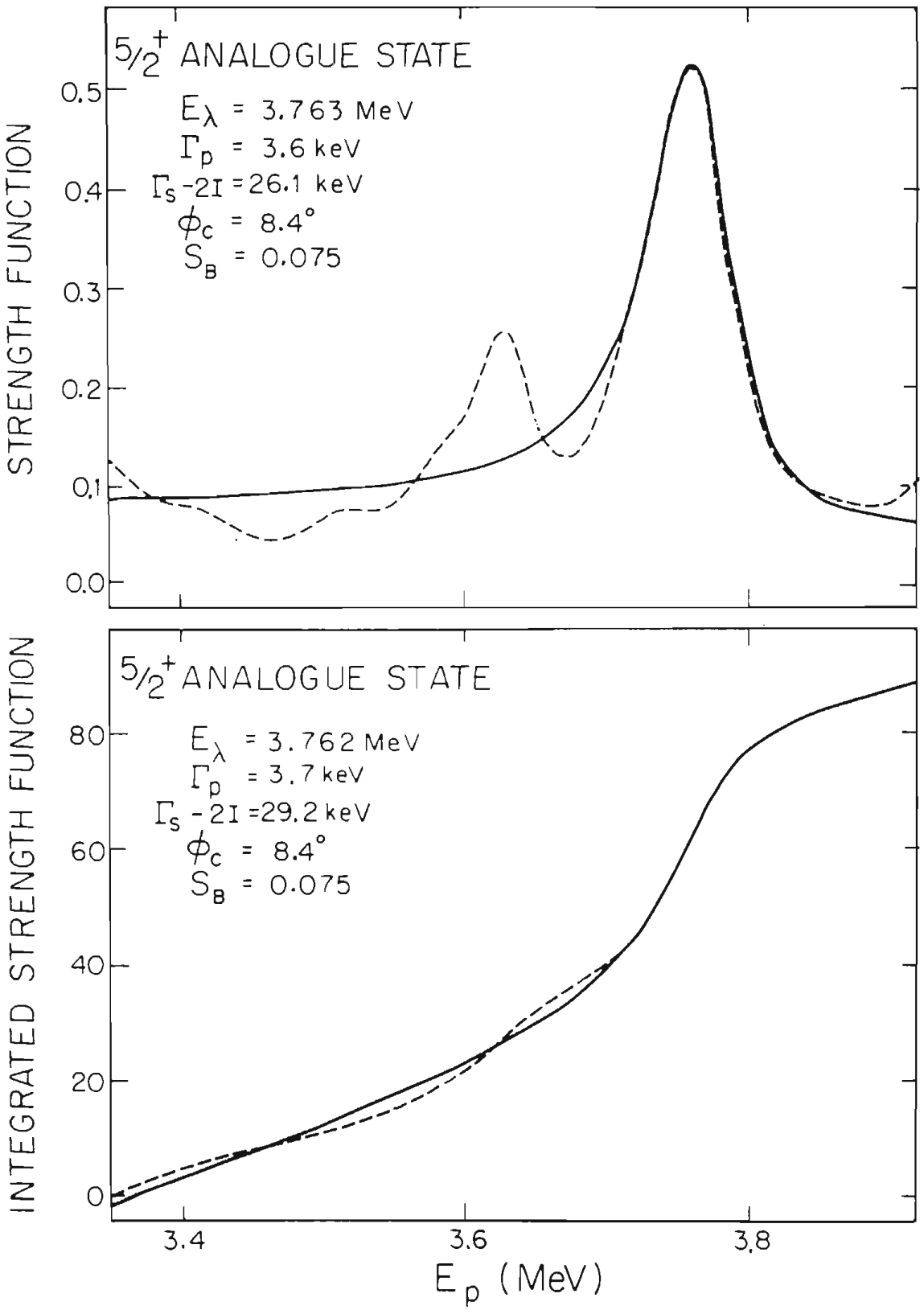
5/2+ ANALOGUE STATE
Eλ = 3.763 MeV
Γp = 3.6 keV
Γs-2I = 26.1 keV
φc = 8.4°
SB = 0.075
STRENGTH FUNCTION
0.5
0.4
0.3
0.2
0.1
0.0
5/2+ ANALOGUE STATE
Eλ = 3.762 MeV
Γp = 3.7 keV
Γs - 2I = 29.2 keV
φc = 8.4°
SB = 0.075
INTEGRATED STRENGTH FUNCTION
80
60
40
20
0
3.4
3.6
3.8
Ep (MeV)

The $5/2^+$ fine structure (figure 5.3) is a little more interesting in that the background strength function is not small (0.075 - 0.080). The spreading width (24 ± 12 keV) is also rather large, and the mixing parameter is approximately one. The Robson estimate for $\Gamma^{\downarrow}$ is 40 keV, therefore external mixing can account for all of the observed spreading width. The background strength function was held fixed at 0.075 for these fits because the chi-squared search tended to produce smaller values, inconsistent with other (global) analyses. This difficulty (as well as the large error bars for the other parameters) was caused by the strong background level at E_p = 3.63 MeV. (Strong background strengths generally result in similar problems due to the large fluctuations in a Porter-Thomas type of distribution.) The observed asymmetry (ϕ = 8^o ± 8^o) is larger than for the first two states, although the uncertainty still allows a symmetric fit.

The $3/2^-$ analogue state is interesting in that widths are available for three separate channels. Unfortunately, fewer than a dozen fragments of the analogue state were observed, so that detailed comparisons of the three distributions are not justified. Fits to the elastic scattering strength function are shown in figure 5.4, and the fits to the two inelastic channels are shown in figure 5.5. Most of the differences among the three are the result of the state at 3.856 MeV. Because this state (which is 30 keV below the center of the analogue) has a larger inelastic

Figure 5.4 (a) Lorentz-weighted strength function for the $3/2^-$ analogue state at E_p = 3.890 MeV. The width of the Lorentzian function is 25 keV.

(b) Integrated strength function for the $3/2^-$ analogue state. The solid curves are least squares fits to the data.

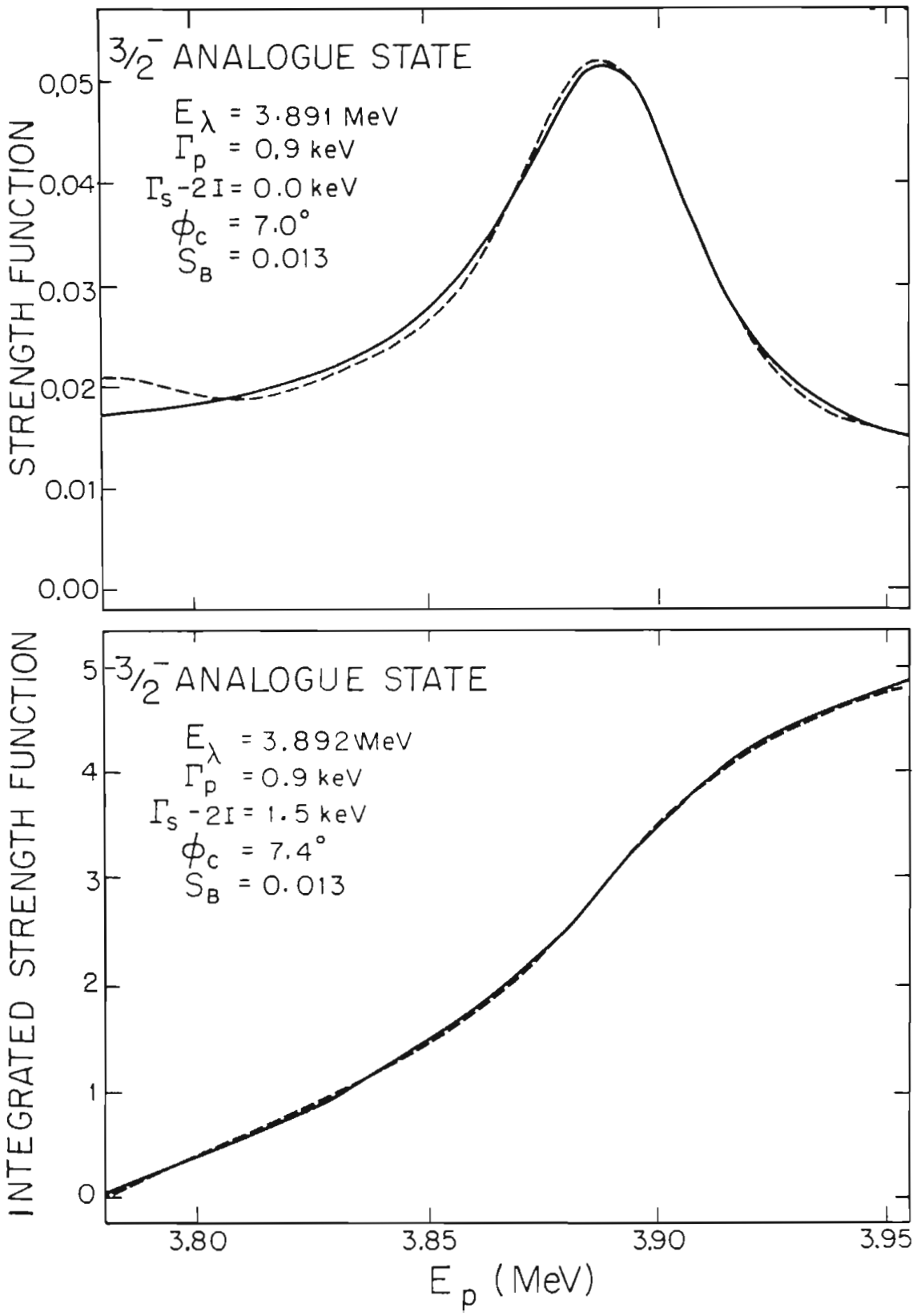
3/2⁻ ANALOGUE STATE
E_λ = 3.891 MeV
Γ_p = 0.9 keV
Γ_s - 2I = 0.0 keV
ϕ_c = 7.0°
S_B = 0.013
STRENGTH FUNCTION
0.05
0.04
0.03
0.02
0.01
0.00
3/2⁻ ANALOGUE STATE
E_λ = 3.892 MeV
Γ_p = 0.9 keV
Γ_s - 2I = 1.5 keV
ϕ_c = 7.4°
S_B = 0.013
INTEGRATED STRENGTH FUNCTION
5
4
3
2
1
0
3.80
3.85
3.90
3.95
E_p (MeV)

Figure 5.5 (a) Lorentz-weighted strength function for the s' = 3/2 inelastic channel for the $3/2^-$ analogue state.

(b) Lorentz-weighted strength function for the s' = 5/2 inelastic channel. The solid curves are least squares fits to the data (dashed curves).

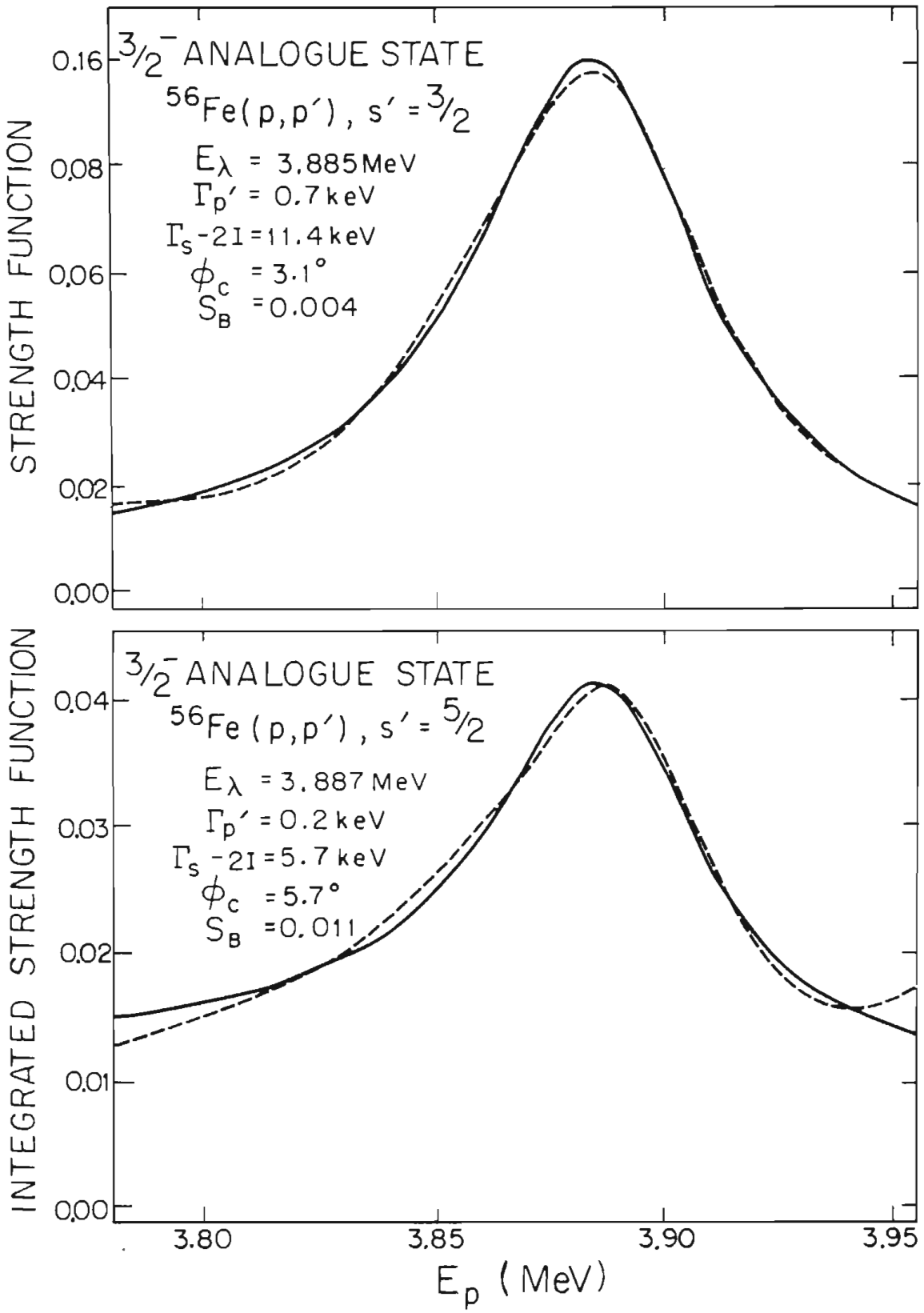
$3/2^-$ ANALOGUE STATE
$^{56}Fe(p,p')$, $s' = 3/2$
E_λ = 3.885 MeV
$\Gamma_{p'}$ = 0.7 keV
$\Gamma_s - 2I$ = 11.4 keV
ϕ_c = 3.1°
S_B = 0.004
STRENGTH FUNCTION
0.16
0.08
0.06
0.04
0.02
0.00
$3/2^-$ ANALOGUE STATE
$^{56}Fe(p,p')$, $s' = 5/2$
E_λ = 3.887 MeV
$\Gamma_{p'}$ = 0.2 keV
$\Gamma_s - 2I$ = 5.7 keV
ϕ_c = 5.7°
S_B = 0.011
INTEGRATED STRENGTH FUNCTION
0.04
0.03
0.02
0.01
0.00
3.80
3.85
3.90
3.95
E_p (MeV)

width than elastic width, the analogue state energy extracted from the inelastic distributions is lower than for the elastic distribution. However, the differences are only on the order of one error bar. Similarly, the inelastic distributions have larger spreading widths than the elastic distribution (9 keV and 4 keV vs. 0 keV). Because the spreading width is a property of the whole analogue state and not just of any one channel, the final parameters quoted are weighted averages of the three observed values. The $3/2^-$ state, with $\Gamma^{\downarrow}$ = 2 keV, is another case of weak mixing (λ = 0.15), and the Robson estimate for $\Gamma^{\downarrow}$ (1 keV) is again very close to the observed value. The mixing angles also differ for the three distributions, but the differences are smaller and the fractional errors are larger.

Remember that the width of the observed distribution is a sum of the Lorentz width (2I), the analogue width (Γ_λ), and the spreading width ($\Gamma^{\downarrow}$). The analogue width is a sum of all partial widths (1.8 keV), so that each distribution must be fit before the spreading width can be extracted. The value of 0. $\pm$ 5. keV for the elastic fine structure distribution means that the width of the distribution was essentially the particle width of the state.

The analysis of the $1/2^-$ analogue state at E_p = 3.958 MeV was complicated by not having enough data above the analogue to use a sufficiently large value for I without encountering edge effects. A compromise of I = 20 keV was chosen, with the fit covering all but the highest 25 keV of

Figure 5.6 (a) Lorentz-weighted strength function for the $1/2^-$ analogue state at E_p = 3.958 MeV. The width of the Lorentzian is 20 keV.

(b) Integrated strength function for the $1/2^-$ analogue state. The solid curves are least squares fits to the data.

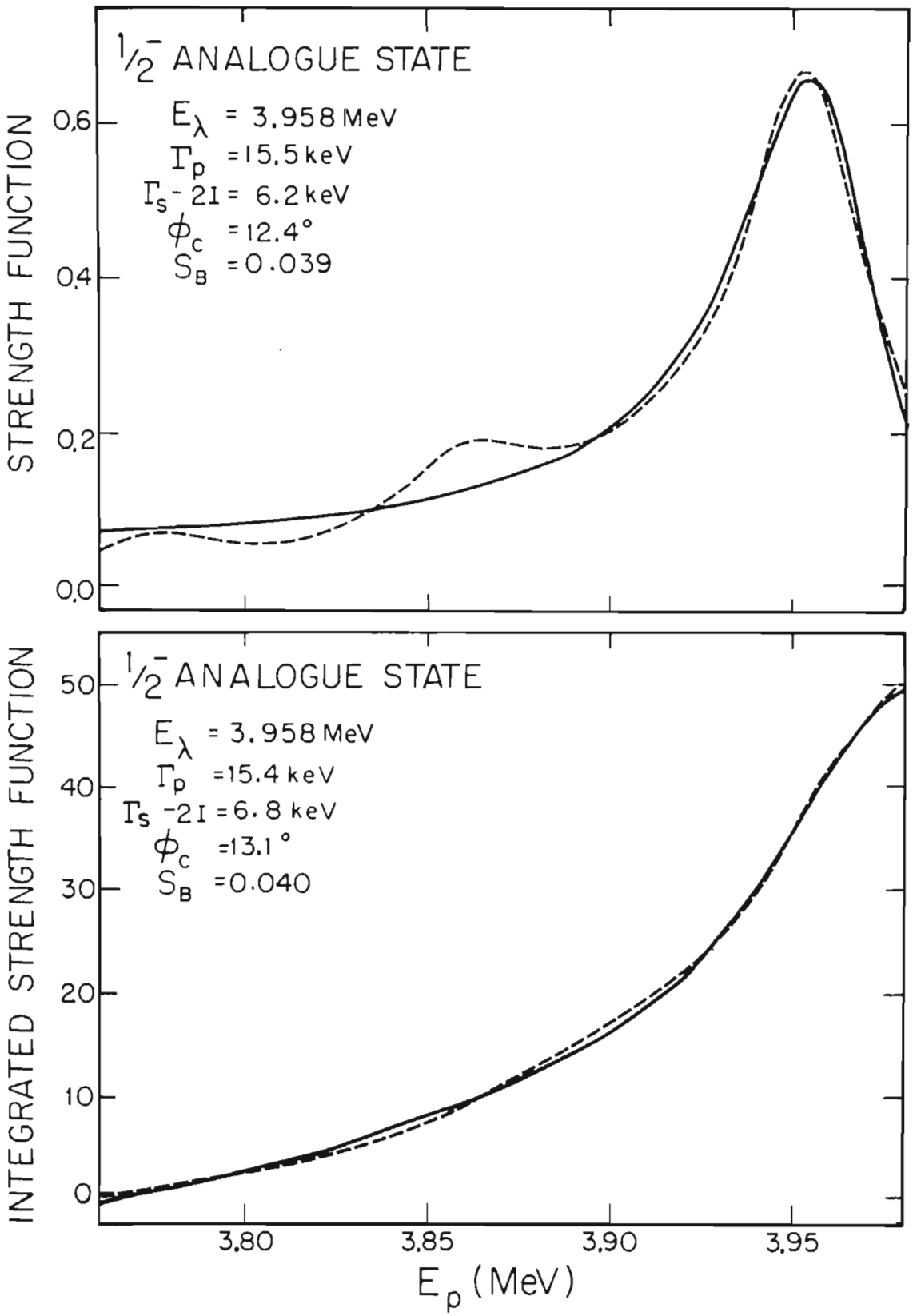
1/2⁻ ANALOGUE STATE
E_λ = 3.958 MeV
Γ_p = 15.5 keV
$\Gamma_s - 2I$ = 6.2 keV
ϕ_c = 12.4°
S_B = 0.039
STRENGTH FUNCTION
0.0
0.2
0.4
0.6
1/2⁻ ANALOGUE STATE
E_λ = 3.958 MeV
Γ_p = 15.4 keV
$\Gamma_s - 2I$ = 6.8 keV
ϕ_c = 13.1°
S_B = 0.040
INTEGRATED STRENGTH FUNCTION
0
10
20
30
40
50
3.80
3.85
3.90
3.95
E_p (MeV)

data. The fine structure fits are shown in figure 5.6. The uncertainty in all of the parameters is rather large, again due to edge effects. The width of the observed distribution causes some difficulty in that it implies a spreading width less than zero. I.e., the analogue particle width is larger than $\Gamma_s^{\downarrow} - 2I$. This means that the spreading width is very small compared with the particle width, and the difficulty probably arises because the number of strong fragments is so small (two). It is safe to conclude that this is a case of very weak mixing ($\lambda << 1$). The Robson estimate of the spreading width (18 keV) considerably overestimates $\Gamma^{\downarrow}$ for this state. In fact, this is one of the strongest discrepencies of this kind observed to date. The distribution is also definitely asymmetric in that several stronger than average levels are observed below the analogue and none above it.

Although it cannot be identified as a fragmented analogue state, an anomalous clustering of s-wave strength was observed in the neighborhood of E_p = 3.8 MeV. (A similar, though much stronger, cluster was observed in ^{54}Fe(p,p) near 4.1 MeV.) The integrated strength function was fit as though it were an analogue state for the sake of characterizing the strength; this fit is shown in figure 5.7. An averaging interval of 50 keV was used for this figure. If this anomaly is a doorway state of some kind, then the parameters extracted describe the mixing of the doorway with the background states. In this case, the large spreading width (100 keV) indicates very strong mixing.

Figure 5.7 Lorentz-weighted integrated s-wave strength function. The solid curve is a least squares fit to the integral of an asymmetric Lorentzian distribution. See text for discussion.

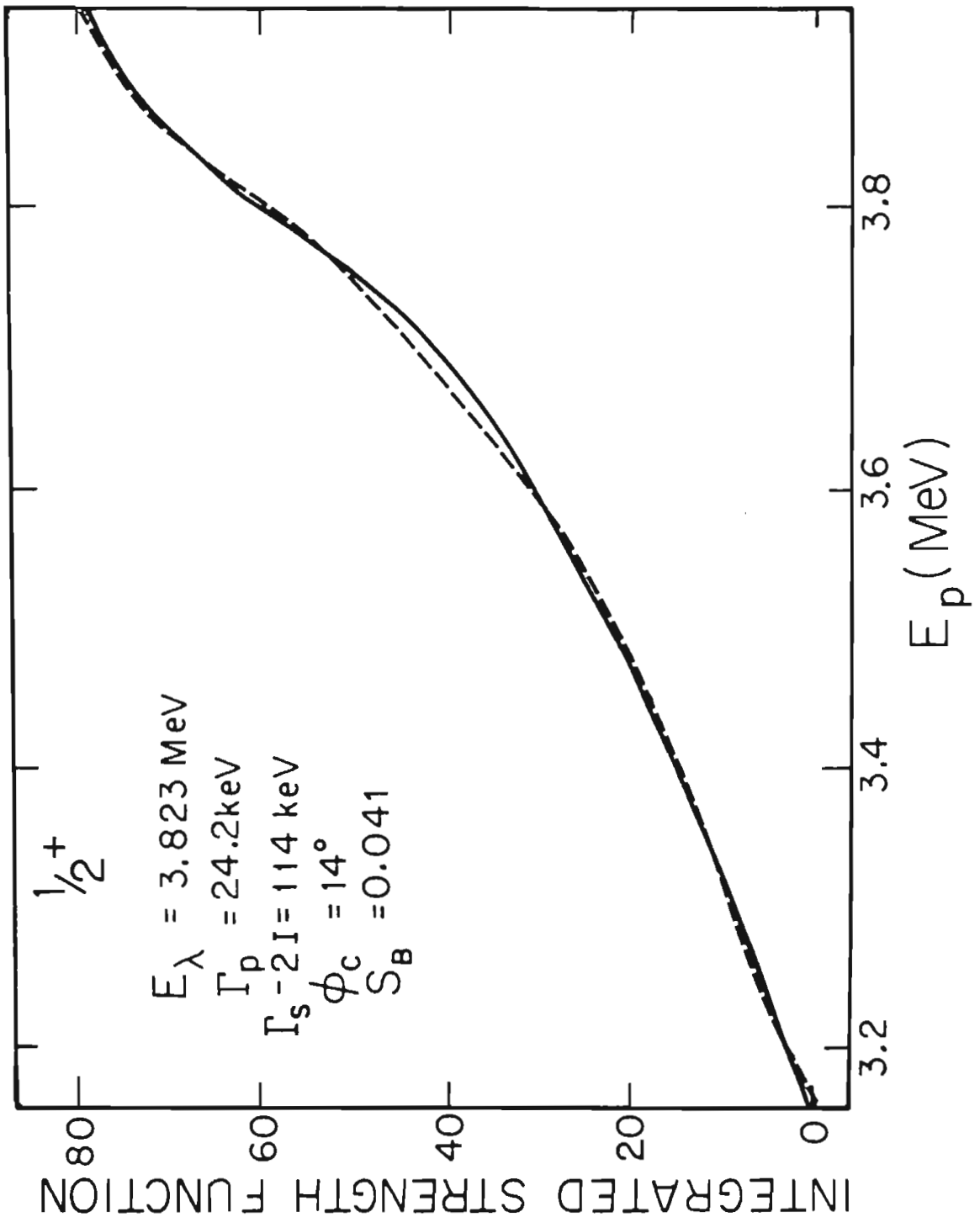
INTEGRATED STRENGTH FUNCTION
0
20
40
60
80
3.2
3.4
3.6
3.8
E_p (MeV)
$J^\pi = 1/2^+$
E_λ = 3.823 MeV
Γ_p = 24.2keV
Γ_s = 2I = 114 keV
ϕ_c = 14°
S_B = 0.041

5.4.4 Spectroscopic Factors

Spectroscopic factors were calculated for both the elastic and inelastic proton widths for the five analogue states:

$$S_p = \Gamma_p^{\uparrow} (2T_o+1)/\Gamma^{\uparrow}(s.p.) \qquad (5.91)$$

$\Gamma_p^{\uparrow}$ and $\Gamma^{\uparrow}(s.p.)$ are the laboratory and single particle widths in channel c, and T_o is the isospin of the target. The single particle widths were calculated using the method of Harney and Weidenmuller (1969). (Analogue spectroscopic factors are discussed in a review of analogue states by Bilpuch et al. (1976).) The spectroscopic factors for the analogue states observed in the present work are given in table 5.3, which also contains the (d,p) spectroscopic factors for the parent states. As in previous work, the analogue spectroscopic factors are generally lower than the (d,p) measurements. The exception to this trend in the present work is the $5/2^+$ analogue state. The large error bars for the proton width for that analogue state preclude drawing any conclusions from this measurement.

Table 5.3 Spectroscopic Factors

Isobaric Analogue States in $^{56}Fe(p,p)$, (p,p')

J^{π}	E_p (MeV)	E_x (MeV)	Configuration	Γ (keV)	S_p	S_{dp}
$5/2^-$	3.422	2.207	$f_{5/2} \otimes 0^+$	0.020±0.004	0.03	0.08
			$p \otimes 2^+$	0.016±0.004	0.003	
$9/2^+$	3.713	2.454	$g_{9/2} \otimes 0^+$	0.058±0.006	0.037	0.038
$5/2^+$	3.763	2.506	$d_{5/2} \otimes 0^+$	3.6 ± 1.5	0.22	0.14
$3/2^-$	3.890	2.565	$p_{3/2} \otimes 0^+$	1.0 ± 0.1	0.017	0.03
			$p \otimes 2^+$	0.9 ± 0.2	0.05	
$1/2^-$	3.958	2.687	$p_{1/2} \otimes 0^+$	16.0 ± 4.0	0.26	0.38
			$p_{3/2} \otimes 2^+$	0.4 ± 0.1	0.02	

Chapter 6

STATISTICAL PHENOMENA

6.1 Introduction

The investigation of the average properties of nuclear levels began in the 1930's when various models were proposed to explain the behavior of the nucleus. For example, Bethe (1936,1937) derived a useful form for the energy and spin dependence of the level density based on a Fermi gas model and simple counting arguments. Since that time, many different models have been used to predict the average properties of nuclear states, as well as the variations about the average. The use of random matrices to represent the system's Hamiltonian, pioneered by Wigner (1957), has provided a great deal of insight into the statistical properties of nuclei. This random matrix model will form the basis for most of the analysis of this chapter.

For a simple quantum mechanical system, one attempts to specify all interactions through a Hamiltonian H, and solve the Schroedinger equation $H\psi_\lambda = E_\lambda \psi_\lambda$. Moderate success has been achieved in this fashion when the system is

sufficiently small, such as the hydrogen atom. Low-lying states of nuclei have also been treated with some success because of the simple nature of the excitations involved, either single particle or collective. As the excitation energy is increased, however, the number of possible configurations eventually becomes unmanageable. In describing unbound states (as in scattering experiments) there may be thousands or millions of states between the ground state of the nucleus and the states of interest. It would seem that a better understanding of the system would be gained by studying average behavior than by attempting a complete specification of every level.

The two properties to be studied in this chapter are (1) the energy distribution of levels (overall level density and spacing distributions), and (2) the widths or strengths of these levels (strength functions and reduced width distributions). It will be seen that fairly simple statistical assumptions are sufficient to explain the local behavior of these properties, and that the global features are best described by more specific nuclear models.

In treating the nucleus in a statistical sense, one takes the viewpoint that the observed spectra of levels are the result of a random sampling from a certain probability distribution. For example, the spacing between two adjacent levels, x_i, is a random sampling of the random variable X with a probability distribution P(X). This is not to say that the spacing between two particular levels is in any

sense random--each time it is measured, it will be the same. But because it is impossible to predict each spacing from the limited knowledge available, local properties such as spacings will be treated as though they were random. All detailed knowledge of the system will be ignored, and only general symmetries will be used as a basis for predictions. The justification here is empirical, and must necessarily depend on the complexity of the system under investigation.

6.2 The Gaussian Orthogonal Ensemble

6.2.1 The Random Matrix Hypothesis

In most statistical theories, the Hamiltonian itself is treated as a random variable, with a probability distribution P(H). In this framework, the Hamiltonian of a particular nucleus is a random sampling from the ensemble of Hamiltonians described by P(H), and may in fact not be a very representative sampling. (A representative sample would be 'near' the mean of the distribution P(H)). It is only on the average (over many nuclei) that H is described by P(H). To make predictions about P(H), it is convenient to use a matrix representation of the Hamiltonian with components defined by

$$H_{ij} = \int \varphi_i^* H \varphi_j \, d\tau \qquad (6.1)$$

where the integration is over all 3A variables of the A particle nucleus. The φ_i are a set of basis vectors which span the Hilbert space on which H is defined. Only a finite

subspace of these basis vectors will be used, $\{\varphi_N\}$, making H_{ij} an NxN submatrix of the full Hamiltonian, where N is very much larger than the number of levels under consideration.

Wigner was a pioneer in the use of random matrices to describe the local behavior of level spacings and widths (1957), and has written many papers relating to that topic (see Porter, 1965). Some of the earliest analysis of the experimental data is given by Porter and Rosenzweig (1960), who also present a fairly complete treatment of the statistical hypotheses. The following discussion begins by presenting the framework of the random matrix theory which has remained unchanged since that time. The mathematical aspects of random matrices are discussed in detail by Mehta in Random Matrices (1967).

6.2.2 The Joint Probability Distribution

The following arguments seek to provide a form for P(H) by placing simple symmetry constraints on H and P(H). First note that because H is Hermetian,

$$H^{+} = (H^{T})^{*} = H \tag{6.2}$$

It is easy to show that the requirements of time reversal invariance (already assumed in chapter 2) and rotational invariance make H a real, symmetric matrix (see, for example, Porter, 1965). The group which preserves these properties is the orthogonal group. For an NxN real symmetric matrix there are N(N+1)/2 independent elements H_{ij}, chosen to be those for which $i \leq j$:

$$P(H)dH = P(H_{11}, H_{22}, \ldots, H_{12}, \ldots, H_{N-1,N})\, dH_{11}\, dH_{22} \ldots dH_{N-1,N} \tag{6.3}$$

For P(H) to be independent of the choice of basis vectors (rotational invariance),

$$P(H')dH' = P(H)dH \tag{6.4}$$

where

$$H' = O\ H\ O^T$$

$$O^T O = 1$$

and O is a member of the orthogonal group. If O is a function of parameters α, rotational invariance can be specified as

$$dP/d\alpha = 0 \tag{6.5}$$

The second constraint necessary to derive a form for P(H) is that the N(N+1)/2 independent elements of H_{ij} are statistically independent. In other words, P(H) is separable:

$$P(H) = \prod_{i \le j} f_{ij}(H_{ij}) \tag{6.6}$$

where the f_{ij} are independently normalized.

To derive an explicit form for P(H), consider the transformation

$$H = O^T H' O \tag{6.7}$$

where

$$O = \begin{bmatrix} \cos(\theta) & \sin(\theta) & 0 & \cdots & 0 \\ -\sin(\theta) & \cos(\theta) & 0 & \cdots & 0 \\ 0 & 0 & 1 & \cdots & \vdots \\ \vdots & \vdots & \vdots & \cdots & \vdots \\ 0 & 0 & 0 & \cdots & 1 \end{bmatrix}$$

Following Mehta (1968),

$$dH/d\theta = dO^T/d\theta H' O + O^T H' dO/d\theta \tag{6.8}$$

$$= dO^T/d\theta O H + H O^T dO/d\theta$$

$$= A\ H\ +\ H\ A^T \tag{6.9}$$

where

$$A = \begin{bmatrix} 0 & -1 & 0 & \dots & 0 \\ 1 & 0 & 0 & \dots & 0 \\ 0 & 0 & 0 & \dots & 0 \\ \vdots & \vdots & \vdots & \dots & \vdots \\ 0 & 0 & 0 & \dots & 0 \end{bmatrix} \tag{6.10}$$

Let

$$\ln(P) = \sum g_{ij}(H_{ij}) \tag{6.11}$$

where

$$g_{ij} = \ln(f_{ij})$$

From equation (6.5)

$$d \ln(P) / d\theta = P^{-1} dP/d\theta = 0 \tag{6.12}$$

therefore

$$\sum_{i<j} dg_{ij}/dH_{ij} \; dH_{ij}/d\theta = 0 \tag{6.13}$$

$$\{ (-\frac{\partial g_{11}}{\partial H_{11}} + \frac{\partial g_{22}}{\partial H_{22}}) 2H_{12} + \frac{\partial g_{12}}{\partial H_{12}}(H_{11}-H_{22}) + \sum_K (-\frac{\partial g_{1K}}{\partial H_{1K}} H_{2K} + \frac{\partial g_{2K}}{\partial H_{2K}} H_{1K}) \} = 0 \tag{6.14}$$

For this to hold true for all values of H , each of the last terms must vanish, hence for k>2

$$\frac{1}{H_{1K}} \frac{\partial g_{1K}}{\partial H_{1K}} = \frac{1}{H_{2K}} \frac{\partial g_{2K}}{\partial H_{2K}} = \text{const.} = -4a \text{ (say)} \tag{6.15}$$

therefore

$$f_{1K}(H_{1K}) \propto \exp(-2a \cdot H_{1K}) \tag{6.16}$$

Similarly,

$$\frac{1}{2H_{12}} \frac{\partial g_{12}}{\partial H_{12}} = (\frac{\partial g_{11}}{\partial H_{11}} - \frac{\partial g_{22}}{\partial H_{22}}) \frac{1}{H_{11}-H_{22}} = \text{const.} = -2a \tag{6.17}$$

where the constant was chosen to be consistent with the choice above, thus

$$\frac{\partial g_{11}}{\partial H_{11}} + 2aH_{11} = \frac{\partial g_{22}}{\partial H_{22}} + 2aH_{22} = \text{const.} = b \tag{6.18}$$

$$f_{11}(H_{11}) \propto \exp(-aH_{11}^2 + bH_{11}) \tag{6.19}$$

The general expression for P(H) is then

$$P(H) = \exp(-a \; tr(H^2) + b \; tr(H) + c) \tag{6.20}$$

where

$$\mathrm{tr}(A) = \text{trace of } A = \sum_i A_{ii} \tag{6.21}$$

In summary, then, the requirements of rotational invariance and statistical independence lead to a Gaussian distribution for each matrix element, in which the dispersion for the off-diagonal elements is half that of the diagonal elements. (This last feature has been objected to by some, but no convenient way around this problem has been found.) The ensemble of matrices described by P(H) is called the Gaussian Orthogonal Ensemble (GOE).

6.2.3 Width Distributions

The distribution of reduced width amplitudes may be obtained in a manner similar to that above. Recall the definition

$$\gamma_{\lambda c} = \int \varphi_c \chi_\lambda \, dS_c$$

where φ_c is the channel surface function and χ_λ is the eigenvector corresponding to the eigenvalue E_λ:

$$H \chi_\lambda = E_\lambda \chi_\lambda$$

The distribution of eigenvectors χ_λ implies the distribution of reduced widths $\gamma_{\lambda c}$, and a linear transformation of the vectors χ_λ results in a linear transformation of the $\gamma_{\lambda c}$:

$$\underset{\sim}{\chi} = O^T \underset{\sim}{\chi}', \qquad \underset{\sim}{\chi} = (\chi_1, \chi_2, \ldots, \chi_N) \tag{6.22}$$

implies

$$\underset{\sim}{\gamma_c} = O^T \underset{\sim}{\gamma_c}', \qquad \underset{\sim}{\gamma_c} = (\gamma_{1c}, \gamma_{2c}, \ldots, \gamma_{Nc}) \tag{6.23}$$

where

$$\underset{\sim}{\gamma_c} = \int \varphi_c \underset{\sim}{\chi} \, dS \tag{6.24}$$

Following the arguments of equations (6.6) to (6.20),

$$P(\{\gamma_{\lambda c}\}) = \prod_\lambda f_\lambda(\{\gamma_{\lambda c}\}) \tag{6.25}$$

$$\sum_{\lambda c} \frac{\partial g_\lambda}{\partial \gamma_{\lambda c}} \frac{\partial \gamma_{\lambda c}}{\partial \theta} = 0 \tag{6.26}$$

$$\frac{\partial \gamma_c}{\partial \theta} = \frac{\partial O^T}{\partial \theta} \gamma_c' \tag{6.27}$$

$$= \frac{\partial O^T}{\partial \theta} O \gamma_c \tag{6.28}$$

$$\sum_c \left[\frac{\partial g_1}{\partial \gamma_{1c}} (-\gamma_{2c}) + \frac{\partial g_2}{\partial \gamma_{2c}} \gamma_{1c} \right] = 0 \tag{6.29}$$

$$\frac{1}{\gamma_{1c}} \frac{\partial g_1}{\partial \gamma_{1c}} = \frac{1}{\gamma_{2c}} \frac{\partial g_2}{\partial \gamma_{2c}} = \text{const.} = -2a_c \tag{6.30}$$

Therefore,

$$g_1 = -a_c/2 \, \gamma_{1c}^2 + b_{1c}(\gamma_{1c'}, \gamma_{1c''}, \ldots) \tag{6.31}$$

where b_{1c} is not a function of γ_{1c}. In general, then,

$$g_\lambda = -1/2 \sum_{cc'} \gamma_{\lambda c} M_{cc'} \gamma_{\lambda c'} + \text{const.} \tag{6.32}$$

where

$$M_{cc} = a_c, \qquad b_{\lambda c} = \sum_{c' \neq c} M_{cc'} \gamma_{\lambda c'} + \text{const.} \tag{6.33}$$

Finally,

$$P(\{\gamma_{\lambda c}\}) \propto \prod_\lambda \exp[-1/2(\gamma_\lambda, M \gamma_\lambda)] \tag{6.34}$$

Defined in this fashion, M can be shown to be equal to the inverse of the covariance matrix:

$$M = \Sigma^{-1} \tag{6.35}$$

where

$$\Sigma_{cc'} = \overline{\gamma_{\lambda c} \gamma_{\lambda c'}} \tag{6.36}$$

where the bar indicates an average over levels. The two requirements of invariance and independence permit the existence of channel-channel amplitude correlations, given by

$$C_{cc'} = \Sigma_{cc'} / (\Sigma_{cc} \Sigma_{c'c'})^{1/2} \tag{6.37}$$

The reduced width (γ^2) correlation is given by

$$C^{\gamma^2}_{cc'} = \frac{\overline{\gamma_c^2 \gamma_{c'}^2} - \overline{\gamma_c^2} \cdot \overline{\gamma_{c'}^2}}{[\overline{\gamma_c^4} - (\overline{\gamma_c^2})^2]^{1/2} [\overline{\gamma_{c'}^4} - (\overline{\gamma_{c'}^2})^2]^{1/2}} \tag{6.38}$$

$$= (C_{cc'})^2 \geq 0$$

i.e., the width correlations are predicted to be non-negative. While width correlations have been observed in many experiments, it has only been recently that amplitude correlations have been measured for a statistical collection of levels (Wells, 1980, Chou, 1980).

The probability distribution for a single width is obtained by integrating (6.34) over all variables except $\gamma_{\lambda c}$

$$P(\gamma_{\lambda c}) = (2\pi \overline{\gamma_{\lambda c}^2})^{-1/2} \exp\{-\gamma_{\lambda c}^2/(2\overline{\gamma_{\lambda c}^2})\} \qquad (6.39)$$

and transforming from γ to $y = \gamma^2$:

$$P(y) = (2\pi y\bar{y})^{-1/2} \exp\{-y/(2\bar{y})\} \qquad (6.40)$$

This is a chi-squared (χ^2) distribution with one degree of freedom, and was first obtained in analysis of experimental widths by Porter and Thomas (1956) (and is usually referred to as the Porter-Thomas distribution). The remarkable feature of this distribution is the high probability for obtaining very small widths. In hundreds of experiments this distribution has been shown to agree quite well with experimental data.

The global behavior of this distribution, however, is incorrect: it is energy independent and therefore implies a constant average reduced width. A better description of the strength function (average reduced width/average level density) is provided by the shell model. In that framework a single particle state mixes with a background of more complicated states (similar to the mixing of the analogue state, discussed in chapter 5) to produce a distribution of single particle strength centered at the single particle

state energy and spread over several MeV. This point will be returned to in section 6.7 when results of the present work are presented.

6.2.4 Eigenvalue Distributions

Consider the rotation O which diagonalizes H:

$$H = O\, H_D\, O^T = \sum_{ik} O_{ij}\, (E_j \delta_{jk})\, O_{lk} \tag{6.41}$$

The matrix O is specified by only N(N-1)/2 real independent parameters, α_i , because O is restricted by N(N+1)/2 orthonormality conditions:

$$O_{ik} \cdot O^T_{kj} = \delta_{ij} \tag{6.42}$$

H depends on N(N+1)/2 parameters, which, from equation (6.41), can be identified with the N E_λ's and the N(N-1)/2 α's. Rotational invariance requires

$$P(H)dH = P(H')dH' \tag{6.43}$$

thus

$$P(E_\lambda, \alpha) = \exp(-a\sum_\lambda E_\lambda^2 + b\sum E_\lambda + c)\; J_N(E_\lambda, \alpha) \tag{6.44}$$

where J is the Jacobian of the transformation dH -> dH':

$$J_N = \frac{\partial(H_{11}, H_{22}, \ldots, H_{12}, \ldots, H_{N-1,N})}{\partial(E_1, E_2, \ldots, E_N, \alpha_1, \alpha_2, \ldots \alpha_{N(N-1)/2})} \tag{6.45}$$

$$= \begin{vmatrix} \frac{\partial H_{11}}{\partial E_1} & \frac{\partial H_{11}}{E_2} & \cdots & \frac{\partial H_{11}}{\partial \alpha_{N(N-1)/2}} \\ \vdots & \vdots & \vdots & \vdots \\ \frac{\partial H_{N-1,N}}{\partial E_1} & \frac{\partial H_{N-1,N}}{\partial E_2} & \cdots & \frac{\partial H_{N-1,N}}{\partial \alpha_{N(N-1)/2}} \end{vmatrix} \tag{6.46}$$

Because the H_{ij} are linear functions of the E_λ, the first N columns of the determinant are independent of E_λ, and J_N is a polynomial of order N(N+1)/2 in the E_λ. If any pair of E_λ's are identical, the transformation is not unique and J_N must vanish. Therefore J_N must have the form

$$J_N = \prod_{\mu<\lambda=1}^{N} |E_\lambda - E_\mu|\, \exp[-a(E_\lambda - E_0)^2] \tag{6.47}$$

Thus the eigenvalues are distributed according to

$$P(\{E_\lambda\}) \propto \prod_{\mu<\lambda} |E_\lambda - E_\mu| \exp[-a(E_\lambda - E_o)^2] \qquad (6.48)$$

This distribution is known as the Wishart distribution.

The single eigenvalue distribution (or level density) is extracted from this equation by integrating over all eigenvalues except one. Unfortunately, the mathematics involved is exceedingly complex and the answer cannot be provided in closed form. In the limit of $N \to \infty$, Mehta and Gaudin (1960) show

$$P_N(\theta) \to \begin{cases} \frac{2}{N\pi}\sqrt{N-\theta^2} & \theta < \sqrt{N} \\ 0 & \theta \geq \sqrt{N} \end{cases} \qquad (6.49)$$

where θ is proportional to $(E_\lambda - E_o)$. This is the well known "semi-circle law" of Wigner (1957), and does not even remotely resemble the experimentally observed exponentially increasing level density. Again, the statistical theory fails to describe the global behavior of nuclear levels.

To calculate the spacings between nearest neighbors, it is necessary to integrate equation (6.48) over all but two adjacent eigenvalues, again a formidable task. In 1956, Wigner proposed a form for the spacing distribution based on a 2x2 random matrix. Setting N=2 in equation (6.48),

$$P(E_1', E_2') \propto |E_2' - E_1'| \exp[-a(E_1'^2 + E_2'^2)] \qquad (6.50)$$

where $E_i' = E_i - E_o$. Changing to new independent coordinates

$$x = E_2' - E_1' = E_2 - E_1 \qquad (6.51)$$

$$y = E_1' + E_2' = E_1 + E_2 + 2E_o$$

yields the result

$$P(x) \propto x \exp(-ax^2) \qquad (6.52)$$

which, when normalized, gives Wigner's "surmise":

$$P(x) = \frac{\pi}{2} \frac{x}{\overline{x^2}} \exp(-\pi x^2/4\overline{x^2}) \qquad (6.53)$$

This simple form displays the most important feature of the spacings--level repulsion. The probability of two levels of the same spin and parity having the same energy is zero, in agreement with the Pauli exclusion principle. The most remarkable thing about this probability distribution (considering how it was obtained) is that the probability it gives is within 0.02 of the correct expression obtained by Mehta and Gaudin (1960, 1961). These authors derived a form for P(x) as an integral equation in which x occurs as a parameter, and tabulated the result for $x<3.2$.

6.3 Other Ensembles

The major theoretical objections to the GOE are (1) the unphysical semi-circular level density, (2) the factor of two between the variances of the diagonal and off-diagonal matrix elements, and (3) the assumption of statistical independence of the H_{ij}. These difficulties have motivated the development of other ensembles, each with their own advantages and disadvantages.

From a physical point of view, it would be preferable to drop the restriction of statistical independence, since it is conceivable that certain interactions may be correlated. French and Wong (1970) and independently Bohigas and Flores (1971) introduced an ensemble in which

the matrix elements of a two-body interaction (instead of the Hamiltonian matrix elements) are presumed to be independent. This ensemble, based on the shell model, is referred to as the Two Body Random Ensemble (TBRE). Mello (1978) has used this ensemble in Monte Carlo calculations, and has shown remarkable agreement with the GOE. The energy dependence of the level density is approximately Gaussian, which has the possible advantage of a positive curvature on the low energy side of the distribution (duplicating the positive curvature of an exponential, and in contrast with the negative curvature of the semi-circular GOE distribution). In this low energy region, some differences in spacing distributions have been noted between the GOE and the TBRE--the later is peaked at a slightly lower value of the spacing. Present experimental data, however, are not sufficient to distinguish between these two distributions.

The other ensemble of considerable interest here is the Circular Orthogonal Ensemble (COE) introduced by Dyson (1962). This ensemble lacks the physical framework of the TBRE, but is mathematically more tractable. The quantum mechanical system is represented by an NxN unitary matrix S with eigenvalues $e^{i\theta_j}$, where θ_j is real and lies on the interval $[0,2\pi]$. S is a function of H (of unspecified form), such that for small ranges of variation, the θ_j are linear functions of the eigenvalues E_λ of H. The statistical hypothesis is that "the behavior of n consecutive levels of an actual system, where n is small

compared with the total number of levels, is statistically equivalent to ... n consecutive angles θ_i on the unit circle, where n is small compared with N" (Dyson, 1962). For $N \to \infty$, Mehta (1971) has shown that the spacing distributions (nearest neighbor, next nearest neighbor, etc.) of the COE and GOE converge to the same limit. The COE has the advantage of a simpler joint probability density,

$$P(\{\theta_j\}) \propto \prod_{j<k} |e^{i\theta_j} - e^{i\theta_k}| \qquad (6.54)$$

and a uniform level density (which is obvious from the translational invariance of equation (6.54). The main disadvantage lies in its inability to deal with eigenvector (width) distributions. The purpose in introducing this ensemble is to use certain results derived from the COE--the Dyson F statistic and the Dyson-Mehta Δ_3 statistic--which provide statistical tests of the quality of a set of levels.

6.4 Statistical Tests of Data and Theory

"A 'statistic' is a quantity which can be calculated from an observed sequence of levels alone without other information, and whose average value and variance are known from the theoretical model" (Mehta, 1971). For example, the arithmetic mean of a sample $(1/N \sum_i x_i)$ is a statistic whose expectation value is the mean of the parent distribution, P(X). If the number of elements in the sample is large,

this statistic is a good estimator of the true mean, and provides a test of how well the parent distribution is known.

Similarly, there are several useful statistics defined in the study of nuclear levels which serve as points of comparison between data and theory. A few of these statistics are very sensitive to the quality of the data, i.e., their values change rapidly as the data becomes poorer. These statistics are not too useful for verifying the theory, bacause experimental errors would invalidate any conclusions. However, they can be very useful in checking (and sometimes improving) the quality of a set of levels. Other statistics are less sensitive to experimental errors, and so serve to check the theory.

6.4.1 The F-Statistic

To test the accuracy of some of the random matrix results, it is necessary to have a 'pure' level sequence, i.e., no missing levels and no spurious levels. The Dyson F statistic was designed to provide this purity test, and was first used by Liou *et al.* (1972) to improve the quality of level sequences in the Erbium isotopes. It is defined for the i^{th} level as

$$F_i = \sum_j f((E_j - E_i)/L) \tag{6.55}$$

where

$$f(x) = \begin{cases} \frac{1}{2}\ell n \left| \frac{1+(1-x^2)^{1/2}}{1-(1-x^2)^{1/2}} \right| & |x| < 1 \\ 0 & |x| \geq 1 \end{cases} \tag{6.56}$$

For L = nD (where D is the average spacing) the expectation value of F_i for a true member of a sequence is

$$\langle F_i \rangle \quad n - \ln(n) - 0.656 \tag{6.57}$$

and its standard deviation is

$$= [\langle F_i^2 \rangle - \langle F_i \rangle^2]^{1/2} \quad [\ln(n)]^{1/2} \tag{6.58}$$

For a spurious level,

$$\langle F_i \rangle \approx n \tag{6.59}$$

In other words, the spurious level will appear as a fluctuation in F of order ln(n), compared with the natural scatter in F given by its standard deviation, $(\ln(n))^{1/2}$. It is apparent that the larger the value of n (which must be small enough so that nD is small compared with the total region studied), the more sensitive the test is. This effect is caused by the large weighting in f(x) given to small values of x. For a pure sequence, level repulsion guarantees that small values of x occur infrequently. A spurious level increases the number of small spacings, and results in a large value of F_i for that level. A missing level does not have quite as large an effect, but will appear as a dip in F_i, evaluated at the nearest observed level. It is apparent that a certain amount of luck is required in detecting a flaw in the sequence: if a spurious level occurs within a large spacing, it will go unnoticed. The effect of the spurious level on F is offset by the natural dip (in this case) in F. Even so, the distribution of values of F_i will reflect the overall quality of a sequence.

For convenience, the G statistic is defined as a normalized F statistic:

$$G_i = (F_i - \langle F \rangle_{theory}) \; / \; (\sigma_F)_{theory} \qquad (6.60)$$

G is then normally distributed with zero mean and unit variance.

6.4.2 The Δ_3 Statistic

A second statistic useful in checking the overall quality of a level sequence is the Dyson-Mehta Δ_3 statistic (1963). Δ_3 is a measure of the long range order of a sequence, and is defined as the difference between a staircase plot of the number of levels vs. energy, and a straight line:

$$\Delta_3 = \min_{A,B} \frac{1}{2L} \int_{-L}^{L} [N(E) - AE - B]^2 \, dE \qquad (6.61)$$

where A and B are the parameters of the straight line. The expectation value and variance of Δ_3 are

$$\langle \Delta_3 \rangle = \frac{1}{\pi^2} [\ln(n) - 0.0687] \qquad (6.62)$$

$$\sigma^2_{\Delta_3} = 0.012 \qquad (6.63)$$

That Δ_3 is proportional to ln(n) and not to (n) demonstrates the extreme rigidity of a level sequence: the mean square deviation from a straight line for 1000 levels is less than one! Another way of saying this is that there are no large fluctuations in the level density (which would carry N(E) away from a straight line). A large value of Δ_3 might indicate regions of missing or spurious levels.

Implicit in the definition of Δ_3 is a constant level density. Thus to compare with experimental data, the

exponential increase in level density must first be unfolded from the observed sequence. This will be discussed with the analysis of the data.

6.4.3 Linear Correlation Coefficient

If a set of levels has been shown to be relatively pure, as indicated by the F and Δ_3 statistics, there are several other statistics which may be calculated and compared with theory. The two which will be used in this work are the standard deviations (or widths) of the k-th nearest neighbor spacing distributions, σ_k , and the linear correlation coefficient, ρ_0 . This coefficient measures the correlation between adjacent spacings, and is defined as

$$\rho_0 = \frac{\overline{x_i\, x_{i+1}} - \overline{x_i}\;\overline{x_{i+1}}}{[\overline{x_i^2} - (\overline{x_i})^2]^{1/2}\,[\overline{x_{i+1}^2} - (\overline{x_{i+1}})^2]^{1/2}} \tag{6.64}$$

For the orthogonal ensembles, $\rho_0 = -0.27$ (Mehta, 1971). Larger than average spacings tend to be followed by smaller than average spacings, and similarly small spacings tend to be followed by large spacings.

6.4.4 Standard Deviations of the Spacing Distributions

The k-th order spacing distributions give the probability of the spacing between two levels, with k levels in between:

$$S_i^k = (E_{i\cdot(k+1)} - E_{i\cdot(k+1)}) \tag{6.65}$$

$$x_i^k = S_i^k / [\overline{S^k}/(k+1)] = (k+1) S_i^k / \overline{S^k} \tag{6.66}$$

The mean of these distributions are uninteresting,

$$\overline{S^k} = (k+1)\overline{S^0} \quad \text{or} \quad \overline{x^k} = (k+1) \tag{6.67}$$

but the variances provide useful comparisons of data and theory:

$$\sigma_k^2 = \overline{(x^k)^2} - (\overline{x^k})^2 \qquad (6.68)$$

These have been calculated by Mehta (given by Bohigas, et al., 1975) for small k:

k	0	1	2	3	4	5
σ_k	.534	.645	.705	.745	.775	.798

For $k \geq 1$, French et al. (1978) give an approximate (and accurate) expression:

$$\sigma_k^2 = \frac{2}{\pi^2}\{\ln[2\pi(k+1)] + \gamma + 1\} - 5/12 \qquad (6.69)$$

where γ = Euler's constant, 0.577. The rigidity of the sequence is again demonstrated by the very slow increase in σ_k for increasing k--if the levels were uncorrelated, σ_k would increase as $(k+1)^{1/2}$. (The ensemble of uncorrelated spacings will be referred to as the Uncorrelated Wigner (UW) ensemble.)

6.5 Reduced Width Distributions

Figures 6.1 to 6.5 show comparisons of the present data with the Porter-Thomas distribution. The vertical and horizontal scales were chosen to accentuate the long tail in the distribution for small widths. The agreement in each case is good, except in figure 6.2a. In this figure, the number of large experimental widths far exceeds the prediction. These large widths are part of the analogue

state at E_p = 3.95 MeV. When this region is excluded (6.2b) the agreement is excellent. Obviously, then, known non-statistical regions must be excluded from this type of analysis. In each of the other figures, regions around analogue states have been omitted.

The next and most useful point to notice in these figures is that the data is truncated on the low side. This corresponds to the inability to experimentally resolve very small widths. As discussed in chapter 3, this truncation occurs for widths below about 10 eV, although in units of average widths y_{cutoff} ranges from 0.02 to 0.2 for the present work. Integrating P(y) from 0 to y_{cutoff} gives the fraction of levels missed (f^-). Likewise, integrating yP(y) from 0 to y_{cutoff} yields the fraction of the total width missed (W^-) in units of the average width, $\bar{y}$. The procedure used to obtain the best estimate of N (the true number of levels) and $\bar{y}$ (the average reduced width) is: (1) with $N=N_x$ (the number of observed levels), and $y = \bar{y}_x$ (the average of the observed widths), compare the data with $N \cdot P(y)$; (2) using the value of y_{cutoff} obtained from the histogram, compute a new normalization $N = N_x/f^-$, and a new average width $\bar{y} = \bar{y}_x N_x/(1-W^-)/N$; (3) compare the data with the new distribution--if y_{cutoff} has changed (because of a change in $\bar{y}$), repeat step (2). Using this procedure, reasonable estimates of the true number of levels, N, and the true strength, $N \cdot \bar{y}$, may be obtained. With the exception of 6.2a, each figure shows the final fit obtained with this method.

Figure 6.1 (a) Elastic channel width distribution for 56 $1/2^+$ levels from E_p = 3.1 to 4.0 MeV. The smooth curve is a Porter-Thomas distribution normalized to 62 levels (see text for discussion).

(b) Inelastic width distributions (both channels combined) for 39 $1/2^+$ levels from E = 3.1 to 4.0 MeV. The two curves correspond to correlated decay (smooth) and uncorrelated decay (dashed).

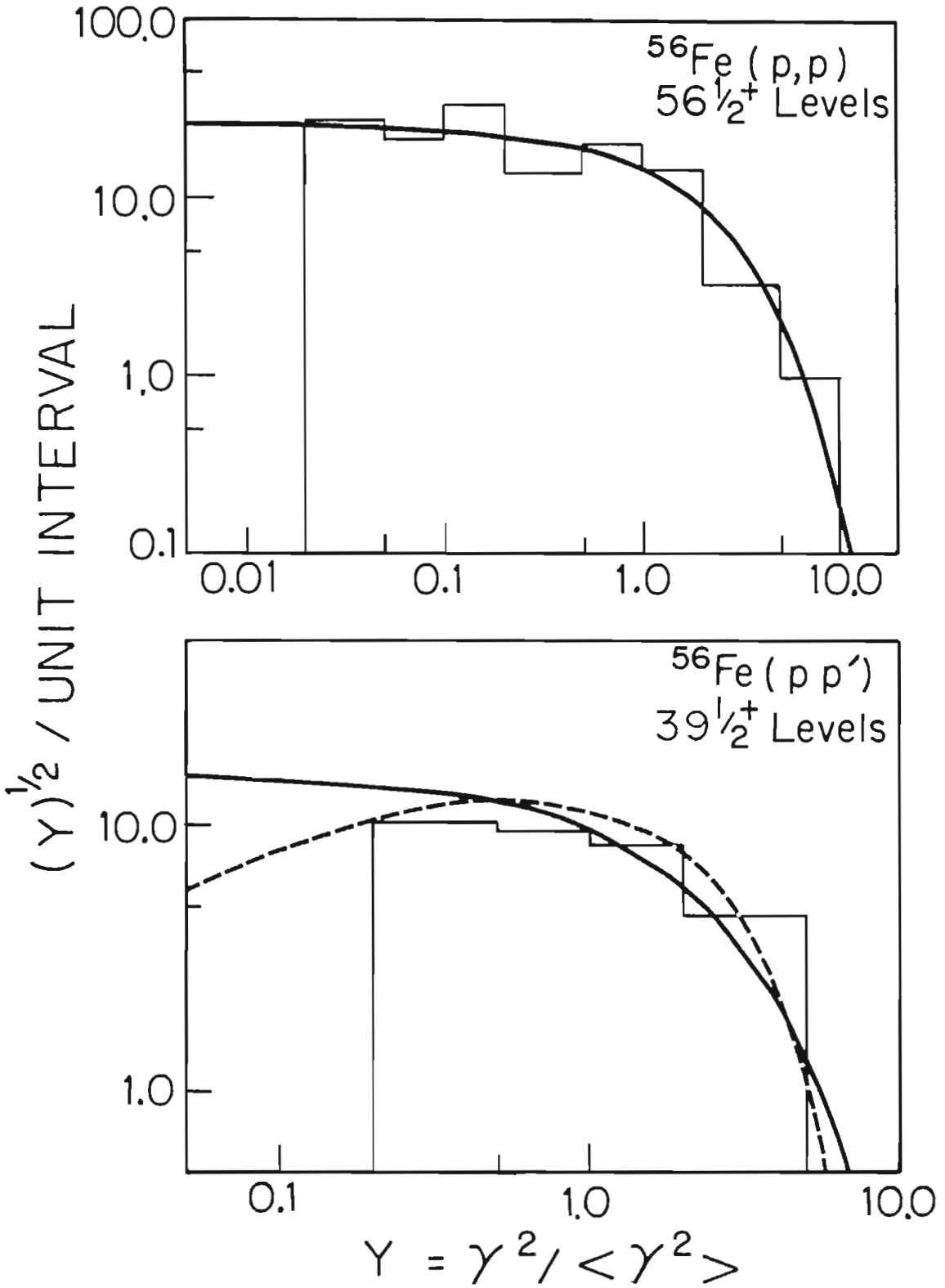
100.0
10.0
1.0
0.1
0.01
0.1
1.0
10.0
^{56}Fe (p,p)
$56\ 1/2^+$ Levels
^{56}Fe (p p′)
$39\ 1/2^+$ Levels
$(Y)^{1/2}$ / UNIT INTERVAL
$Y = \gamma^2 / \langle \gamma^2 \rangle$

Figure 6.2 (a) Elastic width distribution for 35 $1/2^-$ levels from E_p = 3.1 to 4.0 MeV. The excess large widths are due to an analogue state at 3.95 MeV.

(b) $1/2^-$ elastic width distribution from 3.1 to 3.8 MeV. The smooth curve is a Porter-Thomas distribution normalized to 32 widths.

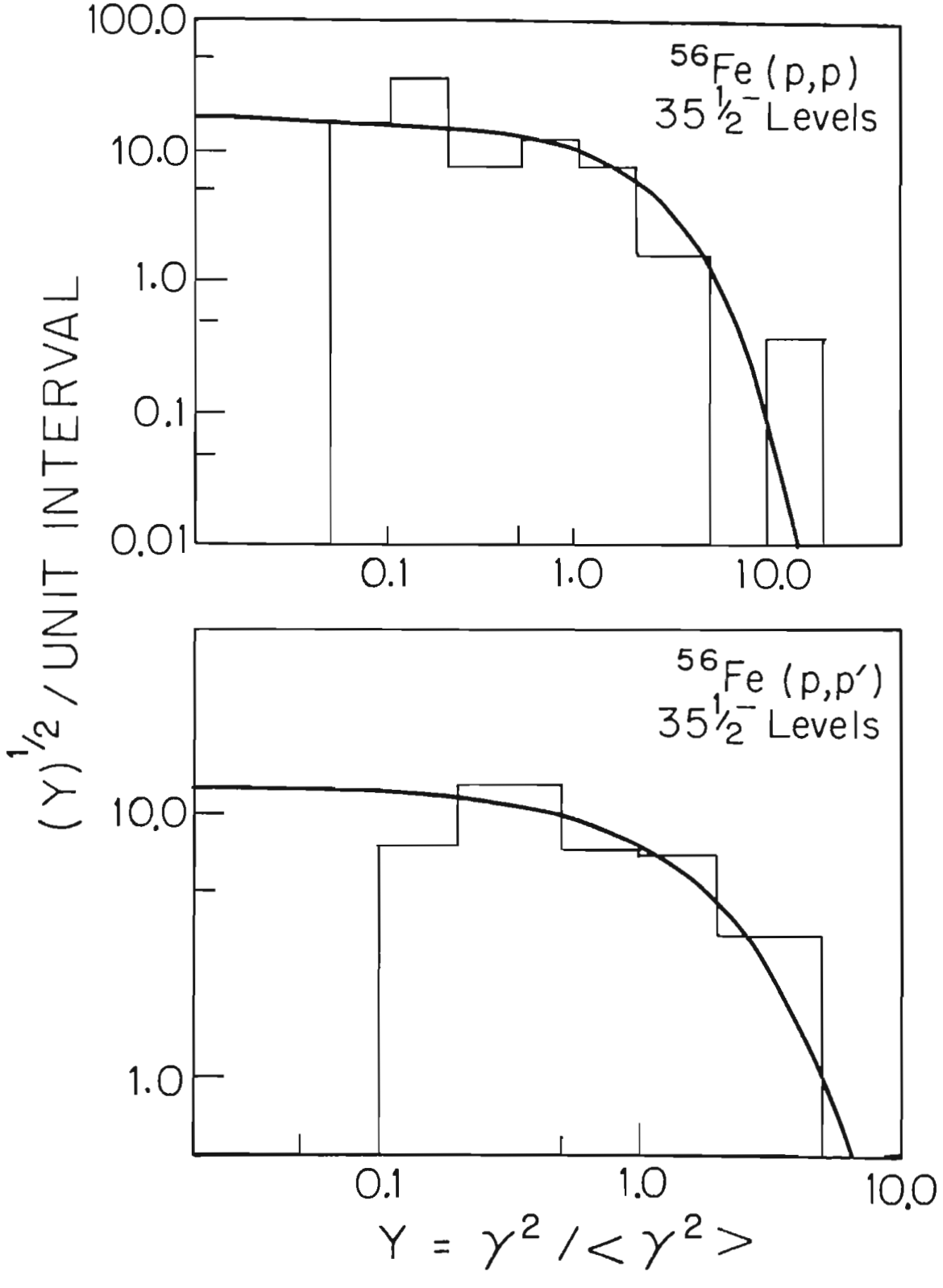
100.0
10.0
1.0
0.1
0.01
^{56}Fe (p,p)
35 1/2$^-$ Levels
0.1
1.0
10.0
^{56}Fe (p,p′)
35 1/2$^-$ Levels
10.0
1.0
0.1
1.0
10.0
$(Y)^{1/2}$ / UNIT INTERVAL
$Y = \gamma^2 / \langle \gamma^2 \rangle$

Figure 6.3 (a) Elastic width distribution for 38 $3/2^-$ levels from 3.1 to 3.8 MeV. The smooth curve is a Porter-Thomas distribution normalized to 52 levels.

(b) Combined inelastic width distribution for 60 widths observed in the two inelastic channels. The smooth curve is a Porter-Thomas distribution normalized to 80 widths.

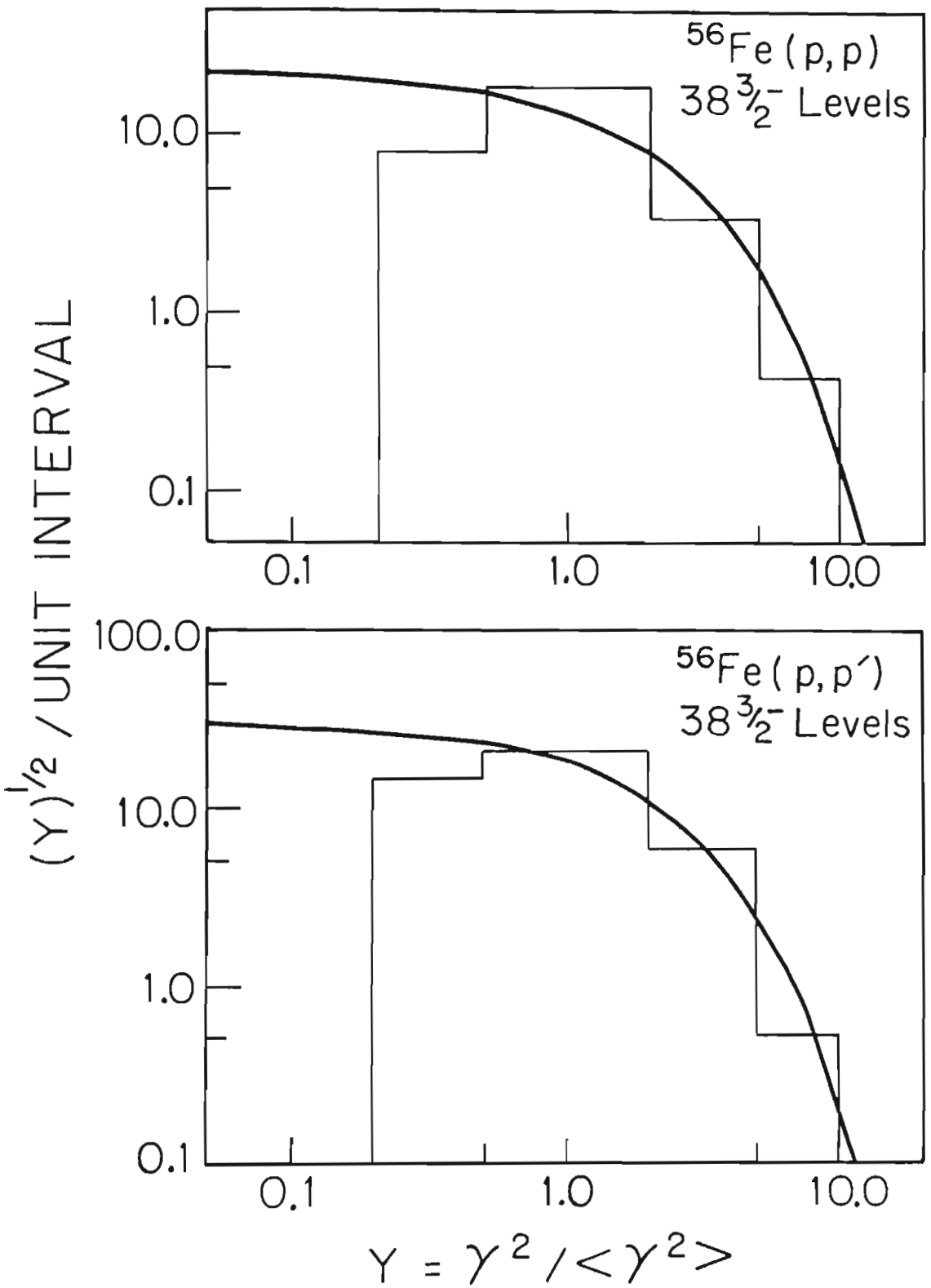
^{56}Fe (p, p)
$38\ 3/2^-$ Levels
10.0
1.0
0.1
0.1
1.0
10.0
^{56}Fe (p, p′)
$38\ 3/2^-$ Levels
100.0
10.0
1.0
0.1
0.1
1.0
10.0
$(Y)^{1/2}$ / UNIT INTERVAL
$Y = \gamma^2 / \langle \gamma^2 \rangle$

Figure 6.4 (a) Elastic width distribution for 35 $3/2^+$ levels from E_p = 3.1 to 4.0 Mev. The smooth curve is a Porter-Thomas distribution normalized to 46 widths.

(b) Total inelastic width distribution for the $3/2^+$ levels. The smooth curve is a Porter-Thomas distribution.

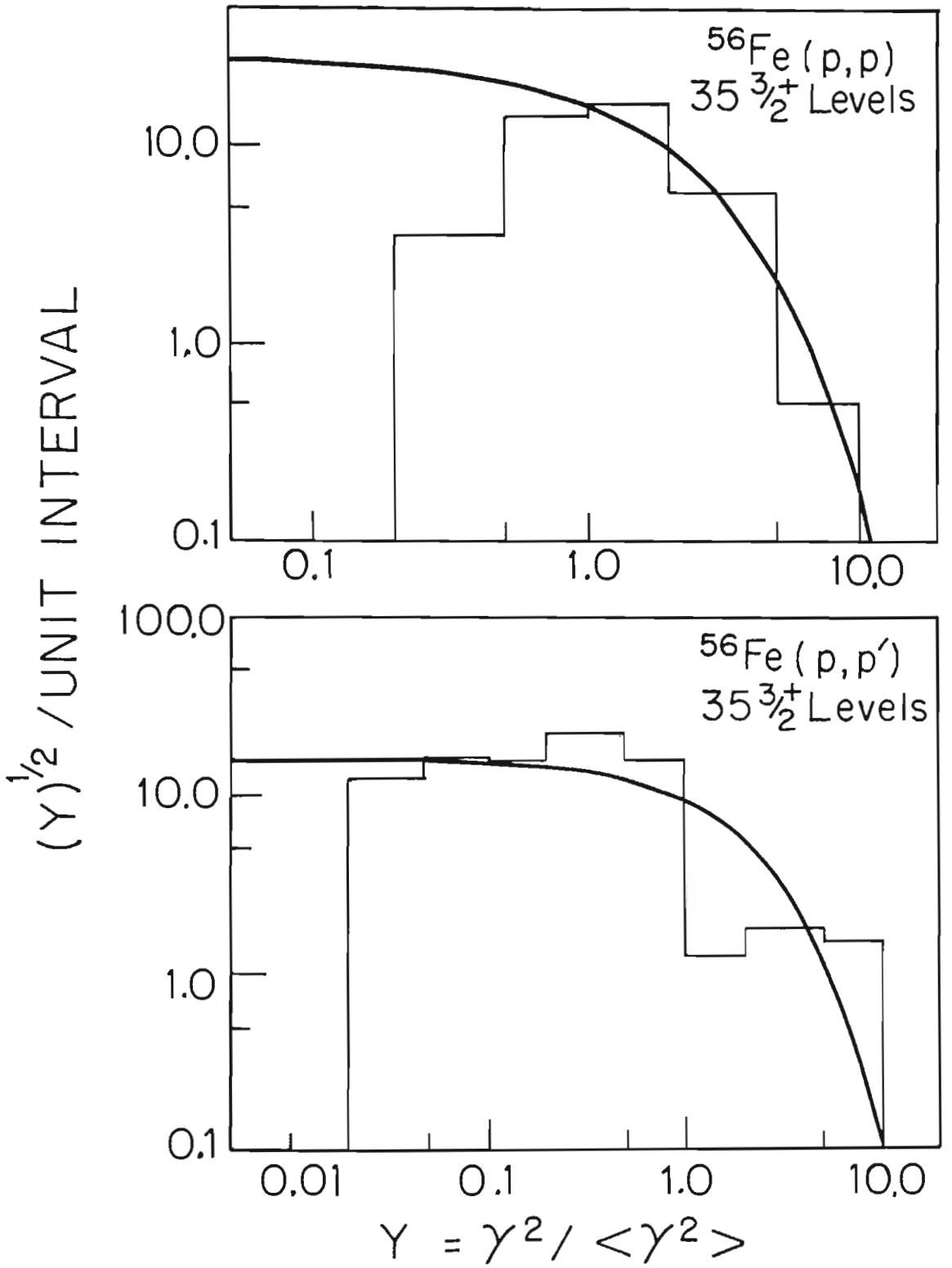
^{56}Fe (p,p)
35 3/2$^+$ Levels
10.0
1.0
0.1
0.1
1.0
10.0
^{56}Fe (p,p′)
35 3/2$^+$ Levels
100.0
10.0
1.0
0.1
0.01
0.1
1.0
10.0
$(Y)^{1/2}$ /UNIT INTERVAL
$Y = \gamma^2 / \langle \gamma^2 \rangle$

Figure 6.5 (a) Elastic width distribution for 47 $5/2^+$ levels from E_p = 3.1 to 3.6 MeV. The smooth curve is a Porter-Thomas distribution normalized to 58 widths.

(b) Inelastic width distribution for the same levels. The normalization for the Porter-Thomas distribution is again 58.

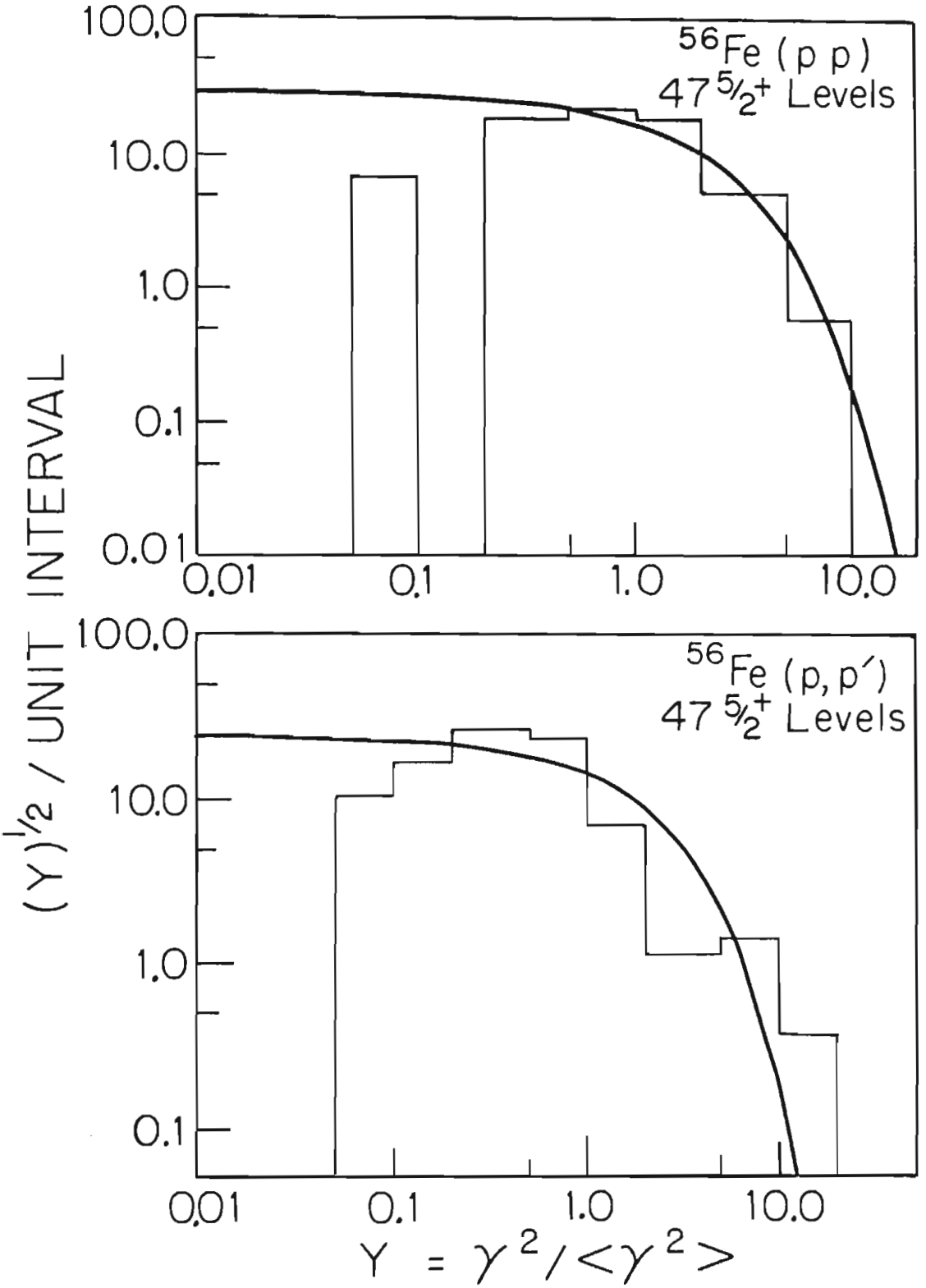
100.0
10.0
1.0
0.1
0.01
^{56}Fe (p p)
47 5/2^{+} Levels
0.01
0.1
1.0
10.0
100.0
10.0
1.0
0.1
^{56}Fe (p, p′)
47 5/2^{+} Levels
0.01
0.1
1.0
10.0
$(Y)^{1/2}$ / UNIT INTERVAL
$Y = \gamma^2 / \langle \gamma^2 \rangle$

For the 56 s-wave resonances, the average elastic reduced width was 1.5 keV, with a cutoff of y = 0.02. (In the following discussion, 'average width' refers to the corrected average, as described above.) This implies that the smallest observable lab width was approximately 10 eV, as expected. The agreement with the Porter-Thomas distribution is excellent, despite the concentration of strength around 3.8 MeV. (See chapter 5 for a discussion of the feature.) This small value for the cutoff also implies that the number of levels missed is on the order of 10%. Therefore the s-wave level sequence is a good candidate for further statistical tests, which will be discussed in a later section.

There are two possible inelastic decay channels for the $1/2^+$ resonances. Figure 6.1b shows the distribution of the 28 observed total inelastic widths. (The cutoff for the inelastic laboratory widths is 3 eV). There is no way to experimentally distinguish the two channels (all decays are isotropic) except in the presence of an interfering resonance. The solid curve was prepared under the assumption that the decay proceeds through one channel only. This situation is also equivalent to the two channels being completely correlated. An alternate hypothesis would be that the two channels are uncorrelated, and have equal mean values. The sum of the widths in the two channels would then be distributed as a chi-squared of two degrees of freedom:

$$P(w) = 1/\overline{w}\ \exp(-w/\overline{w}) \qquad (6.70)$$

This is shown as a dashed curve in figure 6.1b. (Because the distributions are different, the cutoff implies different fractions of missing widths, with the result that $\bar{w} = 1.25\ \bar{y}$.) Apparently, the second assumption (uncorrelated decay) provides a somewhat better fit.

Figures 6.2a and b show the distributions of elastic widths for $1/2^-$ resonances from 3.10 to 4.00 MeV and 3.10 to 3.88 MeV, respectively. The first plot contains the region around the $1/2^-$ analogue state and therefore contains two exceptionally large widths. The average reduced width for the 25 levels in the second figure is 1.0 keV, and the cutoff corresponds to a laboratory width of 20 eV. Smaller widths than this should have been observable, but spin assignments for small p-waves were often uncertain, and resonances for which the spin is unknown have been excluded from the analysis. (Only two additional levels would be needed to extend the data down to 10 eV, so the high cutoff is not considered significant).

The elastic and inelastic width distributions for $3/2^-$ resonances are shown in figures 6.3a and b, respectively. The 38 elastic reduced widths had a corrected average of 0.14 keV, with a cutoff corresponding to a laboratory width of approximately 8 eV. This improvement over the $1/2^-$ case results from a higher probability for making a definite spin assignment for $3/2^-$ resonances (as discussed in chapter 4).

There are two inelastic decay channels for $3/2^-$ resonances, and because they result in different angular

distributions, some confidence can be placed in the assigned widths. If one channel dominates the decay for a particular level, however, the small admixture from the other channel would go undetected, so that very small widths in either channel are not observed. Because the average reduced widths in each channel were identical (0.2 keV), the two distributions were added together (to improve the statistics) and fit with a Porter-Thomas distribution normalized to the sum of the number of widths (corrected for missing widths). The cutoff in each channel is approximately 2 eV (laboratory width).

The average elastic reduced width for the $3/2^+$ resonances (figure 6.4a) is 1.6 keV, and the cutoff for the laboratory width is near 8 eV. Figure 6.4b shows the distribution of total inelastic widths. Because there are three inelastic decay channels (one with $l'=0$, two with $l'=2$), and the angular distributions do not provide unique solutions, widths for each channel could not be analyzed separately with any confidence. The agreement with the Porter-Thomas distribution is fair, indicating that the decay is primarily in one channel (this is not suprising since the penetrabilities favor the single $l'=0$ channel by a factor of ten over the $l'=2$ channels). The cutoff occurs at 1.4 eV (laboratory width).

To avoid the effects of the $5/2^+$ analogue state at 3.76 MeV, only levels from 3.1 to 3.6 MeV were included in figures 6.5a and b. The average elastic reduced width in

this region was 0.8 keV, and the cutoff (taken to be 0.2 in the figure, despite the occurance of one smaller level) corresponds to a laboratory width of approximately 8 eV. Bear in mind that only resonances for which there is a preferred spin assignment have been included in this analysis.

The inelastic widths suffer the same problems as discussed for the $3/2^+$ resonances. Again, the $\ell'=0$ widths are expected to dominate, although the agreement with the Porter-Thomas distribution is not as good. The average reduced width is 0.8 keV and the cutoff (0.1 in the figure) occurs at a laboratory width of approximately 4 eV.

In summary, the agreement with the Porter-Thomas distribution is good, and the comparison supplies an estimate of the number of missing widths (and the total strength missed). The lower limits of the experimental distribution are in the neighborhood of 10 eV for the elastic (laboratory) widths, and 2 eV for the inelastic widths.

6.6 Spacing Distributions

The experimental spacing distributions generally show poor agreement with the Wigner distribution unless a large fraction (over 80%, say) of the levels were observed. The primary cause for the disagreement is an incorrect estimate

of the average spacing--the average of the experimental spacings is too large. If x = spacing/average observed spacing, an excess number of small values of x is observed. This may be corrected by assuming a smaller average spacing (smaller by an amount determined, for example, from an analysis of the width distribution). If the average spacing is correctly estimated, then an excess number of large values of x = spacing/corrected average spacing is observed (due to missing resonances). The experimental spacing distribution is actually a sum of nearest neighbor, next nearest neighbor, and higher order distributions. For example, if 20% of the levels are missed at random (e.g., because the widths are too small), then the experimental distribution consists of 80% nearest neighbor, 16% next nearest neighbor, etc., spacing distributions.

Using numerical tables calculated by Gaudin (1961) and by Mehta and des Cloizeaux (1971) it is possible to compute the first half dozen of these distributions for values of the spacing up to five times the average spacing. For all reasonable experimental distributions (in which at least half of the levels were observed) it is sufficient to keep the k-th order distributions with k=0 to 4 to get an accurate theoretical approximation for values of x up to five. If the fraction of levels observed is f^+, the contribution of the k-th order distribution is given by

$$c_k = f^+(1-f^+)^k \qquad (6.71)$$

In the figures that follow, two methods of presenting the data are used. In the first method, a histogram of the spacing distribution is constructed in which x = spacing/average experimental spacing. A value for the fraction of levels observed, f^+, is obtained from the width distribution or a comparison of the level density with the Gilbert and Cameron predictions. Then, a theoretical curve is generated assuming a level density of $\rho_i = \rho_{exp} / f^+$. This calculation is shown in the figures as a solid curve. (If two sequences are superimposed, the ratio of level densities is assumed to be the same as the ratio given by Gilbert and Cameron. The total level density is assumed to be $\rho = \rho_{exp} / f^+$, where f^+ is now the fraction of levels observed for the combined sequence. A derivation of the probability distribution for combined sequences, a generalization of the derivation given by Mehta (1967), is given in appendix B.) Also drawn in each figure is the calculation assuming $f^+ = 1$; for single sequences this is the Wigner distribution. Note that the mean of each theoretical distribution is one for this method.

In the second method, the histogram is constructed using x = spacing/ corrected average spacing. The theoretical calculation taking into account the missing levels now has a mean greater than one, i.e., the average spacing is greater than the inverse of the true level density. The uncorrected calculation (assuming $f^+ = 1$) is identical to the one in the first method, and has a mean of one.

For the s-wave sequence, 90% or more of the levels were observed, and therefore adding higher order distributions to the k=0 distribution does little to improve the fit to the data. (In fact, it appears to make the fit poorer). Figure 6.6 presents a comparison of the s-wave level spacing distribution and the theoretical nearest neighbor distribution (essentially the Wigner distribution). The energy dependence of the level density is shown in figure 6.6a, where the straight line is a least squares fit to the log of the density. The slope of the line gives the nuclear temperature, T = 2.2±0.7 MeV. Figures 6.6b and 6.6c compare the experimental results with the theory before and after, respectively, unfolding the temperature. (The procedure by which this 'unfolding' is done is discussed in section 6.9.) In both cases the agreement is good, and the effects of unfolding the temperature are not significant.

The spacing distribution for the p-wave and d-wave distributions suffer to some extent from the problems of spin misassignments. Contamination by a second sequence is easily mistaken for the effects of missing levels--both produce spacings which are too small compared with the average experimental spacing. For this reason, the analysis of the single sequence distributions was performed using only those resonances for which the spin assignment was fairly certain. It is then only necessary to consider the effects of missing levels. For the analysis of two sequences (all p-wave levels or all d-wave levels) it is not

Figure 6.6 (a) Average spacing for $1/2^+$ levels as a function of energy. The straight line is a least squares fit whose slope gives the nuclear temperature, $T = 2.2 \pm 0.7$ MeV.

(b) Spacing distribution for the uncorrected s-wave level sequence. The solid curve is the Wigner distribution. The average spacing (1 unit of x) is 16 keV.

(c) Spacing distribution for the $1/2^+$ resonances in which the energy dependence of the level density has been unfolded from the data. See text for discussion.

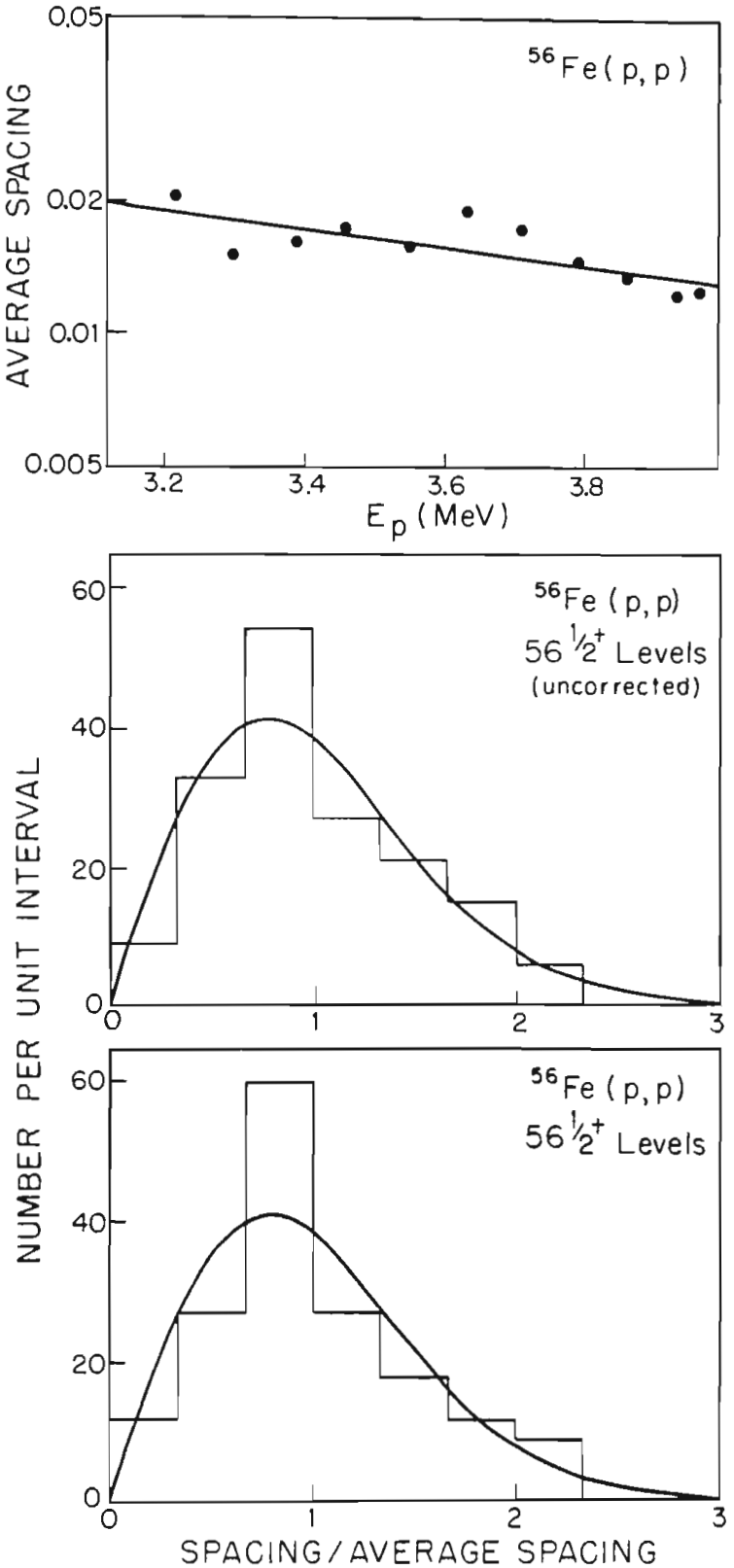
0.05
0.02
0.01
0.005
AVERAGE SPACING
^{56}Fe (p, p)
3.2
3.4
3.6
3.8
E_p (MeV)
60
40
20
0
^{56}Fe (p, p)
56 1/2$^+$ Levels
(uncorrected)
0
1
2
3
NUMBER PER UNIT INTERVAL
^{56}Fe (p, p)
56 1/2$^+$ Levels
SPACING / AVERAGE SPACING

necessary to be concerned about spin assignments, so all levels were used.

Figures 6.7a and b show the $1/2^-$ spacing distribution for 15 resonances from 3.83 to 4.00 MeV (the region around the $1/2^-$ analogue state). The solid curves were calculated assuming that 10% of the levels were missed and the dashed curves (as discussed above) are Wigner distributions. Few levels seem to have been missed, although the statistics (14 spacings) are poor.

The $3/2^-$ spacing distribution for 18 levels from 3.78 to 4.00 MeV is shown in figures 6.8a and b. (Again, the region is centered about an analogue state.) The upper figure was calculated using the experimental average spacing of 12.3 keV (method 1). In the lower figure, a corrected average spacing of 10.0 keV was used (i.e., $f^+ = 0.8$). Each of the solid curves assumes a density of one per 6.1 keV and 40% missing levels. The Wigner distribution is shown as a dashed curve.

The spacing distribution for the superimposed p-wave sequences is shown in figure 6.9. The energy interval (3.78 to 4.00 MeV) was chosen to overlap both the $1/2^-$ and the $3/2^-$ analogue states. The distribution of the 40 spacings is consistent with having missed only 10% of the p-wave resonances. Therefore, the total p-wave level density is on the order of 200/MeV, which is consistent with the Gilbert and Cameron predictions.

Figure 6.7 (a) Spacing distribution for 15 $1/2^-$ resonances from 3.83 to 4.00 MeV. The average experimental spacing is 11.8 keV. The dashed curve is the Wigner distribution, and the solid curve is calculated assuming 10% of the levels were missed.

(b) Spacing distribution for the levels in (a) assuming an average spacing of 10.8 keV.

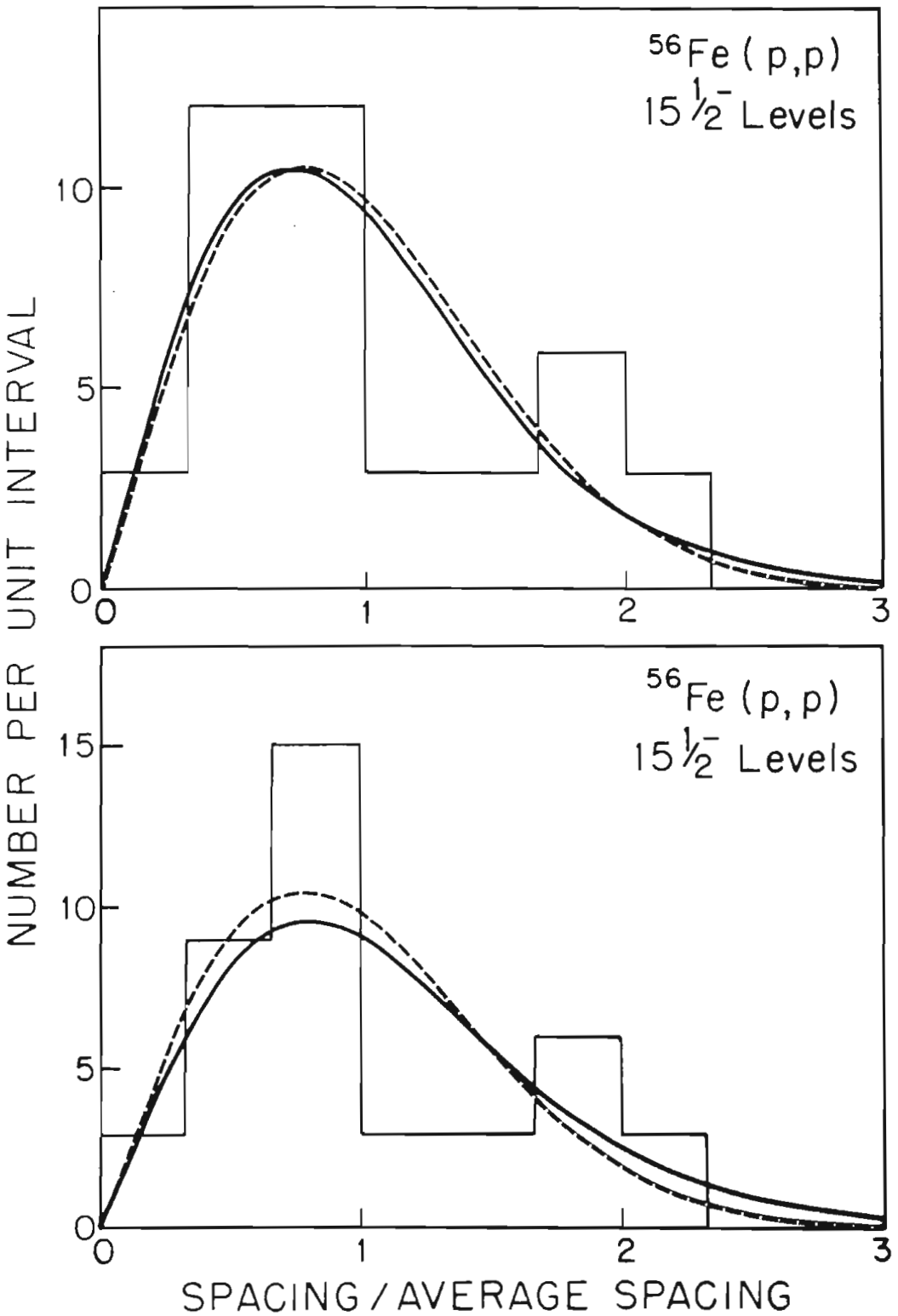
^{56}Fe (p,p)
15 ½⁻ Levels
^{56}Fe (p, p)
15 ½⁻ Levels
NUMBER PER UNIT INTERVAL
SPACING / AVERAGE SPACING
0
5
10
15
1
2
3

Figure 6.8 (a) Spacing distribution for 18 $3/2^-$ levels from 3.78 to 4.00 MeV. The average experimental spacing is 12.3 keV. The solid curve is calculated assuming 20% of the levels were missed; the dashed curve is the Wigner distribution.

(b) Spacing distribution for the levels in (a) using a corrected average spacing of 10 keV.

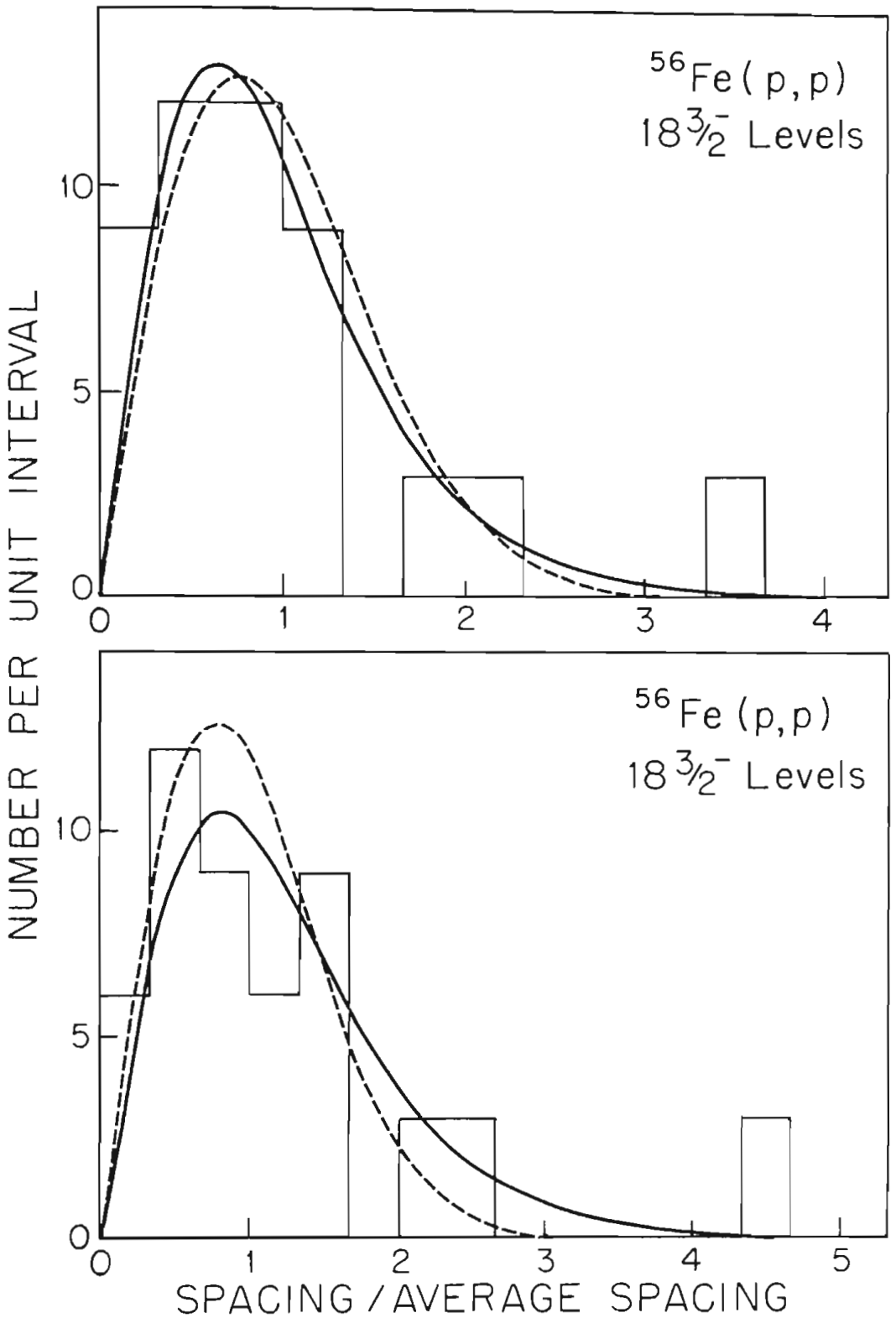
^{56}Fe (p, p)
18 3/2$^-$ Levels
^{56}Fe (p,p)
18 3/2$^-$ Levels
NUMBER PER UNIT INTERVAL
SPACING / AVERAGE SPACING
0
5
10
0
1
2
3
4
5

Figure 6.9 (a) Spacing distribution for 41 p-wave resonances from 3.78 to 4.00 MeV. The average experimental spacing is 5.4 keV. The dashed curve is a superposition of two sequences whose densities are 0.38 and 0.62 times the total experimental density. The solid curve is a superposition of two sequences in which 5% of the $1/2^-$ and 10% of the $3/2^-$ sequences were missed.

(b) Spacing distribution for the levels in (a) using a corrected average spacing of 5 keV.

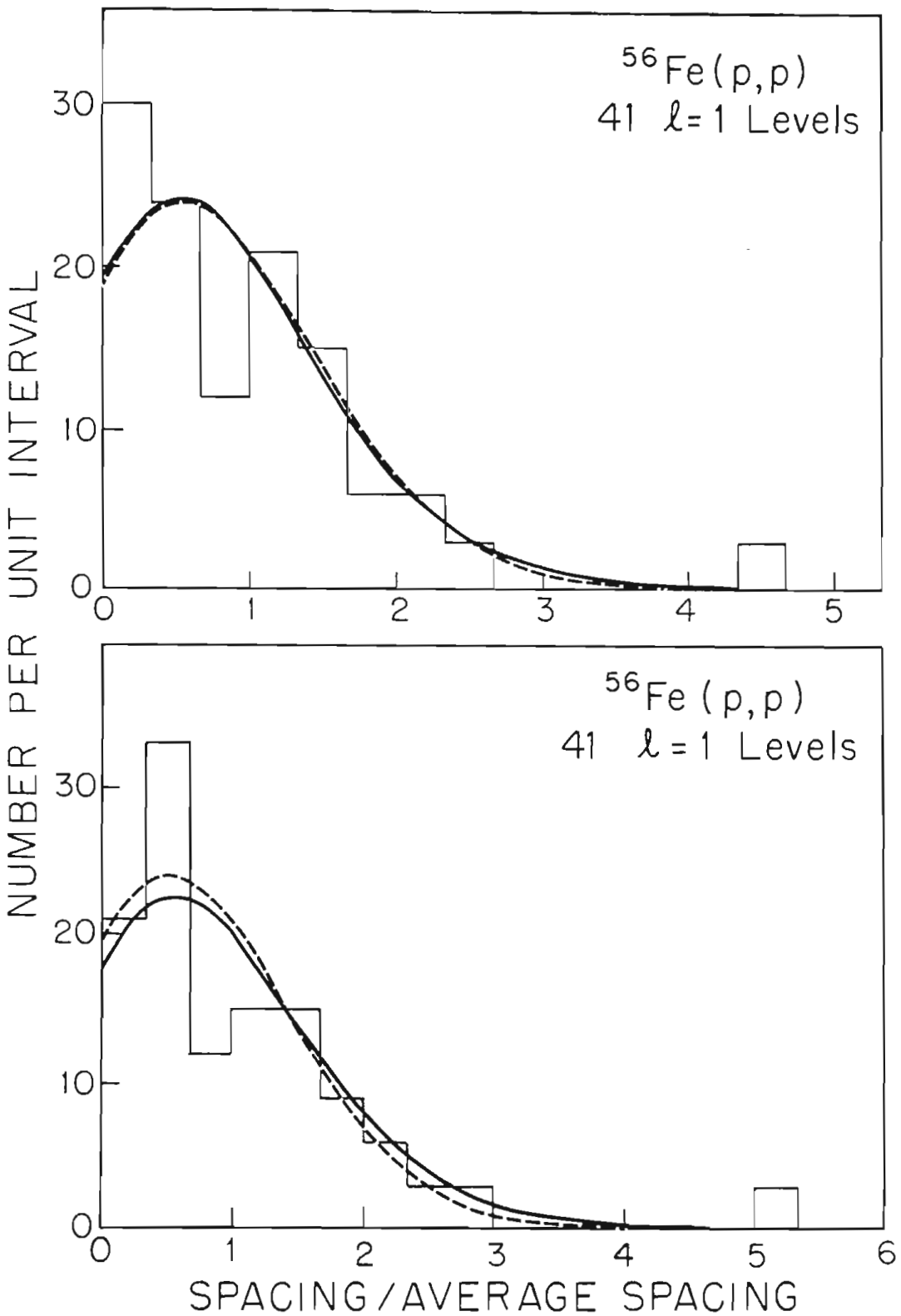
^{56}Fe(p,p)
41 ℓ=1 Levels
^{56}Fe(p,p)
41 ℓ=1 Levels
NUMBER PER UNIT INTERVAL
SPACING/AVERAGE SPACING
0
10
20
30
0
1
2
3
4
5
6

The $3/2^+$ sequence has many missing levels simply because it was difficult to assign a spin of 3/2 to an $\ell=2$ resonance. (This problem is discussed in section 2 of chapter 4.) The spacing distribution for the 35 levels for which a spin assignment of 3/2 was made is shown in figure 6.10. The estimate of 60% missing levels is consistent with the result of 50% obtained in the analysis of the width distribution. (The sensitivity of either method is +10%.)

For the $5/2^+$ sequence, a higher percentage of the levels was observed (in the sense of having a preferred spin assignment). The spacing distribution for these 90 resonances is shown in figure 6.11a. The solid curve was calculated assuming 25% of the levels were missed, a number consistent with the level density estimates from the reduced width analysis.

An even higher percentage of the $5/2^+$ levels was observed in the neighborhood of the $5/2^+$ analogue state at 3.76 MeV. The spacing distribution for 17 resonances from 3.70 to 3.82 MeV is shown in figure 6.11b. For this distribution, no improvement was obtained by assuming missing levels, so only one curve is shown--the Wigner distribution. The observed level density in this interval (140/MeV) is slightly larger than the Gilbert and Cameron prediction (125/MeV).

The analysis of the superimposed d-wave sequences includes 53 d-wave resonances not considered for the separate sequences. These extra levels account for most of

Figure 6.10(a) Spacing distribution for 35 $3/2^+$ resonances from 3.1 to 4.0 MeV. The average experimental spacing is 24.7 keV. The dashed curve is the Wigner distribution and the solid curve was calculated assuming 60% of the levels were missed.

(b) Spacing distribution for the levels in (a) assuming a corrected average spacing of 10 keV.

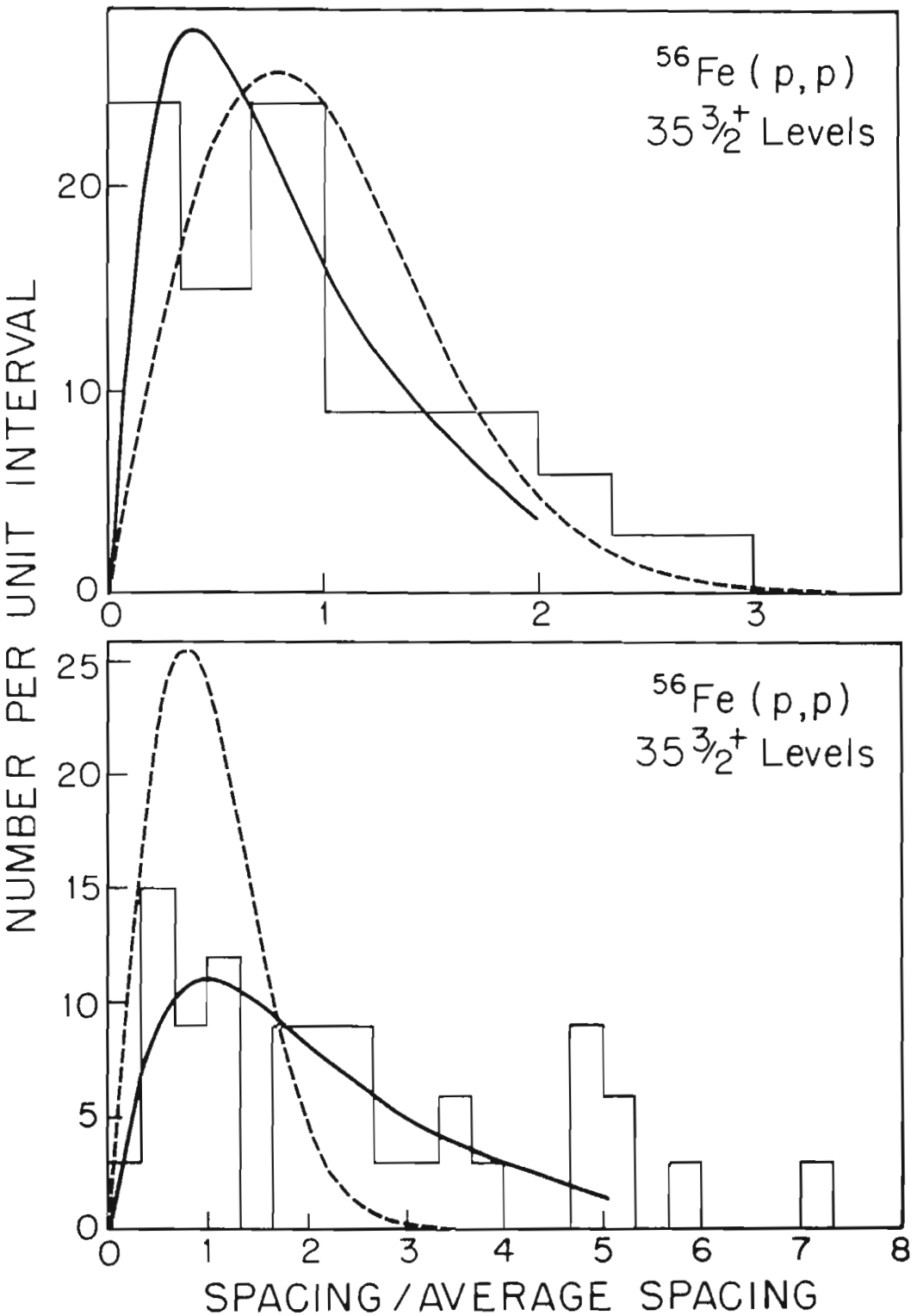
^{56}Fe (p, p)
35 3/2^{+} Levels
^{56}Fe (p, p)
35 3/2^{+} Levels
NUMBER PER UNIT INTERVAL
SPACING / AVERAGE SPACING
0
10
20
1
2
3
0
5
15
25
4
5
6
7
8

Figure 6.11(a) Spacing distribution for 90 $5/2^+$ resonances (with preferred spin assignments) in the energy range 3.1 to 4.0 MeV. The average experimental spacing is 9.9 keV. The solid curve was calculated assuming 25% of the levels were missed; the dashed curve is the Wigner distribution.

(b) Spacing distribution for 17 $5/2^+$ levels from 3.70 to 3.82 MeV. The average experimental spacing is 7.2 keV. The solid curve was calculated assuming no levels were missed.

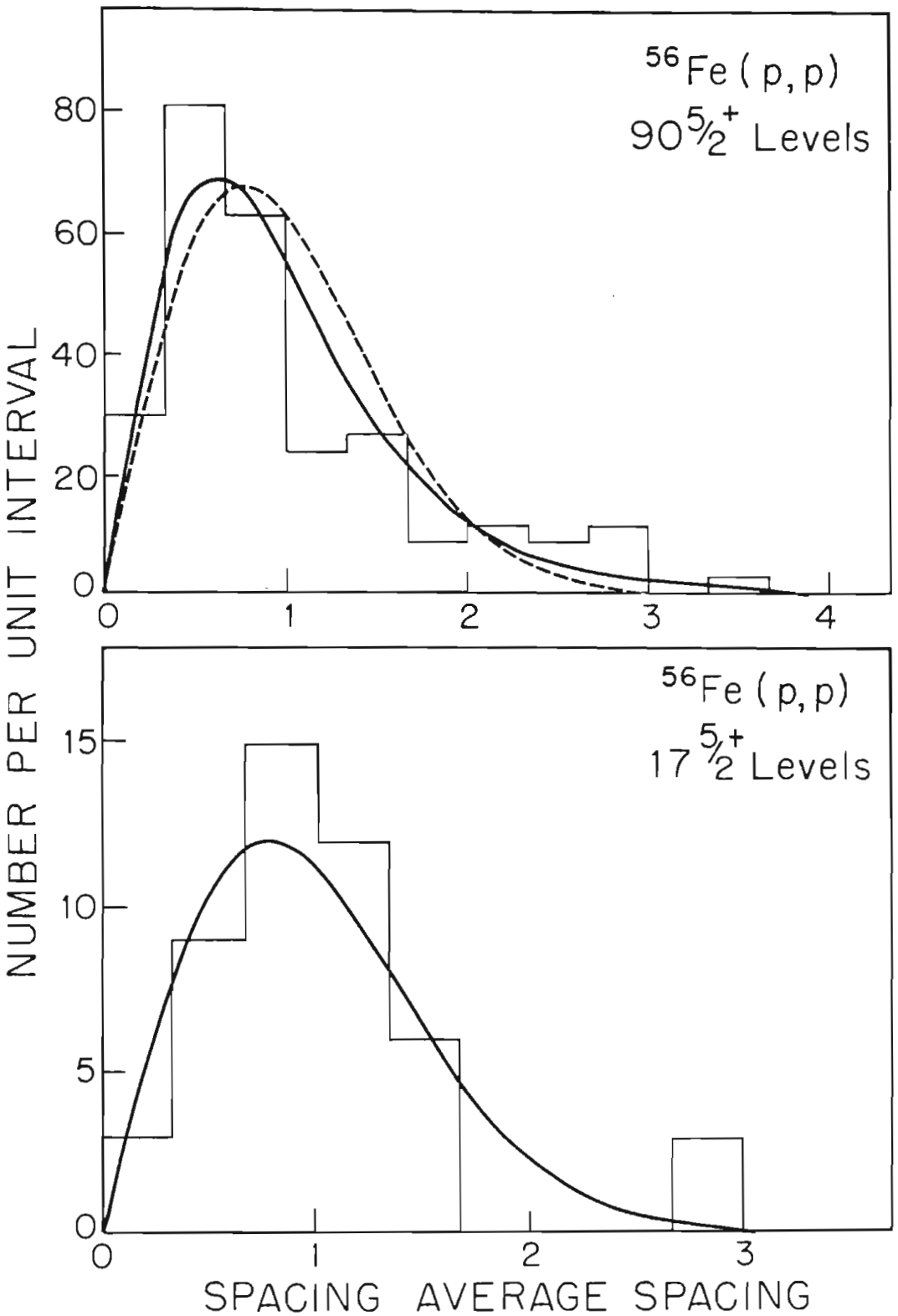
^{56}Fe (p, p)
90 5/2^{+} Levels
^{56}Fe (p, p)
17 5/2^{+} Levels
NUMBER PER UNIT INTERVAL
SPACING AVERAGE SPACING
0
20
40
60
80
0
1
2
3
4
0
5
10
15
0
1
2
3

the levels considered 'missed' in those analyses. They were missed only to the extent that spin assignments could not be made. Figures 6.12a and 6.12b show the spacing distribution for these 179 d-wave levels for methods 1 and 2, respectively. It is not possible to say with any confidence what fraction of each sequence was missed, although comparison of the total observed d-wave level density with Gilbert and Cameron indicates that approximately 15% of the combined sequence was missed. The solid curves in the figures assume (somewhat arbitrarily) that 20% of the $3/2^+$ and 10% of the $5/2^+$ levels were missed.

In conclusion it should be said that this type of analysis of spacing distributions, in which the effects of randomly missing levels are included to a fair approximation, is a useful check of the reduced width analysis presented in the previous section. Also, in regions (e.g., near analogue states) where the widths may not follow a Porter-Thomas distribution, the analysis of the spacings may provide information not obtainable by any other means.

The present work shows good agreement with the orthogonal ensemble, primarily in the sense that analyses of the width and spacing distributions give results which are consistent with each other and consistent with global calculations, such as those of Gilbert and Cameron. Although the data is quite good, problems with spin assignments prevent making strong statements in support of

Figure 6.12(a) Spacing distribution for 179 d-wave resonances from 3.1 to 4.0 MeV. The average experimental spacing is 5.0 keV. The solid curve was calculated assuming 80% of the $3/2^+$ and 90% of the $5/2^+$ levels were observed; the dashed curve is a superposition of two Wigner distributions.

(b) Spacing distribution for the levels in (a) using a corrected average spacing of 4.3 keV.

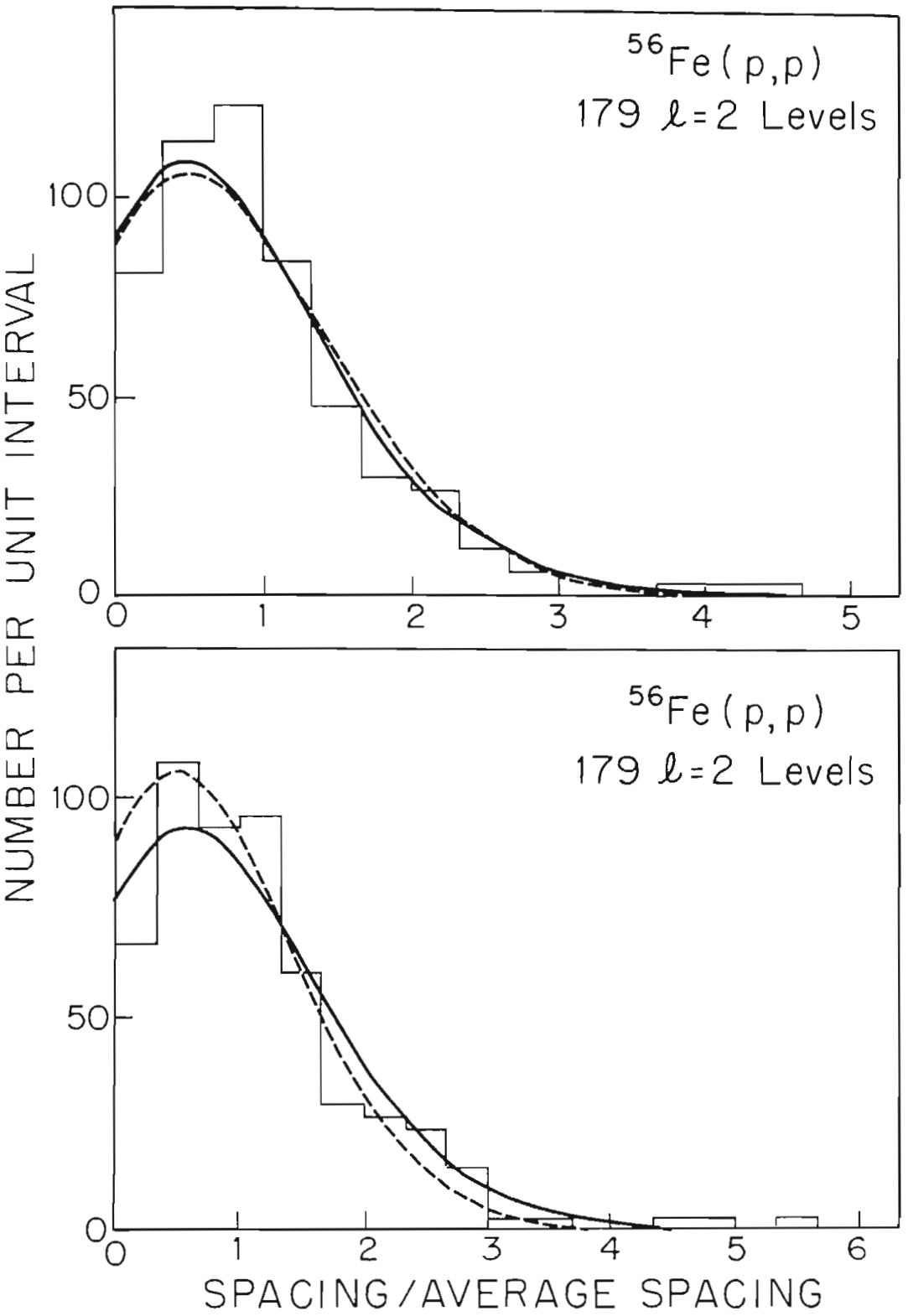
^{56}Fe(p,p)
179 ℓ=2 Levels
^{56}Fe(p,p)
179 ℓ=2 Levels
NUMBER PER UNIT INTERVAL
SPACING/AVERAGE SPACING
0
50
100
0
1
2
3
4
5
6

the orthogonal ensemble over an uncorrelated Wigner ensemble. Such comparisons are best dealt with using a pure sequence, such as the s-wave sequence which will be analyzed further in section 6.9.

6.7 Strength Functions

As discussed in section 6.3, the global parameters are not well described by the random matrix model, and are better understood in terms of more specific models. From the shell model, the strength functions are expected to exhibit giant resonance behavior in the neighborhood of a (dissolved) single particle state. The excitation energy at which any given state will occur is a function of the mass of the system. Therefore, the resonance may also be observed for fixed energy by varying the mass (or size) of the target--hence the term 'size' resonance.

The bulk of the data on strength functions comes from s-wave neutron resonances. In that data (see Lynn, 1968, for example) the 3s and 4s states (where 3 and 4 are the shell model principle quantum numbers and the s indicates ℓ=0 resonances) are observed as complex structures located (for low energy neutrons) at A = 55 and 150, respectively. The data show the effects of the coupling of the single particle state to collective modes of excitation.

Most of the data on proton strength functions comes from a series of high resolution proton elastic scattering experiments performed at TUNL, of which the present experiment is the most recent. In comparing the present results with this body of data, two problems must be considered: the channel radius used to fit the data, and the excitation energy at which the strength function is evaluated. The previous data were fit to an R-matrix cross section using a channel radius of the form

$$a_c = r_o \left(1 + A^{1/3} \right) \qquad (6.72)$$

where r_o = 1.25 fm. For A = 56 (target mass), a_c = 6.03 fm. The analysis of strength functions in terms of a shell model potential is usually performed with a potential radius of the form

$$r = r_o A^{1/3} \qquad (6.73)$$

where r_o is approximately 1.35 fm. For A = 57 (system mass in this case), r = 5.20 fm. This smaller radius is in better agreement with other determinations of the nuclear size. The present data was analyzed with a radius intermediate between these two values, a_c = 5.65 fm (or, r_o = 1.17 in equation (6.72)). This radius is approximately the distance at which the nuclear density falls to 1/10 its maximum value.

While the laboratory widths are nearly independent of the channel radius, the reduced widths (and therefore the strength functions) are strongly dependent (through the penetrabilities) on the choice of this parameter. Table 6.1

Table 6.1 $^{56}Fe(p,p)$ Strength Functions

Configuration	r_o = 1.17 fm	r_o = 1.25 fm
$s_{1/2}$	$0.095 \begin{smallmatrix} +0.012 \\ -0.025 \end{smallmatrix}$	$0.075 \begin{smallmatrix} +0.01 \\ -0.02 \end{smallmatrix}$
$p_{1/2}$	0.02 ± 0.01	0.015 ± 0.008
$p_{3/2}$	0.012 ± 0.004	0.009 ± 0.003
$d_{3/2}$	0.06 ± 0.015	0.04 ± 0.01
$d_{5/2}$	0.08 ± 0.02	0.055 ± 0.015

gives the strength functions for the current work for two values of the channel radius: r_o = 1.25 fm (to aid in comparing with previous work), and r_o = 1.17 fm (in better agreement with estimates of the nuclear size). The quoted values come from two sources: (1) the background strength function determined in fitting an analogue fine structure pattern (see chapter 5), and (2) the sum of the reduced widths minus the analogue reduced width (if necessary) divided by the interval of observation:

$$s = \sum_i (\gamma_i^2 - \gamma_A^2)/\Delta E \qquad (6.74)$$

The correction for missing small widths (never more than 2%) was insignificant compared with the 20%-50% fluctuations in the strength observed as a function of energy (these fluctuations were caused primarily by the analogue states). The large error for the s-wave strength function indicates the difference between the first 500 keV and the second 500 kev--the latter contains a region of anomalously large widths not identified with an analogue state.

In addition to considering the effects of channel radius, it is necessary to also consider the effects of excitation energy. The present experiment was performed from E_p = 3.1 to 4.0 MeV, on the order of 1 MeV higher than the bulk of the previous proton data. A rough estimate of the relationship between mass and energy can be made by noting the following: (1) the energy of the 3s single particle state (the state of primary interest here) is

$$E(3s) = 3\hbar\omega \qquad (6.75)$$

(2) the A dependence of the oscillator frequency is given by

$$\hbar\omega = 41\ A^{-1/3}\ \text{MeV} \tag{6.76}$$

Therefore,

$$\frac{\partial E}{\partial A} \approx 123(-\tfrac{1}{3} A^{-4/3})\ \text{MeV} \tag{6.77}$$

$$\approx -0.2\ \text{MeV}$$

Under this approximation, increasing the mass by 5 is equivalent to increasing the energy by 1 MeV. The 'width' of the size resonance is on the order of 20 mass units, so this correction is not negligible, although it is a much smaller problem than the experimental errors.

For completeness, the previous s-wave data is presented in figure 6.13. The present measurement, again ignoring the problem of excitation energy, is the larger of the two measurements for mass 56. The other determination for this mass comes from an experiment 1 MeV lower in energy (Lindstrom, 1970).

The two p-wave strength functions given in the table are low, which is expected since mass 56 is somewhere between the 2p and 3p size resonances. That the $3/2^-$ strength function is significantly smaller is probably due to the spin-orbit splitting of the 2p size resonance. This splitting has been observed more clearly at lower masses.

There is also a significant difference between the two d-wave strength functions. This is probably caused by the spin-orbit splitting of the 2d size resonance. If so, the 2d state must lie at a higher mass than 56, although perhaps not too much higher since the observed values of the strength functions are not small.

Figure 6.13 S-wave strength functions for masses from A = 25 to A = 70. The present measurement is the larger of the two points for mass 56.

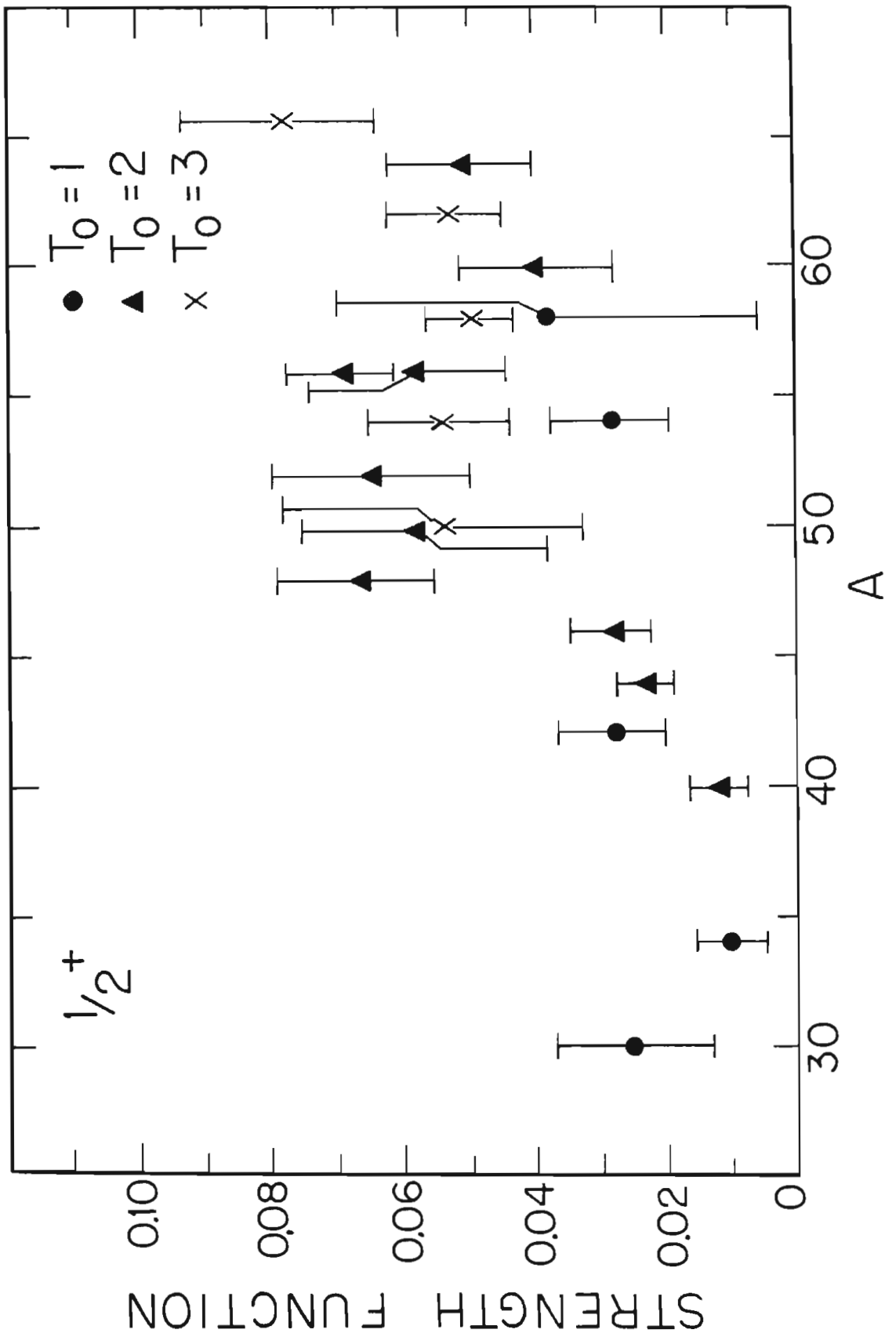
STRENGTH FUNCTION
0.10
0.08
0.06
0.04
0.02
0
30
40
50
60
A
$1/2^+$
$T_0 = 1$
$T_0 = 2$
$T_0 = 3$

6.8 Level Densities

Bethe (1936,1937) derived an expression for the level density as a function of energy and spin, based on a Fermi gas model of the nucleus:

$$\rho(E,J) \propto (2J+1)(E-\Delta)^{-5/4} e^{-J(J+1)/2\sigma^2} \; e^{2a\sqrt{E-\Delta}} \qquad (6.78)$$

where the "temperature" of the gas is $T = \sqrt{E}/a$. Gilbert and Cameron (1965) modified this form slightly to obtain a better fit to low energy data:

$$\rho(E,J) \propto (2J+1)\exp[-J(J+1)/2\sigma^2] \; \exp[E/T] \qquad (6.79)$$

where now T is a constant (independent of the energy). This form for the level density is the same as that used in statistical mechanics to calculate evaporation properties, and can be derived by thermodynamics techniques (Lynn, 1968).

Because the experimental energies in this work only span 1 MeV, it is not expected that reliable parameters for the energy dependence could be extracted for the level density. This is agravated by the occurance of analogue states at the higher energies, which make more levels visible and therefore make the level density appear to increase more rapidly than is actually the case. The only exception to this is the $1/2^+$ sequence, for which the observed temperature is 2.4 ± 0.8 MeV. This is more than one error bar higher than the Gilbert and Cameron value (1.3 MeV) and may indicate missing levels for the higher energies, although such a conclusion is not consistent with other analysis of the s-wave resonances (presented below).

Of perhaps more interest than the energy dependence is the J dependence of the level density. As discussed above, a large fraction of the levels for each sequence may not be observed because the widths are too small. However, by assuming that the widths follow a Porter-Thomas distribution, it is possible to estimate the number of small widths missed, leaving an overall fractional error in the level densities of 20% or less. For some of the sequences, a better estimate of the level density can be obtained in the neighborhood of an analogue state, where most of the levels are observed and the error in the average spacing is therefore smaller.

Figure 6.14 compares the J-dependence of the level density with the Gilbert and Cameron values for E_p = 3.8 MeV. Level densities measured at other energies (or measured over regions centered at other energies) were corrected by assuming a temperature of 2 MeV. (This is a compromise between the observed temperature of 2.4 MeV for the s-wave sequence and the Gilbert and Cameron value of 1.3 MeV.)

The $1/2^+$ level density is taken from the 56 observed levels, corrected 10% for missing levels, and extrapolated from 3.5 MeV (the center of the region of observation) to 3.8 MeV (a 10% increase). The $1/2^-$ result comes from 12 spacings observed in the vicinity of the analogue state at E_p = 3.95 MeV. The level density for J = 1/2 is parity independent, to within experimental errors.

Figure 6.14 Spin Dependence of the Level Density. The solid curve shows the Gilbert and Cameron predictions.

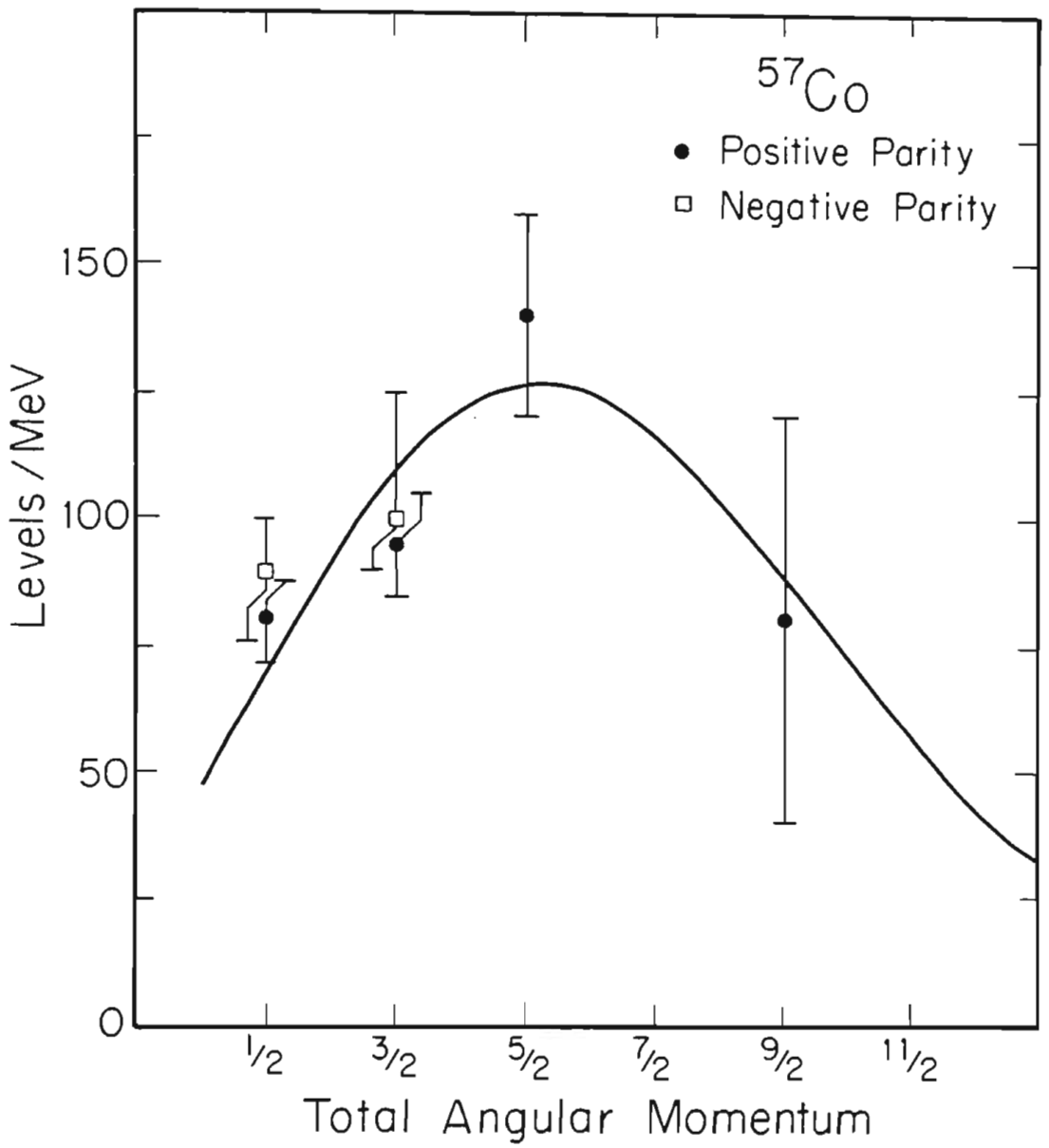
^{57}Co
Positive Parity
Negative Parity
Levels / MeV
150
100
50
0
1/2
3/2
5/2
7/2
9/2
11/2
Total Angular Momentum

The $3/2^-$ level density is an average of the density observed away from the analogue state (corrected for missing levels and extrapolated to 3.8 MeV), and the density observed near the analogue state. There was no $3/2^+$ analogue state, so the $3/2^+$ level density is obtained by correcting the observed density by 50% for missing levels. Again, the results for $J = 3/2$ are independent of the parity.

Although a $5/2^-$ analogue state was observed, the fragments were not strong enough to indicate that none were missed. Thus, for $J = 5/2$, only the results for the positive parity are given. Again, an average was taken between the observed density near the analogue and away from the analogue, corrected for missing levels.

Finally, the $9/2^+$ data demonstrates the effects of the "spin cutoff" of the level density. The value for this spin comes from the observed spacing of five analogue fragments, and the error bar reflects the uncertainty of such poor statistics. The overall trend of the J dependence of the level density is well reproduced by the semi-empirical curve.

6.9 Statistical Tests of the $1/2^+$ Level Sequence

6.9.1 The Δ_3 Statistic

The elastic width distribution of the s-wave resonances indicates that on the order of 90% of the levels were

observed. This is only an estimate because the presence of a possible doorway (or some special state) near E_p = 3.8 MeV could be distorting the distribution away from a Porter-Thomas shape (with which it was compared). The evidence at least indicates a relatively complete sequence which should be further investigated.

Before making any comparison of the data with ensemble predictions, it was necessary to 'unfold' the energy dependence of the level density. This was done in two ways, the first of which was straightforward: the density (averaged over ten adjacent spacings) was fit to the constant temperature form

$$\rho(E) = \rho_0 \exp(E/T) \tag{6.80}$$

giving the result T = 2.2 ± 0.7 MeV. A new set of energy levels was then generated:

$$E' = E_{min} + (E_{max} - E_{min}) \left\{ \frac{e^{(E-E_{min})/T} - 1}{e^{(E_{max}-E_{min})/T} - 1} \right\} \tag{6.81}$$

Note that the endpoints E_{min} and E_{max} are not changed in this transformation so that the new level density assumes a constant value equal to its old energy averaged value.

The second method of unfolding the energy dependence of the level density makes use of the extreme rigidity of a pure sequence. It was shown above that for the COE the number of levels up to a certain energy vs. energy is a straight line whose parameters are determined by minimizing Δ_3. Then the 'best' temperature, i.e., the temperature which removes the energy dependence of the level density, is that which also minimizes Δ_3:

$$\Delta_3 = \min_{A,B,T} \frac{1}{2L} \int_{-L}^{L} [N(E) - AE - B]^2 \, dE \tag{6.82}$$

This gives the result T = 2.6 ± 0.8 MeV, consistent with the first method. The number of $1/2^+$ levels up to an energy E vs. energy is shown in figure 6.15a. Figure 6.15b shows the corrected sequence (given by the transformation (6.81)) superimposed on the 'best straight line' which minimizes Δ_3. The value obtained for Δ_3, 0.421, is in good agreement with the theoretical value for 56 levels, 0.401 ± 0.11. In fact, the experimental value of Δ_3 is less than 0.51 (one standard deviation above the mean) for values of the nuclear temperature from 1.9 to 4.5 MeV. So the agreement with theory is not overly sensitive to the process of unfolding the change in the level density.

6.9.2 The F Statistic

The next statistical test applied to the $1/2^+$ set was the Dyson F statistic. It was necessary to use a rather small value (10) for n, where E + nD is the averaging interval over which F is calculated. (To get a signal to noise ratio of two, in which the signal is a spurious level and the noise is the natural scatter, the value of n must be 8 or larger.) Thus the first and last ten (approximately) resonances could not be tested with this statistic. A larger value of n would have made the test more sensitive, but would have excluded too many resonances. The G statistic (the re-normalized F statistic) is shown as a function of energy in figure 6.16a, and a histogram of the values assumed by the statistic are shown in figure 6.16b. The solid curve in the latter figure is the theoretical

Figure 6.15(a) Cumulative number of $1/2^+$ levels vs. energy (uncorrected data)

(b) Straight line fit to the corrected $1/2^+$ level sequence

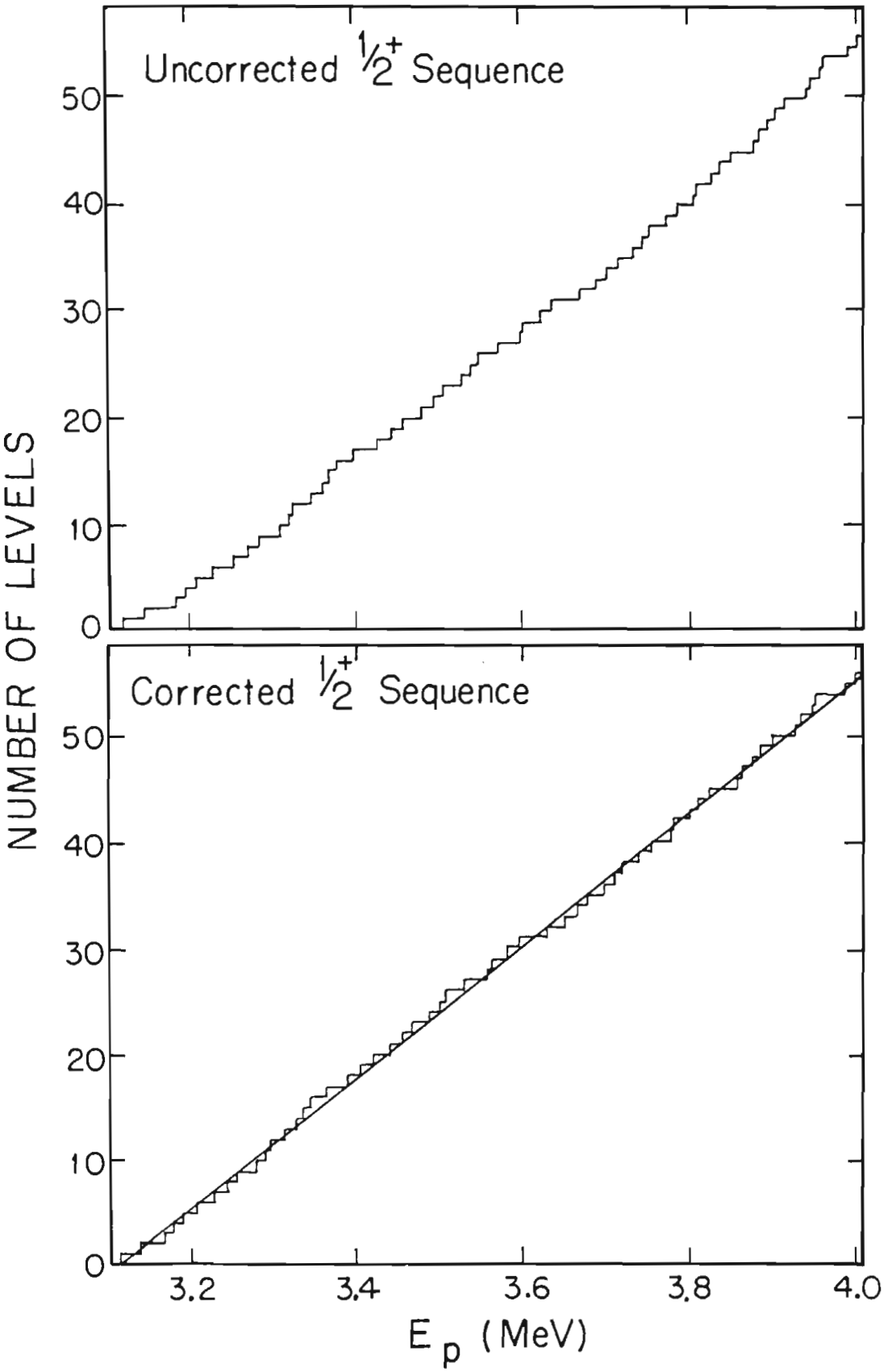
Uncorrected $\frac{1}{2}^+$ Sequence
Corrected $\frac{1}{2}^+$ Sequence
NUMBER OF LEVELS
0
10
20
30
40
50
3.2
3.4
3.6
3.8
4.0
E_p (MeV)

Figure 6.16(a) The G statistic as a function of energy for the $1/2^+$ level sequence. The statistic was calculated using an averaging interval given by n=10.

(b) The distribution of observed values of the G statistic. The smooth curve is the normal distribution, normalized to the number of levels tested.

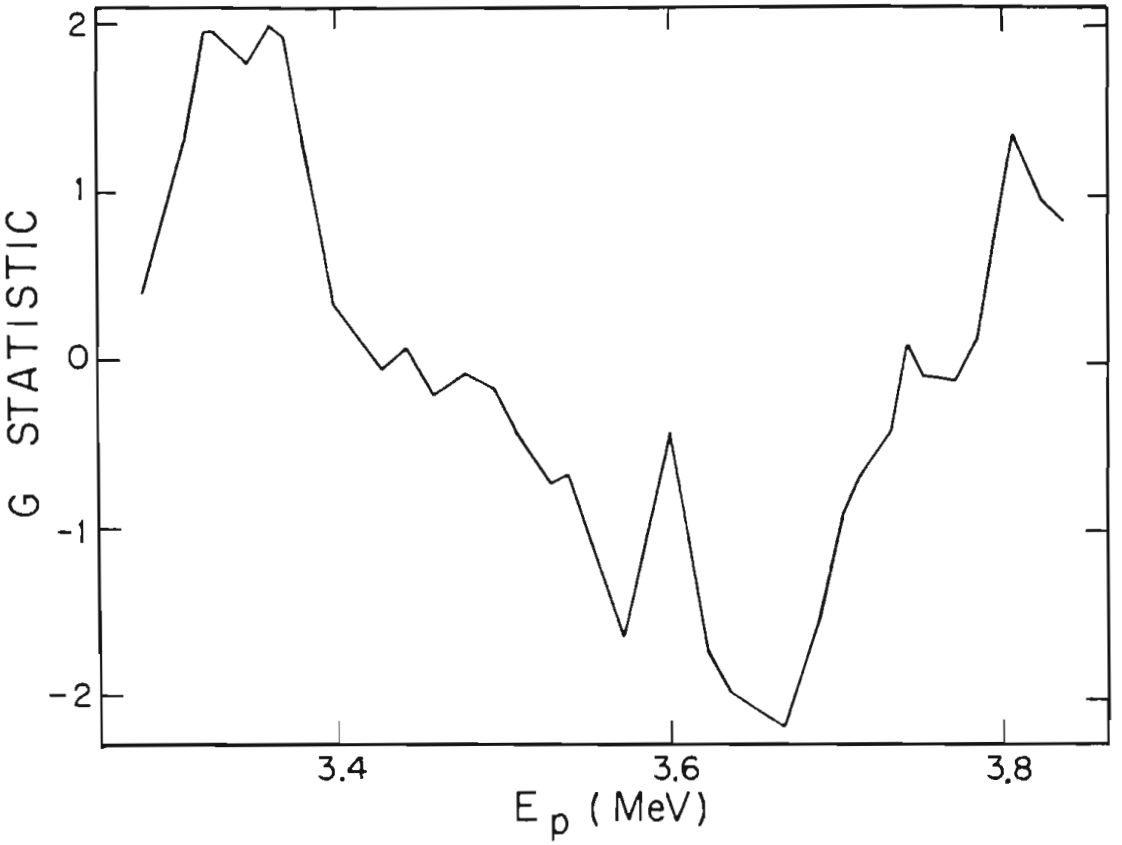
G STATISTIC
2
1
0
-1
-2
3.4
3.6
3.8
E p (MeV)

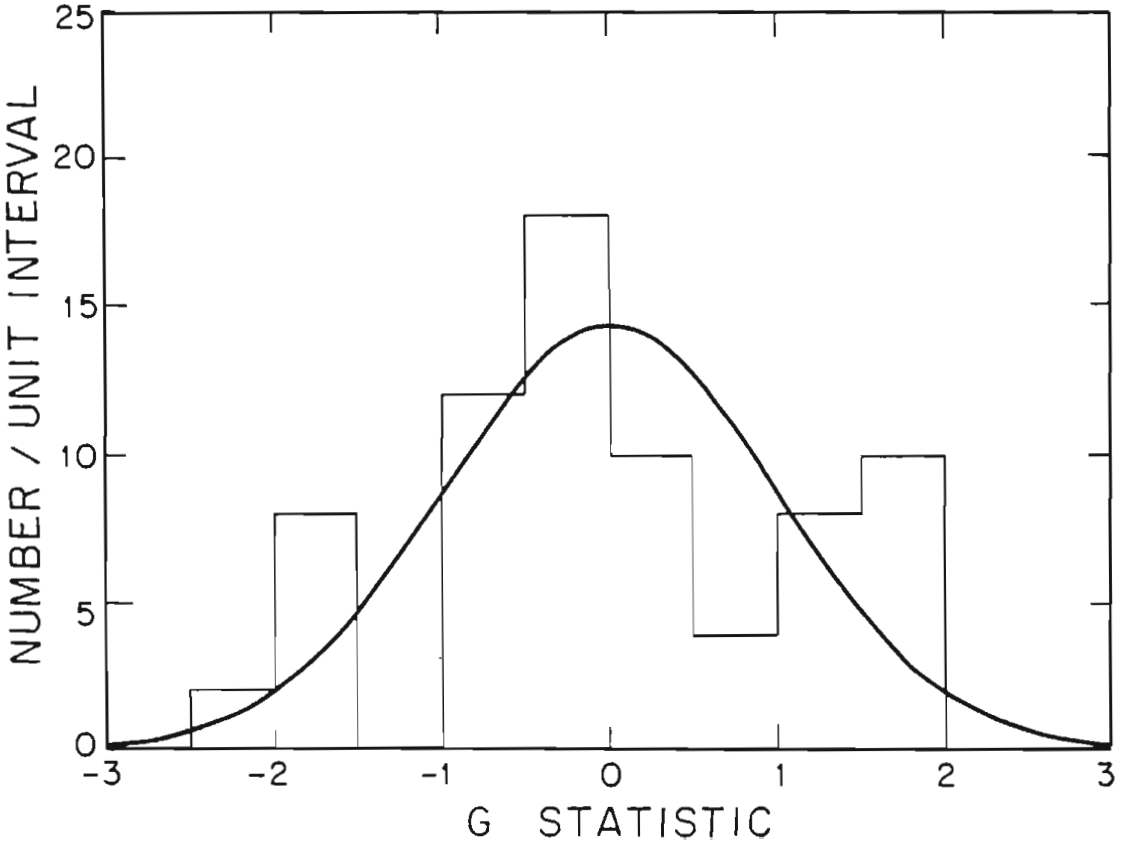
NUMBER / UNIT INTERVAL
25
20
15
10
5
0
-3
-2
-1
0
1
2
3
G STATISTIC

distribution for the G statistic, a normal distribution with zero mean and unit variance normalized to the number (36) of levels tested. Qualitatively, the agreement of theory and experiment is excellent considering the small sample size. Quantitatively, the mean of the experimental F statistic is within 1/2% of the theoretical mean for n = 8, 10, and 12. This small error is well within the statistical uncertainty for 30-40 levels. The experimental standard deviations (square root of the variance) of the G statistic for n = 8, 10, and 12 are 1.10, 1.16, and 1.18, respectively. These values fall just within one standard deviation of the statistical distribution of standard deviations expected for 30-40 levels. So, for the two statistics which were designated primarily as tests of the data, the agreement between theory and experiment is quite good and is consistent with having no or few missing or spurious levels.

6.9.3 Correlation Coefficients

The adjacent spacing correlation coefficient, ρ_o, for the 55 spacings in the s-wave level sequence is -0.23, in good agreement with the orthogonal prediction of -0.27. There is no simple way to estimate the statistical uncertainty associated with a measurement of the correlation for the given sample size, but Wilson et al. (1975) show that the width of the statistical distribution is about 0.1, so the agreement is indeed satisfactory. Previous measurements for ρ_o for neutron resonances yield values from -0.14 to -0.37 (Mello, 1978).

In addition to looking at spacing correlations, it is also of some theoretical interest to examine the correlation between the reduced width of a level and its spacing from the next (or previous) level. Because the joint probability density separates into terms which depend upon the eigenvalues and terms which do not, these two variables (eigenvalues and eigenvectors or spacings and widths) are independent. Therefore the correlation between the two should be zero (± statistical fluctuations). Note that it is necessary to have a relatively pure sequence to test this property--reliable measurements of the spacings are needed. The correlation was measured between the elastic reduced width of a level and the spacing between it and the next (previous) level; the value obtained was 0.14 (0.01). There is a 20% chance of obtaining a value greater than 0.14 for a sample of 55 drawn from an uncorrelated distribution function, so these correlations are not significant, and once again agreement with the GOE is observed.

6.9.4 k-th Order Spacing Distributions

Before presenting the results of measurements of the k-th order spacing distributions, it is necessary to comment upon how these measurements are made. For all except the k=0 distribution (with which the present discussion is not primarily concerned) the theoretical distributions are approximately normal with means μ_k and variances σ_k^2. To correctly estimate μ_k and σ_k, it is necessary to have a sample of independent measurements of the k-th order spacing. Then the best estimate of μ is the sample mean,

$$\bar{x} = \frac{1}{N} \sum x_i \tag{6.83}$$

and the best estimate of σ^2 is

$$S^2 = \frac{1}{N-1} \sum (x_i - \bar{x})^2 \tag{6.84}$$

The normalization factor of 1/(N-1) is necessary because $\bar{x}$ is not equal to μ, but rather is an estimate of μ. A discussion of this point can be found in any elementary statistics book. It is important that the measurements, x_i, be independent--if they are not S^2 will not be a good estimate of the theoretical variance. Unfortunately, previous analyses of higher order spacing distributions have not used samples in which all the measurements were uncorrelated. An example will demonstrate the problem.

Suppose we have a sequence of n+1 levels, or n spacings, and we wish to measure the variance of the k-th order distribution for k=n-1. If the i-th spacing is defined as

$$x_i = E_{i+k+1} - E_i \tag{6.85}$$

then the sample consists of two elements, x_1 and x_2. Let $z = E_n - E_2$; then $x_1 = z + (E_2 - E_1)$, $x_2 = z + (E_{n+1} - E_n)$. The average value of x is

$$\bar{x} = (x_1 + x_2)/2 = z + (s_1 + s_2)/2 \tag{6.86}$$

where

$$s_1 = E_2 - E_1 \qquad s_2 = E_{k+1} - E_n \tag{6.87}$$

and the variance of x is

$$\begin{aligned} V(x) &= \overline{x^2} - (\bar{x})^2 \qquad (6.88) \\ &= 1/2(z^2 + 2zs_1 + s_1^2 + z^2 + 2zs_2 + s_2^2) \\ &\quad - (z^2 + z(s_1 + s_2) + (s_1 + s_2)^2/4) \\ &= 1/2(s_1^2 + s_2^2) - \left(\frac{s_1 + s_2}{2}\right)^2 \end{aligned}$$

$$= \overline{s^2} + (\bar{s})^2$$

$$= V(s)$$

I.e., the variance of the set is completely determined by nearest neighbor spacings: the expectation value of the variance is the variance of the k=0 distribution. Obviously this is wrong, and the reason it is wrong is that x_1 and x_2 are not independent measurements of a k-th order spacing. For the measurements to be independent, it is necessary that they not overlap, equation (6.65).

To see that the difficulty arises even for small values of k, consider k=1: let $x_1 = E_3 - E_1$, $x_2 = E_5 - E_3$, and $x_3 = E_4 - E_2$. Obviously, x_3 is not independent of x_1 and x_2 because $x_3 \leq x_1 + x_2$. Therefore, in measuring k=1 distributions, only the odd (or only the even) eigenvalues will be used.

Because of the arbitrariness of the choice, odd or even (or similar choices for k>1), all sample sets of the largest possible size were constructed for each value of k. The mean and variance of each set were determined and then these were averaged. Thus if there are an even number of spacings, there are two sample sets (odd and even) for the k=1 distribution, and the final result would be an average over the two sets. This has the advantage of using as much of the data as possible, but avoids the pitfalls of non-random samples.

For high order spacings, the number of members in a sample will be small--for n+1 levels it is n/(k+1). It is important to ask what statistical fluctuations can be

expected for the sample mean and variance. From elementary statistics, the sample mean $\bar{s}$ has an expectation value of μ and a variance of σ^2/n. In other words, $s = \mu \pm \sigma/\sqrt{n}$. The expectation value of S^2 (equation (6.84)) is σ^2. For $k>0$, the spacings are approximately normally distributed and therefore

$$z_k = \frac{N-1}{\sigma_k^2} S^2(k) \qquad (6.89)$$

has a chi-squared distribution with N-1 degrees of freedom, where N is the size of the sample (=n/(k+1)). (For k=0 this result does not hold exactly, but is still a fair approximation.) For large N, the chi-squared distribution can be approximated by a normal distribution, with the result that S^2 has a mean of σ^2 and a variance of $\sigma^2/2(N-1)$. I.e.,

$$(\sigma_k^2)_{exp} = \sigma_K^2 \left(1 \pm \frac{1.3}{\sqrt{2N-2}}\right) \qquad (6.90)$$

where the factor of 1.3 corresponds to taking the 10% and 90% limits of the distribution. For smaller values of N (<10) the 10% and 90% limits can be obtained from tables of the chi-squared distribution.

The k-th order spacing distributions are plotted in figure 6.17 for k=0 to 5. The histograms are sums over the different sample sets which may be constructed from the data. The widths of the distributions are given in table 6.2 and are plotted in figure 6.18. The two solid curves are the theoretical predictions based on an uncorrelated Wigner distribution (upper curve) and the orthogonal ensemble (lower curve). The dashed lines are the 10% and

Figure 6.17 K-th order spacing distributions for 56 $1/2^+$ levels. The solid curves in the first three figures are predictions from the orthogonal ensemble. See text for discussion.

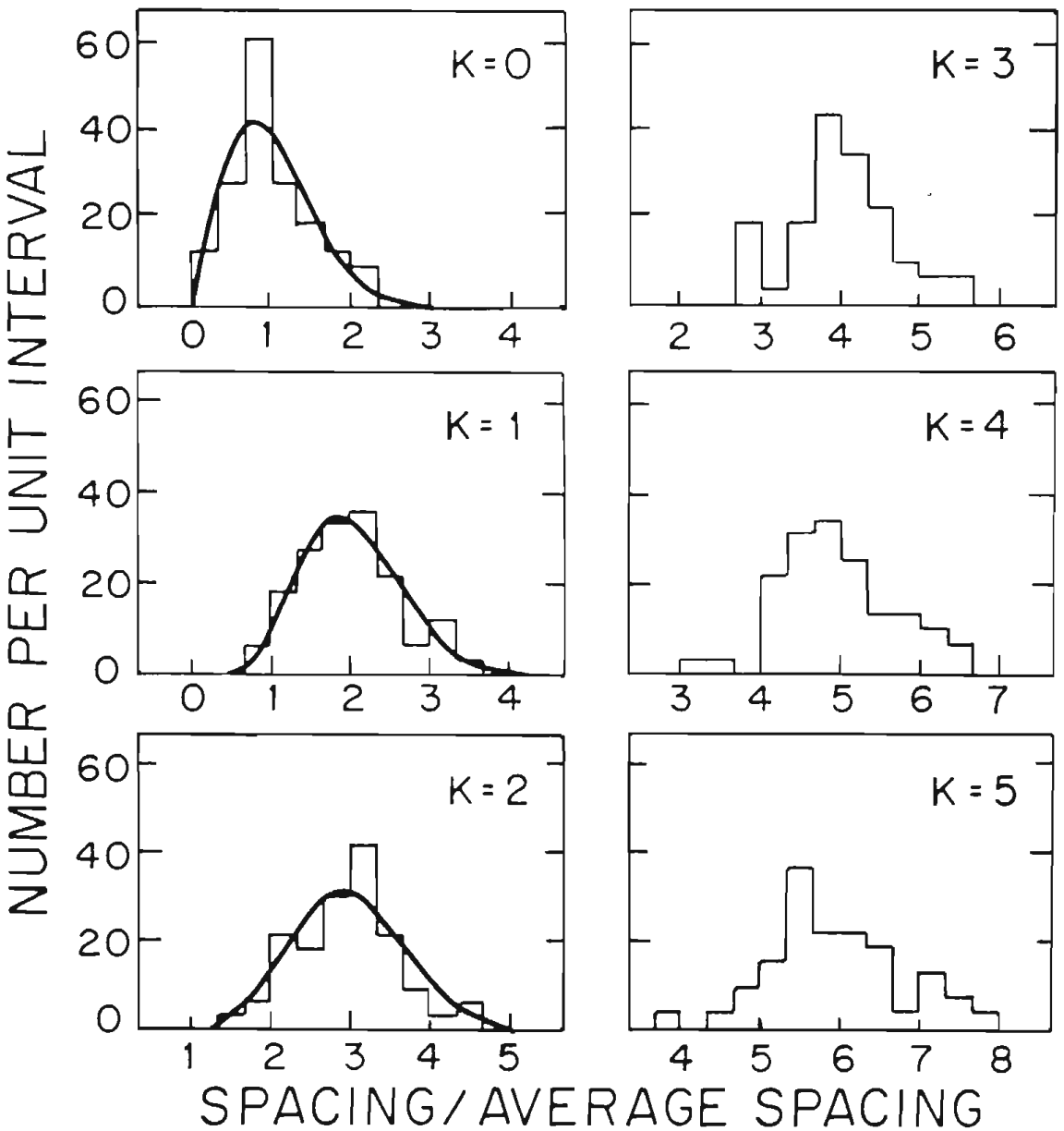
NUMBER PER UNIT INTERVAL
SPACING/AVERAGE SPACING
K=0
K=1
K=2
K=3
K=4
K=5
60
40
20
0
0 1 2 3 4
2 3 4 5 6
3 4 5 6 7
1 2 3 4 5
4 5 6 7 8

Table 6.2 Widths of the k-th Order Spacing Distributions

k	$(\sigma_k^2)_{exp}$ 56 $1/2^+$ Levels	σ_k^2 O.E. Predictions
0	0.50	0.53
1	0.58	0.65
2	0.74	0.71
3	0.74	0.75
4	0.92	0.78
5	1.09	0.80
6	1.15	0.82
7	0.95	0.83
8	0.90	0.85
9	0.97	0.86
10	0.94	0.87

Figure 6.18 Widths of the k-th order spacing distribution for 56 $1/2^+$ levels as a function of k. The two solid curves are the theoretical predictions based on an uncorrelated Wigner distribution (upper curve) and the orthogonal ensemble (lower curve). The dashed lines are the 10% and 90% limits of the statistical distribution for a sample of 56 levels.

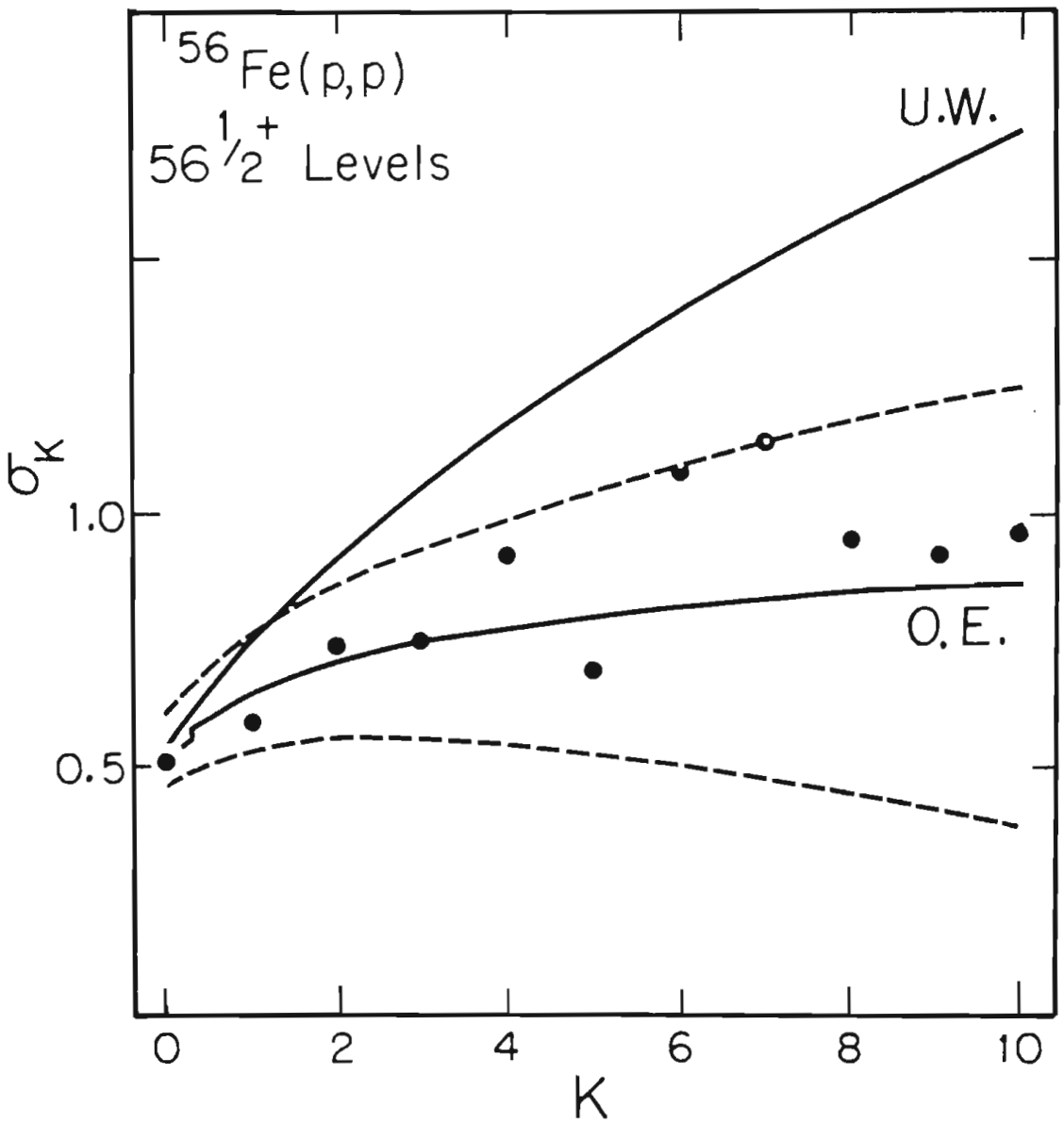
56 Fe(p,p)
56 1/2+ Levels
U.W.
O.E.
σK
1.0
0.5
0
2
4
6
8
10
K

90% limits of the statistical distribution for a sample of 56 levels. The agreement with the O.E. is quite good, and the data points are scattered above and below the O.E. in a manner consistent with the statistical analysis.

In summary, the local statistical properties of resonances have been shown to be well reproduced by the random matrix model. The present experiment is particularly important in that good agreement has been found for proton resonances, whereas almost all of the previous work involved neutron resonances. Conclusive proof of the theory, however, has not been provided to date because of the large samples needed to prove a statistical theory. A re-analysis of the previous data to extract the widths of the spacing distributions correctly for the larger neutron data sets would help to quantify the agreement between experiment and the random matrix model.

Chapter 7

CONCLUSIONS

Excitation functions for the $^{56}Fe(p,p)$ and $^{56}Fe(p,p')$ reactions were measured from E_p = 3.1 to 4.0 MeV at five scattering angles. Resonance parameters for over 340 levels in ^{57}Co were extracted from this data using an R-matrix formalism. Angular distributions of de-excitation γ-rays were measured for the stronger d-wave resonances to help resolve ambiguities in spin assignments. Favorable Coulomb penetrabilities allowed a high percentage of the levels with $\ell \leq 2$ to be observed in both the elastic and inelastic channels.

The analysis of the resonance parameters was divided into two topics: analogue states (or non-statistical phenomena) and statistical phenomena. The fine structure distributions of the five analogue states were fit to a Lorentz-weighted strength function. A derivation of this strength function combining the approaches of Lane and MacDonald was given in chapter 5. In general, the analogue state energies and proton widths are fairly well determined by the fitting procedure, but the spreading widths, asymmetries, and background strength functions are poorly

determined. Despite the improvements in mathematical technique of the Lorentz-weighted strength function over the previously used summed strength function, large uncertainties in fine structure parameters were still observed, especially for those cases classified as weak mixing. Even in the case of intermediate to strong mixing (for example, the $5/2^+$ state), background width fluctuations can produce a chi-squared minimum which is quite broad in the directions of the last three parameters ($\Gamma^{\downarrow}$, ϕ_c, and S_β). For this reason, it is expected that a re-analysis of the existing body of fine structure data using the Lorentz-weighted strength function will not yield significant differences from the previous analysis.

The statistical properties of the observed resonances were compared with the predictions of the random matrix model. When the effects of missing levels are taken into account, good agreement is found between observed spacing and width distributions and the orthogonal ensemble distributions. For the width distributions, the correction consisted of computing an average width which was smaller than the observed average by an amount which compensated for not observing small widths. For the spacing distributions, the correction consisted of folding in higher-order spacing distributions (which were also calculated under the orthogonal ensemble). With these factors taken into account, the comparison of data with theory is limited primarily by poor statistics. It should also be pointed

out, however, that these corrections also make the data a less sensitive test of theory (because there are adjustable parameters).

For one of the observed sequences, the s-wave sequence, almost all of the levels were seen. Therefore a number of statistical tests were performed on this set of data to test its quality (in terms of missing or spurious levels) and to test the agreement with orthogonal ensemble predictions. Two test were designated as tests of quality: the Dyson F statistic and the Dyson-Mehta Δ_3 statistic. The experimental values for these statistics were within theoretical error limits, indicating no or few missing or spurious levels. (The sample size was not large enough to permit stronger conclusions than this). Since very few high quality sequences of proton resonances exist, these 56 s-wave levels are an important addition to the larger neutron data sets which form the bulk of the support for the random matrix model.

Two other statistics were calculated from the data as tests of the theory--the adjacent spacing correlation coefficient and the k-th order spacing distribution widths. The observed correlation (-0.23) was within statistical errors of the theoretical value (-0.27). Likewise, the widths of the k-th order distributions for k=0 to 10 were all within statistical errors of the orthogonal ensemble predictions. A discussion of the method of extracting these widths from a set of experimental resonance parameters

indicated that previous analyses of k-th order distributions were biased toward small widths and small fluctuations. It now appears that very large data sets will be needed to measure with any statistical accuracy widths beyond k = 10. Because the spacing distribution widths form a significant part of the support for the orthogonal ensemble, it would be desirable to re-analyze the existing neutron spacing data. While each individual data set may no longer provide strong evidence in support of the orthogonal ensemble (because of statistical fluctuations), it is expected that, as a whole, the data will continue to support the random matrix model.

APPENDIX A

Table A.1 ^{57}Co Resonance Parameters

Ep (MeV)	J^{π}	ℓ'	s'	Γ (eV)	γ^2 (keV)
3.1055	3/2-			9	0.10
		1	3/2	2	0.17
		1	5/2	2	0.17
3.1084	1/2-			40	0.45
		1	3/2	4	0.44
3.1117	(5/2)+			34	1.63
		0	5/2	10	0.46
		2	5/2	1	0.28
3.1212	1/2+			48	0.26
		2	3/2	2	1.08
3.1221	3/2+			50	2.27
		0	3/2	10	0.44
		2	3/2	1	0.54
3.1256	5/2+			48	2.16
		0	5/2	12	0.52
		2	3/2	4	2.12
		2	5/2	2	1.06
3.1314	5/2+			6	0.27
		0	5/2	3	0.13
		2	3/2	1	0.26
3.1341	(3/2,5/2)+			70	3.09
		0	3/2	1	0.04
3.1390	(3/2)-			12	0.13
		1	3/2	5	0.49
		1	5/2	1	0.10
3.1438	(5/2,3/2)+			4	0.15
		0	5/2	34	1.44
		2	5/2	1	0.50
3.1484	1/2+			400	2.06
		2	3/2	12	5.84
3.1554	5/2+			55	2.41
		0	5/2	24	0.95
3.1572	3/2+			18	0.76
		0	3/2	12	0.47
		2	3/2	1	0.24
3.1614	(3/2)-			7	0.07
		1	3/2	6	0.55
		1	5/2	4	0.37
3.1617	3/2+			28	1.17
		0	3/2	4	0.16
3.1638	5/2+			28	1.16
		0	5/2	46	1.78
3.1669	5/2+			22	0.95
		0	5/2	90	3.44
		2	3/2	10	4.55
		2	5/2	3	1.37
3.1769	(3/2)-			14	0.15
3.1839	5/2+			22	0.87
		0	5/2	16	0.58
		2	3/2	5	2.14
3.1848	1/2+			350	1.70
		2	3/2	5	2.13
3.1869	(5/2)+			24	0.99
3.1887	(3/2)-			18	0.18
		1	3/2	8	0.67
3.1894	(5/2,3/2)+			10	0.39
		0	5/2	12	0.43
3.1908	(1/2)-			80	0.78
3.1951	5/2+			180	7.13
		0	5/2	120	4.20
		2	3/2	12	4.94
		2	5/2	6	2.47
3.1962	1/2+			165	0.80
		2	3/2	5	2.05
3.2007	3/2+			30	1.15
		0	3/2	120	4.13
		2	3/2	1	0.40

Table A.1 (continued)

Ep (MeV)	J^π	ℓ'	s'	Γ (eV)	γ^2 (keV)
3.2076	3/2-			40	0.38
		1	3/2	4	0.31
		1	5/2	3	0.24
3.2080	3/2-			75	0.71
		1	3/2	5	0.39
		1	5/2	10	0.78
3.2086	1/2+			960	4.47
3.2109	(5/2)+			28	1.05
		0	5/2	6	0.20
		2	3/2	2	0.78
		2	5/2	4	1.56
3.2159	(1/2)-			36	0.33
3.2191	5/2+			12	0.48
		0	5/2	20	0.65
3.2214	(5/2+,3/2+)			5	0.18
		0	5/2	20	0.65
3.2268	3/2+			115	4.17
		0	3/2	34	1.08
		2	3/2	10	4.05
3.2286	1/2+			210	0.95
		2	3/2	24	9.15
3.2346	(5/2)+			16	0.61
3.2386	3/2+			44	1.56
		0	3/2	2	0.06
3.2442	5/2+			85	3.08
		0	5/2	65	1.99
		2	3/2	14	4.86
		2	5/2	18	6.24
3.2468	3/2-			46	0.41
3.2468	5/2+			55	2.02
		0	5/2	6	0.18
		2	3/2	2	0.86
		2	5/2	2	0.52
3.2514	(3/2)-			14	0.12
		1	3/2	3	0.20
		1	5/2	3	0.20
3.2536	1/2+			115	0.50
3.2536	(3/2,1/2)-			30	0.26
		1	5/2	2	0.14
3.2552	5/2+			60	2.05
		0	5/2	8	0.23
		2	3/2	5	1.67
		2	5/2	1	0.33
3.2663	(5/2)+			16	0.53
		0	5/2	8	0.23
		2	3/2	2	0.58
3.2712	1/2+			36	0.15
3.2739	5/2+			36	1.18
		0	5/2	12	0.33
		2	3/2	3	0.94
		2	5/2	3	0.94
3.2751	3/2-			28	0.24
3.2788	(3/2)+			20	0.65
		0	3/2	1	0.03
3.2835	5/2+			22	0.71
		0	5/2	24	0.67
3.2844	1/2+			290	1.21
		2	3/2	14	4.54
3.2867	5/2+			38	1.22
		0	5/2	4	0.11
		2	5/2	8	2.41
3.2957	(3/2)-			9	0.07
		1	3/2	4	0.24
		1	5/2	8	0.48
3.3005	5/2+			110	3.43
		0	5/2	160	4.08
		2	5/2	4	1.15
3.3040	(3/2)-			16	0.13
		1	3/2	2	0.12

Table A.1 (continued)

Ep (MeV)	J^π	ℓ' s'	Γ (eV)	γ^2 (keV)
3.3057	(5/2)+		10	0.34
		0 5/2	7	0.18
		2 3/2	5	1.41
		2 5/2	2	0.42
3.3070	3/2+		34	1.05
		0 3/2	60	1.50
		2 3/2	2	0.51
3.3099	1/2+		22	0.09
3.3104	(5/2)+		12	0.40
		0 5/2	14	0.37
		2 5/2	1	0.28
3.3163	(5/2,3/2)+		16	0.48
		0 5/2	8	0.20
		2 5/2	1	0.27
3.3168	5/2+		24	0.75
		0 5/2	50	1.32
		2 5/2	2	0.54
3.3193	3/2-		60	0.46
3.3205	1/2+		50	0.19
3.3262	1/2+		780	3.04
3.3282	1/2-		330	2.50
3.3293	(5/2)+		8	0.24
		0 5/2	10	0.24
		2 5/2	1	0.26
3.3335	5/2+		46	1.34
		0 5/2	34	0.81
		2 3/2	3	0.77
		2 5/2	1	0.26
3.3369	3/2-		8	0.06
		1 3/2	5	0.26
		1 5/2	6	0.31
3.3392	1/2-		150	1.12
		1 3/2	24	1.25
3.3403	(5/2)+		9	0.26
		0 5/2	10	0.23
		2 3/2	5	1.26
		2 5/2	1	0.25
3.3471	1/2+		20	0.07
3.3476	5/2+		100	2.84
		0 5/2	400	9.27
		2 3/2	30	7.39
		2 5/2	14	3.70
3.3545	(5/2)+		50	1.40
		0 5/2	20	0.46
		2 3/2	3	0.72
		2 5/2	6	1.45
3.3602	(5/2,3/2)+		12	0.33
		0 5/2	4	0.09
3.3604	1/2+		16	0.06
		2 3/2	10	2.37
3.3656	(3/2)+		26	0.74
		0 3/2	4	0.09
		2 3/2	1	0.19
3.3690	1/2+		55	0.20
		2 3/2	16	3.69
3.3733	(5/2)+		30	0.81
		0 5/2	10	0.21
3.3767	1/2+		70	0.26
3.3811	5/2+		34	0.93
		0 5/2	16	0.33
3.3917	(1/2)-		500	3.40
		1 3/2	150	6.71
3.3920	(3/2)+		210	5.60
		0 3/2	16	0.32
		2 5/2	2	0.43
3.3978	(5/2+,3/2+)		10	0.26
3.3982	5/2+		34	0.87
		0 5/2	65	1.26

Table A.1 (continued)

Ep (MeV)	J^π	ℓ' s'	Γ (eV)	γ^2 (keV)
3.3983	1/2+		800	2.76
3.3987	(5/2,3/2)+		16	0.44
		0 5/2	2	0.04
3.4033	(3/2)-		24	0.16
3.4068	(5/2)+		12	0.30
		0 5/2	18	0.34
		2 5/2	4	0.82
3.4104	(5/2,3/2)+		8	0.20
		0 5/2	14	0.26
3.4141	5/2-		5	0.97
3.4152	(5/2)+		40	1.00
		0 5/2	34	0.65
		2 5/2	1	0.20
3.4176	1/2-		48	0.31
		1 3/2	8	0.33
3.4188	3/2-		10	0.07
		1 3/2	12	0.50
3.4197	(5/2,3/2)+		12	0.30
		0 5/2	12	0.24
3.4203	1/2-		210	1.36
		1 3/2	14	0.62
3.4205	5/2+		55	1.36
		0 5/2	8	0.15
		2 5/2	1	0.10
3.4213	3/2-		38	0.25
		1 5/2	4	0.16
3.4274	1/2+		680	2.25
3.4280	5/2-		14	2.47
		1 3/2	7	0.28
		1 5/2	9	0.36
3.4325	(5/2+,3/2+)		5	0.12
		0 5/2	20	0.36
		2 5/2	4	0.76
3.4330	1/2-		180	1.15
3.4424	(5/2,3/2)+		10	0.24
		0 5/2	3	0.05
3.4429	1/2+		140	0.45
		2 3/2	10	1.83
3.4439	3/2+		105	2.48
		0 3/2	8	0.14
		2 3/2	3	0.55
		2 5/2	6	1.10
3.4462	(5/2)+		18	0.45
		0 5/2	20	0.36
		2 5/2	4	0.73
3.4511	(5/2,3/2)+		5	0.12
		0 5/2	14	0.25
		2 3/2	3	0.54
		2 5/2	2	0.27
3.4579	1/2+		460	1.50
3.4623	(5/2,3/2)+		8	0.18
		0 5/2	10	0.16
3.4704	1/2-		370	2.22
		1 3/2	10	0.36
3.4707	(5/2,3/2)+		18	0.43
		0 5/2	18	0.29
		2 5/2	1	0.17
3.4743	5/2+		34	0.78
		0 5/2	18	0.29
3.4794	1/2+		155	0.48
		2 3/2	10	1.64
3.4829	3/2-		34	0.20
		1 3/2	2	0.07
		1 5/2	2	0.07
3.4879	1/2-		420	2.45
3.4945	1/2+		34	0.11
3.4948	3/2+		65	1.40
		0 3/2	300	4.55
		2 3/2	10	1.57

Table A.1 (continued)

Ep (MeV)	J^π	ℓ' s'	Γ (eV)	γ^2 (keV)
3.4987	5/2+		12	0.26
		0 5/2	14	0.21
		2 3/2	4	0.62
3.4990	(5/2,3/2)+		12	0.26
		2 3/2	3	0.47
3.5034	5/2+		16	0.34
		0 5/2	22	0.33
		2 3/2	2	0.31
3.5056	1/2+		195	0.58
3.5058	5/2-		3	0.43
3.5096	(3/2-,1/2-)		5	0.03
		1 3/2	4	0.13
3.5104	(5/2,3/2)+		5	0.10
		0 5/2	20	0.29
3.5141	5/2+		105	2.18
		0 5/2	55	0.84
		2 5/2	1	0.15
3.5155	(3/2-,1/2-)		5	0.03
		1 3/2	20	0.64
3.5195	3/2+		175	3.60
		0 3/2	30	0.43
		2 3/2	6	0.88
		2 5/2	12	1.76
3.5219	(5/2)+		24	0.49
		0 5/2	4	0.06
		2 5/2	1	0.07
3.5245	(5/2)+		4	0.08
		0 5/2	16	0.23
		2 5/2	6	0.87
3.5276	1/2+		370	1.06
		2 3/2	30	4.29
3.5348	3/2-		44	0.24
		1 3/2	7	0.21
		1 5/2	10	0.30
3.5366	3/2+		65	1.30
		0 3/2	42	0.57
3.5387	(5/2,3/2)+		5	0.10
		0 5/2	50	0.68
		2 3/2	10	1.39
3.5395	1/2+		460	1.30
3.5417	(5/2,3/2)+		8	0.16
		0 5/2	20	0.27
		2 3/2	4	0.55
		2 5/2	4	0.55
3.5421	1/2-		240	1.29
3.5438	(5/2,3/2)+		4	0.08
		0 5/2	8	0.11
		2 3/2	1	0.14
		2 5/2	1	0.14
3.5477	1/2+		1200	3.36
		2 3/2	60	8.11
3.5504	(3/2)-		48	0.25
		1 5/2	8	0.23
3.5525	(5/2)+		22	0.43
		0 5/2	16	0.21
		2 3/2	4	0.53
3.5546	(5/2)+		9	0.17
		0 5/2	9	0.12
3.5605	5/2+		40	0.76
		0 5/2	50	0.65
		2 5/2	4	0.52
3.5612	(5/2,3/2)+		14	0.29
		0 5/2	22	0.28
		2 5/2	1	0.13
3.5629	(3/2,1/2)-		16	0.09
		1 5/2	220	6.21
3.5659	(3/2)-		24	0.13
		1 3/2	7	0.20
		1 5/2	3	0.08
3.5664	(5/2,3/2)+		4	0.08
		0 5/2	80	1.02

Table A.1 (continued)

Ep (MeV)	J^π	ℓ'	s'	Γ (eV)	γ^2 (keV)
3.5678	(5/2,3/2)+			10	0.21
		0	5/2	5	0.06
3.5716	1/2+			420	1.15
		2	3/2	10	1.26
3.5743	(3/2)-			9	0.05
		1	3/2	7	0.19
		1	5/2	5	0.14
3.5774	(5/2)+			42	0.80
		0	5/2	10	0.14
3.5790	5/2+			80	1.48
		0	5/2	40	0.49
		2	3/2	4	0.49
		2	5/2	4	0.49
3.5804	(3/2)-			75	0.38
		1	5/2	36	0.97
3.5812	(5/2,3/2)+			14	0.28
		0	5/2	50	0.62
		2	3/2	10	1.23
		2	5/2	14	1.85
3.5828	(5/2,3/2)+			10	0.18
		0	5/2	36	0.44
		2	5/2	4	0.49
3.5862	5/2+			105	1.92
		0	5/2	2	0.03
		2	5/2	1	0.12
3.5874	3/2+			50	0.95
		0	3/2	50	0.61
3.5930	1/2-			60	0.32
3.5938	(5/2+,3/2+)			5	0.09
		0	5/2	14	0.18
3.5963	3/2-			50	0.26
		1	3/2	2	0.05
		1	5/2	3	0.08
3.5989	1/2+			1400	3.66
3.6008	1/2+			210	0.55
3.6011	(5/2,3/2)+			20	0.36
		0	5/2	6	0.07
		2	3/2	2	0.23
		2	5/2	4	0.47
3.6064	5/2+			50	0.88
		0	5/2	100	1.16
		2	3/2	5	0.57
		2	5/2	5	0.57
3.6105	5/2+			90	1.61
		0	5/2	135	1.59
		2	3/2	5	0.57
		2	5/2	4	0.45
3.6130	(5/2)+			95	1.66
		0	5/2	5	0.06
		2	5/2	10	1.13
3.6183	5/2+			14	0.25
		0	5/2	120	1.35
		2	5/2	14	1.67
3.6207	1/2+			1150	2.92
		2	3/2	60	6.62
3.6241	(3/2)-			38	0.18
		1	3/2	5	0.12
3.6295	5/2+			580	10.00
		0	5/2	170	1.87
		2	3/2	14	1.62
3.6307	(1/2)-			30	0.14
3.6316	3/2-			32	0.16
		1	3/2	20	0.50
		1	5/2	7	0.17
3.6336	3/2-			16	0.07
3.6348	5/2+			14	0.24
3.6351	(3/2)+			34	0.59
		0	3/2	200	2.17
		2	3/2	200	21.24
3.6352	1/2+			480	1.20

Table A.1 (continued)

Ep (MeV)	J^π	ℓ' s'	Γ (eV)	γ^2 (keV)
3.6406	(5/2)+		9	0.15
		0 5/2	14	0.15
		2 5/2	1	0.10
3.6416	1/2-		175	0.81
3.6455	5/2+		40	0.66
		0 5/2	38	0.40
		2 5/2	1	0.10
3.6495	5/2+		26	0.43
		0 5/2	14	0.16
		2 5/2	1	0.10
3.6508	(3/2)-		9	0.04
3.6515	(5/2)+		22	0.36
		0 5/2	70	0.73
		2 3/2	10	1.02
		2 5/2	20	2.03
3.6522	3/2+		80	1.37
		0 3/2	280	2.93
		2 3/2	10	1.01
3.6525	(3/2)-		22	0.10
		1 5/2	10	0.23
3.6531	(3/2)-		22	0.10
		1 5/2	10	0.23
3.6591	(3/2)+		12	0.21
		0 3/2	24	0.26
		2 3/2	3	0.30
		2 5/2	6	0.60
3.6613	(5/2,3/2)+		12	0.21
		0 5/2	4	0.04
3.6673	(5/2+,3/2+)		8	0.13
		0 5/2	5	0.05
		2 3/2	1	0.10
		2 5/2	2	0.19
3.6680	1/2+		250	0.60
		2 3/2	14	1.46
3.6696	(3/2)-		44	0.20
		1 3/2	4	0.09
3.6708	5/2+		60	0.95
		0 5/2	145	1.46
		2 3/2	5	0.48
		2 5/2	5	0.48
3.6784	3/2-		55	0.25
		1 3/2	20	0.45
		1 5/2	14	0.32
3.6803	(5/2,3/2)+		9	0.14
		0 5/2	100	0.98
		2 5/2	5	0.47
3.6815	(5/2+,3/2+)		8	0.12
		0 5/2	300	2.94
		2 5/2	10	0.94
3.6872	(5/2,3/2)+		20	0.31
		0 5/2	2	0.02
3.6878	(5/2,3/2)+		100	1.54
		0 5/2	5	0.05
		2 5/2	1	0.09
3.6882	1/2+		1750	4.11
		2 3/2	75	6.92
3.6908	(3/2,1/2)-		24	0.11
3.6940	3/2-		48	0.21
		1 3/2	36	0.74
		1 5/2	65	1.35
3.6984	9/2+		8	9.09
		2 5/2	38	3.42
3.7016	(5/2+,3/2+)		8	0.12
3.7023	1/2+		720	1.65
		2 3/2	150	13.35
3.7024	5/2+		70	1.08
		0 5/2	48	0.45
		2 3/2	48	4.27
		2 5/2	14	1.25
3.7035	9/2+		10	11.64
		2 5/2	1	0.09

Table A.1 (continued)

Ep (MeV)	J^π	ℓ'	s'	Γ (eV)	γ^2 (keV)
3.7125	(5/2)+			300	4.42
		0	5/2	60	0.55
		2	5/2	14	1.30
3.7130	5/2+			60	0.94
		0	5/2	8	0.07
		2	5/2	2	0.17
3.7140	1/2+			3100	7.02
		2	5/2	150	12.95
3.7154	3/2+			44	0.66
		0	3/2	400	3.64
		2	3/2	80	6.88
3.7183	9/2+			32	33.81
		2	5/2	55	4.78
3.7204	5/2+			60	0.87
		0	5/2	9	0.08
		2	3/2	26	2.29
		2	5/2	3	0.25
3.7207	3/2-			34	0.15
3.7227	(3/2,1/2)-			14	0.06
3.7233	3/2+			145	2.14
		0	3/2	65	0.59
		2	3/2	8	0.67
3.7271	(3/2-,1/2-)			8	0.03
3.7276	5/2+			140	2.01
		0	5/2	220	2.00
		2	3/2	14	1.25
		2	5/2	14	1.25
3.7312	9/2+			5	4.98
		2	5/2	20	1.65
3.7331	1/2+			65	0.14
3.7333	(5/2)+			48	0.68
		0	5/2	32	0.28
		2	3/2	8	0.66
		2	5/2	32	2.63
3.7341	3/2-			30	0.13
		1	3/2	6	0.11
3.7379	(5/2)+			18	0.27
		0	5/2	20	0.18
		2	3/2	6	0.49
		2	5/2	3	0.24
3.7422	5/2+			340	4.78
		0	5/2	220	1.94
		2	3/2	14	1.21
		2	5/2	7	0.56
3.7438	1/2+			110	0.24
3.7491	5/2+			640	9.03
		0	5/2	34	0.30
		2	3/2	14	1.18
3.7513	(9/2)+			7	6.68
3.7521	1/2+			230	0.50
3.7547	5/2+			24	0.34
		0	5/2	38	0.32
		2	5/2	2	0.16
3.7578	5/2+			280	3.84
		0	5/2	220	1.83
		2	3/2	44	3.48
		2	5/2	14	1.16
3.7597	(5/2,3/2)+			16	0.22
		0	5/2	32	0.27
		2	3/2	4	0.31
		2	5/2	1	0.08
3.7662	5/2+			1200	16.56
		0	5/2	160	1.31
		2	3/2	40	3.03
		2	5/2	70	5.30
3.7690	(5/2,3/2)+			28	0.38
		0	5/2	20	0.16
3.7704	(5/2+,3/2+)			10	0.13
3.7716	1/2+			1200	2.54
3.7725	(5/2+,3/2+)			14	0.19
3.7730	(3/2-,1/2-)			10	0.04
		1	5/2	10	0.17

Table A.1 (continued)

Ep (MeV)	J^π	ℓ' s'	Γ (eV)	γ^2 (keV)
3.7741	1/2-		800	3.08
		1 3/2	40	0.68
3.7769	3/2-		160	0.62
		1 3/2	12	0.20
		1 5/2	10	0.17
3.7838	(5/2+,3/2+)		12	0.16
3.7842	3/2-		110	0.42
		1 3/2	22	0.37
		1 5/2	8	0.13
3.7846	1/2+		1300	2.76
		2 5/2	50	3.62
3.7855	5/2+		240	3.15
		0 5/2	14	0.12
		2 5/2	5	0.36
3.7863	(5/2+,3/2+)		26	0.35
		0 5/2	200	1.57
		2 3/2	100	7.20
		2 5/2	60	4.32
3.7904	3/2+		40	0.52
		0 3/2	34	0.27
		2 3/2	6	0.43
3.7938	5/2+		85	1.10
		0 5/2	60	0.46
		2 3/2	24	1.70
		2 5/2	12	0.85
3.7945	(1/2)-		40	0.15
3.7952	(1/2)-		65	0.24
3.7960	3/2+		200	2.64
		0 3/2	42	0.32
		2 3/2	4	0.28
3.7983	3/2-		46	0.17
		1 5/2	16	0.28
3.7992	5/2+		70	0.92
		0 5/2	170	1.32
		2 3/2	28	1.95
		2 5/2	24	1.67
3.8026	(3/2+,5/2+)		10	0.13
		0 3/2	100	0.76
		2 3/2	5	0.35
3.8052	1/2+		4700	9.56
		2 3/2	175	12.03
3.8077	5/2+		80	1.01
		0 5/2	65	0.49
		2 5/2	5	0.34
3.8078	1/2+		390	0.79
3.8102	(5/2+,3/2+)		16	0.20
		0 5/2	220	1.65
		2 5/2	22	1.49
3.8127	(3/2,1/2)-		12	0.04
		1 3/2	2	0.03
		1 5/2	8	0.13
3.8182	5/2+		30	0.37
		0 5/2	2	0.02
3.8203	(1/2)-		110	0.40
		1 3/2	220	3.48
3.8230	(5/2+,3/2+)		8	0.10
		0 5/2	8	0.06
3.8239	(5/2,3/2)+		10	0.12
		0 5/2	8	0.06
		2 5/2	2	0.13
3.8245	3/2-		75	0.27
		1 3/2	6	0.09
		1 5/2	26	0.40
3.8255	(5/2+,3/2+)		12	0.15
3.8261	1/2+		1250	2.48
3.8262	(3/2,1/2)-		18	0.06
		1 5/2	7	0.11
3.8287	3/2+		185	2.27
		0 3/2	38	0.27
		2 3/2	6	0.39

Table A.1 (continued)

Ep (MeV)	J^π	ℓ'	s'	Γ (eV)	γ^2 (keV)
3.8311	1/2-			200	0.72
		1	3/2	10	0.15
3.8341	3/2-			60	0.23
		1	5/2	5	0.08
3.8362	1/2+			720	1.42
3.8387	(5/2+,3/2+)			7	0.08
		0	5/2	4	0.03
		2	5/2	1	0.06
3.8399	(1/2)-			60	0.21
		1	3/2	50	0.74
3.8406	3/2-			44	0.16
3.8414	5/2+			48	0.58
		0	5/2	130	0.93
		2	3/2	6	0.38
		2	5/2	14	0.88
3.8447	3/2+			65	0.81
		0	3/2	20	0.14
		2	3/2	3	0.19
3.8457	(5/2)-			14	1.04
		1	3/2	42	0.61
3.8473	1/2+			4500	8.73
		2	3/2	100	6.21
3.8529	1/2-			600	2.09
		1	3/2	20	0.29
3.8537	5/2+			70	0.85
		0	5/2	100	0.69
		2	3/2	65	3.98
		2	5/2	10	0.61
3.8559	1/2-			300	1.04
		1	3/2	30	0.43
3.8565	3/2-			30	0.10
		1	3/2	120	1.72
		1	5/2	60	0.86
3.8637	1/2-			1400	4.80
3.8642	(3/2)+			100	1.16
		0	3/2	14	0.10
		2	3/2	3	0.18
3.8662	5/2+			115	1.33
		0	5/2	36	0.24
		2	3/2	8	0.48
		2	5/2	14	0.83
3.8683	5/2-			4	0.29
3.8710	1/2-			420	1.45
3.8739	3/2+			75	0.89
		0	3/2	34	0.23
		2	3/2	5	0.29
3.8768	(5/2)+			14	0.17
		0	5/2	30	0.20
3.8778	1/2+			100	0.19
		2	3/2	120	6.94
3.8780	3/2+			100	1.14
		0	3/2	14	0.09
3.8795	3/2-			270	0.91
		1	3/2	220	3.00
3.8831	(5/2+,3/2+)			10	0.11
3.8834	1/2+			480	0.91
3.8836	3/2-			200	0.67
		1	5/2	60	0.81
3.8838	(5/2)+			30	0.34
3.8845	3/2+			220	2.53
		0	3/2	90	0.58
3.8869	(5/2+,3/2+)			8	0.09
		0	5/2	2	0.01
3.8881	1/2-			75	0.25
		1	3/2	30	0.40
3.8899	3/2-			520	1.73
		1	3/2	230	3.07
		1	5/2	110	1.47

Table A.1 (continued)

Ep (MeV)	J^π	ℓ'	s'	Γ (eV)	γ^2 (keV)
3.8936	1/2+			30	0.06
3.8953	3/2-			100	0.33
		1	3/2	65	0.90
		1	5/2	24	0.33
3.8962	1/2-			620	2.08
		1	3/2	20	0.26
3.8970	3/2-			22	0.07
3.8985	3/2-			50	0.16
		1	3/2	20	0.26
3.9030	1/2+			660	1.23
3.9066	1/2-			400	1.30
3.9068	5/2+			70	0.76
		0	5/2	12	0.07
		2	5/2	1	0.05
3.9083	3/2-			44	0.14
		1	3/2	10	0.13
		1	5/2	10	0.13
3.9108	(5/2+,3/2+)			10	0.11
		0	5/2	10	0.06
3.9151	1/2+			960	1.76
		2	3/2	34	1.86
3.9158	3/2+			160	1.72
		0	3/2	60	0.37
		2	3/2	1	0.05
3.9198	1/2-			1250	4.08
3.9234	5/2+			240	2.60
		0	5/2	190	1.15
		2	3/2	20	1.04
		2	5/2	5	0.26
3.9268	5/2+			270	2.85
		0	5/2	6	0.04
		2	5/2	1	0.05
3.9306	(5/2,3/2)+			9	0.09
		0	5/2	20	0.12
3.9330	3/2+			210	2.20
		0	3/2	8	0.05
3.9382	1/2+			125	0.22
		2	3/2	20	1.01
3.9385	(5/2+,3/2+)			8	0.08
3.9402	(5/2)+			20	0.22
		0	5/2	8	0.05
		2	5/2	1	0.05
3.9414	3/2+			85	0.88
		0	3/2	44	0.26
		2	3/2	1	0.05
		2	5/2	1	0.05
3.9445	1/2-			500	1.55
		1	3/2	100	1.20
3.9451	1/2+			90	0.16
3.9454	3/2+			115	1.18
		0	3/2	50	0.31
3.9514	1/2-			10000	30.78
		1	3/2	260	3.06
3.9516	5/2+			38	0.39
		0	5/2	8	0.05
		2	5/2	2	0.07
3.9524	3/2-			65	0.20
3.9559	3/2+			370	3.74
		0	3/2	115	0.65
3.9567	1/2+			640	1.12
		2	3/2	85	4.10
3.9573	(3/2)+			28	0.28
		0	3/2	3	0.02
		2	3/2	1	0.05
		2	5/2	2	0.10
3.9579	1/2-			2900	8.86
		1	3/2	180	2.09
3.9598	3/2-			32	0.10

Table A.1 (continued)

Ep (MeV)	J^π	ℓ'	s'	Γ (eV)	γ^2 (keV)
3.9598	1/2+			1100	1.89
		2	3/2	24	1.20
3.9608	(5/2,3/2)+			14	0.14
3.9614	3/2+			120	1.20
		0	3/2	44	0.25
3.9636	5/2+			50	0.54
		0	5/2	44	0.25
		2	5/2	2	0.10
3.9653	(3/2)-			8	0.02
		1	5/2	30	0.34
3.9679	1/2-			105	0.32
		1	3/2	10	0.11
3.9690	5/2+			30	0.30
		0	5/2	48	0.27
		2	5/2	24	1.13
3.9696	3/2-			105	0.32
		1	5/2	40	0.45
3.9737	5/2+			14	0.14
		0	5/2	18	0.10
3.9764	5/2+			16	0.16
		0	5/2	20	0.11
		2	5/2	5	0.23
3.9792	3/2-			30	0.09
		1	3/2	50	0.56
		1	5/2	30	0.33
3.9799	5/2+			65	0.65
		0	5/2	110	0.60
		2	3/2	8	0.37
		2	5/2	4	0.18
3.9876	1/2-			44	0.13
		1	3/2	18	0.20
3.9895	1/2+			32	0.05
3.9937	3/2-			28	0.08
3.9965	1/2-			135	0.39
		1	3/2	44	0.49
3.9968	(5/2,3/2)+			20	0.19
		0	5/2	22	0.12
		2	5/2	4	0.18
3.9993	(3/2)-			38	0.11
		1	5/2	50	0.54
4.0005	1/2+			50	0.08
4.0016	5/2+			90	0.85
		0	5/2	150	0.79
		2	3/2	10	0.44
		2	5/2	40	1.75

Notes:

1. Absolute uncertainties in the resonance energies are 3 keV. The relative uncertainties (difference between two resonances) are 1 keV for resonances separated by more than 100 keV, 1% for resonances separated by more than 10 keV but less than 100 keV, and 100 eV for resonances separated by less than 10 keV.
2. Uncertainties in laboratory widths are 10% for widths greater than 50 eV. For widths smaller than 50 eV, the uncertainties are 5 eV.
3. For d-wave resonances, the total inelastic widths have errors as described in (2.) but the errors for each channel may be considerably larger.

Table A.2 ^{57}Co Resonance Parameters

Ep (MeV)	ℓ' s'	Γ (eV)	γ^2 (keV)	Ep (MeV)	ℓ' s'	Γ (eV)	γ^2 (keV)
	1/2+			3.4579		460	1.50
				3.4794		155	0.48
					2 3/2	10	1.64
3.1212		48	0.26				
	2 3/2	2	1.08	3.4945		34	0.11
3.1484		400	2.06	3.5056		195	0.58
	2 3/2	12	5.84				
				3.5276		370	1.06
3.1848		350	1.70		2 3/2	30	4.29
	2 3/2	5	2.13				
				3.5395		460	1.30
3.1962		165	0.80				
	2 3/2	5	2.05	3.5477		1200	3.36
					2 3/2	60	8.11
3.2086		960	4.47				
				3.5716		420	1.15
3.2286		210	0.95		2 3/2	10	1.26
	2 3/2	24	9.15				
				3.5989		1400	3.66
3.2536		115	0.50				
				3.6008		210	0.55
3.2712		36	0.15				
				3.6207		1150	2.92
3.2844		290	1.21		2 3/2	60	6.62
	2 3/2	14	4.54				
				3.6352		480	1.20
3.3099		22	0.09				
				3.6680		250	0.60
3.3205		50	0.19		2 3/2	14	1.46
3.3262		780	3.04	3.6882		1750	4.11
					2 3/2	75	6.92
3.3471		20	0.07				
				3.7023		720	1.65
3.3604		16	0.06		2 3/2	150	13.35
	2 3/2	10	2.37				
				3.7140		3100	7.02
3.3690		55	0.20		2 5/2	150	12.95
	2 3/2	16	3.69				
				3.7331		65	0.14
3.3767		70	0.26				
				3.7438		110	0.24
3.3983		800	2.76				
				3.7521		230	0.50
3.4274		680	2.25				
				3.7716		1200	2.54
3.4429		140	0.45				
	2 3/2	10	1.83	3.7846		1300	2.76
					2 5/2	50	3.62

Table A.2 (continued)

Ep (MeV)		ℓ' s'	Γ (eV)	γ^2 (keV)
3.8052			4700	9.56
		2 3/2	175	12.03
3.8078			390	0.79
3.8261			1250	2.48
3.8362			720	1.42
3.8473			4500	8.73
		2 3/2	100	6.21
3.8778			100	0.19
		2 3/2	120	6.94
3.8834			480	0.91
3.8936			30	0.06
3.9030			660	1.23
3.9151			960	1.76
		2 3/2	34	1.86
3.9382			125	0.22
		2 3/2	20	1.01
3.9451			90	0.16
3.9567			640	1.12
		2 3/2	85	4.10
3.9598			1100	1.89
		2 3/2	24	1.20
3.9895			32	0.05
4.0005			50	0.08
		1/2-		
3.1084			40	0.45
		1 3/2	4	0.44
3.1908	a		80	0.78
3.2159	a		36	0.33
3.3282			330	2.50
3.3392			150	1.12
		1 3/2	24	1.25
3.3917	a		500	3.40
		1 3/2	150	6.71
3.4176			48	0.31
		1 3/2	8	0.33
3.4203			210	1.36
		1 3/2	14	0.62
3.4330			180	1.15
3.4704			370	2.22
		1 3/2	10	0.36
3.4879			420	2.45
3.5421			240	1.29
3.5930			60	0.32
3.6307	a		30	0.14
3.6416			175	0.81
3.7741			800	3.08
		1 3/2	40	0.68
3.7945	a		40	0.15
3.7952	a		65	0.24
3.8203	a		110	0.40
		1 3/2	220	3.48
3.8311			200	0.72
		1 3/2	10	0.15
3.8399	a		60	0.21
		1 3/2	50	0.74
3.8529			600	2.09
		1 3/2	20	0.29
3.8559			300	1.04
		1 3/2	30	0.43
3.8637			1400	4.80

Table A.2 (continued)

Ep (MeV)		ℓ s'	Γ (eV)	γ^2 (keV)
3.8710			420	1.45
3.8881			75	0.25
		1 3/2	30	0.40
3.8962			620	2.08
		1 3/2	20	0.26
3.9066			400	1.30
3.9198			1250	4.08
3.9445			500	1.55
		1 3/2	100	1.20
3.9514			10000	30.78
		1 3/2	260	3.06
3.9579			2900	8.86
		1 3/2	180	2.09
3.9679			105	0.32
		1 3/2	10	0.11
3.9876			44	0.13
		1 3/2	18	0.20
3.9965			135	0.39
		1 3/2	44	0.49
		3/2-		
3.1055			9	0.10
		1 3/2	2	0.17
		1 5/2	2	0.17
3.1390	a		12	0.13
		1 3/2	5	0.49
		1 5/2	1	0.10
3.1614	a		7	0.07
		1 3/2	6	0.55
		1 5/2	4	0.37
3.1769	a		14	0.15
3.1887	a		18	0.18
		1 3/2	8	0.67
3.2076			40	0.38
		1 3/2	4	0.31
		1 5/2	3	0.24
3.2080			75	0.71
		1 3/2	5	0.39
		1 5/2	10	0.78
3.2468			46	0.41
3.2514	a		14	0.12
		1 3/2	3	0.20
		1 5/2	3	0.20
3.2536	b		30	0.26
		1 5/2	2	0.14
3.2751			28	0.24
3.2957	a		9	0.07
		1 3/2	4	0.24
		1 5/2	8	0.48
3.3040	a		16	0.13
		1 3/2	2	0.12
3.3193			60	0.46
3.3369			8	0.06
		1 3/2	5	0.26
		1 5/2	6	0.31
3.4033	a		24	0.16
3.4188			10	0.07
		1 3/2	12	0.50
3.4213			38	0.25
		1 5/2	4	0.16
3.4829			34	0.20
		1 3/2	2	0.07
		1 5/2	2	0.07
3.5096	c		5	0.03
		1 3/2	4	0.13
3.5155	c		5	0.03
		1 3/2	20	0.64

Table A.2 (continued)

Ep (MeV)		ℓ' s'	Γ (eV)	γ^2 (keV)
3.5348			44	0.24
		1 3/2	7	0.21
		1 5/2	10	0.30
3.5504	a		48	0.25
		1 5/2	8	0.23
3.5629	b		16	0.09
		1 5/2	220	6.21
3.5659	a		24	0.13
		1 3/2	7	0.20
		1 5/2	3	0.08
3.5743	a		9	0.05
		1 3/2	7	0.19
		1 5/2	5	0.14
3.5804	a		75	0.38
		1 5/2	36	0.97
3.5963			50	0.26
		1 3/2	2	0.05
		1 5/2	3	0.08
3.6241	a		38	0.18
		1 3/2	5	0.12
3.6316			32	0.16
		1 3/2	20	0.50
		1 5/2	7	0.17
3.6336			16	0.07
3.6508	a		9	0.04
3.6525	a		22	0.10
		1 5/2	10	0.23
3.6531	a		22	0.10
		1 5/2	10	0.23
3.6696	a		44	0.20
		1 3/2	4	0.09
3.6784			55	0.25
		1 3/2	20	0.45
		1 5/2	14	0.32
3.6908	b		24	0.11
3.6940			48	0.21
		1 3/2	36	0.74
		1 5/2	65	1.35
3.7207			34	0.15
3.7227	b		14	0.06
3.7271	c		8	0.03
3.7341			30	0.13
		1 3/2	6	0.11
3.7730	c		10	0.04
		1 5/2	10	0.17
3.7769			160	0.62
		1 3/2	12	0.20
		1 5/2	10	0.17
3.7842			110	0.42
		1 3/2	22	0.37
		1 5/2	8	0.13
3.7983			46	0.17
		1 5/2	16	0.28
3.8127	b		12	0.04
		1 3/2	2	0.03
		1 5/2	8	0.13
3.8245			75	0.27
		1 3/2	6	0.09
		1 5/2	26	0.40
3.8262	b		18	0.06
		1 5/2	7	0.11
3.8341			60	0.23
		1 5/2	5	0.08
3.8406			44	0.16
3.8565			30	0.10
		1 3/2	120	1.72
		1 5/2	60	0.86
3.8795			270	0.91
		1 3/2	220	3.00

Table A.2 (continued)

Ep (MeV)		ℓ' s'	Γ (eV)	γ^2 (keV)
3.8836			200	0.67
		1 5/2	60	0.81
3.8899			520	1.73
		1 3/2	230	3.07
		1 5/2	110	1.47
3.8953			100	0.33
		1 3/2	65	0.90
		1 5/2	24	0.33
3.8970			22	0.07
3.8985			50	0.16
		1 3/2	20	0.26
3.9083			44	0.14
		1 3/2	10	0.13
		1 5/2	10	0.13
3.9524			65	0.20
3.9598			32	0.10
3.9653	a		8	0.02
		1 5/2	30	0.34
3.9696			105	0.32
		1 5/2	40	0.45
3.9792			30	0.09
		1 3/2	50	0.56
		1 5/2	30	0.33
3.9937			28	0.08
3.9993	a		38	0.11
		1 5/2	50	0.54
		3/2+		
3.1221			50	2.27
		0 3/2	10	0.44
		2 3/2	1	0.54
3.1341	b		70	3.09
		0 3/2	1	0.04
3.1572			18	0.76
		0 3/2	12	0.47
		2 3/2	1	0.24
3.1617			28	1.17
		0 3/2	4	0.16
3.2007			30	1.15
		0 3/2	120	4.13
		2 3/2	1	0.40
3.2268			115	4.17
		0 3/2	34	1.08
		2 3/2	10	4.05
3.2386			44	1.56
		0 3/2	2	0.06
3.2788	a		20	0.65
		0 3/2	1	0.03
3.3070			34	1.05
		0 3/2	60	1.50
		2 3/2	2	0.51
3.3656	a		26	0.74
		0 3/2	4	0.09
		2 3/2	1	0.19
3.3920	a		210	5.60
		0 3/2	16	0.32
		2 5/2	2	0.43
3.4439			105	2.48
		0 3/2	8	0.14
		2 3/2	3	0.55
		2 5/2	6	1.10
3.4948			65	1.40
		0 3/2	300	4.55
		2 3/2	10	1.57
3.5195			175	3.60
		0 3/2	30	0.43
		2 3/2	6	0.88
		2 5/2	12	1.76
3.5366			65	1.30
		0 3/2	42	0.57

Table A.2 (continued)

Ep (MeV)		ℓ' s'	Γ (eV)	γ^2 (keV)
3.5874			50	0.95
		0 3/2	50	0.61
3.6351	a		34	0.59
		0 3/2	200	2.17
		2 3/2	200	21.24
3.6522			80	1.37
		0 3/2	280	2.93
		2 3/2	10	1.01
3.6591	a		12	0.21
		0 3/2	24	0.26
		2 3/2	3	0.30
		2 5/2	6	0.60
3.7154			44	0.66
		0 3/2	400	3.64
		2 3/2	80	6.88
3.7233			145	2.14
		0 3/2	65	0.59
		2 3/2	8	0.67
3.7904			40	0.52
		0 3/2	34	0.27
		2 3/2	6	0.43
3.7960			200	2.64
		0 3/2	42	0.32
		2 3/2	4	0.28
3.8026	c		10	0.13
		0 3/2	100	0.76
		2 3/2	5	0.35
3.8287			185	2.27
		0 3/2	38	0.27
		2 3/2	6	0.39
3.8447			65	0.81
		0 3/2	20	0.14
		2 3/2	3	0.19
3.8642	a		100	1.16
		0 3/2	14	0.10
		2 3/2	3	0.18
3.8739			75	0.89
		0 3/2	34	0.23
		2 3/2	5	0.29
3.8780			100	1.14
		0 3/2	14	0.09
3.8845			220	2.53
		0 3/2	90	0.58
3.9158			160	1.72
		0 3/2	60	0.37
		2 3/2	1	0.05
3.9330			210	2.20
		0 3/2	8	0.05
3.9414			85	0.88
		0 3/2	44	0.26
		2 3/2	1	0.05
		2 5/2	1	0.05
3.9454			115	1.18
		0 3/2	50	0.31
3.9559			370	3.74
		0 3/2	115	0.65
3.9573	a		28	0.28
		0 3/2	3	0.02
		2 3/2	1	0.05
		2 5/2	2	0.10
3.9614			120	1.20
		0 3/2	44	0.25
		5/2+		
3.1117	a		34	1.63
		0 5/2	10	0.46
		2 5/2	1	0.28
3.1256			48	2.16
		0 5/2	12	0.52
		2 3/2	4	2.12
		2 5/2	2	1.06
3.1314			6	0.27
		0 5/2	3	0.13
		2 3/2	1	0.26

Table A.2 (continued)

Ep (MeV)		ℓ' s'	Γ (eV)	γ^2 (keV)
3.1438	b		4	0.15
		0 5/2	34	1.44
		2 5/2	1	0.50
3.1554			55	2.41
		0 5/2	24	0.95
3.1638			28	1.16
		0 5/2	46	1.78
3.1669			22	0.95
		0 5/2	90	3.44
		2 3/2	10	4.55
		2 5/2	3	1.37
3.1839			22	0.87
		0 5/2	16	0.58
		2 3/2	5	2.14
3.1869	a		24	0.99
3.1894	b		10	0.39
		0 5/2	12	0.43
3.1951			180	7.13
		0 5/2	120	4.20
		2 3/2	12	4.94
		2 5/2	6	2.47
3.2109	a		28	1.05
		0 5/2	6	0.20
		2 3/2	2	0.78
		2 5/2	4	1.56
3.2191			12	0.48
		0 5/2	20	0.65
3.2214	c		5	0.18
		0 5/2	20	0.65
3.2346	a		16	0.61
3.2442			85	3.08
		0 5/2	65	1.99
		2 3/2	14	4.86
		2 5/2	18	6.24
3.2468			55	2.02
		0 5/2	6	0.18
		2 3/2	2	0.86
		2 5/2	2	0.52
3.2552			60	2.05
		0 5/2	8	0.23
		2 3/2	5	1.67
		2 5/2	1	0.33
3.2663	a		16	0.53
		0 5/2	8	0.23
		2 3/2	2	0.58
3.2739			36	1.18
		0 5/2	12	0.33
		2 3/2	3	0.94
		2 5/2	3	0.94
3.2835			22	0.71
		0 5/2	24	0.67
3.2867			38	1.22
		0 5/2	4	0.11
		2 5/2	8	2.41
3.3005			110	3.43
		0 5/2	160	4.08
		2 5/2	4	1.15
3.3057	a		10	0.34
		0 5/2	7	0.18
		2 3/2	5	1.41
		2 5/2	2	0.42
3.3104	a		12	0.40
		0 5/2	14	0.37
		2 5/2	1	0.28
3.3163	b		16	0.48
		0 5/2	8	0.20
		2 5/2	1	0.27
3.3168			24	0.75
		0 5/2	50	1.32
		2 5/2	2	0.54
3.3293	a		8	0.24
		0 5/2	10	0.24
		2 5/2	1	0.26
3.3335			46	1.34
		0 5/2	34	0.81
		2 3/2	3	0.77
		2 5/2	1	0.26

Table A.2 (continued)

Ep (MeV)		ℓ' s'	Γ (eV)	γ^2 (keV)
3.3403	a		9	0.26
		0 5/2	10	0.23
		2 3/2	5	1.26
		2 5/2	1	0.25
3.3476			100	2.84
		0 5/2	400	9.27
		2 3/2	30	7.39
		2 5/2	14	3.70
3.3545	a		50	1.40
		0 5/2	20	0.46
		2 3/2	3	0.72
		2 5/2	6	1.45
3.3602	b		12	0.33
		0 5/2	4	0.09
3.3733	a		30	0.81
		0 5/2	10	0.21
3.3811			34	0.93
		0 5/2	16	0.33
3.3978	c		10	0.26
3.3982			34	0.87
		0 5/2	65	1.26
3.3987	b		16	0.44
		0 5/2	2	0.04
3.4068	a		12	0.30
		0 5/2	18	0.34
		2 5/2	4	0.82
3.4104	b		8	0.20
		0 5/2	14	0.26
3.4152	a		40	1.00
		0 5/2	34	0.65
		2 5/2	1	0.20
3.4197	b		12	0.30
		0 5/2	12	0.24
3.4205			55	1.36
		0 5/2	8	0.15
		2 5/2	1	0.10
3.4325	c		5	0.12
		0 5/2	20	0.36
		2 5/2	4	0.76
3.4424	b		10	0.24
		0 5/2	3	0.05
3.4462	a		18	0.45
		0 5/2	20	0.36
		2 5/2	4	0.73
3.4511	b		5	0.12
		0 5/2	14	0.25
		2 3/2	3	0.54
		2 5/2	2	0.27
3.4623	b		8	0.18
		0 5/2	10	0.16
3.4707	b		18	0.43
		0 5/2	18	0.29
		2 5/2	1	0.17
3.4743			34	0.78
		0 5/2	18	0.29
3.4987			12	0.26
		0 5/2	14	0.21
		2 3/2	4	0.62
3.4990	b		12	0.26
		2 3/2	3	0.47
3.5034			16	0.34
		0 5/2	22	0.33
		2 3/2	2	0.31
3.5104	b		5	0.10
		0 5/2	20	0.29
3.5141			105	2.18
		0 5/2	55	0.84
		2 5/2	1	0.15
3.5219	a		24	0.49
		0 5/2	4	0.06
		2 5/2	1	0.07
3.5245	a		4	0.08
		0 5/2	16	0.23
		2 5/2	6	0.87

Table A.2 (continued)

Ep (MeV)		ℓ' s'	Γ (eV)	γ^2 (keV)
3.5387	b		5	0.10
		0 5/2	50	0.68
		2 3/2	10	1.39
3.5417	b		8	0.16
		0 5/2	20	0.27
		2 3/2	4	0.55
		2 5/2	4	0.55
3.5438	b		4	0.08
		0 5/2	8	0.11
		2 3/2	1	0.14
		2 5/2	1	0.14
3.5525	a		22	0.43
		0 5/2	16	0.21
		2 3/2	4	0.53
3.5546	a		9	0.17
		0 5/2	9	0.12
3.5605			40	0.76
		0 5/2	50	0.65
		2 5/2	4	0.52
3.5612	b		14	0.29
		0 5/2	22	0.28
		2 5/2	1	0.13
3.5664	b		4	0.08
		0 5/2	80	1.02
3.5678	b		10	0.21
		0 5/2	5	0.06
3.5774	a		42	0.80
		0 5/2	10	0.14
3.5790			80	1.48
		0 5/2	40	0.49
		2 3/2	4	0.49
		2 5/2	4	0.49
3.5812	b		14	0.28
		0 5/2	50	0.62
		2 3/2	10	1.23
		2 5/2	14	1.85
3.5828	b		10	0.18
		0 5/2	36	0.44
		2 5/2	4	0.49
3.5862			105	1.92
		0 5/2	2	0.03
		2 5/2	1	0.12
3.5938	c		5	0.09
		0 5/2	14	0.18
3.6011	b		20	0.36
		0 5/2	6	0.07
		2 3/2	2	0.23
		2 5/2	4	0.47
3.6064			50	0.88
		0 5/2	100	1.16
		2 3/2	5	0.57
		2 5/2	5	0.57
3.6105			90	1.61
		0 5/2	135	1.59
		2 3/2	5	0.57
		2 5/2	4	0.45
3.6130	a		95	1.66
		0 5/2	5	0.06
		2 5/2	10	1.13
3.6183			14	0.25
		0 5/2	120	1.35
		2 5/2	14	1.67
3.6295			580	10.00
		0 5/2	170	1.87
		2 3/2	14	1.62
3.6348			14	0.24
3.6406	a		9	0.15
		0 5/2	14	0.15
		2 5/2	1	0.10
3.6455			40	0.66
		0 5/2	38	0.40
		2 5/2	1	0.10
3.6495			26	0.43
		0 5/2	14	0.16
		2 5/2	1	0.10

Table A.2 (continued)

Ep (MeV)		ℓ' s'	Γ (eV)	γ^2 (keV)
3.6515	a		22	0.36
		0 5/2	70	0.73
		2 3/2	10	1.02
		2 5/2	20	2.03
3.6613	b		12	0.21
		0 5/2	4	0.04
3.6673	c		8	0.13
		0 5/2	5	0.05
		2 3/2	1	0.10
		2 5/2	2	0.19
3.6708			60	0.95
		0 5/2	145	1.46
		2 3/2	5	0.48
		2 5/2	5	0.48
3.6803	b		9	0.14
		0 5/2	100	0.98
		2 5/2	5	0.47
3.6815	c		8	0.12
		0 5/2	300	2.94
		2 5/2	10	0.94
3.6872	b		20	0.31
		0 5/2	2	0.02
3.6878	b		100	1.54
		0 5/2	5	0.05
		2 5/2	1	0.09
3.7016	c		8	0.12
3.7024			70	1.08
		0 5/2	48	0.45
		2 3/2	48	4.27
		2 5/2	14	1.25
3.7125	a		300	4.42
		0 5/2	60	0.55
		2 5/2	14	1.30
3.7130			60	0.94
		0 5/2	8	0.07
		2 5/2	2	0.17
3.7204			60	0.87
		0 5/2	9	0.08
		2 3/2	26	2.29
		2 5/2	3	0.25
3.7276			140	2.01
		0 5/2	220	2.00
		2 3/2	14	1.25
		2 5/2	14	1.25
3.7333	a		48	0.68
		0 5/2	32	0.28
		2 3/2	8	0.66
		2 5/2	32	2.63
3.7379	a		18	0.27
		0 5/2	20	0.18
		2 3/2	6	0.49
		2 5/2	3	0.24
3.7422			340	4.78
		0 5/2	220	1.94
		2 3/2	14	1.21
		2 5/2	7	0.56
3.7491			640	9.03
		0 5/2	34	0.30
		2 3/2	14	1.18
3.7547			24	0.34
		0 5/2	38	0.32
		2 5/2	2	0.16
3.7578			280	3.84
		0 5/2	220	1.83
		2 3/2	44	3.48
		2 5/2	14	1.16
3.7597	b		16	0.22
		0 5/2	32	0.27
		2 3/2	4	0.31
		2 5/2	1	0.08
3.7662			1200	16.56
		0 5/2	160	1.31
		2 3/2	40	3.03
		2 5/2	70	5.30
3.7690	b		28	0.38
		0 5/2	20	0.16

Table A.2 (continued)

Ep (MeV)		ℓ' s'	Γ (eV)	γ^2 (keV)	Ep (MeV)		ℓ' s'	Γ (eV)	γ^2 (keV)
3.7704	c		10	0.13	3.8414			48	0.58
							0 5/2	130	0.93
3.7725	c		14	0.19			2 3/2	6	0.38
							2 5/2	14	0.88
3.7838	c		12	0.16					
					3.8537			70	0.85
3.7855			240	3.15			0 5/2	100	0.69
		0 5/2	14	0.12			2 3/2	65	3.98
		2 5/2	5	0.36			2 5/2	10	0.61
3.7863	c		26	0.35	3.8662			115	1.33
		0 5/2	200	1.57			0 5/2	36	0.24
		2 3/2	100	7.20			2 3/2	8	0.48
		2 5/2	60	4.32			2 5/2	14	0.83
3.7938			85	1.10	3.8768	a		14	0.17
		0 5/2	60	0.46			0 5/2	30	0.20
		2 3/2	24	1.70					
		2 5/2	12	0.85	3.8831	c		10	0.11
3.7992			70	0.92	3.8838	a		30	0.34
		0 5/2	170	1.32					
		2 3/2	28	1.95	3.8869	c		8	0.09
		2 5/2	24	1.67			0 5/2	2	0.01
3.8077			80	1.01	3.9068			70	0.76
		0 5/2	65	0.49			0 5/2	12	0.07
		2 5/2	5	0.34			2 5/2	1	0.05
3.8102	c		16	0.20	3.9108	c		10	0.11
		0 5/2	220	1.65			0 5/2	10	0.06
		2 5/2	22	1.49					
					3.9234			240	2.60
3.8182			30	0.37			0 5/2	190	1.15
		0 5/2	2	0.02			2 3/2	20	1.04
							2 5/2	5	0.26
3.8230	c		8	0.10					
		0 5/2	8	0.06	3.9268			270	2.85
							0 5/2	6	0.04
3.8239	b		10	0.12			2 5/2	1	0.05
		0 5/2	8	0.06					
		2 5/2	2	0.13	3.9306	b		9	0.09
							0 5/2	20	0.12
3.8255	c		12	0.15					
					3.9385	c		8	0.08
3.8387	c		7	0.08					
		0 5/2	4	0.03	3.9402	a		20	0.22
		2 5/2	1	0.06			0 5/2	8	0.05
							2 5/2	1	0.05

Table A.2 (continued)

Ep (MeV)		ℓ' s'	Γ (eV)	γ^2 (keV)	Ep (MeV)		ℓ' s'	Γ (eV)	γ^2 (keV)
3.9516			38	0.39					
		0 5/2	8	0.05			5/2-		
		2 5/2	2	0.07					
3.9608	b		14	0.14	3.4141			5	0.97
3.9636			50	0.54	3.4280			14	2.47
		0 5/2	44	0.25			1 3/2	7	0.28
		2 5/2	2	0.10			1 5/2	9	0.36
3.9690			30	0.30	3.5058			3	0.43
		0 5/2	48	0.27					
		2 5/2	24	1.13	3.8457	c		14	1.04
							1 3/2	42	0.61
3.9737			14	0.14					
		0 5/2	18	0.10	3.8683			4	0.29
3.9764			16	0.16					
		0 5/2	20	0.11			9/2+		
		2 5/2	5	0.23					
3.9799			65	0.65	3.6984			8	9.09
		0 5/2	110	0.60			2 5/2	38	3.42
		2 3/2	8	0.37					
		2 5/2	4	0.18	3.7035			10	11.64
							2 5/2	1	0.09
3.9968	b		20	0.19					
		0 5/2	22	0.12	3.7183			32	33.81
		2 5/2	4	0.18			2 5/2	55	4.78
4.0016			90	0.85	3.7312			5	4.98
		0 5/2	150	0.79			2 5/2	20	1.65
		2 3/2	10	0.44					
		2 5/2	40	1.75	3.7513	c		7	6.68

Notes:

a. Spin assignment uncertain but preferred.
b. Spin assignment unknown, ℓ assignment certain.
c. ℓ assignment uncertain.

See also notes at the end of Table A.1.

APPENDIX B

The Spacing Probability Distribution for a Random Superposition of n Unrelated Sequences with Missing Levels

The purpose of this appendix is to generalize slightly the derivation given by Mehta in appendix A22 of Random Matrices (1971). The major change is that we wish to work with a probability distribution function (PDF) whose mean is not one. Let $p_i'(\rho_i S)\,dS$ be the probability that an observed spacing in the i-th sequence is between S and S+dS where the fraction of levels observed for that sequence is f_i^+. If $p_i^K(\rho_i S)$ is the PDF for the k-th order spacing distribution, then

$$p_i'(\rho_i S) = \sum_{K=0}^{\infty} f_i^+ (1-f_i^+)^K \, p_i^K(\rho_i S) \tag{B.1}$$

Thus

$$\int_0^\infty p'(x)\,dx = \sum_{K=0}^{\infty} f^+(1-f^+)^K = 1 \tag{B.2}$$

$$\int_0^\infty x\,p'(x)\,dx = \sum f^+(1-f^+)^K\,(k+1) = 1/f^+ \tag{B.3}$$

The probability of observing a spacing less than or equal to x is

$$F_i(x) = \int_0^x p_i'(y)\,dy = 1 - \int_x^\infty p_i'(y)\,dy \tag{B.4}$$

$$= 1 - \int_0^\infty p_i'(x+y)\,dy \tag{B.5}$$

The probability that an interval from E to E+x is empty is equal to the probability that a level lies between E+y and E+y+dy times the probability of observing a spacing greater than y (stretching from E to E+y) integrated over all values of $y > x$:

$$E_i(x) \propto \int_x^\infty (1 - F_i(y))\,dy \tag{B.6}$$

$$= \int_x^\infty [\int_o^\infty p_i'(y+z)\,dz]\,dy$$

$$= \int_o^\infty \int_o^\infty p_i'(x+y+z)\,dy\,dz$$

$$= \int_o^\infty y p_i'(x+y)\,dy$$

Using $E(0) = 1$ for a normalization condition gives

$$E_i(x) = f_i^+ \int_o^\infty y p_i'(x+y)\,dy \qquad (B.7)$$

Following Mehta, consider the superposition of n sequences with a total density given by

$$\rho = \sum_i \rho_i \qquad (B.8)$$

The total observed density is $\rho' = \sum \rho_i f_i^+$. Let $P(\rho S)\,dS$ be the probability that an observed spacing will lie between S and S+dS for the combined sequence. Then

$$F(x) = \int_o^x P(y)\,dy = 1 - \int_o^\infty P(x+y)\,dy \qquad (B.9)$$

and

$$E(x) = \frac{\rho'}{\rho} \int_o^\infty y\, P(x+y)\,dy \qquad (B.10)$$

If the sequences are unrelated then the probability that an interval will not contain any (observed) levels is the product of the probabilities that the interval will not contain a level from any sequence:

$$E(\rho S) = \prod_i E_i(\rho_i S) \qquad (B.11)$$

Let $r_i = \rho_i/\rho$, $\sum r_i = 1$, then

$$E(x) = \prod_i E_i(r_i x) \qquad (B.12)$$

Differentiating twice gives

$$P(x) = \frac{\rho}{\rho'}\, d^2E(y)/dy^2 \qquad (B.13)$$

$$= \frac{\rho}{\rho'} E(x) \{ \sum r_i^2 f_i^+ p_i(r_i x)/E_i(r_i x)$$

$$+ (\sum r_i f_i^+ [1-F_i(r_i x)]/E_i(r_i x))^2 - \sum (r_i f_i^+ [1-F_i(r_i x)]/E_i(r_i x))^2 \}$$

(Note that x is in units of the true average level spacing.) This expression was used for calculating the superimposed PDF for the p-wave and d-wave level spacings.

LIST OF REFERENCES

R. R. Auble, Nuclear Data Sheets 20 (1977) 248.

Y. Baubinet-Robinet, Nucl. Phys. A222 (1974) 525.

H. A. Bethe, Phys. Rev. 47 (1935) 747.

E. G. Bilpuch, A. M. Lane, G. E. Mitchell, J. D. Moses, Phys. Rep. 28 (1976) 145.

M. E. Bleck, unpublished Ph.D. dissertation, Duke University (1978).

N. Bohr, Nature 137 (1936) 344.

T. A. Brody, J. Flores, P. A. Mello, J. B. French, and S. S. M. Wong, Notas de Fisica 1 (1978).

B. H. Chou, unpublished Ph.D. dissertation, North Carolina State University (1980).

F. J. Dyson, J. Math. Phys. 3 (1962) 140.

F. J. Dyson, J. Math. Phys. 3 (1962) 166.

F. J. Dyson and M. L. Mehta, J. Math. Phys. 4 (1963) 70.

J. B. French, P. A. Mello, and A. Pandey, Ann. Phy. 11B (1978) 277.

M. Gaudin, Nucl. Phys 25 (1961) 447.

A. Gilbert and A. G. W. Cameron, Can. J. Phys. 43 (1965) 1446.

H. L. Harney and H. A. Weidenmuller, Nucl. Phys. A139 (1969) 241.

J. Jänecke, Isospin in Nuclear Physics, ed. D. H. Wilkinson (North-Holland, Amsterdam, 1969) 297.

P. L. Kapur and R. E. Peierls, Proc. Roy. Soc. A166 (1938) 277.

A. M. Lane, Nucl. Phys. 35 (1962) 676.

A. M. Lane and R. G. Thomas, Rev. Mod. Phys. 30 (1958) 257.

A. M. Lane, Isospin in Nuclear Physics, ed. D. H. Wilkinson (North-Holland, Amsterdam, 1969) 509.

H. I. Liou, H. S. Camarda, and F. Rahn, Phys. Rev. C5 (1972) 1002.

H. I. Liou, H. S. Camarda, S. Wynchank, M. Slagowitz, G. Hacken, F. Rahn, and J. Rainwater, Phys. Rev. C5 (1972) 974.

J. E. Lynn, The Theory of Neutron Resonance Reactions (Oxford, London, 1968).

W. M. MacDonald, Phys. Rev. C20 (1979) 426.

W. M. MacDonald, Ann. of Phys. 125 (1980) 253.

M. L. Mehta, Random Matrices (Academic, New York, 1967).

M. L. Mehta and J. des Cloizeaux, Ind. J. Math. 3 (1972) 329.

M. L. Mehta and M. Gaudin, Nucl. Phys. 18 (1960) 420.

P. A. Mello, Ann. Phys. 45 (1967) 240.

P. L. Meyer, Introductory Probability and Statistical Applications (Addison-Wesley, Reading, Mass., 1970).

C. E. Porter, Statistical Theories of Spectra: Fluctuations (Academic, New York, 1965).

C. E. Porter and R. G. Thomas, Phys. Rev. 104 (1956) 384.

D. Robson, Isospin in Nuclear Physics, ed. D. H. Wilkinson (North-Holland, Amsterdam, 1969) 461.

D. Robson, Phys. Rev. 137 (1965) B535.

W. K. Wells, unpublished Ph.D. dissertation, Duke University (1978).

E. P. Wigner, Oak Ridge National Laboratory Report ORNL-2309 (1967) 59.

E. P. Wigner and L. Eisenbud, Phys. Rev. 72 (1947) 29.

D. H. Wilkinson, Isospin in Nuclear Physics, ed. D. H. Wilkinson (North-Holland, Amsterdam, 1969).

W. M. Wilson, unpublished Ph.D. dissertation, Duke University (1973).

W. M. Wilson, E. G. Bilpuch, and G. E. Mitchell, Nucl. Phys. A245 (1975) 285.

BIOGRAPHY

William Alter Watson III

Personal: Born 5 May, 1954, Jackson, Mississippi

Education: B. S. in Physics, Georgia Institute of Technology, 1975

Positions: James B. Duke Fellow, Duke University, 1975-1978
Research Assistant, Duke University, 1978-present

Articles: "Inelastic Proton Amplitudes for f-Wave Resonances in ^{55}Co," W. A. Watson III, E. G. Bilpuch and G. E. Mitchell, Z. Physik A294 (1980) 153.

Abstracts: "High Resolution Proton Inelastic Scattering on ^{54}Fe," W. A. Watson III, E. G. Bilpuch, C. R. Westerfeldt, G. E. Mitchell and K. B. Sales, B. A. P. S. 24 (1979) 107.

"High Resolution Proton Elastic and Inelastic Scattering on ^{56}Fe," W. A. Watson III, E. G. Bilpuch, C. R. Westerfeldt, G. E. Mitchell and K. B. Sales, B. A. P. S. 25 (1980) 595.